CONTINUAL TRAVELING WAVES IN FINITE STRUCTURES : THEORY, SIMULATIONS, AND EXPERIMENTS

VIJAYA VENKATA NARASIMHA SRIRAM MALLADI

Dissertation submitted to the Faculty of the
Virginia Polytechnic Institute and State University
in partial fulfillment of the requirements for the degree of

DOCTOR OF PHILOSOPHY
IN
MECHANICAL ENGINEERING

PABLO A. TARAZAGA, CHAIR
DANIEL J. INMAN
ANDREW J. KURDILA
MICHAEL K. PHILEN
MARK P. EMBREE

10^{th} MAY, 2016
Blacksburg, Virginia

Keywords: Traveling Waves, Piezo-ceramics, Vibrations, Phase-selection, Dynamics, Actuation, Plates, Beams

CONTINUAL TRAVELING WAVES IN FINITE STRUCTURES : THEORY, SIMULATIONS, AND EXPERIMENTS

VIJAYA VENKATA NARASIMHA SRIRAM MALLADI

Abstract

A mechanical wave is generated as a result of an external force interacting with the well-defined medium and it propagates through that medium transferring energy from one location to another. The ability to generate and control the motion of the mechanical waves through the finite medium opens up the opportunities for creating novel actuation mechanisms not possible before. However, any impedance to the path of these waves, especially in the form of finite boundaries, disperses this energy in the form of reflections. Therefore, it is impractical to achieve steady state traveling waves in finite structures without any reflections. In-spite of all these conditions, is it possible to generate waveforms that travel despite reflections at the boundaries? The work presented in this thesis develops a framework to answer this question by leveraging the dynamics of the finite structures without any active control.

Therefore, this work investigates how mechanical waves are developed in finite structures and identifies the factors that influence steady state wave characteristics. Theoretical and experimental analysis is conducted on 1D and 2D structures to realize different type of traveling waves. Owing to the robust characteristics of the piezoceramics (PZTs) in vibrational studies, we developed piezo-coupled structures to develop traveling waves through experiments.The results from this study provided the fundamental physics behind the generation of mechanical waves and their propagation through finite mediums. This research will consolidate the outcomes and develop a structural framework that will aid with the design of adaptable structural systems built for the purpose. The present work aims to generate and harness structural traveling waves for various applications.

CONTINUAL TRAVELING WAVES IN FINITE STRUCTURES : THEORY, SIMULATIONS, AND EXPERIMENTS

VIJAYA VENKATA NARASIMHA SRIRAM MALLADI

General Abstract

A mechanical wave is generated as a result of an oscillating force interacting with the well-defined medium and it propagates through that medium transferring energy from one location to another. The ability to generate and control the motion of the mechanical waves through the finite medium opens up the opportunities for creating novel actuation mechanisms. By manipulating the wave propagation in a solid medium, the structure can interact with its surrounding in various ways: (a) materials in its surroundings can be moved when inside its effective domain (i.e. conveyer like transport, pumps, non-contact fluid mixing etc.), (b) the host structure can flip the previous effect and it can propel itself through a medium (i.e. swimming and flapping with minimal parts count) and (c) the material can manipulate incoming external disturbances (i.e. vibro-acoustic camouflage). The highly controlled and multidimensional surface wave resulting from this work will lead to very innovative ways of surface to medium interaction that can have significant effects in multiple engineering domains. We aim to study how mechanical waves are formed and propagate in solid system and what are the determining factors in their behavior, as well as how they can be manipulated for adaptable performance using integrated smart materials.

कर्मणयेवाधिकारस्ते मा फलेषु कदाचन |

मा कर्मफलहेतुर्भूर्मा ते सङ्गोऽस्त्वकर्मणि ||

Gita 2.47

సర్వం శ్రీ ఉమాపరమేశ్వరార్పణమస్తు

Meaning: You have a right to perform your prescribed duty, but you are not entitled to the fruits of action. Never consider yourself to be the cause of the results of your activities, and never be attached to not doing your duty.

Acknowledgements

Finally... it is time for me to acknowledge and appreciate all the help and support I received over last five years. First and foremost, I am so fortunate to work with such an understanding and supportive advisor. Dr. Tarazaga, Thank you very much !!! I am deeply grateful to you for giving me this opportunity to pursue my dreams in a very cheerful and conducive environment. You have been more than patient with me in all those times I got distracted and changed my focus. You have supported all my efforts and been very broad-minded to give me chance after chance to correct all my mistakes. I appreciate all your guidance in channeling my energies in the right directions through our long conversations (sometimes even after 5pm). I am grateful to you and your family for helping me stay sane all those holidays away from home. I always know I can share my problems and look up to you for advice, be it academics or life.

I would also like to thank my committee members, Dr. Dan Inman, Dr. Andrew Kurdila, Dr. Mike Philen and Dr. Mark Embree. I always knew that I could turn to you for the insight and advice I needed in the course of my research. All the discussions I had with my committee has broadened my understanding of the subject and allowed me to focus my efforts in a more fruitful manner. I would take this opportunity to recognize the efforts of all professors with whom I have interacted over years, be it in Virginia Tech or Indian School of Mines. In this regard, I would like to express my gratitude to Dr. Kurdila and Dr. Gugercin, who shaped my research endeavors through in class and out of class interactions in a timely and effective manner. I greatly appreciate the discussions I had on various issues with Dr. Kasarda and Dr. Jeff Borggaard. I would love to thank AFOSR and CENTIRE are financially supporting me over last three years.

I immensely enjoyed my time at Virginia Tech and strongly believe it was only possible due to the vibrant and friendly atmosphere of our lab. I acknowledge the help of all my colleagues namely Dr. Bryan Joyce, Dr. Dragan Avirovik, Mohammad Albakri, Mico Woolard, Austin Pheonix, Dustin Bales, Patrick Musgrave, Rodrigo Sarlo, Dr. Ipar Ferhat, Howard Chung, Jeff Poston, Sa'ed Alajlouni, Malihe Ghadimi, Daniel Wu, Mark Hurtado and Joseph Hamilton. I also had a lot of fun working with undergraduates in different projects, Carlos E Garcia, Mathieu Vandaele, Tarek Alkhulaidy, Kevin Lefeave, Jeff Pope to name a few. The jolly banter and occasional pranks in the lab have kept a smile on my face even in the most stressful situations over the last five years. I have to specially thank Beth Howell for all the help and advice I got anytime and every time. She has made my time in CIMSS/VAST/VT-SIL pleasant and hassle free. Other than all the help I got from Dr. Tarazaga, I cannot forget to thank Dr. Bryan Joyce and Mohammad Albakri for helping

me bringing this thesis to a reality.

I would specially like to thank my roommates and friends: Dr. SaiDhiraj Amuru, Vireshwar Kumar, Deepak Mane, Amiya Behera,KC, Prasad, Prashant Kumar for all the good and glories days we had in Blacksburg. For last five years, I had a social life due to the high energies and fun at our own Shawnee theater. I had fun in discussions, in movies, in gossip, in cooking, in traveling etc. Thanks Dr. SaiDhiraj Amuru and Vireshwar Kumar for making my time in the USA pleasant and enjoyable. I have to thank Usha for being a friend, more than a cousin and helping me in times of need.

Sanata Dharma or 'eternal order', says *Matru Devo Bhava* (revere your mother as God) and *Pitru Devo Bhava* (revere your father as God). Many wonder why parents are given such great respect. But, I have a mother who has an immense will-power to defeat all adversities and is every ready to invent other's futures; and I have a father who has extraordinary patience and discipline to cruise through the most exhausting times in anyone's life with a smile an his face. For me, my parents are the nothing short of divine beings who shaped every good characteristic in me. I humbly bow my head at the feet of my parents, Dr. Varalakshmi Malladi and B.V.L.N.Swamy Malladi. Although, Anupama and I have know each other for just more than an year, I have to thank her for all the emotional support I got from her. Especially for being so understanding and soothing all throughout these last few stressful times. I wish the sweetness of our bond will pave way to a bright and successful future. I would love to thank my sister, Satya Sarvani, for the love and friendship we have developed as siblings. Sarvani, my brother-in-law, Phanisri Pradeep Pratapa and I have had a lot of long unending discussions on various topics over last few years. We have comforted each other and helped each other take smart decisions. Thanks for being there every time I needed you. I am ever grateful to my aunt Dr. Padmavathi Garimella for motivating me to pursue the path of research. You have given me the right thrust at the right time. I thank my in-laws for their trust and their support over last few months. I will always have my grand parents in my thoughts for they believed in me and granted me with their choicest blessings. But none of this is possible with out the love of Almighty.

ఎవ్వనిచే జనించు జగమెవ్వని లోపల నుండు లీనమై,

యెవ్వని యందు డిందుఁ బరమేశ్వరుఁ డెవ్వఁడుమూలకారణం,

బెవ్వఁ డనాదిమధ్యలయుఁ డెవ్వఁడు సర్వముఁ దానయైనవాఁ,

డెవ్వఁడు వాని నాత్మభవు నీశ్వరు నే శరణంబు వేడెదన్.

Meaning: I pay my obeisance to such God by whom this universe is created; in whom it is contained; into whom it is dissolved; who is the supreme ruler; who is the root-cause of this universe; who neither has beginning nor end; who takes the forms of all the animate and the inanimate, the visible and the invisible.

Contents

List of Figures

List of Tables

Nomenclature

Acronyms

CF	Cost Function
FRF	Frequency Response Function
FFT	Fast Fourier Transform
MAC	Modal Assurance Criterion
MFC	Macro-Fiber-Composite
PZT	Piezo-ceramics
PDE	Partial Differential Equation
SLDV	Scanning Laser Doppler Vibrometer
IRKA	Iterative Rational Krylov Algorithm
FEM	Finite Element Model
SVD	Singular Value Decomposition
FSI	Fluid Structure Interaction

Symbolic Notation

$w(x,t)$	Response of the structure at a location 'x' and time 't'
ω_f	Forcing frequency in rad/s
ω	Frequency in rad/s
ζ	Damping coefficient

$\Phi(x)$ or $X(x)$	Spatial solution or analytical mode shape
$\tilde{\Phi}(x)$	Normalized analytical mode shape
Y, E	Young's modulus
$\mathcal{H}(x)$	Heaviside function
$\delta(x)$	Dirac-delta function
ϕ	Phase difference between two forces in radians
$X^{trig.}$	The ordinary trigonometric part of the mode shape $X(x)$
$X^{hype.}$	The hyperbolic trigonometric part of the mode shape $X(x)$
W_1, W_2, W_3, W_4	The four traveling wave components
H_1, H_2	Types of transfer functions
α, β	Proportional damping coefficients
β_n and λ_n	Wave-number and wave-length of modeshapes of the beam

Chapter 1

Introduction

1.1 Introduction

Waves in a finite media has been an area of research for several decades [3–9]; in some cases researchers have tried to subdue the presence of waves in a structure [10], while in others waves are intentionally generated and harnessed [11]. Research since as late as 1950's [12–14] has tried to analyze and understand the occurrence of waves in nature and these studies have been instrumental in the conceptual development of the present work. The goal of this research is to understand waves to determine, generate and design 1D and 2D solid structures for traveling waves. Therefore this work aims to study how mechanical waves are developed in finite structures and identify the factors that influence wave characteristics. The proposed research will consolidate the outcomes and develop a structural framework that will aid with the design of adaptable structural systems built for the purpose. The present work aims to generate and harness structural traveling waves for various applications. As a first step, the occurrence of such waves in nature and some of the potential areas of application where traveling waves can contribute is researched and presented in the next section.

1.2 Motivation

Nature has been the inspiration and guide for a number of inventions, thus an attempt is made to look at those commonplace phenomena that employ traveling waves. A representative review investigating the widespread scope and application of the proposed research is emphasized in Table 1.1. The areas represented here have been loosely categorized into sections, but many of them share multiple categories and the generalized concept of waves is clearly shared by all. What has taken place in these categories and what they have to offer for our research is further explained in the

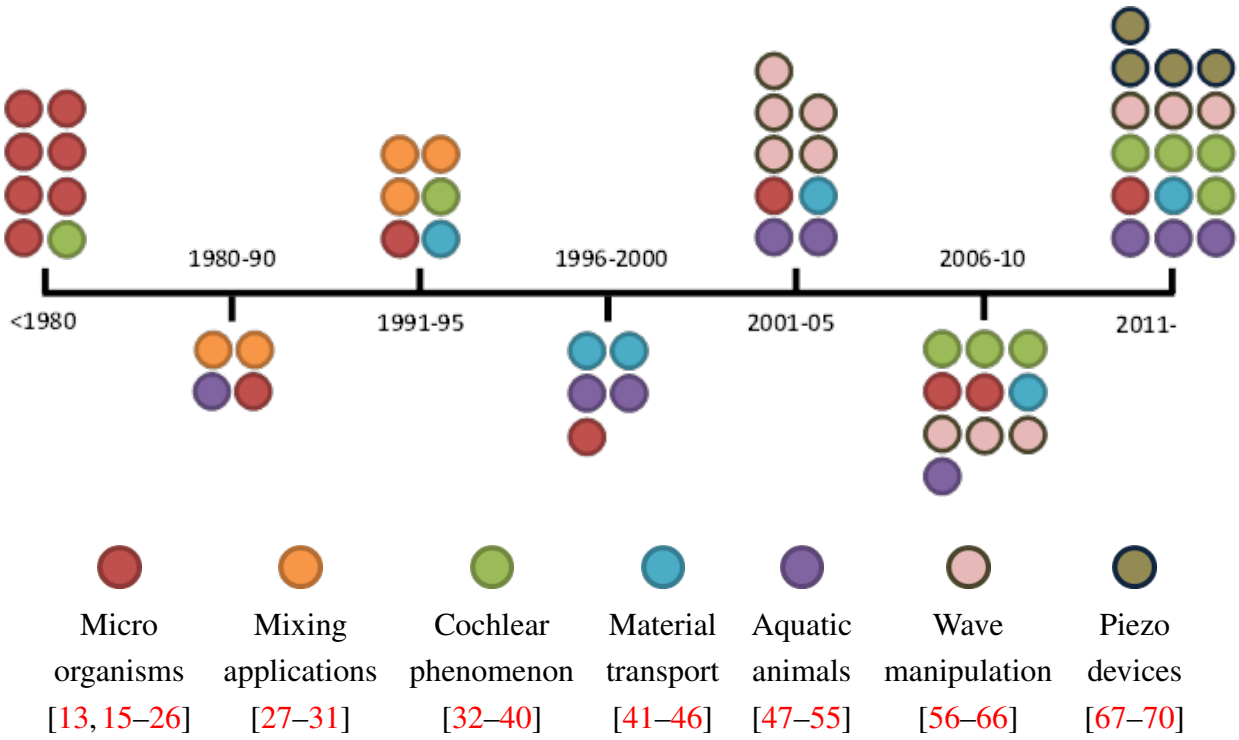

Micro organisms [13, 15–26]	Mixing applications [27–31]	Cochlear phenomenon [32–40]	Material transport [41–46]	Aquatic animals [47–55]	Wave manipulation [56–66]	Piezo devices [67–70]

Table 1.1: Broad review of applications of waves over the years.

following subsections.

1.2.1 Swimming applications

One of the most easily visualized areas where waves occur in nature is the undulatory motion of aquatic animals and micro-organisms. In these bio-mechanisms there is a oscillatory locomotion which results in propulsion as the motion is accompanied by energy transfer from one point to another [12, 13, 15, 16, 18–20, 23, 71]. Previous studies have shown that many microorganisms including spermatozoa and forms of bacteria/ protozoa, vibrate and twist hair-like structures known as flagella or cilia to swim [13, 15, 16]. In these microorganisms a net translational thrust is developed as a wave is transmitted from its head towards its tail [17]. It is shown that in these organisms the direction of the motion of the organism depends on the ratio of tangential viscous force to the normal viscous force. This results in organisms which swim in the same direction as that of the wave, and in contrast, there are others which have opposing directions of the overall motion and the wave [18,19,22]. Some sphere-shaped-micro-organisms such as the cyano-bacteria do not have additional propulsion units like the flagella. It is a type of bacterium, which is driven by the surface flow created by the tangential waves that travel along the outer cell membrane. Researchers have tried to numerically and experimentally simulate the fluidic behavior due to the normal or tangential waves to the surface or the combination of the two [20, 24, 25, 71–75]. These are some of the

most simplistic phenomena in terms of wave generation in symmetric structures.

Such studies have been carried out even in macro-scale; wherein the swimming patterns of aquatic animals have been of much interest in the research community [47, 52–54]. There are many research papers identifying the type of waves in aquatic animals [50, 51, 76–78] and then predicting their propulsive phenomena [26, 79–84]. Lighthill in his 1960 research paper [76] has shown that, theoretically, standing waves in cylindrical structures are highly inefficient to generate propulsive thrust. Additionally, this work has also shown that traveling waves in cylindrical structures can result in a maximum Froude efficient of 90% compared to a maximum efficiency of 50% in cylindrical structures with standing waves.

Recent years have also seen a rise in the replication of the propulsive capabilities of these animals in aquatic robots. The use of smart materials to actuate and mimic the fin and tail characteristics of a fish has been attempted in recent times [48–50, 85–93]. In most of these studies, the undulatory motion of these aquatic robots is achieved by integrating the fin of the robot into multiple segments and syncing the oscillatory motion of individual segments to replicate traveling waves [94]. Although substantial of research is taking place in these areas, most of these attempts do not create pure traveling waves in the structure or develop a framework to generate waves. The present work would pave way for development of solid state structures with higher propulsive characteristics.

1.2.2 Cochlear phenomenon

Another bio-mechanism which uses waves can be see in the ear, where acoustic pressure waves that reach any mammalian ear, actuates the eardrum, which is then transmitted via the middle ear to the inner ear (or the cochlea) [32, 33, 95–97]. The cochlea's sensory unit, also known as the organ of Corti, propagates this sound pressure signal through the basilar membrane (within the Cochlea) as a traveling wave. The propagation of the displacement wave through the basilar membrane is facilitated by the biological fluid-structural coupling [34–36]. The oto-acoustic emissions within the mammalian ear display complex physics that harness the potential of the fluidic coupling mechanism in order to propagate displacement waves. Researchers have shown that the cochlear mechanism to engage multiple frequency traveling waves in the cochlear fluid can be replicated as a system with variable structural stiffness [37–39, 98–101]. The non-linear traveling wave generation and transmission in a cochlea sheds light on the importance of structural design in the propulsive characteristics of a structure. The use of adaptive design to indirectly affect the mechanical impedance distribution and thereby the wave propagation in the structure is a control variable to be studied in this work.

There are many other nature-derived mechanisms for inspiration, such as birds, acoustics,

oceans, etc. that have waves with different functions or applications. But, none of the advancement of research in these topics is focused on generation of structural waves, but rather concentrate on mimicking their biological function. There are some other research areas which are not bio-inspired but analyze and manipulate structural waves. Some of these topics which are significant to the present work in the areas of vibration suppression, propulsion etc. are discussed below.

1.2.3 Wave generation and vibration suppression

It is well know that a wave, when generated in a finite medium, reflects at its boundaries due to the impedance change and thus results in stationary waves [1, 102–105]. Researchers have been able to develop an extensive theoretical background on the role of structural impedance plays in wave propagation [7, 106–108]. Such studies have led to two major fields: vibration suppression and traveling wave generation. Vibration suppression application studies have made use of piezoelectric actuators to dampen the wave propagation by having shunt electrical circuits control the vibration of the structure [10, 109–111]. Such studies highlight the advantages and disadvantages of the active, passive and hybrid theories to suppress vibrations [112–114]. In some cases researchers have considered the use arrays of piezoelectric actuators to study the spatial damping of waves [115–117]. In the generation of traveling waves the concept is to partially suppress the vibrations such that the reflection due to impedance changes is dampened and traveling waves are generated [63, 64, 118]. Researchers have studied experimental methodologies to quantify traveling waves and improve the same [119–121]. Such studies actuate finite media such as beams and plates with high stroke point actuators to develop waves in the structures. An active tuning method has also been employed to sense the wave quality and develop pure traveling waves in structures [62, 120, 122–133]. But most of the studies are not aimed at tapping the potential of smart actuators and intelligent design.

1.2.4 Transportation or propulsion

The propulsive force developed by the wave also facilitates the transport of materials in various trajectories and speeds. As the direction, speed and strength of progressing waves can be manipulated, this can also be used to transport material. Distributed manipulation systems employ multiple actuators that coordinate to produce complex motion in order to transport an object [134]. Researchers have studied many forms of distributed manipulation based on in-plane vibration of plates to an array of multiple robots etc. [135, 136]. Such manipulation generally involves redundant actuators that waste tremendous amount of power [137]. The present technique, which harnesses the use of solid-state waves on the structure, can address some of the concerns of a distributed manipulation system. Our method takes advantage of the host structure and its continuous

nature to develop in essence an inherent distributed actuation system. In the proposed approach the number of actuators employed is an order of magnitude less than the system presently used. The proposed research is not confined by the medium of material i.e. this system can be used to transport both solids and fluids alike.

On the mechanical side, the development of traveling waves has been investigated in order to answer the age-old question, "*Can carpets fly ?*" [44, 138–140]. There are many attempts to use the standing wave behavior of simple structures such as beams to generate motion that results in propulsion of the structure in various media [45, 88, 141–143]. Such behavior can potentially be used to mix fluids and transport particles in fluids [42, 43, 46]. However, the understanding of the physics behind the generation and propagation of traveling waves in a controlled manner is still lacking, and in the great majority of cases has ensued as result of trial and error or PID controllers [69, 144–146]. Without comprehensive understanding of the parameters that govern the wave dynamics, it will be difficulty to adequately take advantage of the phenomenon.

Similar research is also very popular in acoustics to develop techniques that result in levitation of objects [147–150]. With advances of the present technology in this field, acoustic standing waves are generated by using multiple sources so that objects can levitate in air. But any maneuver of these objects levitating in space requires propulsive forces generated by controlled acoustic traveling waves. This is one of the ongoing research topics in this area.

Similarly, another research area where traveling waves have been very popular is in the development of ultrasonic motors that are used in position stages [151–160]. In these applications traveling waves are generated along the circumference of cylinders and this is used to generate rotary motion. In many cases a phased actuation technique is used to generate such traveling waves [161–164]. In some cases a single phase between in actuators is used to generate waves [165–171]; but few attempts have been made to understand the physics behind the generation of waves and optimizing them.

Through this review, covering a wide range of applications that harness traveling waves, it is easy to see the potential of traveling wave generating technology to contribute to each and every field discussed earlier. In the next section a brief overview of traveling wave generation is discussed.

1.3 Wave introduction and outline

The categories of waves can also be associated with energy transfer as in (a) traveling waves, which carry energy across a distance of the medium and b) standing waves, in which energy remains associated with a particular location. The schematic diagram, shown in Fig. 1.1, illustrates the concepts of pure traveling waves, pure standing waves and a combination of the two. When a structure is ex-

cited with a single force, waves are generated and are then reflected due to an impedance change at its boundaries. For example, in the case of a clamped boundary condition and in the absence of any dissipative forces, these reflected waves have the same magnitude as the incident wave, and they travel in the direction opposite to the incident wave. The combination of both these waves generate standing waves, $w(x,t) = Asin(\omega t - kx) \pm Bsin(\omega t + kx)$, where amplitude A and B are equal in magnitude. When a structure is excited at two points at the same frequency, but with a phase difference between them, part of the reflected wave is negated (as $A \neq B$) and correspondingly results in a combination of a stationary wave and a traveling wave. The dominance of the traveling wave over the standing wave behavior depends on two factors: the frequency of the excitation, which is related to the structural response shape, and the fixed phase difference between the two inputs. In order to fully understand the effect of the parameters (mainly frequency and phase) that contribute towards wave propagation through solids, a theoretical framework is established and presented in this work. Theoretical models for prediction and simulation of the dynamical response of a beams, plates and cylinders are presented. These models provide a framework for actuation in order to accomplish the generation of traveling waves. This study encompasses a theoretical and exper-

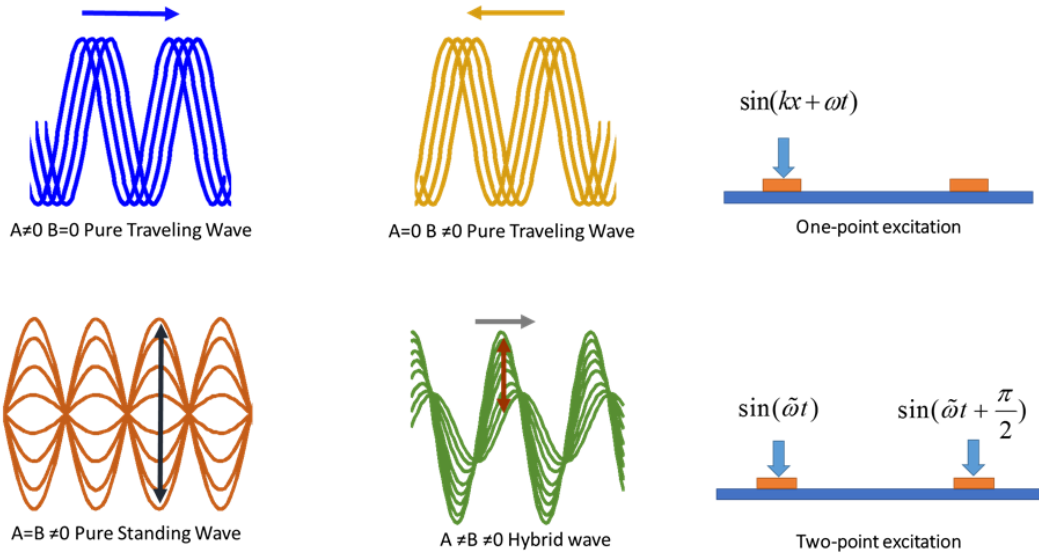

Figure 1.1: Conceptual description for the formation of the waves in finite medium.

imental analysis for the generation of mechanical waves through different boundary conditions: free – free, clamped – free and clamped – clamped. In doing so, it illustrates the simple platform for implementation and the role of control variables. Structures oscillate as a result of an external energy input sources that influences their dynamic response. Thus, by tailoring the excitation methodology it is possible to excite the structure in such a way that will result in the generation of customized net mechanical waves. The work herein utilizes piezoelectric (PZT) elements as the

excitation source for the structure of choice in order to maximize controllability and ease of use.

Generation of pure traveling waves in finite structure is a challenging task. Pure vibrational waves are theoretically observed in infinite structures that do not have any boundaries. Introduction of boundary conditions results in a change of mechanical impedance of the structure. This results in the reflection of waves. Thus, it is not practical to generate such pure traveling waves in structures. However, there have some some attempts to replicate the idea of a traveling or propagating wave. Simply put, these studies try to generate steady state vibrational waves in structures that result in net transfer of energy in one direction. So the critical part of such endeavors is the choice of forces and boundary conditions on the finite structure.

The first attempts in this direction is derived from impedance matching concept in acoustics. In these studies, the actuator excites a structure on one of its ends, inducing a wave traveling along the structure and the energy of the wave is absorbed at the other end. The concept is similar to a passive vibration isolator where the actuator's mechanical impedance is matched with the characteristic impedance of the structure. However, this approach is found to be inefficient and impractical due to high energy losses. In another work [41], it was observed that when a beam was excited by two sinusoidal forces acting at two different locations, but at a phase difference of 90°, a traveling wave was created. This is a result of the partial impedance matching at the excitation points and partial cancellation of wave reflections from its boundaries. Other works [63, 128] have also focused on point forces provided by external systems such as shakers and piezo-based stack actuators. More details on these methods are provided as a part of the discussion throughout the thesis.

1.4 Wave identification

Mechanical waves, based on their behavior, can be classified as standing, traveling or hybrid (combination of standing and traveling). A pure standing wave is associated with nodal points and only transverse harmonic deflection, while the pure traveling wave does not contain any nodal points and propagates with non-varying amplitude. In between is the special case of the hybrid wave, which is a combined response of standing and traveling waves where the amplitude of the wave propagates while oscillating transversely. Visually, when a wave is seen in motion, it is easy to observe it's dynamics and classify if its behavior resembles a standing wave or a traveling wave. Still, it is very difficult to figure out the proportion of standing wave to that of traveling wave. Furthermore, a better quantification which is more dependable and repeatable is required for accurate classification of waves. There are two approaches in literature [63–65, 118, 172] that have been used to classify waves: (1) wave envelope, (2) Fourier's method. Fourier's ellipses have also been used to determine the wavelength of a traveling wave. In addition to these approaches, an intuitive

wave identification method based on the Hilbert transform is developed as a part of the present work. This details of three methods that are used to classify waves are discussed in this section. A cost function (CF) is also developed based on each of these methods, which is later used to carry out parametric studies. Additionally, recently another wave identification approach was developed based on the 2D Fast Fourier Transform (FFT) approach [173]. However, as the present work does not use this method for analysis, the details of this approach are not studied in this section.

1.4.1 Wave envelope

The differences between the types of waves can be observed by the wave envelope, which plots the area swept by the wave over time (it can also be thought of as a displacement trace of all movement over time). In the wave envelope, a sharp nodal point (no displacement) in the wave envelope indicates a pure standing wave while no change in the maximum displacement of the points along the length of the specimen suggests a pure traveling wave. In hybrid waves, there is no clear nodal point and maximum displacements of the points along the length of the specimen are varied. This is illustrated in Fig.1.2. In this figure, the different waves are obtained by simulating

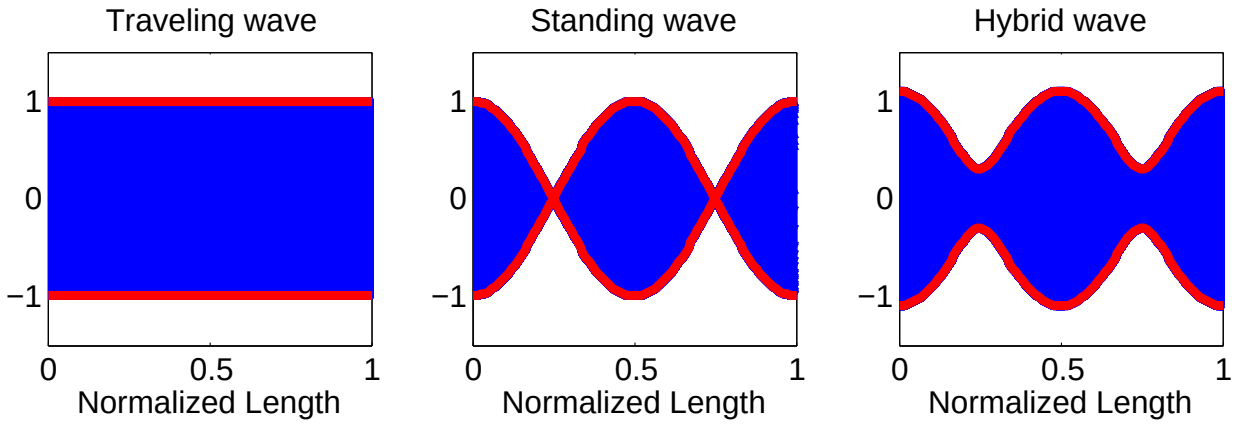

Figure 1.2: Schematic representation of different wave envelopes.

a single wavelength wave on a 1 m normalized structure in one physical structure. The equations used to simulate these representative figures are given by,

$$\begin{aligned} &\text{Traveling wave} : Sin(2\pi x - 200\pi t), \\ &\text{Standing wave} : 0.5Sin(2\pi x - 200\pi t) + 0.5Sin(2\pi x + 200\pi t), \\ &\text{Hybrid wave} : 0.3Sin(2\pi x - 200\pi t) + 0.7Sin(2\pi x + 200\pi t). \end{aligned} \tag{1.1}$$

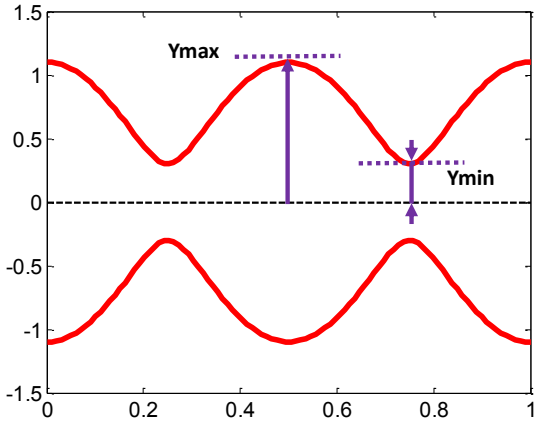

Figure 1.3: Parameters of a wave envelope.

In standing waves, for this case, there are two nodal points as seen in this figure and the distance between them is 0.5 m. The distance between two consecutive nodes is half of the wavelength. In real applications the wavelength is frequency dependent, as most of the structures we are interested in are dispersive in nature. This results in an inter-dependance between the frequency of excitation (ω), the wave-length of the wave (λ) and the speed of the wave (c). The exact relationship between these parameters is dependent on various parameters of the structure such as geometry, material properties, boundary conditions, etc.

In order to classify different waves, consider a general case of a hybrid wave and its wave envelope, as shown in Fig 1.3. In general this plot consists of two curves representing the top and bottom envelopes of the time histories of the wave, and these curves are symmetric over the base line. The maxima and the minima of one of the curves are measured and are denoted as Y_{max} and Y_{min} respectively. While, for a pure standing wave $Y_{min} = 0$ and for a pure traveling wave $Y_{min} = Y_{max}$, for a hybrid wave $Y_{min} \neq Y_{min} \neq 0$. These conditions can be used to represent a cost function (CF) as

$$CF = \frac{Y_{max} - Y_{min}}{Y_{max} + Y_{min}}. \tag{1.2}$$

This cost function will be 0 for a pure traveling wave and 1 for a pure standing wave and a fraction in between for a hybrid wave. For example, a value of 0.3 can be read as a hybrid wave which has 70% traveling wave behavior and 30% standing wave characteristics. In other words, the wave can be represented as the summation of the terms $cos(kx \mp \omega t)$ whose coefficients are in the ratio of 3:7. The resultant wave moves in the direction of the term dominated by the higher coefficient value. This approach is the simplest of all the methods available for wave detection. However, this

technique requires time data for a lot of spatial points, and it is not feasible to have such a large data set in practical situations. Alternate approaches are discussed in the succeeding sections, where ideally the time data of two points is sufficient to evaluate the cost function.

1.4.2 Hilbert's approach

Hilbert's approach is achieved in the time domain, where the response of any structure, such as the free-free beam in this study, is represented in the complex plane. Through experiments, using a laser scanning vibrometer or accelerometers, the response of the system is measured as a real quantity. In order to obtain its orthogonal counterpart, i.e. the imaginary component, the signal goes through a Hilbert's transform described as,

$$w_h(x,t) = w(x,t) + iH(w(x,t)), \tag{1.3}$$

where w_h is the analytical response or analytic signal. This analytical response is the same as the theoretical response of the system when the the PDE of the structure is derived using the exponential form ($e^{j(kx\pm\omega t)}$) for the assumed solution.

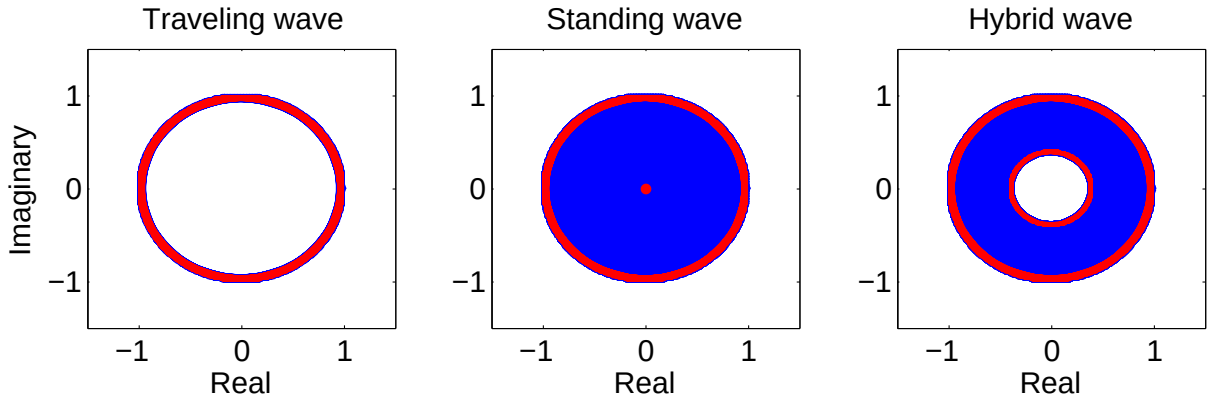

Figure 1.4: Schematic Hilbert's representations of different waves.

Following this approach, the response of an individual point on the structure as a function of time will result in a circle in the complex plane. This is achieved as follows. In Hilbert's transform, the trajectory of each point can be represented by a sinusoidal signal ($w(x,t)$) and its Hilbert transformed signal $iH(w(x,t))$ can also be represented as a sinusoidal wave, but with a phase difference of 90°. When the analytical signal is plotted in the complex plane the response is represented as a circle with radius equal to the amplitude of vibration. Therefore, in a scenario where a pure traveling wave exists, the amplitude of all the points across the structure are the same, hence the result is shown with multiple circles characterized with equal radii (all lying on top of

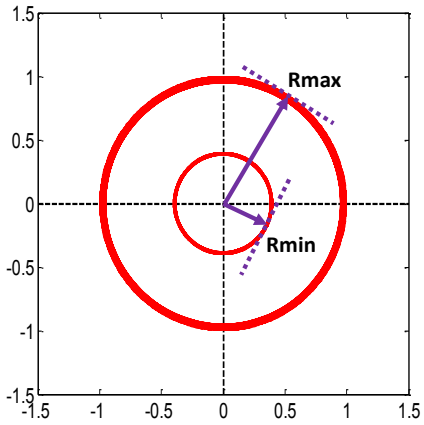

Figure 1.5: Parameters of Hilbert's approach.

each other). Unlike pure traveling waves, pure standing waves have points with zero displacements (nodal points), maximum displacements, and points with amplitudes in between. The results for pure standing wave appear as a filled-in circle when presented in the complex plane. In the case of hybrid waves, the minimum amplitude is never zero since nodal points do not exist,resulting in torus shape. This phenomena can be seen in Fig. 1.4.

Similar to the previous wave envelope approach, a cost function can be developed for the Hilbert's approach. In this case the CF is related to the maximum and the minimum radii of the curves shown in Fig. 1.5. The cost function can be written as

$$CF = \frac{R_{max} - R_{min}}{R_{max} + R_{min}}. \tag{1.4}$$

This approach just gives the information on the type of wave but does not give any extra information, such as the direction of the wave or the wave number of the structure. This approach also requires a large number of spatial points to detect wave type.

1.4.3 Fourier's approach

Contrary to a Hilbert's approach, the Fourier's approach also represents the response of the system in the complex plane, but in the frequency domain. Since all the points are excited at one frequency, the phase and the magnitude of the Fast Fourier Transform (FFT) peak at individual points is of interest. Unlike the Hilbert approach, where a single point traces a circle as a function of time, here, the phase and magnitude of vibration of a point is measured and plotted as a single value in the complex plane. Accordingly, when a pure traveling wave occurs, the amplitudes and phase differences between the consecutive points along the structure form a circle. This is due to the fact

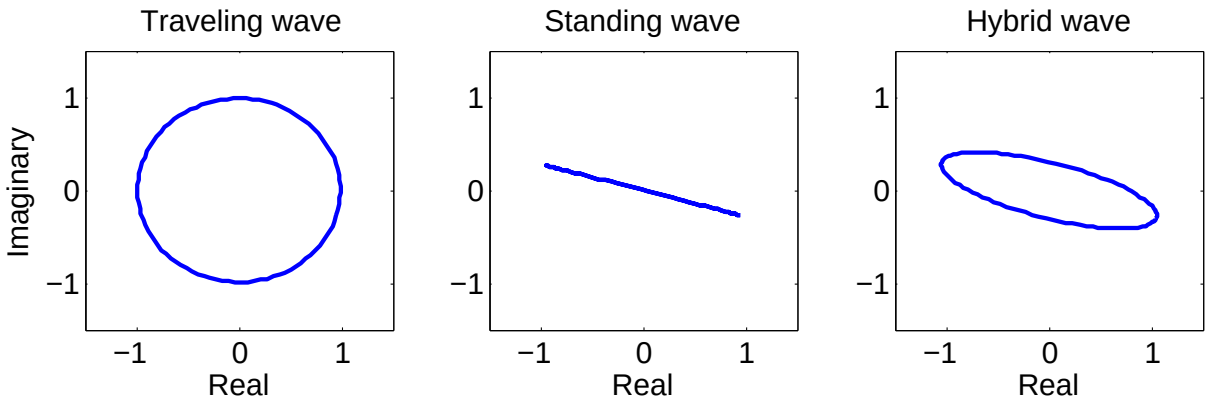

Figure 1.6: Schematic of Fourier's representations of different waves.

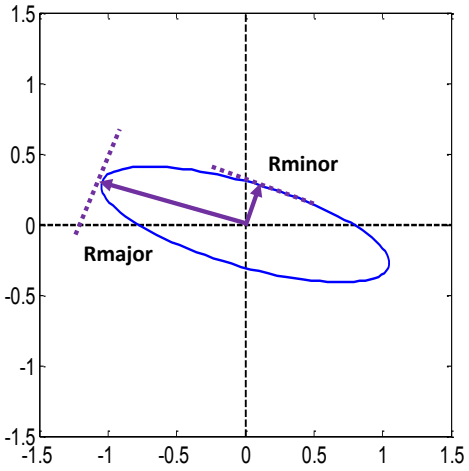

Figure 1.7: Parameters of Fourier's approach.

that there exists phase differences between the consecutive points, hence there is a propagating wave, and since their amplitudes are identical the points lie on a circle. When a standing wave is generated, the phase is either 0° or 180°, and the FFT magnitudes are different, resulting in a straight line, in the complex plane. Lastly, for the hybrid wave case, the existent phase difference and different magnitudes of the FFT will result in a response that is represented by an ellipse. Due to the phase change, the points in the complex plane will not lie along a straight line but rather on an ellipse. If the effect of traveling wave is dominating, the ellipse foci will move closer and approach a circle; conversely, if the standing wave is dominating the response, the ellipse flattens and moves towards the shape of a straight line. These scenarios can be observed in Fig 1.6.

In this case the *CF* is related to the major and the minor radii of the elliptical curve shown in

Fig. 1.7. The cost function can be written as

$$CF = \frac{R_{major} - R_{minor}}{R_{major} + R_{minor}}. \tag{1.5}$$

The ellipse can be fit using regression techniques based on a comparatively smaller number of spatial points, and the major and minor radii are found. This is the advantage of this approach. When there is more than one wavelength in the portion of the structure measured, multiple ellipses will emerge.

1.5 Thesis Outline

The research discussed in the present thesis is divided into six major chapters. A brief literature survey and an introduction to steady state waves is discussed in the present chapter. The next chapter lays an analytical foundation to traveling wave generation in finite structures. The question, *can perpetual traveling waves exist in finite structures?* is explored in this section. A theoretical background is initially developed to study the various parameters that influence the dynamics of one dimensional (1D) beam structures. Later parts of this chapter also extend the results of 1D systems to more complex structures.

In chapter 3, these findings are used to explore in more detail the wave generation in the case of spatially distributed excitation through piezo-ceramic wafers. In this chapter piezo-ceramics are bonded to finite structures with various boundary conditions, such as clamped-clamped, clamped-free and free-free. The use of piezo-ceramics to generate these waves will provide a mechanism that is more versatile, less intrusive, easier to install, controllable over a larger frequency range and an application-friendly way of generating wave propagation in structural components. The work in this chapter will provide the basis required for understanding the fundamentals of executing wave propagation, as the models can be easily extended towards maturing variety of applications.

Chapter 4 is the basis for investigating 2D bending waves in plates. A finite element model is formulated to simulate the dynamics of the plate when actuated by multiple piezo-ceramics. The FE model is used to generate traveling waves by exciting the plate at multiple locations and at multiple frequencies of excitation. These results are validated through experiments. Projection based reduced models are developed in the later sections of this chapter. The plate dynamics are simulated in the state-space domain, and reduced models are tested for steady state frequency and time responses.

In chapter 5, cylindrical traveling waves are investigated. Cylinders provide insight into unique dynamics (i.e.,symmetric and non-symmetric modes) that have yet to be fully defined for two and three dimensional systems. This chapter extends the research findings of 1D beam structures and

applies it to 2D traveling waves in a symmetric cylindrical structure. The work herein will focus on the generation and characterization of traveling waves that propagate along the circumferential direction. The coupled system, given by a free-free cylinder with multiple piezoelectric actuator (PZT) patches, is used to evaluate several traveling wave modes in the cylinder. Finite Element Modeling (FEM), in conjunction with experiments, is conducted to provide a comprehensive understanding of the generation and propagation behavior of the traveling wave modes in a thin walled cylinder. The last chapter discusses the potential application of the present work and some of the future directions of the research discussed in this thesis.

Chapter 2

Theoretical analysis of traveling waves

2.1 Introduction

In the previous chapter the characteristics of pure traveling waves, pure standing waves and hybrid waves have been discussed. In this chapter, we develop a theoretical basis that leverages structural vibrations to generate steady state traveling waves. Initially, an analytical framework to study the response in 1D structures is developed on a simplified, yet representative model of a 1D beam with free-free boundary conditions. The 1D beam is simultaneously excited with two point forces with a phase difference between them. The forcing parameters are varied to investigate (a) the conditions that result in steady state traveling waves in beams, and (b) the physical limits on the optimal quality of the traveling waves. In the later parts of this chapter, a generalized theory that explores traveling wave generation in higher dimensional structures is developed.

2.2 Traveling waves in a 1-D beam due to point forces

In literature [132, 133], there are some studies that discuss the physics behind traveling waves in strings. However, strings have practical problems that limit experimental study of their dynamics to multiple inputs. So, in this present study, we have focused our attention to analytically study traveling waves in beams. There have been some attempts in literature [66, 68] to experimentally generate traveling waves in beams. However, there have been no theoretical investigations that analyze steady state traveling waves in 1D structures excited with multiple forces. This is partially due to the complexity in coupling the beam responses due to multiple inputs in order to study the influence of different parameters. There have been efforts to describe waves in 1D beams as a combination of two dominant modes [41]. However, most of these studies are phenomenological in nature and do not have a concrete theoretical basis. In the present study, we initially start with

a simplified model and analyze traveling wave generation. Later, some of the assumptions are relaxed and a broader framework to understand traveling waves in structures is developed.

2.2.1 Homogeneous equation-of-motion of a beam

Consider a beam of length L having a uniform cross-sectional area A with bilateral symmetry as shown in Figure 2.1. The beam has a density of ρ and a flexural stiffness of EI, where E is the Young's elastic modulus for the beam and I is the cross-sectional area moment-of-inertia. Based on Euler-Bernoulli beam assumptions, the forces and moments acting on this beam in the non-forcing condition are computed, and the homogeneous equation of motion describing the deflection of the beam $w(x,t)$ is given by, [1],

$$\frac{\partial^2 w(x,t)}{\partial t^2} + \left(\frac{EI}{\rho A}\right)\frac{\partial^4 w(x,t)}{\partial x^4} = 0. \tag{2.1}$$

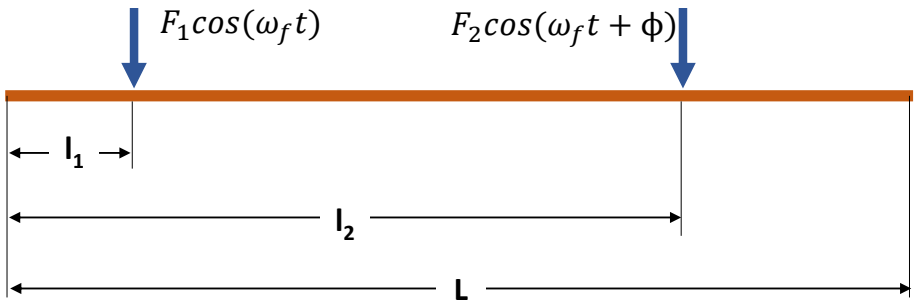

Figure 2.1: Two point forces are applied to a free-free beam at two different locations.

This equation is solved based on the separation-of-variables approach, where the spatial and the temporal part of the out-of-plane deformation $w(x,t)$ are decoupled from each other. Thus, this new form of the transverse displacement, $w(x,t) = X(x)T(t)$, is substituted into the Eq. 2.1 and further simplified to,

$$\begin{aligned} \frac{d^4 X(x)}{dx^4} - \left(\frac{\omega^2}{c^2}\right) &= 0, \\ \frac{d^2 T(t)}{dt^2} + \omega^2 T(t) &= 0, \end{aligned} \tag{2.2}$$

where ω^2 is the choice of the separation constant, $c = \sqrt{\frac{EI}{\rho A}}$ and $\beta^4 = \frac{\omega^2}{c^2}$. Physically, β represents the circular wave number or spatial frequency of the wave and is proportional to reciprocal of the

wave length λ $\left(\text{i.e. } \beta = \frac{2\pi}{\lambda}\right)$.

The spatial solution of the Eq. 2.2 is assumed to be in the form,

$$X(\frac{x}{L}) = a_1 sin\beta\frac{x}{L} + a_2 cos\beta\frac{x}{L} + a_3 sinh\beta\frac{x}{L} + a_4 cosh\beta\frac{x}{L}, \tag{2.3}$$

where the coefficients a_i are determined by the boundary conditions of the beam. Further, for the sake of simplicity the length of the beam, L, is assumed to be of unit length throughout this analysis. These spatial solutions are also called the mode shapes of the beam. Each of the mode shapes have a constant factor σ_n that is dependent on the boundary conditions of the beam [1]. However, for higher mode shapes, this constants can be approximated to 1, i.e., $\sigma_n \approx 1$. Standard mode shapes for various boundary conditions are tabulated in Table 2.1. Mathematically, all modes shapes of the beam are a combination of two type of functions: an ordinary trigonometric part - $X^{trig.}$ and a hyperbolic trigonometric part - $X^{hype.}$. These two parts have two distinct functions pertaining to the dynamics of the beam.

For instance, the hyperbolic part of the mode shape can be simplified as,

$$\begin{aligned} X^{hype.} &= cosh\beta_n x - \sigma_n sinh\beta_n x, \\ &\approx cosh\beta_n x - sinh\beta_n x, \\ &= e^{-\beta_n x}. \end{aligned} \tag{2.4}$$

As β_n is a positive real number, if the value of x increases from 0 to 1 then the value of $e^{-\beta_n x}$ reduces from 1 to 0. Additionally, the value of β_n increases with n and hence, the hyperbolic part of the mode shape tends to zero at a much faster rate in higher mode shapes. In other words, the part of the mode shape $X^{hype.}$ is only significant at the left boundary of the beam, where $x \to 0$.

Similarly, the other part of the mode shape, $X^{trig.}$ can be further simplified as,

$$\begin{aligned} X^{trig.} &= cos\beta_n x - \sigma_n sin\beta_n x, \\ &\approx cos\beta_n x - sin\beta_n x, \\ &= \sqrt{2} cos\left(\beta_n x + \frac{\pi}{4}\right). \end{aligned} \tag{2.5}$$

The values of x where $cos\left(\beta_n x + \frac{\pi}{4}\right) = 0$ are called the strain nodes of the mode shape. This part is a sinusoidal function of the wave number β_n, and hence there is a specific location of the beam where the trigonometric part can be neglected. In other words, the term $X^{trig.}$ is the major contributor of the dynamics of the beam. This will be used in the following sections to derive a systematic approach to wave generation.

Table 2.1: Mode shapes of beam under various boundary conditions [1].

Boundary condition	Spatial solution X(x)	σ_n	value of σ_n
Free-free	$cosh\beta_n x + cos\beta_n x$ $-\sigma_n(sinh\beta_n x + sin\beta_n x)$ $X^{trig.} = cos\beta_n x - \sigma_n sin\beta_n x$ $X^{hype.} = cosh\beta_n x - \sigma_n sinh\beta_n x$ $X(x) = X^{trig.} + X^{hype.}$	$\sigma_n = \frac{cosh\beta_n L - cos\beta_n L}{sinh\beta_n L - sin\beta_n L}$	0.9825 1.0008 0.9999 1.0000 0.9999 1 for n>5
Clamped-free	$cosh\beta_n x - cos\beta_n x$ $-\sigma_n(sinh\beta_n x - sin\beta_n x)$ $X^{trig.} = cos\beta_n x - \sigma_n sin\beta_n x$ $X^{hype.} = cosh\beta_n x - \sigma_n sinh\beta_n x$ $X(x) = -X^{trig.} + X^{hype.}$	$\sigma_n = \frac{sinh\beta_n L - sin\beta_n L}{cosh\beta_n L + cos\beta_n L}$	0.7341 1.0185 0.9992 1.0000 1.0000 1 for n>5
Clamped-clamped	$cosh\beta_n x - cos\beta_n x$ $-\sigma_n(sinh\beta_n x - sin\beta_n x)$ $X^{trig.} = cos\beta_n x - \sigma_n sin\beta_n x$ $X^{hype.} = cosh\beta_n x - \sigma_n sinh\beta_n x$ $X(x) = -X^{trig.} + X^{hype.}$	$\sigma_n = \frac{cosh\beta_n L - cos\beta_n L}{sinh\beta_n L - sin\beta_n L}$	0.9825 1.0008 0.9999 1.0000 1.0000 1 for n>5
Clamped-pinned	$cosh\beta_n x - cos\beta_n x$ $-\sigma_n(sinh\beta_n x - sin\beta_n x)$ $X^{trig.} = cos\beta_n x - \sigma_n sin\beta_n x$ $X^{hype.} = cosh\beta_n x - \sigma_n sinh\beta_n x$ $X(x) = -X^{trig.} + X^{hype.}$	$\sigma_n = \frac{cosh\beta_n L - cos\beta_n L}{sinh\beta_n L - sin\beta_n L}$	1.0008 1 for n>1
Clamped-sliding	$cosh\beta_n x - cos\beta_n x$ $-\sigma_n(sinh\beta_n x - sin\beta_n x)$ $X^{trig.} = cos\beta_n x - \sigma_n sin\beta_n x$ $X^{hype.} = cosh\beta_n x - \sigma_n sinh\beta_n x$ $X(x) = -X^{trig.} + X^{hype.}$	$\sigma_n = \frac{sinh\beta_n L - sin\beta_n L}{cosh\beta_n L + cos\beta_n L}$	0.9825 1 for n>1

2.2.2 Forced response of the beam to two inputs

Let us now consider the scenario when two point forces $F_1 cos(\omega_f t)$ and $F_2 cos(\omega_f t + \phi)$ are acting on the beam at locations l_1 and l_2 respectively. The resulting forced equation of motion is given by

$$\frac{\partial^2 w(x,t)}{\partial t^2} + c^2 \frac{\partial^4 w(x,t)}{\partial x^4} = F_1 cos(\omega_f t)\delta(x-l_1) + F_2 cos(\omega_f t + \phi)\delta(x-l_2), \tag{2.6}$$

where $\delta(x)$ is the Dirac-delta function. Using the separation of variables approach, this equation can be further simplified into

$$\left(\ddot{T}_n(t) + \omega_n^2 T_n(t)\right) X_n(x) = F_1 cos(\omega_f t)\delta(x-l_1) + F_2 cos(\omega_f t + \phi)\delta(x-l_2). \tag{2.7}$$

Applying the orthogonality conditions of the mode shapes, we can further simplify this equation into,

$$\ddot{T}_n(t) + \omega_n^2 T_n(t) = F_1 cos(\omega_f t) X_n(l_1) + F_2 cos(\omega_f t + \phi) X_n(l_2). \tag{2.8}$$

Based on the superposition principle, the non-homogeneous solution of this ODE can be written as summation of responses of the beam to two individual point forces,

$$T_n(t) = \frac{F_1 cos(\omega_f t) X_n(l_1) + F_2 cos(\omega_f t + \phi) X_n(l_2)}{\omega_n^2 - \omega_f^2}. \tag{2.9}$$

The complete forced solution of the beam is the combination of the spatial and temporal solutions and can be written as

$$w(x,t) = \sum_{n=1}^{\infty} X_n(x) T_n(t) = \sum_{n=1}^{\infty} \frac{X_n(x)\left[F_1 cos(\omega_f t) X_n(l_1) + F_2 cos(\omega_f t + \phi) X_n(l_2)\right]}{\omega_n^2 - \omega_f^2}. \tag{2.10}$$

This equation describes the response of the beam as the summation of the individual modal contributions. Each term of the modal contribution ($X_n(x)$) is dependent on two factors : (1) frequency contribution $\frac{1}{\omega_n^2 - \omega_f^2}$, (2) spatial contribution ($X_n(l_1)$ and $X_n(l_2)$). Let us first study the frequency contribution of the wave. If the beam is excited at a frequency ω_f, then the frequency contribution is the reciprocal of the term $\omega_n^2 - \omega_f^2$. The relative distance between the natural frequencies and the excitation frequency guides the individual modal contribution. The farther the natural frequencies are from the frequency of excitation, the smaller the contribution. This principle is useful to further simplify Eq. 2.10 in the next section.

2.2.3 Two mode approximation

In this section, we analyze a part of the response of the beam as a summation of two modes. Let us first evaluate the contribution of any two natural frequencies ω_a and ω_b. The only condition is that ω_a and ω_b correspond to mode shapes that are symmetric and anti-symmetric respectively. Let us also only incorporate the part of the mode shape that contributes to the whole dynamics of the beam ($X^{trig.}$) and neglect the hyperbolic part ($X^{hype.}$) of the mode shape. Based on these approximations, the modal contribution (w_{ab}) of the modes a and b, part of the Eq. 2.10, is given by,

$$w_{ab}^{trig.}(x,t) = \frac{X_a^{trig.}(x)(X_a^{trig.}(l_1)F_1 cos(\omega_f t) + X_a^{trig.}(l_2)F_2 cos(\omega_f t + \phi))}{\omega_a^2 - \omega_f^2} \tag{2.11}$$

$$+ \frac{X_b^{trig.}(x)(X_b^{trig.}(l_1)F_1 cos(\omega_f t) + X_b^{trig.}(l_2)F_2 cos(\omega_f t + \phi))}{\omega_b^2 - \omega_f^2} \tag{2.12}$$

Now, let us first consider the case where the point forces on the beam are equal in magnitude and are located at equal distances from each end of the beam. These two assumptions can be written as,

Assumptions: (1) F_1=F_2=F, and (2) $l_2 = L - l_1$.

The assumption on the location of the point forces results in simplification of the spatial amplification factors as $X_n(l_2) = \pm X_n(l_1)$ (symmetric boundary conditions - free-free and clamped-clamped). The sign of this amplification factor depends on the symmetry of the mode shapes. In 1-D systems, such as beams, the sign of this spatial amplification factors generally alternates after every natural frequency. But in the present scenario, as we are considering the effect of two mode shapes when one of them is symmetric and the other is anti-symmetric, without loss of generality, we can write $X_a^{trig.}(l_2) = X_a^{trig.}(l_1)$ and $X_b^{trig.}(l_2) = -X_b^{trig.}(l_1)$. By substituting these assumptions, Eq. 2.11 yields,

$$\begin{aligned}
w_{ab}^{trig.}(x,t) &= \frac{X_a^{trig.}(x)X_a^{trig.}(l_1)F(cos(\omega_f t) + cos(\omega_f t + \phi))}{\omega_a^2 - \omega_f^2} \\
&\quad + \frac{X_b^{trig.}(x)X_b^{trig.}(l_1)F(cos(\omega_f t) - cos(\omega_f t + \phi))}{\omega_b^2 - \omega_f^2} \\
w_{ab}^{trig.}(x,t) &= \frac{FX_a^{trig.}(l_1)}{\omega_a^2 - \omega_f^2}\left(X_a^{trig.}(x)(cos(\omega_f t) + cos(\omega_f t + \phi))\right) \\
&\quad + \frac{FX_a^{trig.}(l_1)}{\omega_a^2 - \omega_f^2}\left(\frac{X_b^{trig.}(l_1)(\omega_a^2 - \omega_f^2)}{X_a^{trig.}(l_1)(\omega_b^2 - \omega_f^2)}X_b^{trig.}(x)(cos(\omega_f t) - cos(\omega_f t + \phi))\right)
\end{aligned} \tag{2.13}$$

At a constant frequency of excitation (ω_f), and a fixed location of excitation (l_1 and l_2), the factors $(\omega_a^2 - \omega_f^2)$, and $(\omega_b^2 - \omega_f^2)$ are constants and independent of time t and space x. So, we define two new constants P and C as,

$$P = \frac{X_b^{trig.}(l_1)(\omega_a^2 - \omega_f^2)}{X_a^{trig.}(l_1)(\omega_b^2 - \omega_f^2)}, \qquad C = \frac{F X_a^{trig.}(l_1)}{\sqrt{2}(\omega_a^2 - \omega_f^2)}.$$

By substituting these constants, Eq. 2.13 can be further simplified as,

$$w_{ab}^{trig.}(x,t) = \sqrt{2}C\left(X_a^{trig.}(x)(cos(\omega_f t) + cos(\omega_f t + \phi)) + PX_b^{trig.}(x)(cos(\omega_f t) - cos(\omega_f t + \phi))\right).$$

The trigonometric terms of this equation are expanded and like terms are rearranged as a combination of four mode shape excitations. This equation can be put in the form,

$$w_{ab}^{trig.}(x,t) = \sqrt{2}C\left(C_A W_1 + C_B W_2 + C_C W_3 + C_D W_4\right); \tag{2.14}$$

where the beam response is a linear combination of four waves (W_i, $i = 1,\ldots,4$). The phase (ϕ) information is present only in the coefficients (C_A, C_B, C_C, C_D) and the temporal part is only present in the wave terms (W_i). Mathematically, these waves can be written as,

$$\begin{aligned} W_1 &= cos\left(\beta_a x + \frac{\pi}{4}\right) cos\left(\omega_f t - \frac{\pi}{4}\right) + cos\left(\beta_b x + \frac{\pi}{4}\right) cos\left(\omega_f t + \frac{\pi}{4}\right), \\ &= \frac{1}{\sqrt{2}}\left(X_a^{trig.}(x) cos\left(\omega_f t - \frac{\pi}{4}\right) + X_b^{trig.}(x) cos\left(\omega_f t + \frac{\pi}{4}\right)\right), \end{aligned} \tag{2.15}$$

$$\begin{aligned} W_2 &= cos\left(\beta_a x + \frac{\pi}{4}\right) cos\left(\omega_f t + \frac{\pi}{4}\right) + cos\left(\beta_b x + \frac{\pi}{4}\right) cos\left(\omega_f t - \frac{\pi}{4}\right), \\ &= \frac{1}{\sqrt{2}}\left(X_a^{trig.}(x) cos\left(\omega_f t + \frac{\pi}{4}\right) + X_b^{trig.}(x) cos\left(\omega_f t - \frac{\pi}{4}\right)\right), \end{aligned} \tag{2.16}$$

$$\begin{aligned} W_3 &= cos\left(\beta_a x + \frac{\pi}{4}\right) cos\left(\omega_f t + \frac{\pi}{4}\right) - cos\left(\beta_b x + \frac{\pi}{4}\right) cos\left(\omega_f t - \frac{\pi}{4}\right), \\ &= \frac{1}{\sqrt{2}}\left(X_a^{trig.}(x) cos\left(\omega_f t + \frac{\pi}{4}\right) - X_b^{trig.}(x) cos\left(\omega_f t - \frac{\pi}{4}\right)\right), \end{aligned} \tag{2.17}$$

$$\begin{aligned} W_4 &= cos\left(\beta_a x + \frac{\pi}{4}\right) cos\left(\omega_f t - \frac{\pi}{4}\right) + cos\left(\beta_b x + \frac{\pi}{4}\right) cos\left(\omega_f t + \frac{\pi}{4}\right), \\ &= \frac{1}{\sqrt{2}}\left(X_a^{trig.}(x) cos\left(\omega_f t - \frac{\pi}{4}\right) - X_b^{trig.}(x) cos\left(\omega_f t + \frac{\pi}{4}\right)\right). \end{aligned} \tag{2.18}$$

and the coefficients of these traveling waves are given by,

$$\begin{aligned} C_A &= (1+P)+(1-P)cos\phi-(1+P)sin\phi, \\ C_B &= (1+P)+(1-P)cos\phi+(1+P)sin\phi, \\ C_C &= (1-P)+(1+P)cos\phi+(1-P)sin\phi, \\ C_D &= (1-P)+(1+P)cos\phi-(1-P)sin\phi. \end{aligned} \tag{2.19}$$

As the phase information is limited to these coefficients; the linear combination of the waves can be manipulated by changing the phase between the two point forces. Furthermore, these coefficients also have the parameters corresponding to location and frequency. These are inherently present in the parameters P and C. In other words, any change in the location or the frequency of excitation is reflected as a change in the value of the non-dimensional factor P. Thus, this decomposition has separated the variable factors such as locations, forcing frequency and forces in the coefficients (C, C_A, C_B, C_C, C_D). Each of the wave terms is a linear combination of two different mode shapes ($X_a^{trig.}(x)$ and $X_b^{trig.}(x)$) oscillating at the same frequency (ω_f) but with a 90° phase difference (this phase difference arises from the *sin* and the *cos* terms).

Furthermore, while the waves W_1 and W_3 are hybrid traveling waves that move in one direction and waves W_2 and W_4 move in the opposite direction. Additionally, W_1 and W_3 have a phase difference of 90°,

$$\begin{aligned} W_3(\omega_f t) &= -\frac{1}{\sqrt{2}}\left(X_a^{trig.}(x)sin\left(\omega_f t-\frac{\pi}{4}\right)+X_b^{trig.}(x)sin\left(\omega_f t+\frac{\pi}{4}\right)\right), \\ &= W_1\left(\omega_f t+\frac{\pi}{2}\right). \end{aligned} \tag{2.20}$$

A similar relationship can be established between W_2 and W_4. Additionally, these waveforms (W_i) are one of the many optimal combinations that result in traveling waves. Let us consider the generalized waveform equation,

$$W_{ab} = X_a^{trig.}(x)sin\left(\omega_f t+\alpha_1\right)+X_b^{trig.}(x)sin\left(\omega_f t+\alpha_2\right) \tag{2.21}$$

where $|\alpha_1-\alpha_2|$ is the phase difference between the two modes components. In Figure 2.2 the range of these phase angles is varied from -180° to 180° and the cost function of the resulting waves is evaluated. While the blue regions of this plot correspond to the combination that results in traveling waves, the red regions in standing waves. To develop traveling waves, the phase angles α_1 and α_2 are mutually related to each other. For example when $\alpha_1 = 45^\circ$, the waveform is a traveling wave when $\alpha_2 = -45^\circ$ or 135°. However, if $\alpha_2 = 45^\circ$ or -135°, the resulting waveform is a standing wave. Furthermore any phase angles which gives rise to $|\alpha_1-\alpha_2| = 90^\circ$ results in a

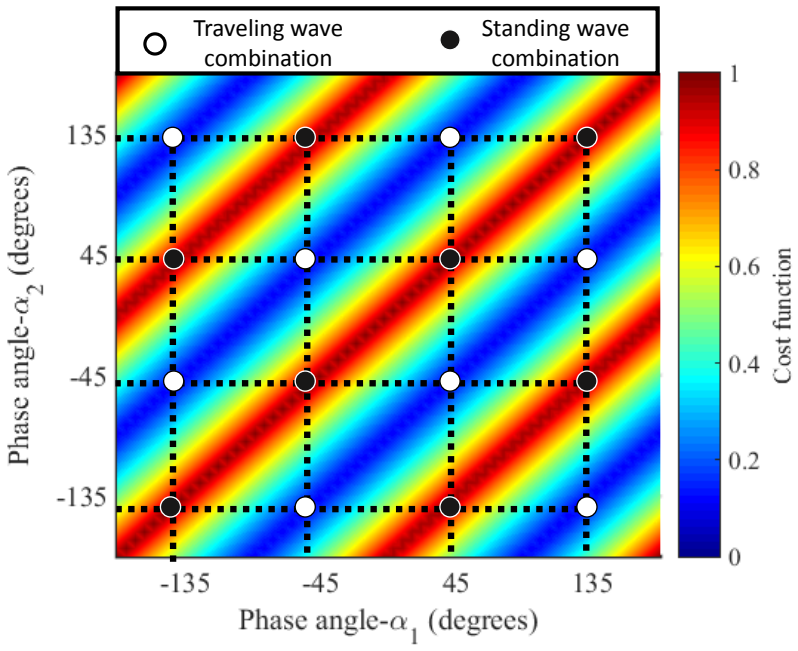

Figure 2.2: Optimality of wave forms based on cost function of the wave.

traveling wave. Thus, the waveforms derived earlier (W_1, W_2, W_3, W_4) are one of many waveforms that satisfy this phase relationship and therefore results in an optimal traveling wave.

This wave phenomena is further elucidated through an example. Let X_b and X_a be the second and the third mode shapes of a free-free beam. Based on these mode shapes, there are eight combinations of temporal solutions possible. Four of these solutions result in standing waves and the rest result in traveling waves. These combinations are further explained through Figures 2.3 and 2.4. Based on the presence/absence of strain nodes in these figures, we can distinguish between a pure standing or hybrid traveling waves. In these figures, while a combination of $X_a^{trig.}(x)cos\left(\omega_f t - \frac{\pi}{4}\right) - X_b^{trig.}(x)cos\left(\omega_f t + \frac{\pi}{4}\right)$ resulted in a standing wave, the complementary combination of $X_a^{trig.}(x)cos\left(\omega_f t - \frac{\pi}{4}\right) + X_b^{trig.}(x)cos\left(\omega_f t + \frac{\pi}{4}\right)$ resulted in a hybrid traveling wave. A similar trend is observed for all eight cases.

2.2.4 Phase relationship based on frequency of excitation

As we are interested in a net traveling wave generation, we further analyze Eq. 2.14, where the beam response has a combination of the four-wave equations W_1, W_2, W_3 and W_4. If the coefficient of all these equations are non-zero, then the net beam response is a component of traveling waves in both directions. This results in a high standing wave content. However, if two of the four coefficients ([C_A and C_C] or [C_B and C_D]) perish, then the net standing wave content is the same as that of the individual waves (W_i). Thus, we can derive a phase relationship by equating each of these coefficients to zero and solving the trigonometric equation. For example, when the coefficient

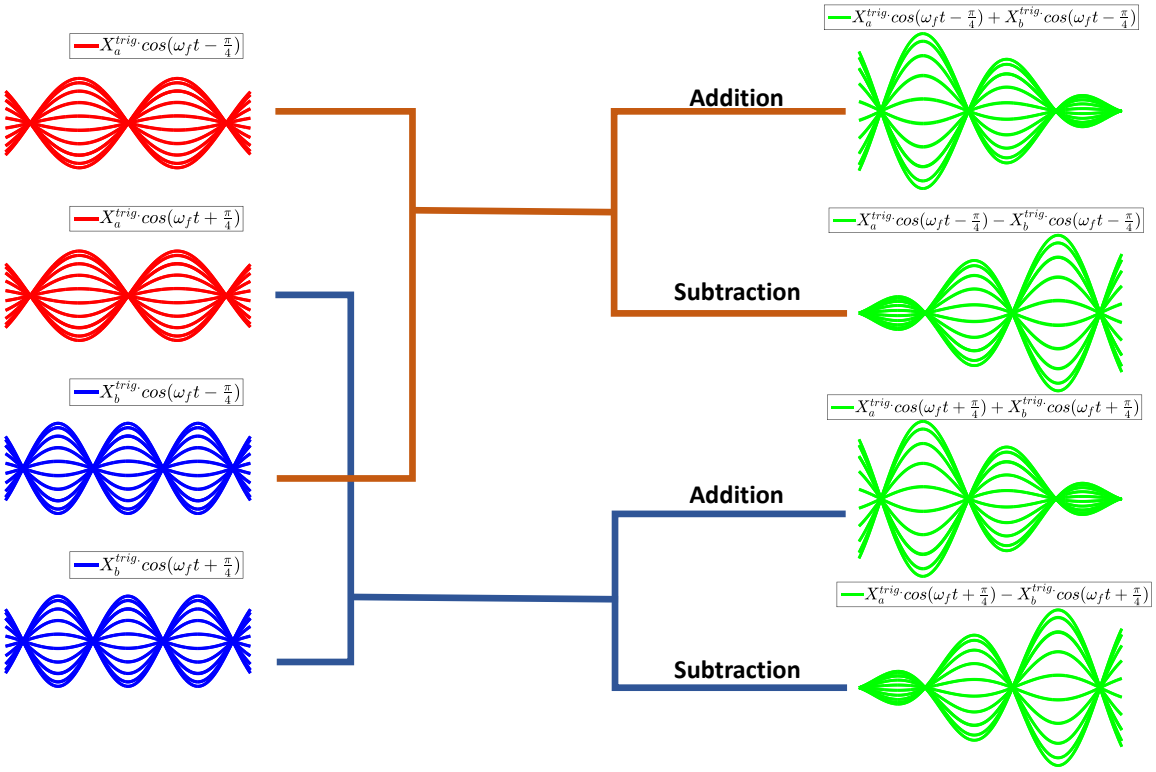

Figure 2.3: Combination of W_1, W_2, W_3 and W_4 that results in standing waves for a free-free beam.

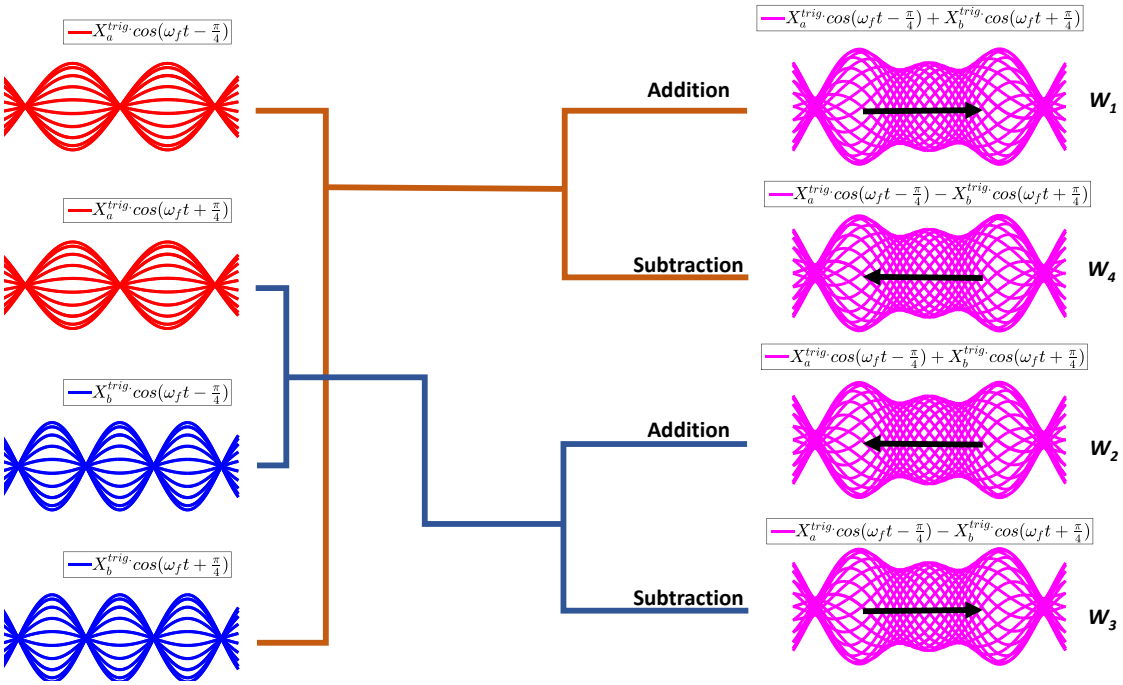

Figure 2.4: Combination of W_1, W_2, W_3 and W_4 that results in traveling waves for a free-free beam.

C_A is equated to zero,

$$
\begin{aligned}
(1+P)+(1-P)cos\phi-(1+P)sin\phi &= 0,\\
(1-P)cos\phi &= (1+P)(sin\phi-1)\\
\frac{cos\phi}{sin\phi-1} &= \frac{1+P}{1-P}\\
\phi = \tan^{-1}\left(\frac{2P}{P^2-1}\right)+2\pi n \quad \text{or} \quad -\frac{\pi}{2}+2\pi n &
\end{aligned}
\tag{2.22}
$$

Similarly, other coefficients are equated to zero, and the corresponding phase conditions are derived and are presented in Table 2.2. This phase relationship shows that for a given location of forces and frequency of excitation, there is a phase relationship that makes two of the four coefficients zero. The resulting response is a traveling wave amplified by the other two coefficients. Based on this table, there are two phase relationships which result in traveling waves, and two others which result in standing waves.

Table 2.2: Phase relationships and the resulting coefficient values.

ϕ	C_A	C_B	C_C	C_D	Resulting wave
$\tan^{-1}\left(\frac{2P}{P^2-1}\right)+m\pi$	0	$\frac{4P(P+1)}{P^2+1}$	0	$\frac{4P(P-1)}{P^2+1}$	Traveling wave ($\Longleftarrow$)
$-\frac{\pi}{2}+2\pi n$	$2(1+P)$	0	0	$2(1-P)$	Standing wave
$\tan^{-1}\left(-\frac{2P}{P^2-1}\right)+m\pi$	$\frac{4P(P+1)}{P^2+1}$	0	$\frac{4P(P-1)}{P^2+1}$	0	Traveling wave ($\Longrightarrow$)
$\frac{\pi}{2}+2\pi n$	0	$2(1+P)$	$2(1-P)$	0	Standing wave

For example, a phase of $\phi = \tan^{-1}\left(\frac{2P}{P^2-1}\right)+m\pi$ results in $C_A = C_C = 0$, $C_B \neq 0$ and $C_D \neq 0$. The variation of this phase is dependent on the location of the forces and frequency of excitation. If $X_a^{trig.}(l_1) = X_b^{trig.}(l_1)$, then the phase is only a function of frequency and this is plotted in Figure 2.5. This extinguishes the two wave components W_1 and W_3 and the resulting beam response is

given by,

$$
\begin{aligned}
w_{ab}^{trig.}(x,t) &= \sqrt{2}C\left(C_B W_2 + C_D W_4\right), \\
&= \sqrt{2}C\frac{4P}{P^2+1}\left((P+1)W_2 + (P-1)W_4\right), \\
&= C\frac{4P}{P^2+1}\left((P+1)X_a(x)cos\left(\omega_f t + \frac{\pi}{4}\right) + (P+1)X_b(x)cos\left(\omega_f t - \frac{\pi}{4}\right)\right) \\
&+ C\frac{4P}{P^2+1}\left((P-1)X_a(x)cos\left(\omega_f t - \frac{\pi}{4}\right) - (P-1)X_b(x)cos\left(\omega_f t + \frac{\pi}{4}\right)\right),
\end{aligned}
\tag{2.23}
$$

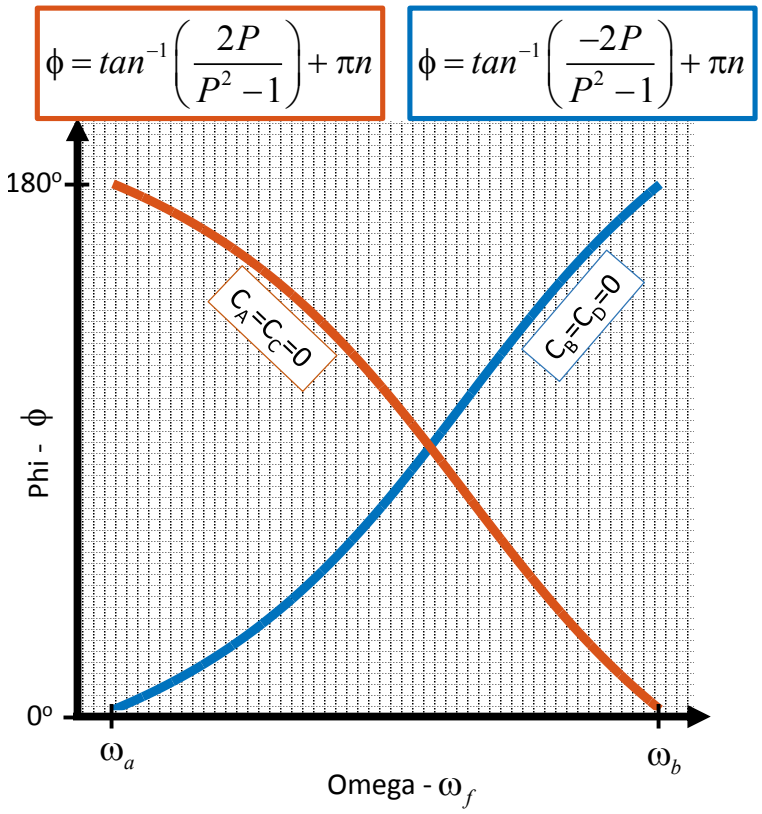

Figure 2.5: Phase relationship that results in traveling waves in free-free beams.

The phase relation $\left(\tan^{-1}\left(\frac{-2P}{P^2-1}\right)\right)$ that perishes the coefficients $C_B = C_B = 0$ is π radians separated from the other phase relationship $\left(\tan^{-1}\left(\frac{2P}{P^2-1}\right)\right)$.

Special case : phase difference of $\frac{\pi}{2}$

However, a phase relation of $\frac{\pi}{2}$ results in $C_A = C_D = 0$ which in-turn results in the beam response to be a linear combination of the waves W_2 and W_3. However, individually these waves move in opposite directions. This results in a higher standing wave content in the wave. However, in the

scenario when $P \to -1$, $C_B \to 0$ and when $P \to 1$, $C_C \to 0$. In these cases, only one of the four coefficients is non zero and hence, the beam response is a traveling wave.

Special case : relating phase relationship with a cost function

For a special case, where $X_a^{trig.}(l_1) = X_b^{trig.}(l_1)$ the phase relation is a function of the frequency of excitation. The cost function is calculated by sweeping the frequency from ω_a to ω_b and the phase from 0° to 180°. The cost function contour is plotted in Figure 2.6. The phase trend that results in a low cost function follows the phase trend shown in Figure 2.5. This shows that the phase relationship established earlier results in an optimal traveling wave.

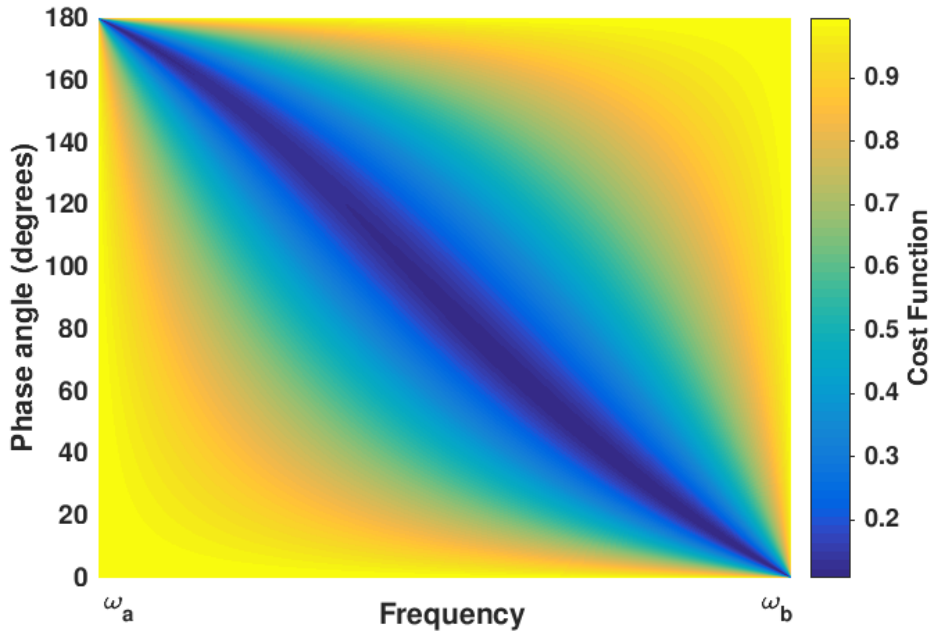

Figure 2.6: Variation of phase between two consecutive mode shapes using a cost function.

In this section, the effect of frequency of excitation on the phase relationship is studied. In the next section, the effect of excitation location on the phase relationship will be discussed.

2.2.5 Phase relationship based on location of excitation

In the previous section, the spatial contribution based on the location of excitation is assumed to be unity i.e. the ratio $\dfrac{X_a^{trig.}(l_1)}{X_b^{trig.}(l_1)} = 1$. In this section, we investigate the relation between the phase angle and the location of excitation. The spatial part is defined as the ratio of the modal

contributions at the location of excitation,

$$S = \frac{X_b^{trig.}(l_1)}{X_a^{trig.}(l_1)}. \tag{2.24}$$

This factor is an integral part of the previously defined parameter P,

$$P = \frac{X_b^{trig.}(l_1)(\omega_a^2 - \omega_f^2)}{X_a^{trig.}(l_1)(\omega_b^2 - \omega_f^2)} = S\frac{\omega_a^2 - \omega_f^2}{\omega_b^2 - \omega_f^2} \tag{2.25}$$

As the location of excitation is varied, the individual modal contributions $X_a(l_1)$ and $X_b(l_1)$ vary

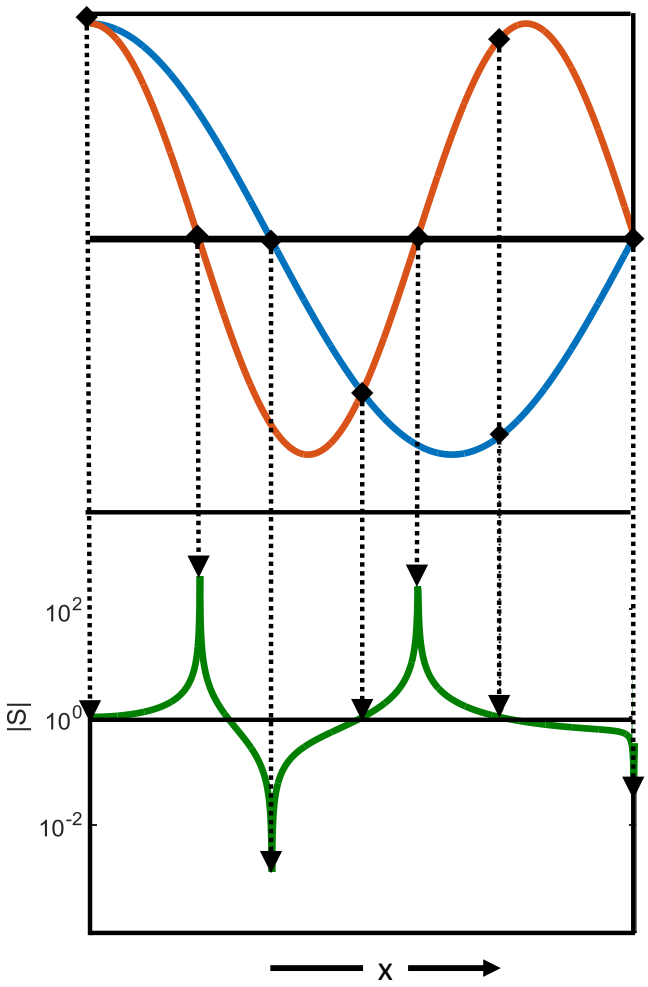

Figure 2.7: Variation of spatial factor (S) over space (x) is expressed as a combination of a low wavelength mode shape (blue) and a high wavelength mode shape (orange).

and the ratio S is also varied. When the location of excitation (l_1) coincides with the strain nodes of $X_a(x)$, then the spatial factor $S = 0$. However, if location of excitation (l_1) coincides with the

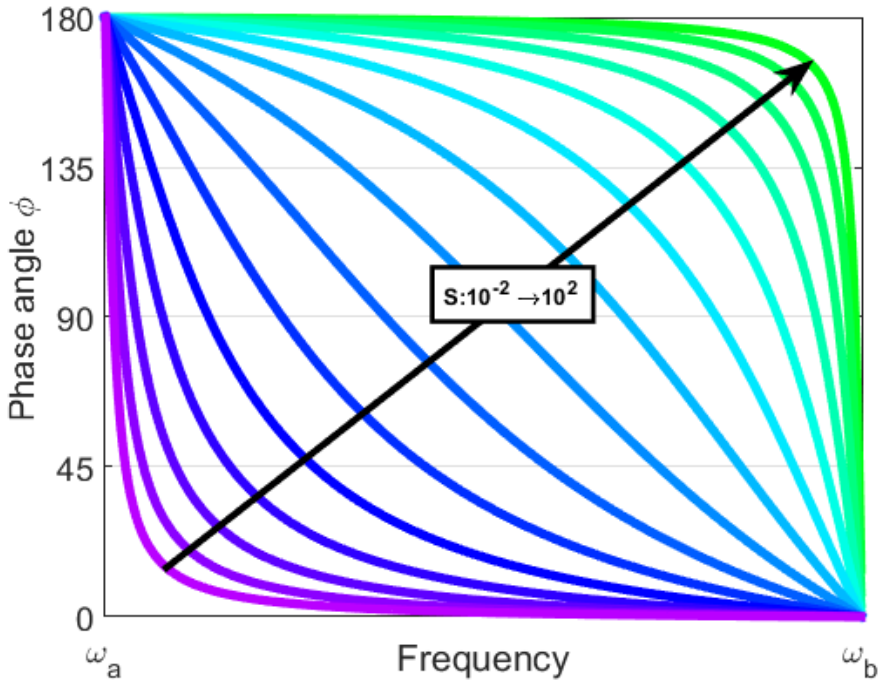

Figure 2.8: Effect of location on the phase relationship over a frequency range.

strain nodes of $X_b(x)$, then the spatial factor $|S| \to \infty$. This is illustrated in Figure 2.7. In this figure initially the modal contributions are equal and the ratio S is equal to 1. Then, both mode shapes diverge from each other, and so does the factor S.

As the spatial factor S is varied from 0 to ∞, the value of P also changes from 0 to ∞. As a result the phase relationship is also effected. This is shown in Figure 2.8. This figure plots the phase relationship as the spatial factor S is varied from 10^{-2} to 10^{2}.

In this section, there is no condition on the choice on 'a' or 'b'. In the next section, a special case of mode combination where restrictions are applied on a and b is discussed.

2.2.6 Dominant mode contibution

In the literature [41], traveling waves are generated by considering the contribution of the two nearest modes shapes. These modes generally correspond to the two natural frequencies, one larger (ω_b) and one smaller (ω_a) than the frequency of excitation (ω_f). So, $\omega_a < \omega_f < (\omega_b = \omega_{a+1})$ and the resulting beam response is given by,

$$\begin{aligned} w_{ab}^{trig.}(x,t) = C\frac{4P}{P^2+1}\left((P+1)X_a(x)cos\left(\omega_f t+\frac{\pi}{4}\right)+(P+1)X_b(x)cos\left(\omega_f t-\frac{\pi}{4}\right)\right) \\ +C\frac{4P}{P^2+1}\left((P-1)X_a(x)cos\left(\omega_f t-\frac{\pi}{4}\right)-(P-1)X_b(x)cos\left(\omega_f t+\frac{\pi}{4}\right)\right), \end{aligned} \tag{2.26}$$

$$
\begin{aligned}
w_{ab}^{trig.}(x,t) &= C\frac{4P}{P^2+1}\left((P+1)cos\left(\omega_f t+\frac{\pi}{4}\right)+(P-1)cos\left(\omega_f t-\frac{\pi}{4}\right)\right)X_a(x)\\
&+C\frac{4P}{P^2+1}\left((P+1)cos\left(\omega_f t-\frac{\pi}{4}\right)-(P-1)cos\left(\omega_f t+\frac{\pi}{4}\right)\right)X_b(x),\\
&=C\frac{2\sqrt{2}P}{P^2+1}[\left(Pcos\left(\omega_f t\right)-sin\left(\omega_f t\right)\right)X_a(x)+\left(Psin\left(\omega_f t\right)+cos\left(\omega_f t\right)\right)X_b(x)],
\end{aligned}
\tag{2.27}
$$

$$
\begin{aligned}
&=\frac{2FX_a^{trig.}(l_1)X_b^{trig.}(l_1)(\omega_a^2-\omega_f^2)(\omega_b^2-\omega_f^2)}{(\omega_a^2-\omega_f^2)^2+(\omega_b^2-\omega_f^2)^2}\left(\frac{X_b^{trig.}(l_1)}{(\omega_b^2-\omega_f^2)}cos\left(\omega_f t\right)-\frac{X_a^{trig.}(l_1)}{(\omega_a^2-\omega_f^2)}sin\left(\omega_f t\right)\right)X_a(x)\\
&+\frac{2FX_a^{trig.}(l_1)X_b^{trig.}(l_1)(\omega_a^2-\omega_f^2)(\omega_b^2-\omega_f^2)}{(\omega_a^2-\omega_f^2)^2+(\omega_b^2-\omega_f^2)^2}\left(\frac{X_b^{trig.}(l_1)}{(\omega_b^2-\omega_f^2)}sin\left(\omega_f t\right)+\frac{X_a^{trig.}(l_1)}{(\omega_a^2-\omega_f^2)}cos\left(\omega_f t\right)\right)X_b(x).
\end{aligned}
\tag{2.28}
$$

For a given location of the forces, the two factors $\frac{1}{(\omega_a^2-\omega_f^2)}$ and $\frac{1}{(\omega_b^2-\omega_f^2)}$ determine the contribution of the modes. The nearer the natural frequencies to the frequency of excitation, the higher the mode contribution towards a traveling wave. Thus, if the natural frequencies are distributed uniformly in the frequency spectrum, then the two nearest modes have the highest contribution and can be approximated as a two-mode excitation. However, if multiple natural frequencies are close to each other, then two-mode excitation approximation is an invalid approach. A multi-mode excitation approach is needed to approximate the beam dynamics.

2.2.7 Amplitude of traveling waves

The other important factor of traveling waves is the amplitude of the traveling waves. To address this question, for a given spatial location of the forces, the amplitude of the traveling waves have to be compared with respect to the excitation frequency. Let

$$
P_1=\frac{X_a^{trig.}(l_1)}{(\omega_a^2-\omega_f^2)},\text{ and }P_2=\frac{X_b^{trig.}(l_1)}{(\omega_b^2-\omega_f^2)}
$$

Then we can write, $C=\frac{FP_1}{\sqrt{2}}$ and $PC=\frac{FP_2}{\sqrt{2}}$. this simplifies Eq. 2.23 into,

$$
\begin{aligned}
w_{ab}^{trig.}(x,t) &= \sqrt{2}C\frac{4P}{P^2+1}\left((P+1)W_2+(P-1)W_4\right),\\
&=\frac{4P_1P_2F}{P_1^2+P_2^2}\left((W_2+W_4)P_1+(W_2-W_4)P_2\right)
\end{aligned}
\tag{2.29}
$$

This equation depends on the ratios $\left|\frac{X_a^{trig.}(l_1)}{X_b^{trig.}(l_1)}\right|$ and $\left|\frac{\omega_a^2-\omega_f^2}{\omega_b^2-\omega_f^2}\right|$. For a given spatial location of the forces on the beam, the relative position of the frequency of excitation with respect to the nearest natural frequencies have an influence on the amplitude of the traveling wave. For example, in the case where $X_a^{trig.}(l_1) = X_b^{trig.}(l_1)$ or $\left|\frac{X_a^{trig.}(l_1)}{X_b^{trig.}(l_1)}\right| = 1$, the beam response further simplifies into

$$w_{ab}^{trig.}(x,t) = \frac{2F(X_a^{trig.}(l_1))^3(\omega_a^2-\omega_f^2)(\omega_b^2-\omega_f^2)}{(\omega_a^2-\omega_f^2)^2+(\omega_b^2-\omega_f^2)^2} \times \left[cos\omega_f t\left(\frac{X_a(x)}{(\omega_b^2-\omega_f^2)}+\frac{X_b(x)}{(\omega_a^2-\omega_f^2)}\right)+sin\omega_f t\left(\frac{X_b(x)}{(\omega_b^2-\omega_f^2)}-\frac{X_a(x)}{(\omega_a^2-\omega_f^2)}\right)\right] \tag{2.30}$$

In this equation, the amplitude of the traveling wave is only dependent on the frequency of excitation ω_f. The factor $2F(X_a^{trig.}(l_1))^3$ is a constant for a given spatial location of excitation i.e. for a given l_1. Neglecting this factor, the dependence of the amplitude of the traveling wave on the frequency of excitation is shown in Figure 2.9.

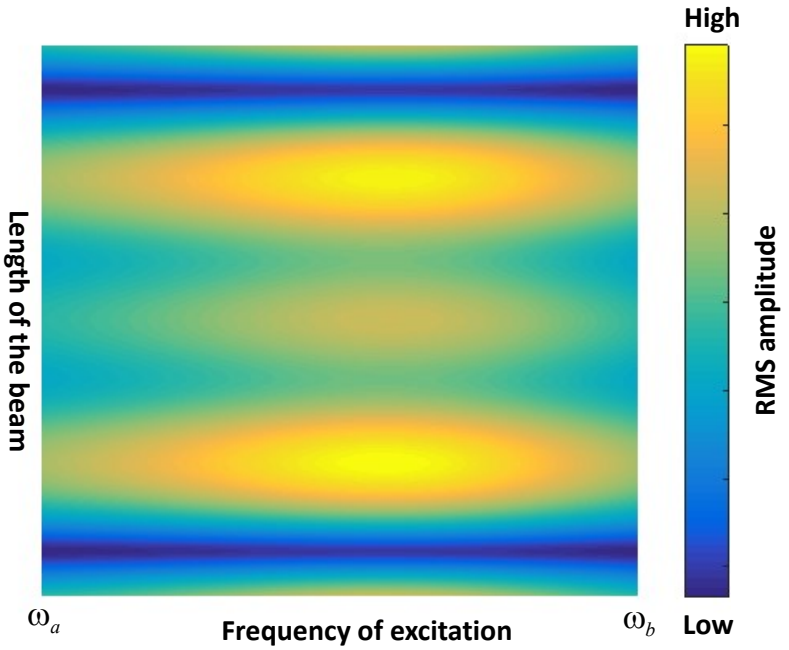

Figure 2.9: Amplitude of traveling waves in free-free beams.

The frequency where the amplitude is maximum is equivalent to minimizing the function

$[(\omega_a^2-\omega_f^2)^2+(\omega_b^2-\omega_f^2)^2]$. Then, the optimal frequency is given by,

$$\omega=\sqrt{\frac{\omega_a^2+\omega_b^2}{2}}.$$

So in this scenario, we have $\left|\frac{\omega_a^2-\omega_f^2}{\omega_b^2-\omega_f^2}\right|=1$ and $\left|\frac{X_a^{trig.}(l_1)}{X_b^{trig.}(l_1)}\right|=1$, which yields $P=\pm 1$

$$w_{ab}^{trig.}=\frac{8FX_a(l_1)}{\omega_a^2+\omega_b^2}W_2 \text{ or } \frac{8FX_a(l_1)}{\omega_a^2+\omega_b^2}W_4. \tag{2.31}$$

As W_2 and W_4 are trigonometric functions with a phase difference, the amplitude of these functions is equal to each other. Furthermore, a similar argument is also valid for the case when $C_B=C_D=0$ where w_{ab} is a linear combination of W_1 and W_4.

It is interesting to note that although $\left|\frac{X_a^{trig.}(l_1)}{X_b^{trig.}(l_1)}\right|=1$, the amplitude of the traveling wave is dependent on the value of $X_a^{trig.}(l_1)$. To further elucidate the effect of location on the magnitude of the traveling wave, consider the scenario when $a=7$ and $b=8$. The corresponding mode shapes of are plotted in Figure 2.10. First step is to find the locations where $X_a^{trig.}(x)=X_b^{trig.}(x)$,

$$\begin{aligned} X_a^{trig.}(x)&=X_b^{trig.}(x),\\ \sqrt{2}cos\left(\beta_a x+\frac{\pi}{4}\right)&=\sqrt{2}cos\left(\beta_b x+\frac{\pi}{4}\right),\\ \beta_a x+\frac{\pi}{4}&=2m\pi\pm\left(\beta_b x+\frac{\pi}{4}\right), \end{aligned} \tag{2.32}$$

where m is any non-negative integer. But for the free-free boundary condition, when $n>5$ we can approximate $\beta_n=\frac{(2n+1)\pi}{2}$.

$$\begin{aligned} \beta_a x+\frac{\pi}{4}&=2m\pi\pm\left(\beta_b x+\frac{\pi}{4}\right),\\ \frac{(2a+1)\pi}{2}x+\frac{\pi}{4}&=2m\pi\pm\frac{(2a+3)\pi}{2}x\pm\frac{\pi}{4} \end{aligned} \tag{2.33}$$

Consider the positive sign,

$$\begin{aligned} \frac{(2a+1)\pi}{2}x&=2m\pi+\frac{(2a+3)\pi}{2}x\\ x&=-2m \end{aligned} \tag{2.34}$$

The only allowed case is when $m = 0$, which yields $x = 0$. Similarly,

$$\frac{(2a+1)\pi}{2}x + \frac{\pi}{4} = 2m\pi \pm \frac{(2a+3)\pi}{2}x \pm \frac{\pi}{4}, \tag{2.35}$$

Consider the negative sign,

$$\begin{aligned} \frac{(2a+1)\pi}{2}x + \frac{\pi}{2} &= 2m\pi - \frac{(2a+3)\pi}{2}x, \\ (2a+2)\pi x + \frac{\pi}{2} &= 2m\pi, \\ x &= \frac{4m-1}{4a+4}. \end{aligned} \tag{2.36}$$

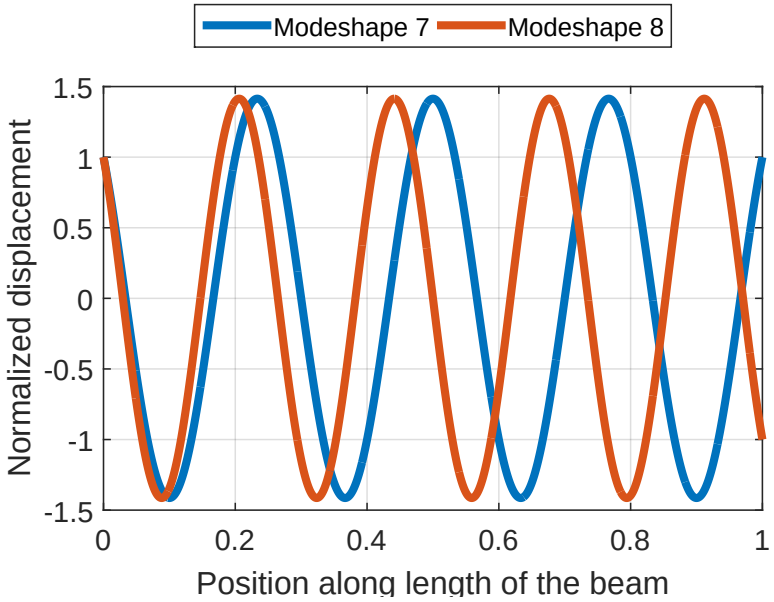

Figure 2.10: Mode shapes of a free-free beam corresponding to the 7^{th} and 8^{th} natural frequencies.

So, in the present case ($a = 7$) there are nine locations where $X_a^{trig.}(x) = X_b^{trig.}(x)$. These values are tabulated in Table 2.3. The next step is to compute the amplitude of the traveling wave using Eq. 2.31. The amplitudes will be proportional to $X_a^{trig.}(l_1)$. For example, in the present case location 2 ($x = \frac{3}{32}$) has the higher amplitude of the traveling wave. This shows that the amplitude of the traveling wave depends on the location of excitation.

2.2.8 Beam excitation at anti-symmetric locations

In the previous discussions, the locations of the forces applied are symmetric i.e. $l_2 = L - l_1$. However, the discussion carried out is also valid for those locations which satisfy the following

Table 2.3: Effect of location on the amplitude of the traveling waves.

	loc 1	loc 2	loc 3	loc 4	loc 5	loc 6	loc 7	loc 8	loc 9
l_1	0	$\frac{3}{32}$	$\frac{7}{32}$	$\frac{11}{32}$	$\frac{15}{32}$	$\frac{19}{32}$	$\frac{23}{32}$	$\frac{27}{32}$	$\frac{31}{32}$
$l_2 = L - l_1$	1	$\frac{29}{32}$	$\frac{25}{32}$	$\frac{21}{32}$	$\frac{17}{32}$	$\frac{13}{32}$	$\frac{9}{32}$	$\frac{5}{32}$	$\frac{1}{32}$
$X_a^{trig.}(l_1)$	1	-1.4	1.33	-1.21	1.05	-0.84	0.61	-0.34	0.07

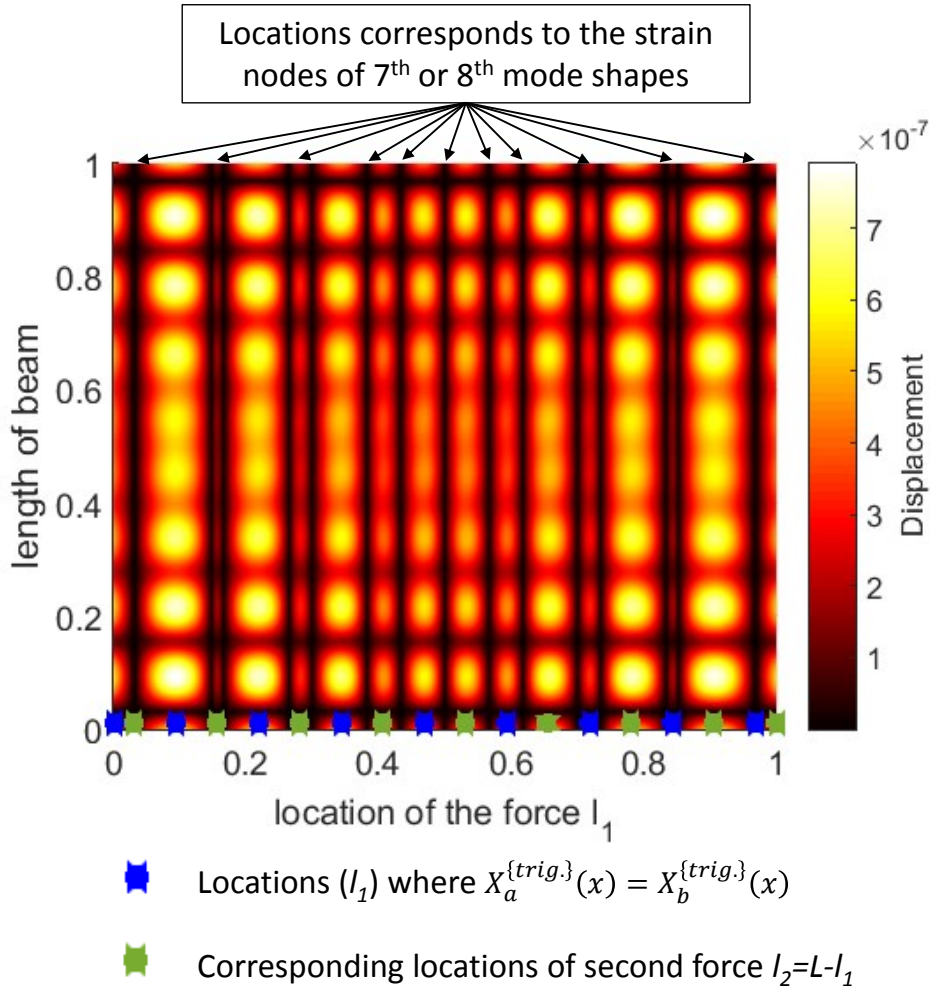

Figure 2.11: Variation of the location of the point forces on the beam for a given frequency.

relationships,

$$\begin{aligned} X_a^{trig.}(l_1) &= X_a^{trig.}(l_2), \\ X_b^{trig.}(l_1) &= -X_b^{trig.}(l_2). \end{aligned} \tag{2.37}$$

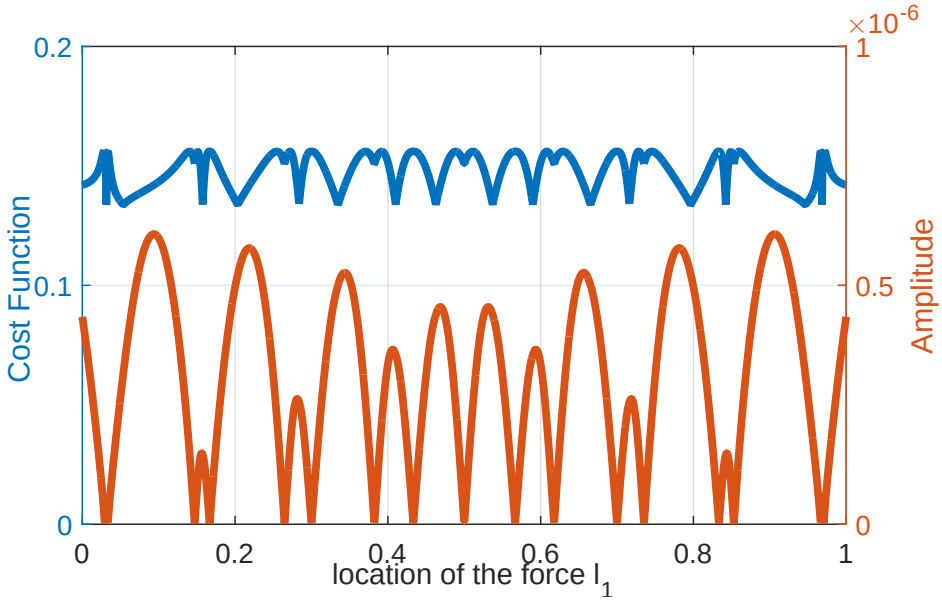

Figure 2.12: Comparison of the cost function and the maximum amplitude of the traveling wave with location of the point force.

If $X_a^{trig.}$ is a symmetric mode shape and $X_b^{trig.}$ is a anti-symmetric mode shape, then all the locations l_1 and $l_2 = L - l_1$ satisfy these relationships. These are the symmetrical excitation locations. However, there are other locations which are anti-symmetric that also satisfy these relationships:

$$\begin{aligned} X_a^{trig.}(l_1) &= X_a^{trig.}(l_2), \\ cos\left(\beta_a l_1 + \frac{\pi}{4}\right) &= cos\left(\beta_a l_2 + \frac{\pi}{4}\right), \end{aligned} \tag{2.38}$$

$$\begin{aligned} \beta_a l_1 + \frac{\pi}{4} &= 2n_1\pi \pm \left(\beta_a l_2 + \frac{\pi}{4}\right), \\ l_1 - l_2 &= \frac{2n_1\pi}{\beta_a}, \text{ or } l_1 + l_2 = \frac{(4n_1 - 1)\pi}{2\beta_a}. \end{aligned} \tag{2.39}$$

Similarly,

$$\begin{aligned} X_b^{trig.}(l_1) &= -X_b^{trig.}(l_2), \\ cos\left(\beta_b l_1 + \frac{\pi}{4}\right) &= cos\left(\pi - \beta_b l_2 - \frac{\pi}{4}\right), \end{aligned} \tag{2.40}$$

$$\begin{aligned} \beta_b l_1 + \frac{\pi}{4} &= 2n_2\pi \pm \left(\pi - \beta_b l_2 - \frac{\pi}{4}\right), \\ l_1 - l_2 &= \frac{(2n_2 - 1)\pi}{\beta_b}, \text{ or } l_1 + l_2 = \frac{(4n_2 + 1)\pi}{2\beta_a}. \end{aligned} \tag{2.41}$$

The wave lengths of the mode shapes are defined by the relation $\lambda_i = \frac{2\pi}{\beta_i}$. Based on this equation, the distance between the two point forces can be written as an integer multiple of the wavelengths

λ_a and λ_b: $l_2 - l_1 = 2n_1\lambda_a$ or $l_2 - l_1 = (2n_2 - 1)\lambda_b$. For free-free mode shapes, the locations of the forces can be simplified by assuming $b = a + 1$, which results in $\beta_a = \frac{(2a+1)\pi}{2}$ and $\beta_b = \frac{(2a+3)\pi}{2}$. This yields,

$$l_1 = \frac{1}{2}\left(\frac{4n_1 - 1}{2a+1} + \frac{4n_2 - 2}{2a+3}\right) \quad l_2 = \frac{1}{2}\left(\frac{4n_1 - 1}{2a+1} - \frac{4n_2 - 2}{2a+3}\right),$$
$$\text{or} \tag{2.42}$$
$$l_1 = \frac{1}{2}\left(\frac{4n_2 + 1}{2a+3} + \frac{4n_1}{2a+1}\right) \quad l_2 = \frac{1}{2}\left(\frac{4n_2 + 1}{2a+3} - \frac{4n_1}{2a+1}\right),$$

where n_1 and n_2 can be any non-negative integers. The only limitation on the location of the forces is that their values should lie in the range of $[0, 1]$. For example, when $a = 7$, there are 10 asymmetrical locations which satisfy the above Eq.2.42. At these locations, the traveling waves are generated using the phase relation $\phi = cos^{-1}\left(\frac{P^2 - 1}{P^2 + 1}\right)$ at the frequency $\omega = \sqrt{\frac{\omega_a^2 + \omega_b^2}{2}}$. These traveling waves are summarized and plotted in Figure 2.13, Figure 2.14 and Figure 2.15.

Cases 1-3 plotted in Figure 2.13 correspond to the locations separated by the wavelength of the 7^{th} mode shape (λ_7). In these cases, although the location of excitation is confined to one end of the beam, there are waves traveling along the whole length of the beam. Furthermore, the amplitude of the traveling wave is higher if these locations are closer to the center of the beam. This is much easier to observe in Figure 2.14, which corresponds to the traveling waves due to point forces at locations separated by $3\lambda_7$ in Cases 4-5 and $5\lambda_7$ in Case 6. The amplitudes of the traveling waves increase from Cases 1-3 to Cases 6 by almost 10 times. Similarly, Figure 2.15 displays traveling waves generated when forces are separated by even integer multiples of the wavelength corresponding to the 8^{th} mode shape. A similar trend is also observed in the amplitudes of the traveling waves.

This theory can also be expanded to a more general case where forces are unequal. Force contributions due to the forces F_1 and F_2 applied at l_1 and l_2 are included in Eq.2.37. This results in,

$$F_1 X_a^{trig.}(l_1) = F_2 X_a^{trig.}(l_2), \text{ and } F_1 X_b^{trig.}(l_1) = -F_2 X_b^{trig.}(l_2). \tag{2.43}$$

This equation illustrates the modal amplification due to the point forces F_1 and F_2, and the spatial amplification due to the selection of the locations l_1 and l_2.

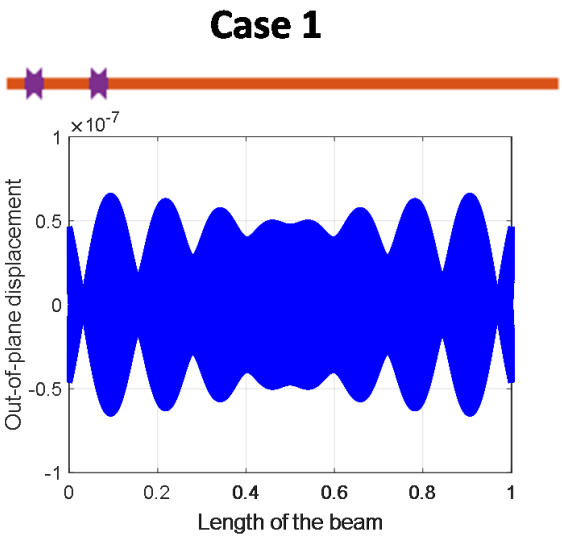

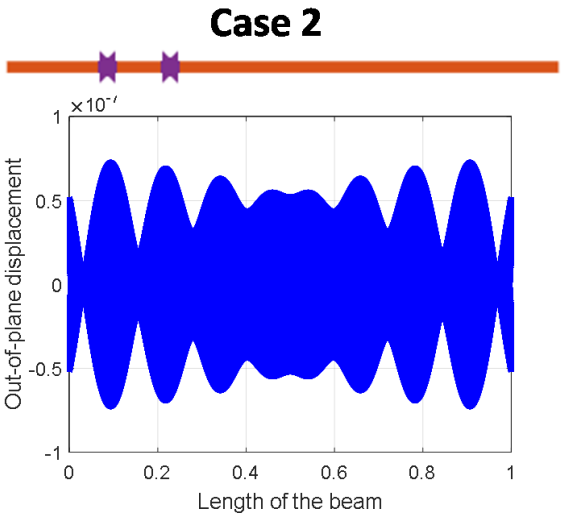

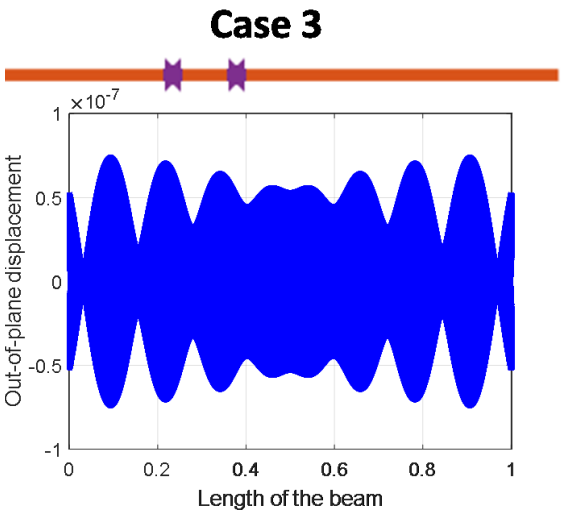

	Case 1	Case 2	Case 3
Location 1	**0.041176**	**0.17451**	**0.307843**
Location 2	**0.158824**	**0.292157**	**0.42549**
Phase	**61.47°**	**30.71°**	**22.74°**

Figure 2.13: Anti-symmetrical excitation with point forces applied in locations separated by λ_7 in Cases 1-3.

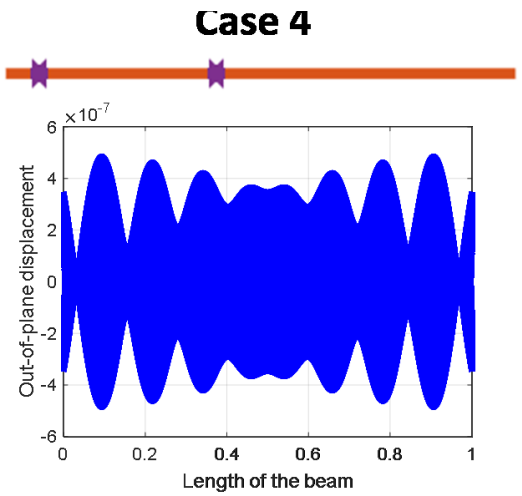

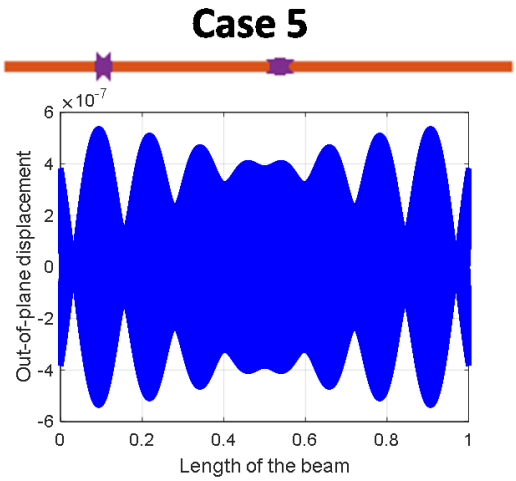

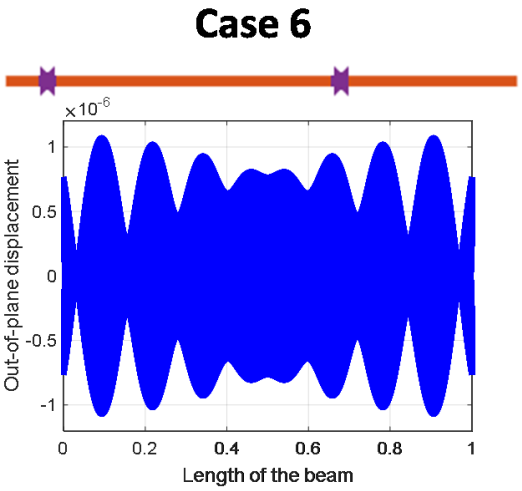

	Case 4	Case 5	Case 6
Location 1	0.409804	0.543137	0.660784
Location 2	0.056863	0.190196	0.072549
Phase	76.38°	59.90°	82.27°

Figure 2.14: Anti-symmetrical excitation with point forces applied in locations separated by $3\lambda_7$ in Cases 4-5 and $5\lambda_7$ in Case 6.

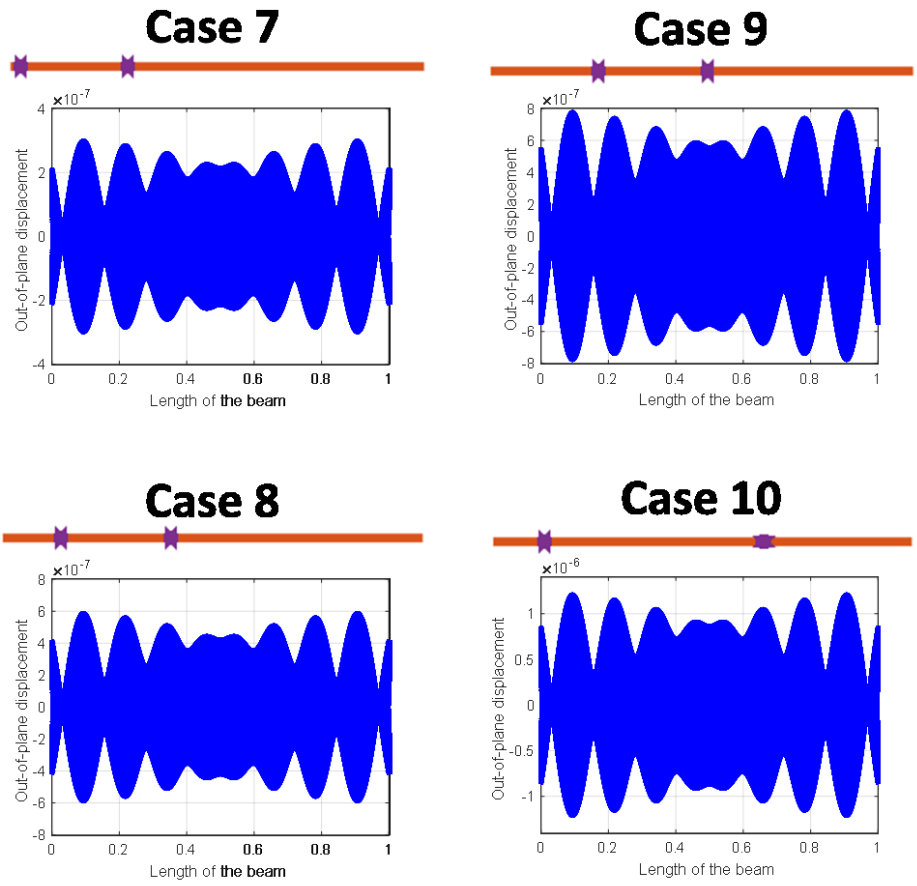

	Case 7	Case 8	Case 9	Case 10
Location 1	**0.0137**	**0.1314**	**0.2490**	**0.1157**
Location 2	**0.2804**	**0.3980**	**0.5157**	**0.6490**
Phase	**95.23**	**122.34**	**132.86**	**102.8930**

Figure 2.15: Anti-symmetrical excitation with point forces applied in locations separated by $2\lambda_8$ in Cases 7-9 and $4\lambda_8$ in Case 10.

2.3 Generalized theory of traveling waves

In this section, the analysis developed in the previous sections can be extended to a multi-dimensional framework. The response of any dimensional system when excited by two point inputs can be written in the form of Eq.2.10. For example for a 2D system, this equation can be written as,

$$w(x,y,t) = \sum_{n=1}^{\infty} \Phi_n(x,y) T_n(t) = \sum_{n=1}^{\infty} \frac{\Phi_n(x,y)\left[F_1 cos(\omega_f t)\Phi_n(l_1) + F_2 cos(\omega_f t + \phi)\Phi_n(l_2)\right]}{\omega_n^2 - \omega_f^2}. \quad (2.44)$$

Similar assumptions can also be made on the magnitude and locations of the point forces.

Sample assumptions: (1) F_1=F_2=F, and (2) Symmetric excitation so that $\Phi_a(l_1) = \Phi_a(l_2)$ and $\Phi_b(l_1) = -\Phi_b(l_2)$. In most scenarios, the second assumption is valid, however, a similar procedure is also applicable when $\Phi_b(l_1) = \Phi_b(l_2)$.

Based on these assumptions, the response of the structure can be written as a summation of two dominant mode shapes.

$$\begin{aligned} w(x,y,t) &= \sum_{n=a,b} \frac{\Phi_n(x,y)F\left[cos(\omega_f t)\Phi_n(l_1) + cos(\omega_f t + \phi)\Phi_n(l_2)\right]}{\omega_n^2 - \omega_f^2}, \\ &= \frac{\Phi_a(x,y)F\left[cos(\omega_f t)\Phi_a(l_1) + cos(\omega_f t + \phi)\Phi_a(l_2)\right]}{\omega_a^2 - \omega_f^2}, \\ &+ \frac{\Phi_b(x,y)F\left[cos(\omega_f t)\Phi_b(l_1) + cos(\omega_f t + \phi)\Phi_b(l_2)\right]}{\omega_b^2 - \omega_f^2} \end{aligned} \quad (2.45)$$

$$\begin{aligned} w(x,y,t) &= \frac{\Phi_a(x,y)\Phi_a(l_1)F\left[cos(\omega_f t) + cos(\omega_f t + \phi)\right]}{\omega_a^2 - \omega_f^2}, \\ &= \frac{\Phi_b(x,y)\Phi_b(l_1)F\left[cos(\omega_f t) - cos(\omega_f t + \phi)\right]}{\omega_b^2 - \omega_f^2} \end{aligned} \quad (2.46)$$

Let,

$$Q_1 = \frac{\Phi_a(l_1)F}{\omega_a^2 - \omega_f^2} \text{ and } Q_2 = \frac{\Phi_b(l_1)F}{\omega_b^2 - \omega_f^2}$$

These definitions reduce Eq. 2.46 to,

$$w(x,y,t) = \Phi_a(x,y)Q_1\left[cos(\omega_f t) + cos(\omega_f t + \phi)\right] + \Phi_b(x,y)Q_2\left[cos(\omega_f t) - cos(\omega_f t + \phi)\right] \quad (2.47)$$

$$
\begin{aligned}
Q_1(cos(\omega_f t)+cos(\omega_f t+\phi)) = &\frac{1}{2\sqrt{2}}cos(\omega_f t+\frac{\pi}{4})\left[(Q_1+Q_2)+(Q_1-Q_2)cos(\phi)+(Q_1+Q_2)sin(\phi)\right] \\
&+\frac{1}{2\sqrt{2}}cos(\omega_f t+\frac{\pi}{4})\left[(Q_1-Q_2)+(Q_1+Q_2)cos(\phi)+(Q_1-Q_2)sin(\phi)\right] \\
&+\frac{1}{2\sqrt{2}}cos(\omega_f t-\frac{\pi}{4})\left[(Q_1+Q_2)+(Q_1-Q_2)cos(\phi)-(Q_1+Q_2)sin(\phi)\right] \\
&+\frac{1}{2\sqrt{2}}cos(\omega_f t-\frac{\pi}{4})\left[(Q_1-Q_2)+(Q_1+Q_2)cos(\phi)-(Q_1-Q_2)sin(\phi)\right]
\end{aligned} \tag{2.48}
$$

This can be written in a simplified form given by,

$$
Q_1(cos(\omega_f t)+cos(\omega_f t+\phi)) = \frac{1}{2\sqrt{2}}cos(\omega_f t+\frac{\pi}{4})\left(\tilde{C}_B+\tilde{C}_C\right)+\frac{1}{2\sqrt{2}}cos(\omega_f t-\frac{\pi}{4})\left(\tilde{C}_A+\tilde{C}_D\right) \tag{2.49}
$$

Similarly,

$$
Q_2(cos(\omega_f t)-cos(\omega_f t+\phi)) = \frac{1}{2\sqrt{2}}cos(\omega_f t+\frac{\pi}{4})\left(\tilde{C}_A-\tilde{C}_D\right)+\frac{1}{2\sqrt{2}}cos(\omega_f t-\frac{\pi}{4})\left(\tilde{C}_B-\tilde{C}_C\right) \tag{2.50}
$$

Substituting Eq.2.49 and Eq. 2.50 in Eq.2.47 yields,

$$
w(x,y,t) = \tilde{C}_A\tilde{W}_1+\tilde{C}_B\tilde{W}_2+\tilde{C}_C\tilde{W}_3+\tilde{C}_D\tilde{W}_4. \tag{2.51}
$$

These equations of the waves ($\tilde{W}_i$) are,

$$
\tilde{W}_1 = \frac{1}{2\sqrt{2}}\left(\Phi_a(x,y)cos\left(\omega_f t-\frac{\pi}{4}\right)+\Phi_b(x,y)cos\left(\omega_f t+\frac{\pi}{4}\right)\right), \tag{2.52}
$$

$$
\tilde{W}_2 = \frac{1}{2\sqrt{2}}\left(\Phi_a(x,y)cos\left(\omega_f t+\frac{\pi}{4}\right)+\Phi_b(x,y)cos\left(\omega_f t-\frac{\pi}{4}\right)\right), \tag{2.53}
$$

$$
\tilde{W}_3 = \frac{1}{2\sqrt{2}}\left(\Phi_a(x,y)cos\left(\omega_f t+\frac{\pi}{4}\right)-\Phi_b(x,y)cos\left(\omega_f t-\frac{\pi}{4}\right)\right), \tag{2.54}
$$

$$
\tilde{W}_4 = \frac{1}{2\sqrt{2}}\left(\Phi_a(x,y)cos\left(\omega_f t-\frac{\pi}{4}\right)-\Phi_b(x,y)cos\left(\omega_f t+\frac{\pi}{4}\right)\right), \tag{2.55}
$$

and the coefficients of these traveling waves are given by,

$$\begin{aligned}
\tilde{C}_A &= (Q_1+Q_2)+(Q_1-Q_2)cos\phi-(Q_1+Q_2)sin\phi,\\
\tilde{C}_B &= (Q_1+Q_2)+(Q_1-Q_2)cos\phi+(Q_1+Q_2)sin\phi,\\
\tilde{C}_C &= (Q_1-Q_2)+(Q_1+Q_2)cos\phi+(Q_1-Q_2)sin\phi,\\
\tilde{C}_D &= (Q_1-Q_2)+(Q_1+Q_2)cos\phi-(Q_1-Q_2)sin\phi.
\end{aligned} \tag{2.56}$$

Based on these equations, phase relationships and amplitude relationships can be developed. As these equations are derived for a generalized case, they can be used to study traveling waves for any boundary condition and any dimensional structure. To illustrate the scope of this theory, a representative traveling wave in a cylindrical system and a 2D plate are shown in Figure 2.16 and Figure 2.17 respectively. This concept is experimentally validated in later sections.

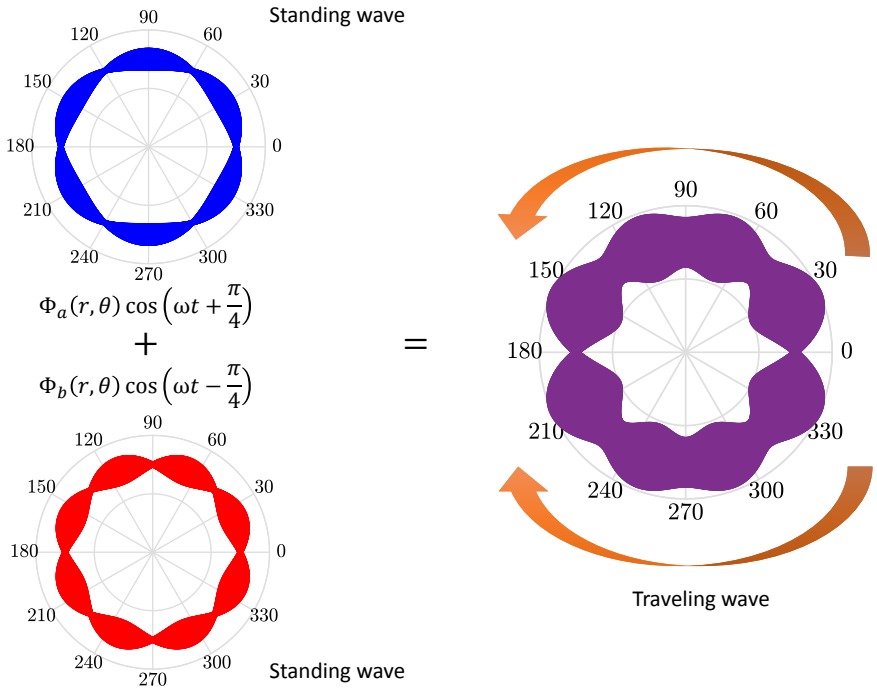

Figure 2.16: A representative example illustrating a cylindrical traveling wave generation.

2.4 Conclusion

In this chapter, theoretical analysis of traveling waves is discussed. As the start of the chapter, a simplified model of a free-free beam is used to study the response of a beam when excited by two point forces. Based on the spatial restrictions on the point force, a phase relationship is developed. The rest of the chapter discusses the effect of other parameters on this phase relationship. Through

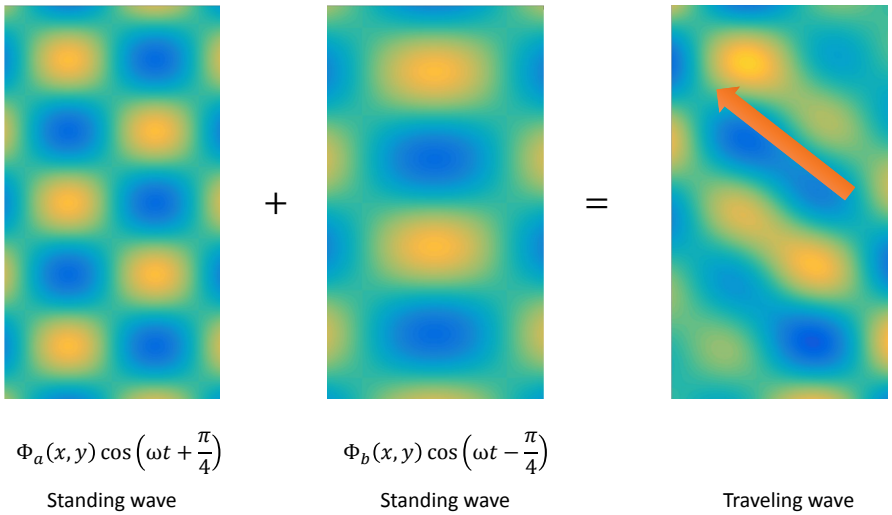

Figure 2.17: A representative example illustrating a planar traveling wave generation.

multiple examples, the influence of location of the point forces and the frequency of excitation on the amplitude and quality of traveling wave is discussed. This theoretical framework developed in this chapter is verified through experiments and simulations in rest of the thesis.

Chapter 3

Traveling waves in 1D beams

3.1 Introduction

The first step in understanding the dynamics of different structures is to be able to simulate the response of the system to any given input. In this chapter, a theoretical model replicating the dynamics of a composite beam with multiple piezo-ceramic patches is developed. This chapter models this beam using the distributed-parameter approach which is later validated through experimental data. The later part of this chapter discusses the two-point excitation methodology to generate traveling waves in a finite media. At first, this work shows that a phase of 90° gives rise to a traveling waves when the frequency of operation is halfway between any two natural frequencies. Then, the effect of the 90° phase difference on the quality of the waves generated at other frequencies is evaluated. This study gives rise to a parametric study that varies the phase difference along with the frequency of excitation. Then, the quality of the response is evaluated under these conditions using cost functions and the results are discussed. Additionally, the effect of boundary conditions on the shape and quality of traveling wave is explored.

3.2 Development of a PZT based beam model

In the previous chapter, theoretically it was shown that when two forces with a phase difference simultaneously actuate a beam structure, traveling waves are generated. In this chapter, this theory is validated through experiments on beam structures with three boundary conditions: free-free, clamped-free, clamped-clamped. We used piezo-ceramic based excitation to vibrate the 1D structures. First, a beam model is developed to replicate the experimental conditions, which is later validated through experiments. A model is developed in which two piezo-ceramic wafers excite a brass beam to generate traveling waves in beams of different boundary conditions.

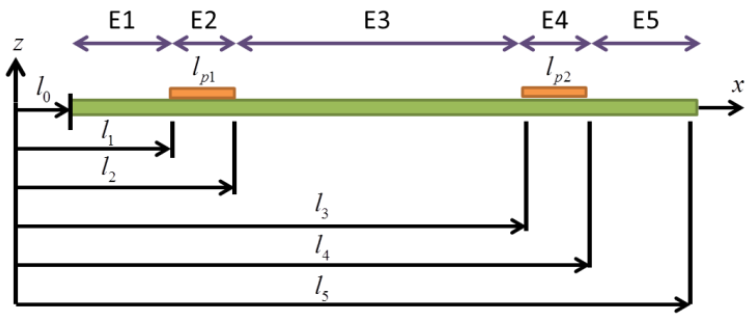

a

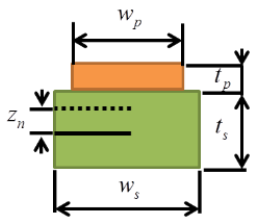

b

Figure 3.1: (a) PZT patches mounted on a beam and the corresponding beam elements (E1-E5). (b) Cross-sectional view of the beam with PZT patches.

The analytical model was derived by calculating the net forces and moments generated by the piezoelectric wafers, both bonded to the same side of the beam. The coupled electromechanical model takes into account the shift in the neutral axis due to these piezoelectric elements and uses voltage as a forcing function. A schematic diagram of the beam with the PZT wafers is presented in Figure 3.1(a). The nomenclature used throughout this paper to describe the relative lengths and positions of the elements present in the beam is displayed in this figure. The beam is modeled as five distinct beam parts ($Ei, i = 1-5$) and each part is referred to as a 'beam element' throughout this chapter. Three parts of the beam are substrate elements ($E1$, $E3$ and $E5$) while the other two parts are composites composed of substrate and PZT wafers ($E2$ and $E4$).

The first step in modeling this complex system is to determine the shift of the neutral axis due to the presence of PZT wafers on one side of the beam. The cross-sectional view of the beam depicting the shift of the neutral axis by a distance(z_n)is shown in Figure 3.1(b).

The new neutral axis is calculated by setting the sum of all the forces in the 1-direction (or along x-axis) over the entire cross-section to be zero,

$$\int_{-t_s/2}^{t_s/2} w_s \sigma_{s11} dz + \int_{t_s/2}^{t_s/2+t_p} w_p \sigma_{p11} dz = 0, \tag{3.1}$$

where the normal stresses of the substrate (σ_{s11}) and the piezo-ceramic (σ_{p11}) are expressed as a function of the beam displacement (w). This is accomplished by using the elastic strain-

displacement relationships and the piezoelectric equations as,

$$\begin{Bmatrix} S_{11} \\ D_3 \end{Bmatrix} = \begin{bmatrix} \frac{1}{Y_1^E} & d_{13} \\ d_{13} & \varepsilon_{33}^T \end{bmatrix} \begin{Bmatrix} T_{11} \\ E_3 \end{Bmatrix}, \tag{3.2}$$

$$\sigma_{11s} = Y_{1s} S_{11s} = -Y_{1s}(z - z_n)\frac{\partial^2 w(x,t)}{\partial x^2}, \tag{3.3}$$

$$\sigma_{11p} = Y_{1p} S_{11p} - Y_{1p} d_{13} E_3 = -Y_{1p}(z - z_n)\frac{\partial^2 w(x,t)}{\partial x^2} - Y_{1p} d_{13} E_3, \tag{3.4}$$

where the subscripts 's' and 'p' denote the properties of the substrate and the piezo-ceramic, respectively. As per standard notation, 'Y' denotes the Young's modulus of the system, d_{13} represents the piezoelectric strain coefficient (in this case they are symmetric $d_{13} = d_{31}$) [174] and the normal strain in the 1-direction is represented by S_{11}. The 31-actuation mode of the piezo-ceramic that generates strain in the 1-direction due to the electric field (E_3) in the 3-direction (or z-axis) is considered for actuating the beam.

The shift in the neutral axis is calculated in the non-actuation case i.e. when the electric field $E_3 = 0$. Upon simplification, the new location of the neutral axis at $z_n$is described by

$$z_n = \frac{Y_{1p} w_p t_p (t_p + t_s)}{2(Y_{1s} w_s t_s + Y_{1p} w_p t_p)}. \tag{3.5}$$

Euler Bernoulli beam equations were used to develop the electro-mechanical model of the brass beam with different boundary conditions. The position of the piezo-ceramic elements on the beam are represented in the equation with the help of two terms: Heaviside function $\mathcal{H}(x)$ and identifier function $\chi_p(x)$. These terms have been used interchangeably depending on the situation. These terms are related by,

$$\chi_p(x) = [\mathcal{H}(x - l_2) - \mathcal{H}(x - l_1)] + [\mathcal{H}(x - l_4) - \mathcal{H}(x - l_3)]. \tag{3.6}$$

Using the nomenclature defined previously, the net sum of the forces acting on the composite beam is determined to be,

$$\frac{\partial S(x,t)}{\partial x} = \underbrace{\rho_s A_s \frac{\partial^2 w(x,t)}{\partial t^2}}_{\text{Substrate}} + \begin{cases} \underbrace{\rho_p A_p [\mathcal{H}(x - l_2) - \mathcal{H}(x - l_1)] \frac{\partial^2 w(x,t)}{\partial t^2}}_{\text{Left Piezo}} \\ \underbrace{\rho_p A_p [\mathcal{H}(x - l_4) - \mathcal{H}(x - l_3)] \frac{\partial^2 w(x,t)}{\partial t^2}}_{\text{Right Piezo}}, \end{cases} \tag{3.7}$$

where $S(x,t)$ is the shear force acting on the beam element and the density and area of substrate and the PZT element are denoted by subscripts 's' and 'p' respectively. Next the moments acting on the beam element were summed and this results in a relationship between the shear force and the bending moment given as,

$$S(x) = -\frac{\partial M(x)}{\partial x}. \tag{3.8}$$

Substitution of this expression into Eq. 3.7 and simplifying, results in the relationship,

$$-\frac{\partial^2 M(x)}{\partial x^2} = [\rho_s A_s + \rho_p A_p \cdot \chi_p(x)]\frac{\partial^2 w(x,t)}{\partial t^2}. \tag{3.9}$$

The stress developed in this composite beam element is the result of both mechanical properties of the composite beam and the electrical properties of the piezo-ceramic material. The stress can be expressed as,

$$\sigma_{11} = \underbrace{-(z-z_n)\frac{\partial^2 w(x,t)}{\partial x^2}(Y_{1s} + Y_{1p}\cdot\chi_p(x))}_{\text{Mechanical}} \underbrace{- Y_{1p} d_{13} E_3 \cdot \chi_p(x)}_{\text{Electrical}}. \tag{3.10}$$

This relationship between the stress induced in the beam and the deflection of the beam was used to determine the mechanical and electrical components of the moments generated in the beam element. Thus,

$$\begin{aligned} M &= M_{mech.} + M_{elec.}, \\ &= [Y_s I_s + (Y_{sp} I_{sp} - Y_s I_s)\cdot\chi_p(x)]\frac{\partial^2 w(x,t)}{\partial x^2} + \frac{Y_{1p} d_{13}}{t_p} QV(x,t)\cdot\chi_p(x), \end{aligned} \tag{3.11}$$

where,

$$\begin{aligned} Y_s I_s &= \frac{Y_{1s} w_s t_s^3}{12}, \\ Y_{sp} I_{sp} &= \frac{Y_{1s} w_s}{3}\left[\left(\frac{t_s}{2} - z_n\right)^3 + \left(\frac{t_s}{2} + z_n\right)^3\right] + \frac{Y_{1p} w_p}{3}\left[\left(\frac{t_s}{2} + t_p - z_n\right)^3 + \left(\frac{t_s}{2} + t_p + z_n\right)^3\right], \end{aligned} \tag{3.12}$$

$$Q = \tfrac{w_p}{2}(t_s + t_p) \quad E = \tfrac{V(x,t)}{t_p}.$$

When Eq. 3.11 is substituted into equation (3.9), a partial differential equation (PDE) that repre-

sents the electromechanical model of the composite beam is obtained as,

$$[\rho_s A_s + \rho_p A_p \cdot \chi_p(x)]\frac{\partial^2 w(x,t)}{\partial t^2} + \frac{\partial^2}{\partial x^2}\left\{[Y_s I_s + (Y_{sp} I_{sp} - Y_s I_s)\cdot \chi_p(x)]\frac{\partial^2 w(x,t)}{\partial x^2}\right\} = -\frac{Y_{1p} d_{13}}{t_p} Q \cdot \frac{\partial^2}{\partial x^2}(V(x,t)\chi_p(x)). \tag{3.13}$$

This PDE for the piezoelectric composite beam is solved by using the separation of variables approach. A detailed discussion is provided in the next section.

3.3 PZT excitation - analytical approach

The distributed parameter equations describing the dynamics of the composite beam are solved using a separation of variable approach [175] with the assumption that $w(x,t) = \Phi(x)T(t)$. This solution is substituted into the equation of motion, Eq. 3.13, to yield,

$$-\frac{\ddot{T}(t)}{T(t)} = \frac{\frac{\partial^2}{\partial x^2}[B(x)\Phi(x)'']}{A(x)\Phi(x)} = \omega^2, \tag{3.14}$$

where,

$$A(x) = \begin{cases} \rho_s A_s & \chi_p = 0 \\ \rho_s A_s + \rho_p A_p & \chi_p = 1, \end{cases} \tag{3.15}$$

and

$$B(x) = \begin{cases} Y_s I_s & \chi_p = 0 \\ Y_{sp} I_{sp} & \chi_p = 1, \end{cases} \tag{3.16}$$

The spatial equation comes from rearrangement of equation (3.14), which results in,

$$\frac{\partial^2}{\partial x^2}[B(x)\Phi(x)''] - \omega^2 A(x)\Phi(x) = 0. \tag{3.17}$$

The beam was modeled as five distinct beam parts, where the relationship between the parts was obtained through the displacement, slope, moment and shear force at their respective boundaries (boundary and continuity conditions). The solution of the PDE for each of the five beam elements

was assumed to be of the form,

$$\Phi_m(x) = a_{1,m}sin\beta x + a_{2,m}cos\beta x + a_{3,m}sinh\beta x + a_{4,m}cosh\beta x, \qquad m \in 1,2,3,4,5 \tag{3.18}$$

where

$$\beta^4(x) = \frac{A(x)\omega^2}{B(x)} \tag{3.19}$$

In the Eq. 3.18 the index m is used to denote the mode shape corresponding to the different elements of the beam.

The bending moment and shear force vanish at the free end of the beam and the displacement and slope at the fixed end. The continuity at the boundary between the substrate element and the composite element was achieved by equating displacement, slope, bending moment and shear forces at l_1, l_2, l_3 and l_4. The various boundary and continuity conditions are shown in the equations below.

Free Boundary

$$\begin{aligned} &\Phi_i''(x = l_j) = 0, \qquad i \in 1,5 \\ &\Phi_i'''(x = l_j) = 0, \qquad j \in 0,5 \end{aligned} \tag{3.20}$$

Fixed Boundary

$$\begin{aligned} &\Phi_i(x = l_j) = 0, \qquad i \in 1,5 \\ &\Phi_i'(x = l_j) = 0, \qquad j \in 0,5 \end{aligned} \tag{3.21}$$

Continuity Boundary

$$\begin{aligned} &\Phi_i(x = l_j) = \Phi_{i+1}(x = l_j), && i \in 1,2,3,4 \\ &\Phi_i'(x = l_j) = \Phi_{i+1}'(x = l_j), && j \in 1,2,3,4 \\ &Y_iI_i\Phi_i''(x = l_j)\Phi_i'(x = l_j) = Y_{i+1}I_{i+1}\Phi_{i+1}''(x = l_j)\Phi_i'(x = l_j), \\ &Y_iI_i\Phi_i'''(x = l_j)\Phi_i'(x = l_j) = Y_{i+1}I_{i+1}\Phi_{i+1}'''(x = l_j)\Phi_i'(x = l_j), \end{aligned} \tag{3.22}$$

These 20 boundary conditions yield 20 equations and 20 unknown constants of integration that

can be written in matrix form as,

$$\begin{bmatrix} C_{1,1} & \cdots & \cdots & C_{1,20} \\ \vdots & \ddots & \vdots & \vdots \\ \vdots & \cdots & C_{19,19} & \vdots \\ C_{20,1} & \cdots & \cdots & C_{20,20} \end{bmatrix}_{20\times 20} \begin{Bmatrix} a_{1,1} \\ a_{2,1} \\ a_{3,1} \\ a_{4,1} \\ \vdots \\ a_{1,5} \\ a_{2,5} \\ a_{3,5} \\ a_{4,5} \end{Bmatrix}_{20\times 1} = \{0\}_{20\times 1} \tag{3.23}$$

The matrix in equation (3.23) will have a nonzero solution for the constants of integration, only if the determinant of the matrix **C** is singular. The elements of this equation are only a function of one variable, the natural frequency ω, as the other variables are either material constants or geometrical constants. By setting the determinant of the matrix **C** as zero, the natural frequencies were obtained from

$$\Delta[C]_{20\times 20} = \begin{vmatrix} C_{1,1} & \cdots & \\ \vdots & \ddots & \vdots \\ & \cdots & C_{20,20} \end{vmatrix} = 0 \tag{3.24}$$

Numerically the value of the determinant is computed at different values of ω and the frequency at which the determinant approaches zero was obtained. The next step is to determine the eigenvectors corresponding to these eigenvalues. There can be infinite solutions for the coefficients a, however a unique solution is obtained by arbitrarily setting one of the coefficients to 1. In this analysis $a_{1,1}$ is set to 1 and the remaining coefficients are calculated numerically as,

$$\left[\begin{array}{c|ccc} C_{1,1} & \cdots & \cdots & C_{1,20} \\ \hline \vdots & C_{2,2} & \vdots & C_{2,20} \\ \vdots & \cdots & \ddots & \vdots \\ C_{20,1} & C_{20,2} & \cdots & C_{20,20} \end{array}\right]_{20\times 20} \begin{Bmatrix} a_{1,1} \\ \vdots \\ a_{3,5} \\ a_{4,5} \end{Bmatrix}_{20\times 1} = \{0\}_{20\times 1}, \tag{3.25}$$

where

$$\left[C'\right]_{19\times19}\begin{Bmatrix} a_{2,1} \\ \vdots \\ a_{3,5} \\ a_{4,5} \end{Bmatrix}_{19\times1} + a_{1,1}\begin{Bmatrix} C_{2,1} \\ \vdots \\ \vdots \\ C_{20,1} \end{Bmatrix}_{19\times1} = \{0\}_{19\times1}, \tag{3.26}$$

This results in

$$\begin{Bmatrix} a_{2,1} \\ \vdots \\ a_{3,5} \\ a_{4,5} \end{Bmatrix}_{19\times1} = -\left[C'\right]^{-1}_{19\times19} \cdot a_{1,1}\begin{Bmatrix} C_{2,1} \\ \vdots \\ \vdots \\ C_{20,1} \end{Bmatrix}_{19\times1}. \tag{3.27}$$

In-order to normalize the mode shapes obtained from the coefficients derived in the previous step, a mass term (N_{mass}) is calculated by using the principle of orthogonality of the mode shapes throughout the length of the beam as,

$$\begin{aligned} N_{mass} = {} & \rho_s A_s \int_{l_0}^{l_1} \Phi_1^2(x)dx + (\rho_s A_s + \rho_p A_p) \int_{l_1}^{l_2} \Phi_2^2(x)dx \\ & + \rho_s A_s \int_{l_2}^{l_3} \Phi_3^2(x)dx + (\rho_s A_s + \rho_p A_p) \int_{l_3}^{l_4} \Phi_4^2(x)dx + \rho_s A_s \int_{l_4}^{l_5} \Phi_5^2(x)dx. \end{aligned} \tag{3.28}$$

The normalized mode shape is the spatial solution of the composite beam and it is defined as,

$$\tilde{\Phi}_i = \frac{\Phi_i}{\sqrt{N_{mass}}} \qquad i = 1,\ldots,5. \tag{3.29}$$

The next modeling step is to find the solution of the temporal part of the composite beam equation. It can be seen from equation (3.13) that the forcing term is presented as the voltage applied to the piezoelectric material. This shows that the temporal solution needs to be derived for those beam elements that include the piezo properties. Applying equation (3.13) for various sections of the beam, the temporal PDE corresponding to the substrate-only part of the beam and the PZT-

substrate part of the beam can be written as

$$\rho_s A_s \frac{\partial^2 w(x,t)}{\partial t^2} + \frac{\partial^2}{\partial x^2}\left\{ Y_s I_s \frac{\partial^2 w(x,t)}{\partial x^2} \right\} = 0 \qquad x \in [l_0, l_1) \cup [l_2, l_3) \cup [l_4, l_5]$$

$$(\rho_s A_s + \rho_p A_p)\frac{\partial^2 w(x,t)}{\partial t^2} + \frac{\partial^2}{\partial x^2}\left\{ Y_{sp} I_{sp} \frac{\partial^2 w(x,t)}{\partial x^2} \right\} \qquad . \tag{3.30}$$

$$= -\frac{Y_{1p} d_{13}}{t_p} Q \cdot \frac{\partial^2}{\partial x^2}(V(x,t)\chi_p(x)) \qquad x \in [l_1, l_2) \cup [l_3, l_4)$$

The particular solution of the PDE is derived for the portions of the beam that lie in the regions $[l_1 l_2)$ and $(l_3 l_4]$. Multiplying equation (3.30) by $\tilde{\Phi}_i$ and integrating over the length of the beam yields,

$$\left[\rho_s A_s \int_{l_0}^{l_1} \tilde{\Phi}_1 \cdot \tilde{\Phi}_1 dx + (\rho_s A_s + \rho_p A_p) \int_{l_1}^{l_2} \tilde{\Phi}_2 \cdot \tilde{\Phi}_2 dx + \rho_s A_s \int_{l_2}^{l_3} \tilde{\Phi}_3 \cdot \tilde{\Phi}_3 dx \right.$$
$$\left. + (\rho_s A_s + \rho_p A_p) \int_{l_3}^{l_4} \tilde{\Phi}_4 \cdot \tilde{\Phi}_4 dx + \rho_s A_s \int_{l_4}^{l_5} \tilde{\Phi}_5 \cdot \tilde{\Phi}_5 dx \right] \left(\ddot{T}(t) + \omega^2 T(t) \right) \tag{3.31}$$

$$= -\frac{Y_{1p} d_{13}}{t_p} Q \left[\int_{l_0}^{l_5} \frac{\partial^2}{\partial x^2}(V(x,t)\chi_p(x)) \cdot \tilde{\Phi}(x) dx \right]. \tag{3.32}$$

Upon simplifying, with the aid of the orthogonality principle and the Dirac delta identities, the equation is reduced to

$$-\frac{Y_{1p} d_{13}}{t_p} Q \left[V e^{j\omega t} \left(\tilde{\Phi}_3'(l_2) - \tilde{\Phi}_2'(l_1) \right) + V e^{j\omega t + \phi} \left(\tilde{\Phi}_5'(l_4) - \tilde{\Phi}_4'(l_3) \right) \right] = \left(\ddot{T}(t) + \omega_n^2 T(t) \right), \tag{3.33}$$

where both the piezo-ceramics are seperated by a phase difference ϕ. The damping term is then introduced into this equation which yields,

$$\left(\ddot{T}(t) + 2\zeta \omega_n \dot{T} + \omega_n^2 T(t) \right) = -\frac{Y_{1p} d_{13}}{t_p} Q \left[V e^{j\omega t} \left(\tilde{\Phi}_3'(l_2) - \tilde{\Phi}_2'(l_1) \right) + V e^{j\omega t + \phi} \left(\tilde{\Phi}_5'(l_4) - \tilde{\Phi}_4'(l_3) \right) \right]. \tag{3.34}$$

Finally the transfer function for a single piezo-ceramic was derived and is shown below as

$$\frac{T(\omega)}{V(\omega)} = \frac{-Y_{1p} d_{13} Q \left(\tilde{\Phi}_3'(l_2) - \tilde{\Phi}_2'(l_1) \right)}{t_p \left(\omega_n^2 - \omega^2 + 2j\zeta\omega\omega_n \right)} \tag{3.35}$$

A damping ratio of $\zeta = 0.1\%$ is used to simulate the responses of the different beam cases in the following sections. In view of the generalized dynamics discussed above, mathematical models for different boundary conditions (free-free, clamped-free and clamped-clamped) were developed to simulate the traveling wave behavior on a rectangular cross-section beam. Validation of the theoretical model was initially conducted by comparing the eigenvalues and eigen-vectors against the experimental ones before any analysis is carried on the traveling wave behavior. This discussion is presented in the experimental section of this thesis. The physical properties of the composite beam are tabulated in Table 3.1.

Table 3.1: Structural properties of the beam.

PARAMETER	DATA
Length of the beam	0.305 m
Material of the beam	Brass
Young's modulus of the substrate	100 GPa
Density of the substrate	8430 kg/m^3
Thickness of the substrate	0.832 mm
Width of the substrate	19.5 mm
Type of piezo-ceramic	PZT-5A
Density of the piezo-ceramic	7800 kg/m^3
Young's modulus of the piezo-ceramic	62 GPa
Thickness of the piezo-ceramic	0.191 mm
$[l_0, l_1, l_2, l_3, l_4, l_5]$	$[0, 0.02, 0.04, 0.265, 0.285, 0.305]$ m

3.4 Experimental setup

In order to validate the previously developed electro-mechanical finite element model and distributed parameter model of a piezoelectric driven beam, an experimental setup was designed and tested. A sinusoidal voltage sweep is applied to actuate the beam using one of the PZTs and the vibratory response is measured using a Laser Scanning Vibrometer (Polytec PSV 400). In the case of a free-free boundary condition, the experiment is conducted by suspending the composite beam on two strings so that the weight of the beam is supported by the string and the reactionary forces are not distributed [70]. The schematic of the free-free beam seen in Figure 3.2 displays two piezo-ceramic patches attached to a brass substrate at the two ends of the beam. Initially tests were performed by actuating a single piezo-patch and the experimental eigenvalues and eigen-vectors

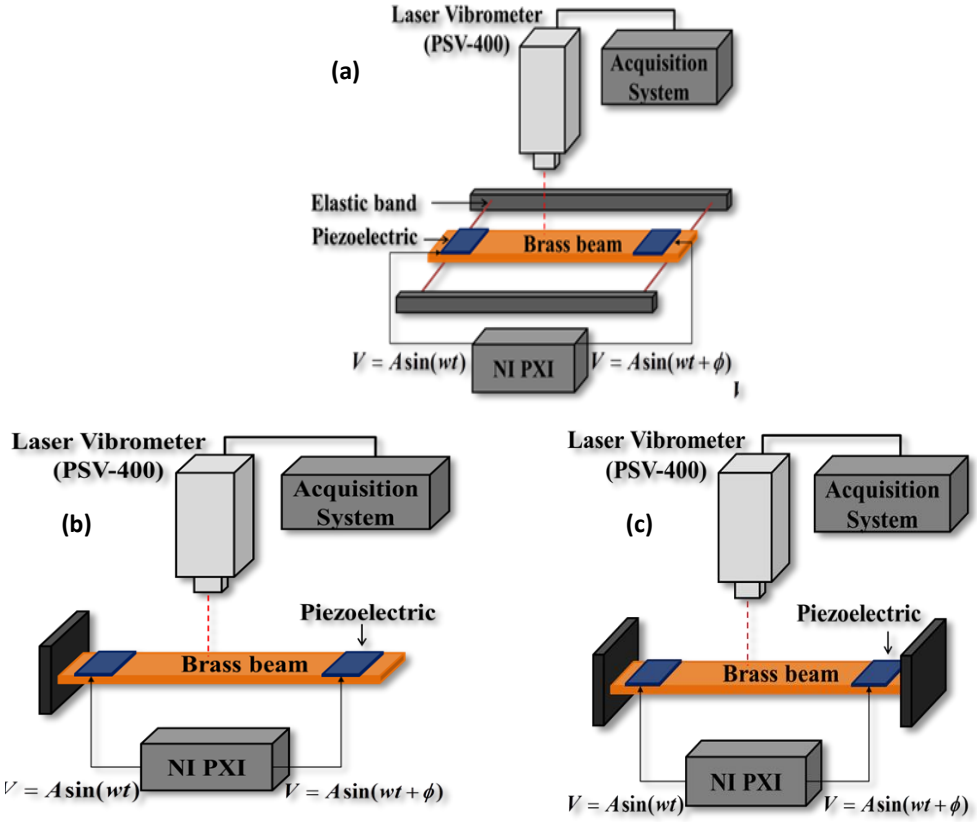

Figure 3.2: Schematic of the experimental setups of a free-free beam, a clamped-free beam and a clamped-clamped beam excited with piezo-ceramic patches.

are used to validate the previously developed models of the beam. The actual test setup displaying the Laser Scanning Vibrometer measuring the response of the beam is shown in Figure 3.3.

Similarly, the clamped boundary condition is realized by placing the end of the beam between two plates and fastening the plates with a bolt. As the bolt mechanism forces the plates together, the end of the beam is pressed in between them and the experimental clamped mechanism is achieved. While, for the clamped-free condition only one end of the beam is fixed, both ends were fixed to realize the clamped-clamped condition.

As explained earlier, the models are validated by comparing the theoretical and experimental responses of beam when excited with a single piezo-ceramic patch. The discussion of these results are presented in the next section. Further, the same setup is also used to measure the dynamics of the beam when both the piezo-ceramics patches are excited. This is also referred to as the two-force excitation. In the succeeding sections the experimental results of various beam configurations are presented and discussed.

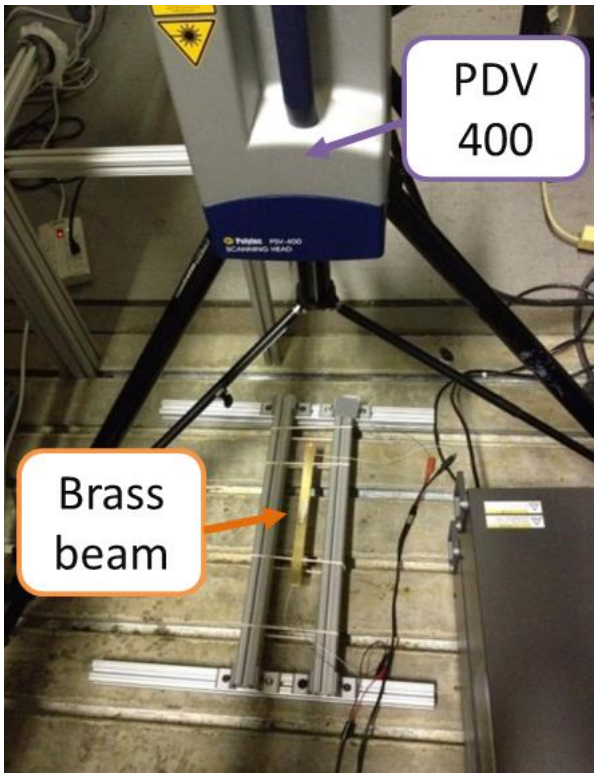

Figure 3.3: Experimental setup used to measure the response of the beam structures with a scanning laser vibrometer of various boundary conditions.

3.5 Single-force results

In this section the simulated responses of the beam are compared against the corresponding experimental values for different beam configurations. The theoretical eigenvalues of the composite beams are obtained by evaluating the determinant of the characteristic equation derived in equation (3.24). The numerical values of the determinant are plotted in Figure 3.4a, Figure 3.5a and Figure 3.6a for all three cases. These theoretical eigenvalues are tabulated along with the experimental values in Table 3.2,Table 3.3 and Table 3.4 corresponding to the free-free, clamped-free and the clamped-clamped case respectively. The errors percentages corresponding to the first three eigenvalues are 13.09%, 5.22% and 0.3% for the clamped-clamped case, 7.248%, 0.55% and 0.05% for the clamped-free case and 4.67%, 0.57% and 0.9% for the free-free case. The corresponding eigen-vectors are obtained by evaluating the equation (3.27) and then normalized using equation (3.29). The corresponding eigen-vectors are validated with the help of the Modal Assurance Criterion (MAC) [176], which represents the orthogonality between the two vectors being compared. In this case, a higher MAC value (closer to 1) shows a better correlation between the experimental and the theoretical results. The results shown in Figure 3.4b, Figure 3.5b and Figure 3.6b have a very good correlation between the experimental and modeling results. Similarly the MAC values

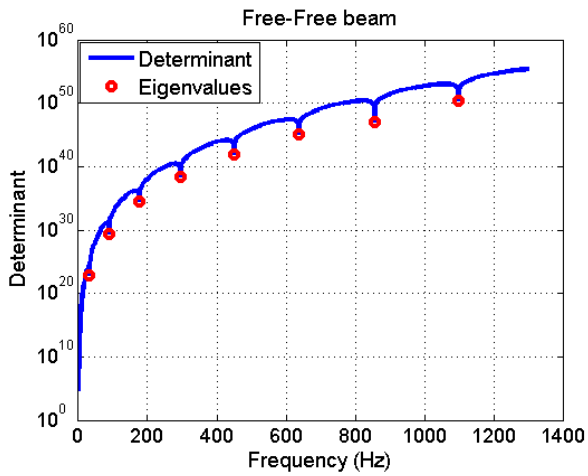

(a)

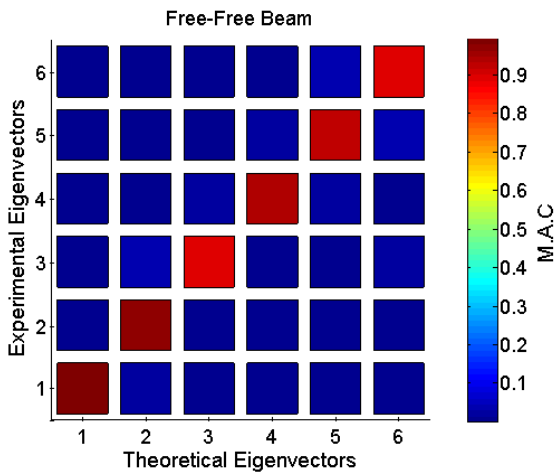

(b)

Figure 3.4: (a) The value of the determinant of the characteristic equation of the free-free beam at different frequencies, (b) MAC chart comparing simulated eigenvalues against the experimental values of a free-free beam.

Table 3.2: Comparison of eigenvalues of a free-free beam.

	Eigenvalues				
Exp.(Hz)	32.8	88.28	176.6	295.7	446.7
Theory(Hz)	31.27	87.78	175	295	449.2
Error(%)	4.67	0.57	0.9	0.23	0.56

stay above 0.9 for most cases with a few as low as 0.8 for the clamped-free case and 0.75 for the clamped-clamped case.

There is extremely good correlation of the eigen-vectors corresponding to the lower eigenvalues, as expected and seen in the MAC chart. Moreover, there is no cross-correlation between other modes demonstrating the high quality of the experimental results. The errors between the experimental and the theoretical values of the eigenvalues and the eigen-vectors can be attributed to the inaccuracies in testing conditions including the ambient noise, pre-stress in the material, clamping effects, etc.

3.6 Two-force results

In this section the response of the beam when both the piezo-ceramics are excited simultaneously is presented. Initially, the case when a fixed phase difference of 90° is between the two forces is discussed. In the later sub-section, the effect of phase on the quality of wave is fully discussed.

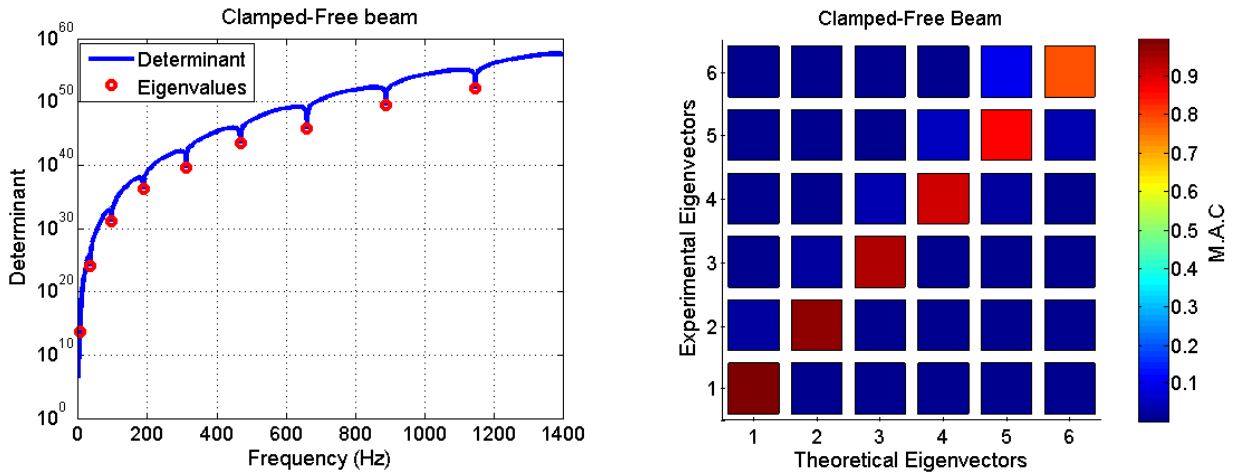

Figure 3.5: (a) The value of the determinant of the characteristic equation of the clamped-free beam at different frequencies, (b) MAC chart comparing simulated eigenvalues against the experimental values of a clamped-free beam.

Table 3.3: Comparison of eigenvalues of a clamped-free beam

	Eigenvalues				
Exp.(Hz)	6.25	34.38	96.6	188.4	312.8
Theory(Hz)	5.797	34.58	96.05	187.5	310.1
Error(%)	7.248	0.55	0.05	0.47	0.86

3.6.1 Fixed-phase case

The dynamics of the beam when actuated with two forces with a phase difference of 90° [41] is studied in this section. First, the response of each individual piezo-ceramic is numerically computed and then the overall response is obtained by the principle of superposition. Furthermore, a comparison of the traveling wave behavior was conducted at a frequency which was half-way (average of the two resonant frequencies) between the third and fourth mode shape, and the phase difference was kept at 90° between the two excitation signals. This comparison for the free-free case and the clamped-clamped case is presented in Figure 3.7, Figure 3.8 and Figure 3.9. Here Figure 3.7a displays the results from the simulated model while the respective experimental results are shown in Figure 3.7b. The figure shows the response of the vibrating beam as a function of time with both the x-y and y-z planes projected. These projections were used to illustrate the existence of the traveling wave and its profile respectively. The blue area on the x-z plane represents the total space covered by the beam during its motion in time (wave envelope). Similarly, the projection on the x-y plane represents the beam amplitude as it changes with time. This can also aid in understanding the travel duration and trajectory from one side to the other.

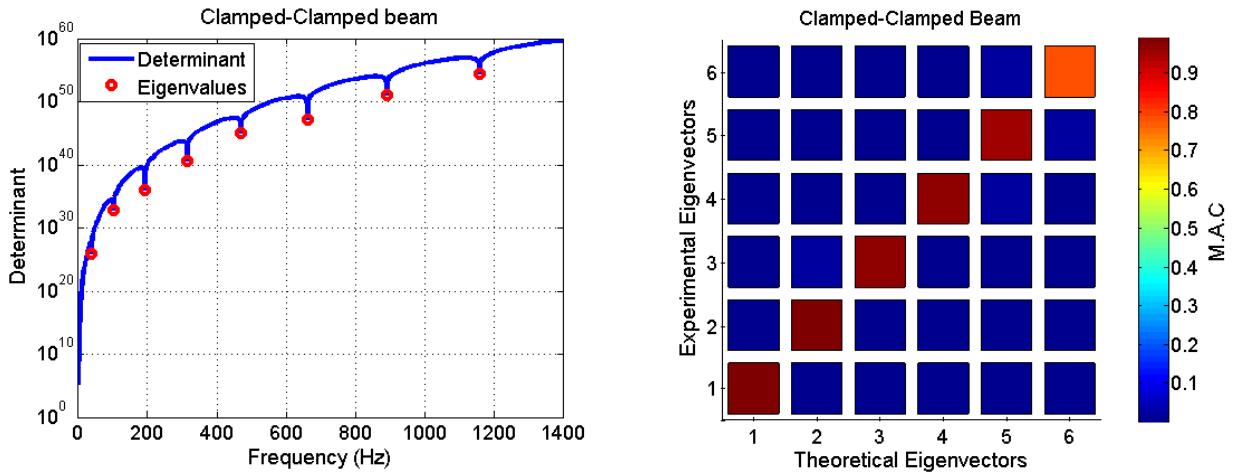

Figure 3.6: (a) The value of the determinant of the characteristic equation of the clamped-clamped beam at different frequencies, (b) MAC chart comparing simulated eigenvalues against the experimental values of a clamped-clamped beam.

Table 3.4: Comparison of eigenvalues of a clamped-clamped beam.

	Eigenvalues				
Exp.(Hz)	34.06	96.56	193.8	320	484.1
Theory(Hz)	38.48	101.6	193.2	314.8	469.9
Error(%)	13.09	5.22	0.3	1.625	2.93

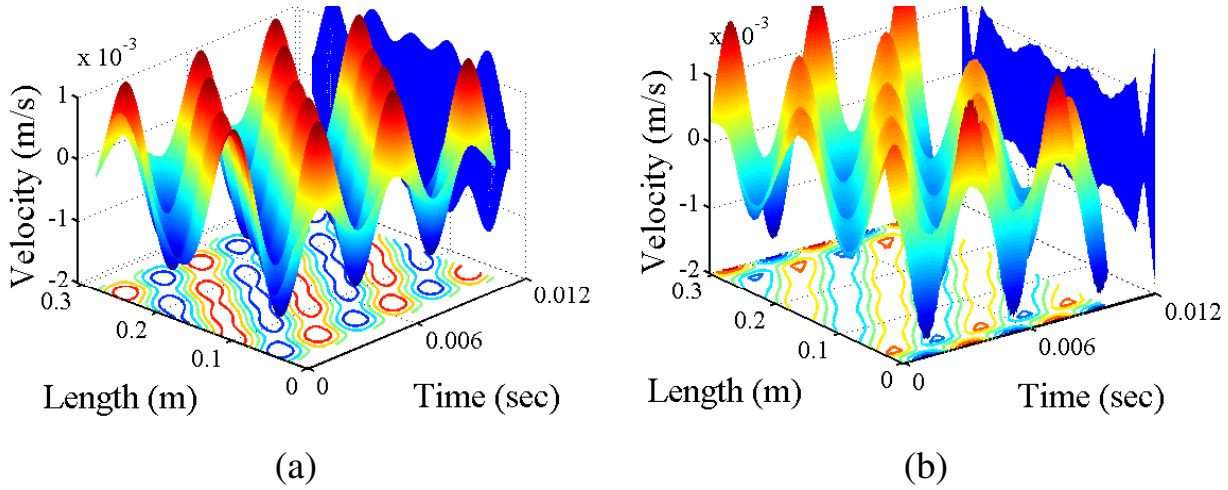

Figure 3.7: 3D representation of traveling waves of a free-free beam obtained (a) theoretically and (b) experimentally.

Once the simulated models are verified for single phase excitation case, additional analysis are conducted in order to better understand the behavior of the structure as it deforms. The re-

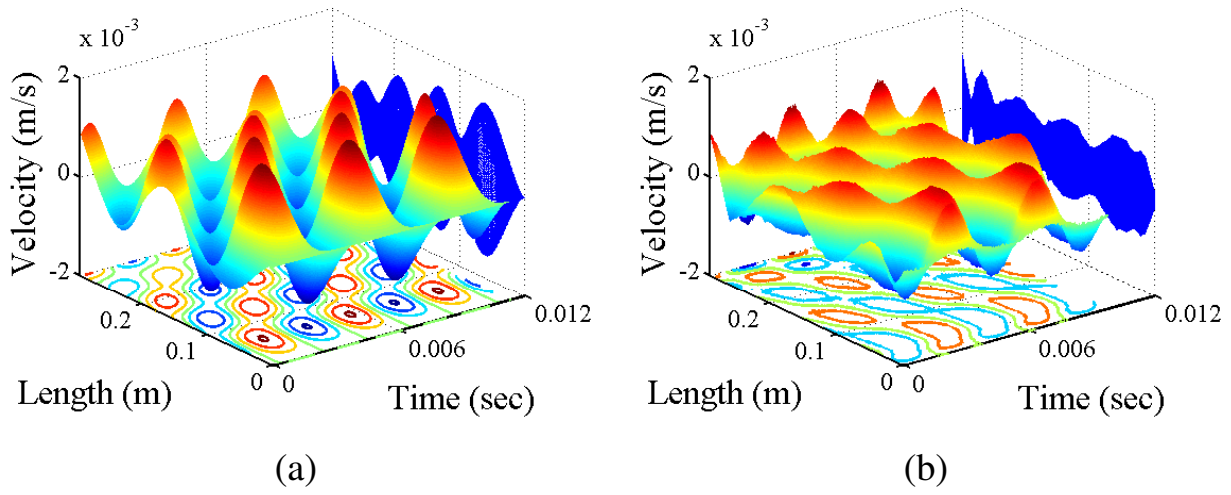

Figure 3.8: 3D representation of traveling waves of a clamped-free beam obtained (a) theoretically and (b) experimentally.

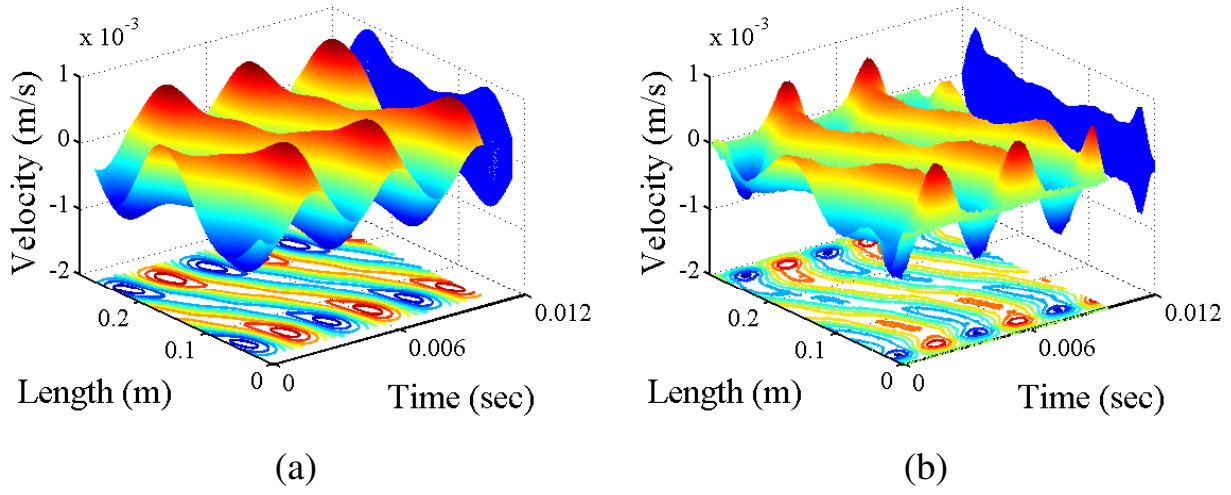

Figure 3.9: 3D representation of traveling waves of a clamped-clamped beam obtained (a) theoretically and (b) experimentally.

sults of this analysis are presented in plots where the response of the beam is calculated and then simulated for different boundary conditions: free-free (Figure 3.10a), clamped-free (Figure 3.10b) and clamped-clamped (Figure 3.10c). Correspondingly, the frequency response function (FRF) for each structure is obtained and the resonance frequencies are identified. The smaller figure insets above the FRF curve corresponds to the profile of the waves generated at the resonance frequency, and the insets below the FRF curve to the ones generated at a frequency that is between two resonant frequencies. A clear distinction between the traveling waves and standing waves can be identified from the insets. The profiles (x-z plane projection envelopes) allure to the fact that

standing waves (above the FRF curve) are associated with nodal points and traveling waves (below the FRF curve) are not, which is expected from the nature of the two waves. In addition, the contour plots associated with each profile compliment the analysis and describe the behavior in further details.

As presented, the contours for standing and the traveling waves are clearly distinct from each other for any frequency or boundary condition. The standing wave contours are discontinuous and the ones for traveling waves are continuous, which suggests the presence or absence of nodal points, respectively. In addition, for the traveling waves, the figures can be used to identify not only the presence of the wave, but also the traveling direction and the corresponding speed. If the slopes are positive, the wave moves from left to right and conversely if the slopes are negative, the direction is then from right to left. The reason why the direction of travel alternates as the excitation frequency moves from $\omega \in (\omega_1, \omega_2)$ to $\omega \in (\omega_2, \omega_3)$ to $\omega \in (\omega_3, \omega_4)$ is due to the existence of even and odd mode shapes, which are coupled with the phase difference between the excitation signals due to intricacies of recreating two clamped boundary conditions in experiments.

These results demonstrate a partial validation of the dynamical model presented in Figure 3.10 ((a),(b) and (c)). However, in order to understand how well the theoretical model predicts the wave profile of a traveling wave, a direct comparison of all previously discussed boundary conditions was conducted. The results are presented in Figure 3.11 ((a),(b) and (c)) at specific frequencies, which resulted in the generation of traveling waves. As shown in this figure, the theoretical model showed a close match with the experimental data. The profile of the traveling wave corresponds with the projection of the x-z plane in Figure 3.7, Figure 3.8 and Figure 3.9. It can be observed that the best match happens in the free-free boundary conditions, which are the easiest to recreate experimentally and is expected.

3.6.2 Variation of phase difference

In the previous section, it was observed that when a beam is excited with two input signals with a specific phase difference of 90° between them, a traveling wave is generated. In this section, first we study the effect of phase variation on the quality of traveling waves in hopes to relax this condition. The cost function formulation, discussed in earlier chapters, is used to determine the quality of traveling waves generated at various frequencies. A full study has been conducted herein for different frequency and phase inputs in order to determine a relationship between frequency and phase. A particular example of these results is presented for a free-free beam at a frequency of $243Hz$ (equal to the arithmetic mean of the 3^{rd} and 4^{th} natural frequencies) and phase difference of 90°. Figure 3.12 presents the results obtained theoretically and experimentally for the previous parameters. Since a hybrid wave was observed, it was intuitive that the waveform would not

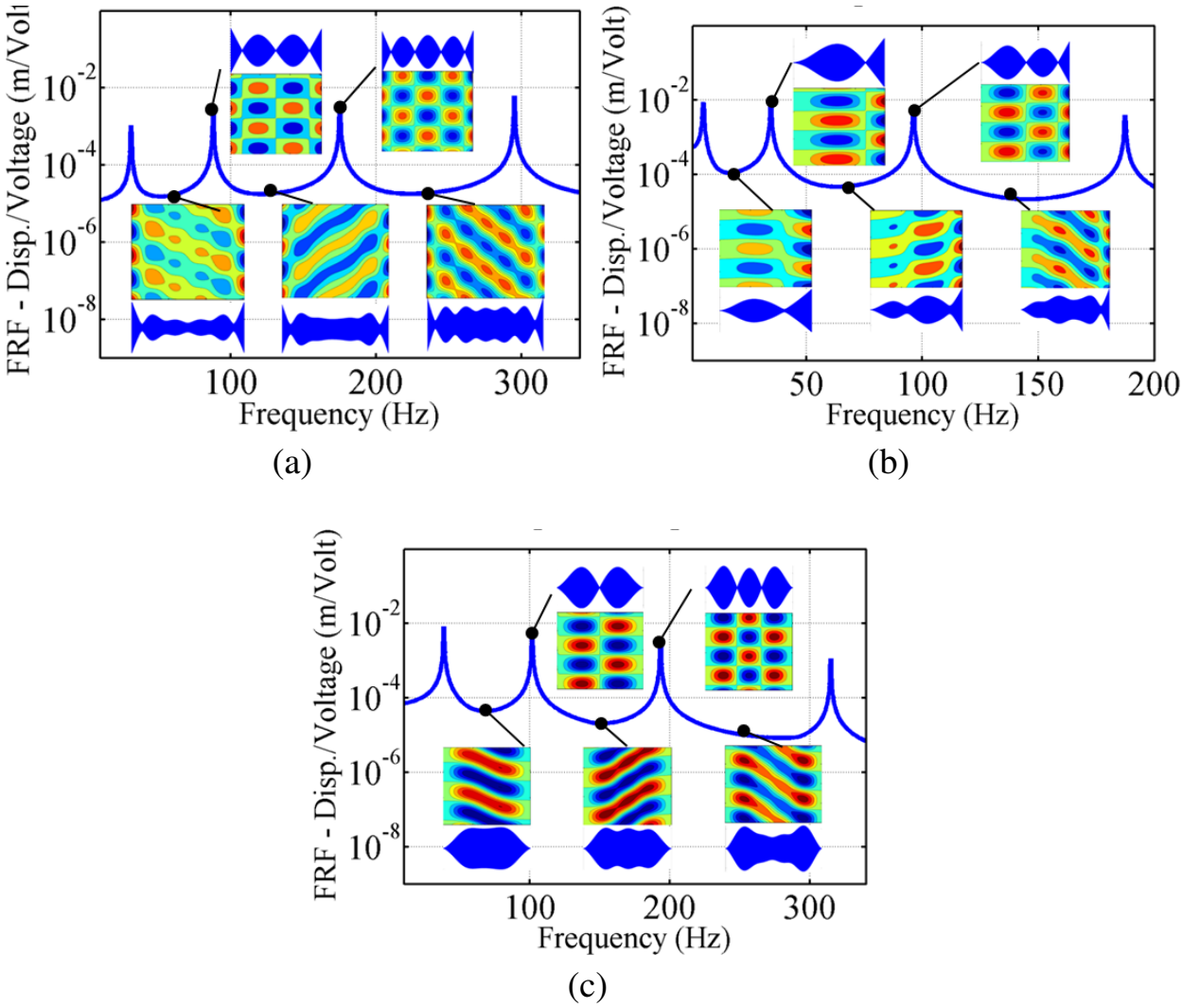

Figure 3.10: Complete analysis of the traveling waves through finite medium when the beam is exited simultaneously by two PZTs with a phase difference of 90°: a) free – free , b) clamped – free, c) clamped – clamped.

indicate any nodal points, as seen in Figure 3.12a. As a result of the previous discussion, two results were expected, a torus shape circle representing the Hilbert's approach shown in Figure 3.12b and an ellipse, obtained using the Fourier's approach, Figure 3.12c.

Similarly, when the boundary conditions of the beam are changed into clamped-free or clamped-clamped cases, traveling waves are also generated by the two-mode excitation. Although a comprehensive analysis on the effect of boundary conditions is discussed in the next section, this section compares the experimental and simulated results of the distributed parameter models developed in earlier section. The enforcement of the boundary conditions on the beam structure is visible at the ends of the beam's response in the wave envelope plot shown in Figure 3.13a and Figure 3.14a. In Figure 3.13a the left boundary is clamped and the right boundary is free; both the boundaries

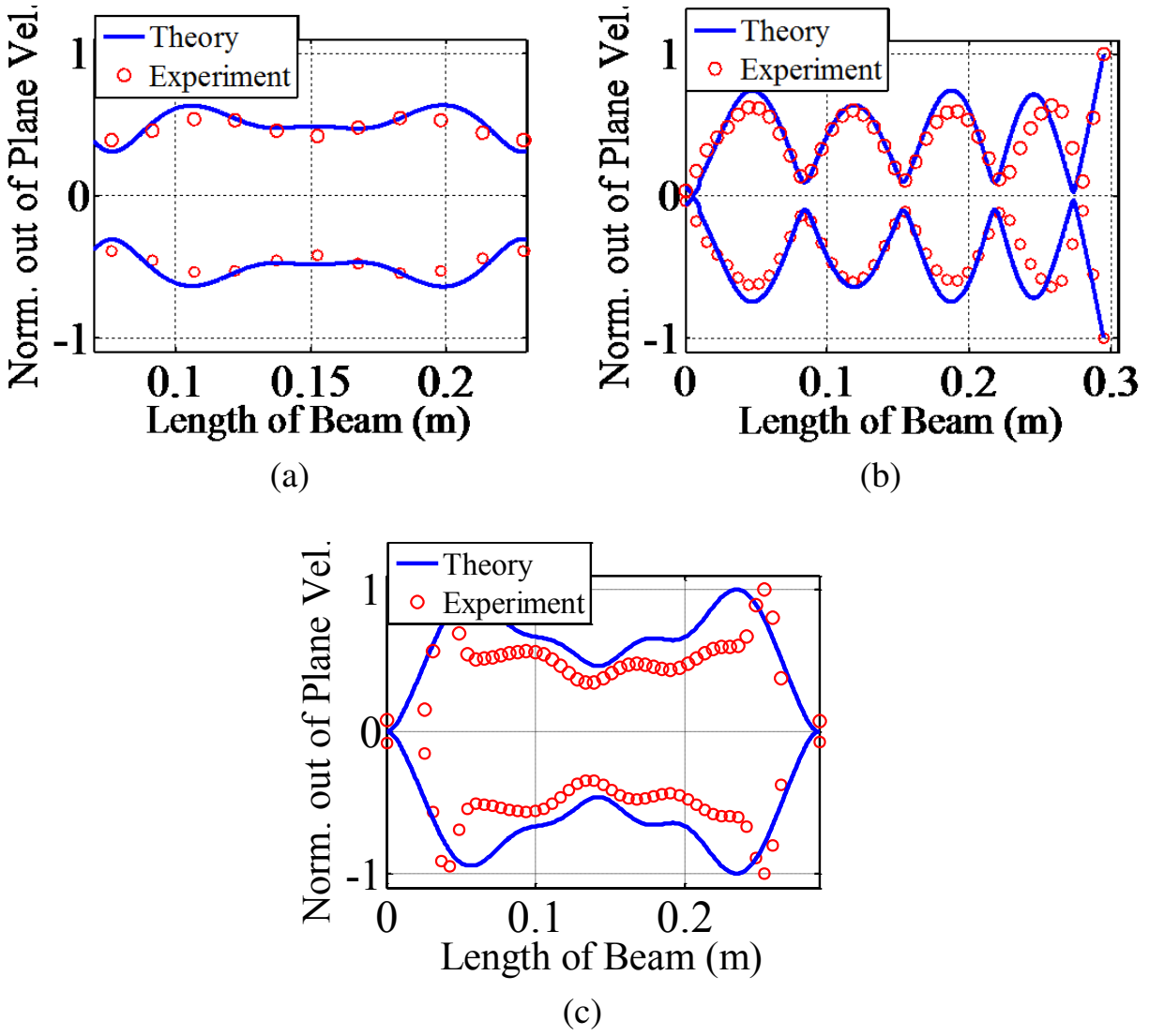

Figure 3.11: Traveling wave envelope obtained experimentally and theoretically. Actuation was conducted at a frequency between two mode shapes with phase difference of 90°:a) free-free boundary condition, 241Hz b) clamped-free boundary condition, 285Hz, c) clamped-clamped boundary conditions, 258Hz.

are clamped in Figure 3.14a. Similar to the free-free case hybrid waves are observed in these two cases. The experimental and theoretical Hilbert's torus and Fourier's ellipse follow similar trend in both these cases. However, when we compare the tori based on Hilbert's approach, for all three boundary conditions, we can observe that the standing wave content is the highest in the clamped-free case. This is evident from the thickness of the rings in Figure 3.12b , Figure 3.13b and Figure 3.14b.

The comparison between the experimental and theoretical results for each case revealed very close correlation, showing the accuracy of the model in predicting the wave response. It is impor-

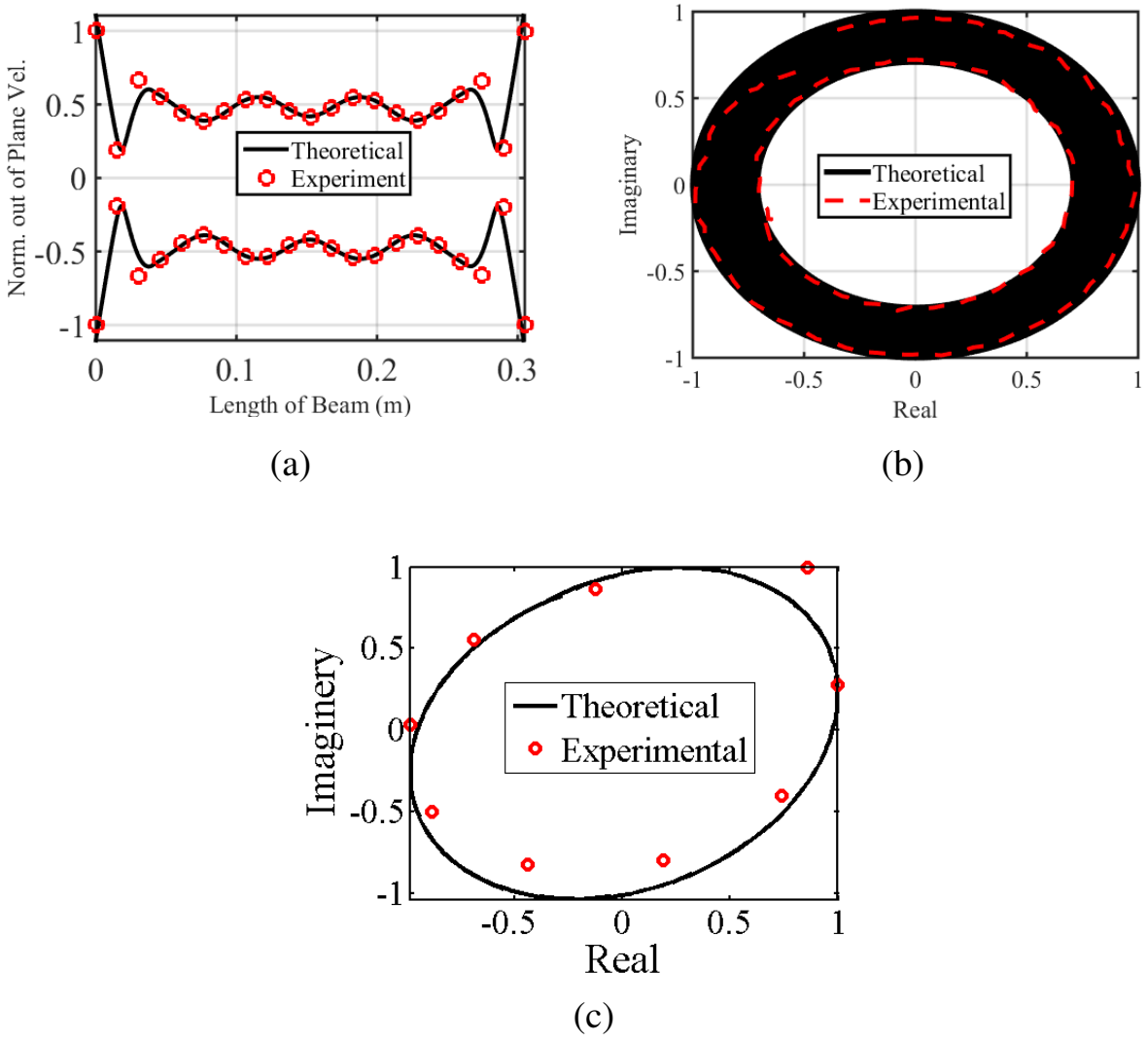

Figure 3.12: Comparison of mechanical waves of a free-free beam obtained experimentally and theoretically at $243Hz$ and phase difference of 90° between the two excitation signals: (a) traveling wave envelope, (b) response of the wave according to the Hilbert's approach, and (c) response of the wave according to the Fourier's method.

tant to note that in Figure 3.12b, Figure 3.13b and Figure 3.14b two experimental points (obtained from the smaller window shown along the length of the beam) were selected (the maxima and minima point on the waveform) in order to better present the approach. This was done for a more convenient visual representation of the results. As shown in Figure 3.12b, the responses for the two points trace a circle (dashed red line) where the inner radius and outer radius equal the values of their vibration amplitudes. On the other side, using Fourier's approach, the phase and magnitude of the FFT response for multiple points across the length of the beam for the specified window, was first calculated and then plotted in complex domain. Accordingly, due to the nature of the waves, the points lie close to an ellipse.

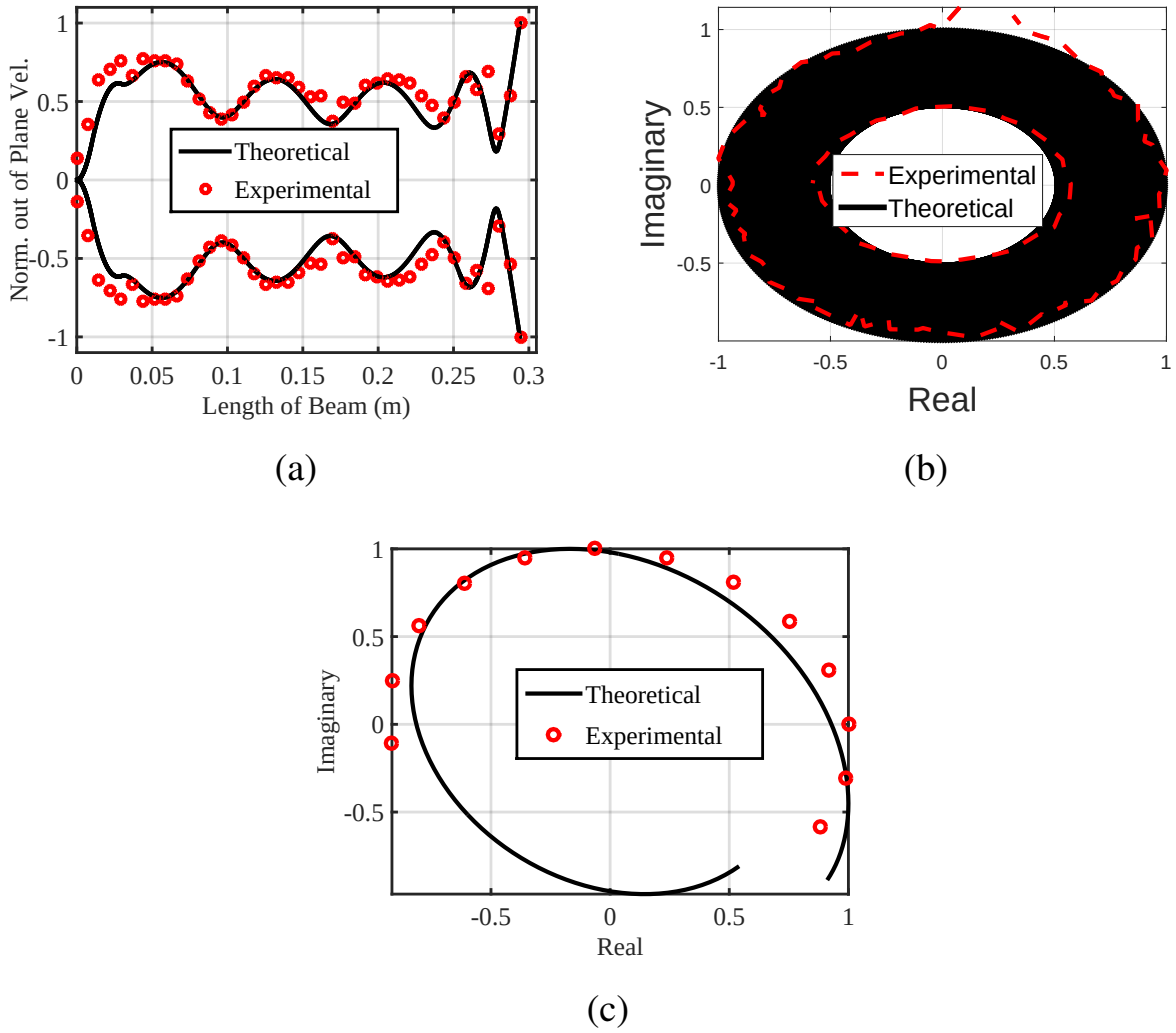

Figure 3.13: Comparison of mechanical waves of a clamped-free beam obtained experimentally and theoretically at $243Hz$ and phase difference of 90° between the two excitation signals: (a) traveling wave envelope, (b) response of the wave according to the Hilbert's approach, and (c) response of the wave according to the Fourier's method.

In the parametric study where the phase difference between the two piezo-ceramics is varied, the CF is defined with the help of Hilbert's approach, but this study can also be carried out using the Fourier approach. Figure 3.15 shows the CF obtained by sweeping the phase angle (-180° to 180°) over the frequency range of [$0Hz$-$650Hz$] through free-free beam simulations. The results clearly indicate that a phase angle of 90° is not the only possible phase required to obtain the traveling waves. More so, it can be observed that each frequency has a corresponding phase that affects the cost of the wave being formed. In this figure, $CF = 1$ corresponds to a pure standing wave, $CF = 0$ to a pure traveling wave, and $0 < CF < 1$ to hybrid waves. Accordingly, the lighter color region that resembles a straight line and connects two corners diagonally for each frequency

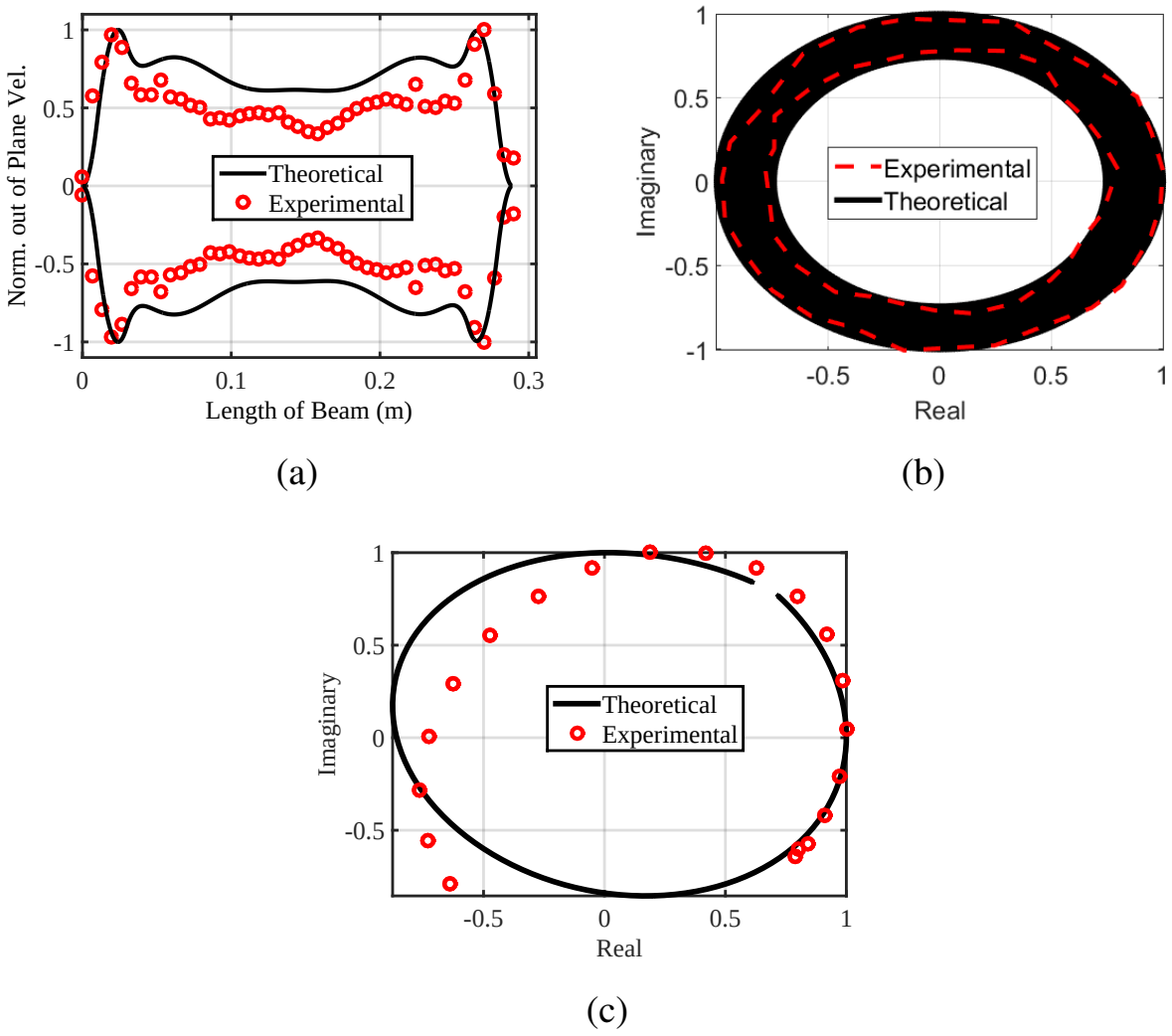

Figure 3.14: Comparison of mechanical waves of a clamped-free beam obtained experimentally and theoretically at $243Hz$ and phase difference of 90° between the two excitation signals: (a) traveling wave envelope, (b) response of the wave according to the Hilbert's approach, and (c) response of the wave according to the Fourier's method.

range ($\omega \in (\omega_1, \omega_2)$, $\omega \in (\omega_2, \omega_3)$, $\omega \in (\omega_3, \omega_4)$) corresponds to the lowest CF, i.e. region at which highest quality traveling waves are formed. It is also important to notice that this allows a traveling wave to be generated at any frequency desired if the correct phase is used.

Besides the CF calculation, this demonstrates the ability of the theoretical model to predict the direction in which the waves travel. The blue color (negative CF) indicates the direction of the waves traveling from right to left, and conversely the red color (positive CF) shows the direction of the waves traveling from left to right. As a consequence, it can be observed that when passing from $\omega \in (\omega_1, \omega_2)$ to $\omega \in (\omega_2, \omega_3)$ to $\omega \in (\omega_n, \omega_{n+1})$), the direction of the traveling waves alternate. More specifically in the $\omega \in (\omega_1, \omega_2)$ region the wave travels from right to left and in the $\omega \in$

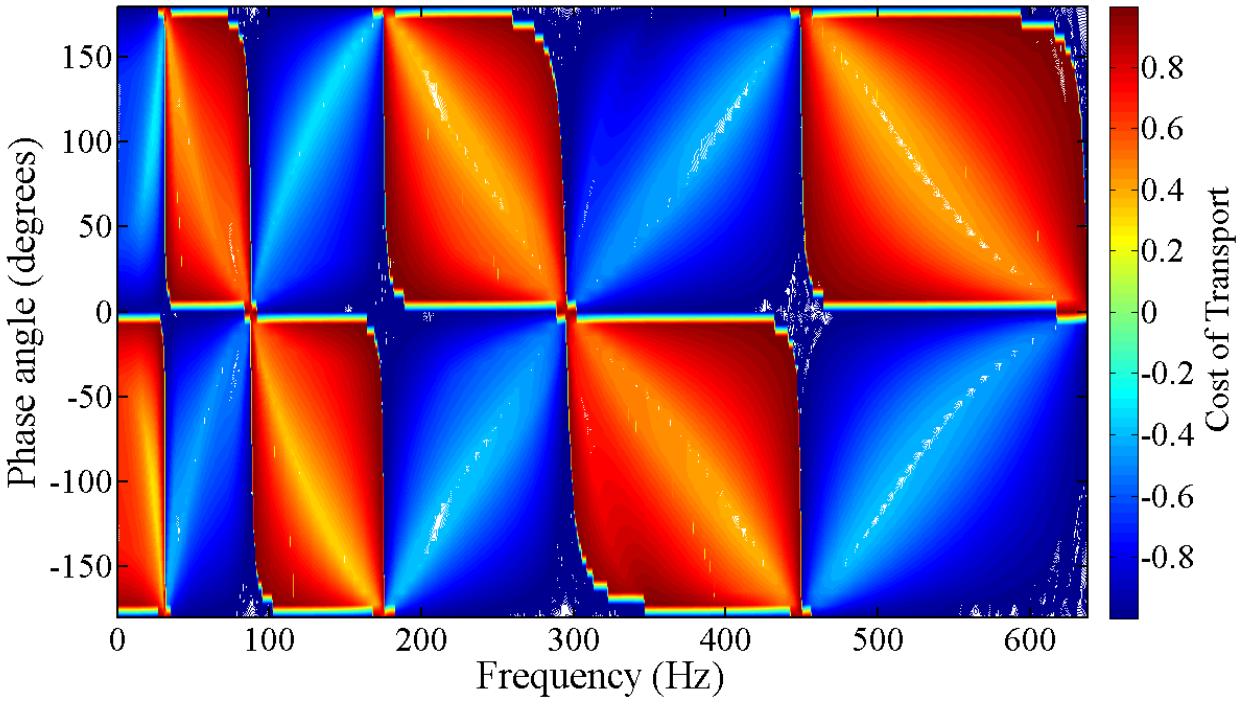

Figure 3.15: Parametric study and cost function analysis of a free-free beam. Red color – wave travels from right to left, blue color – wave travels from left to right.

(ω_2, ω_3) region, the wave moves left to right.

Although, in this figure the phase vs. frequency surface plot is generated for the free-free boundary condition, a similar trend is also observed for the clamped-free and clamped-clamped cases. On the whole some of the observations based on the simulated experiments are, (1) there is a phase that results in traveling wave over a wide spectrum of frequency range, (2) the quality of the traveling wave and its sensitivity to the phase input is dependent on many factors; one of which is the frequency of excitation, (3) if a phase ϕ results in a traveling wave in one direction, a phase of $-\phi$ reverses the direction, (4) in the frequency range between two consecutive resonant frequencies the phase and frequency are related by an monotonically increasing or decreasing function, (5) the direction of the waves and phase relationship alternates after each resonant frequency.

In order to describe in detail the *CF* and its outcome as a result of the two parameters, frequency and phase, as an example, attention is focused on one frequency range for each boundary condition. In the free-free case, the phase difference of $\phi \in (0, 180^\circ)$ is varied in the frequencies ranging from $[\omega_2, \omega_3]$. Figure 3.16a shows the magnified version of Figure 3.15 in the frequency range of interest. In this figure the range of the color bar ranges form $[0, 1]$, where 0 corresponds to a pure traveling wave and 1 to a pure standing wave. These results are validated experimentally as

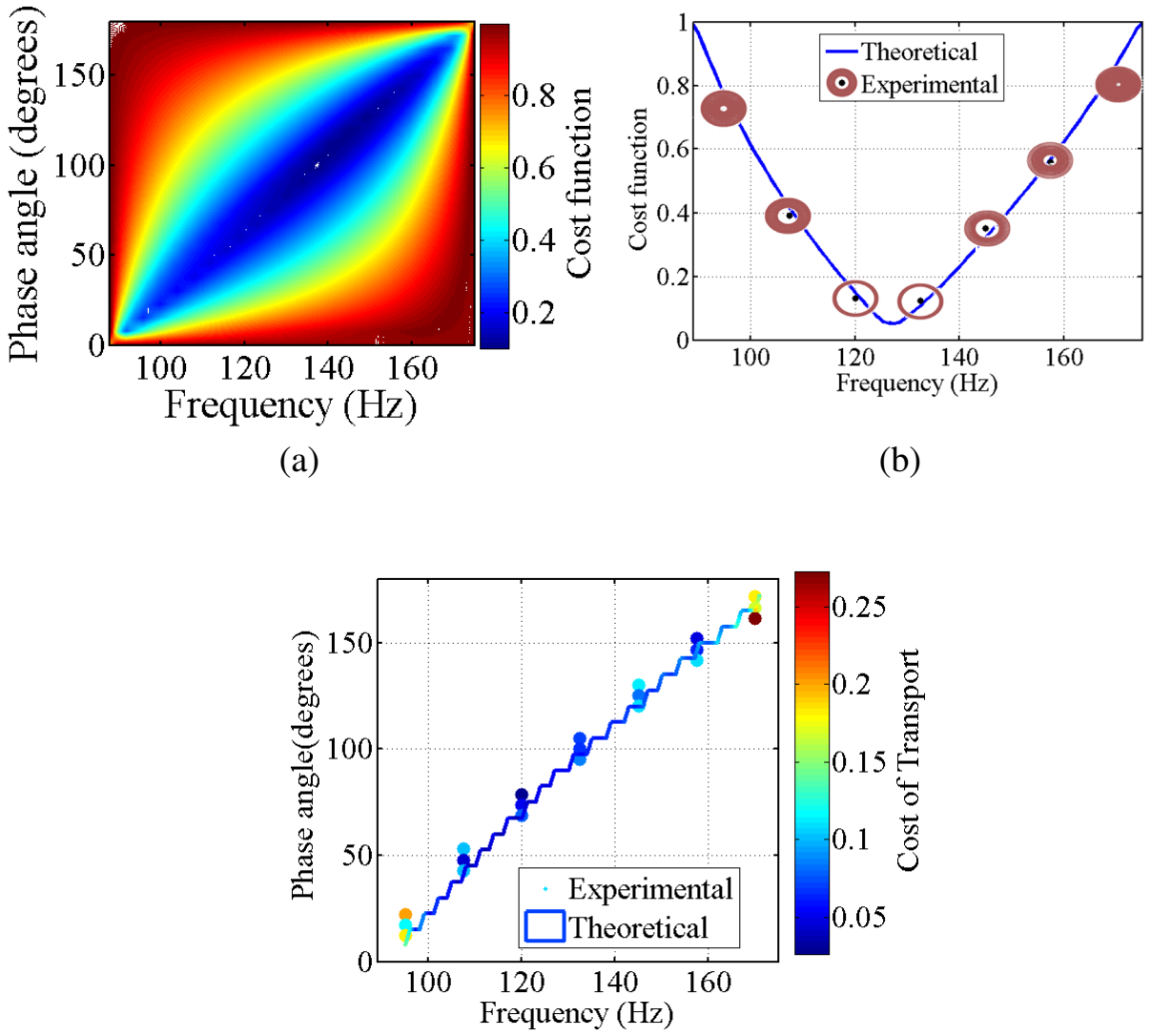

Figure 3.16: Theoretical and experimental results of the cost function of the free-free beam between the 2^{nd} and 3^{rd} mode shapes. (a) Cost Function window between two mode shapes, (b) Theoretical and experimental results of the *CF* as a function of frequency and phase angle 90°, (c) Theoretical and experimental results of the minimal *CF*.

shown in Figure 3.16b, where the phase was kept constant at 90° and the frequency is varied. As expected, a constant phase over a frequency rage does not result in the optimal quality of traveling wave and hence, a 90° phase difference establishes a V-shaped relationship with frequency. This implies that this phase gives the lowest *CF* at approximately half way between two the modes, but at any other region before or after, the *CF* increases proportionally. This can also be seen by the insets representing the responses of the waves for each point along the curve using Hilbert's

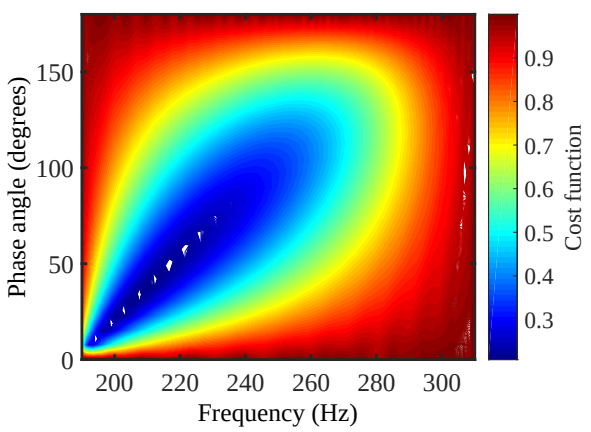

(a)

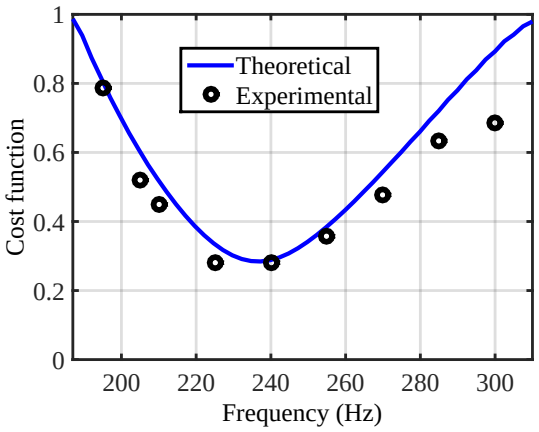

(b)

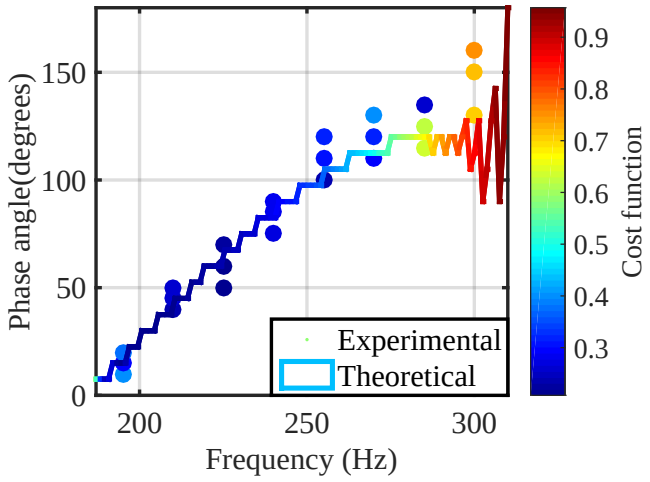

(c)

Figure 3.17: Theoretical and experimental results of the cost function of the clamped-free beam between the 4^{th} and 5^{th} mode shapes. (a) Cost Function window between two mode shapes, (b) Theoretical and experimental results of the *CF* as a function of frequency and phase angle 90°, (c) Theoretical and experimental results of the minimal *CF*.

approach. For the free-free case at a frequency of $130Hz$, the ratio between the outer and inner radius is minimal, alluring to the fact that the *CF* is lowest hence the highest quality traveling wave is obtained. As the excitation frequency approaches any of the natural frequencies nearby (ω_2 or ω_3), the ratio between the radii increases and correspondingly the quality of the traveling wave is reduced. Besides the 90° case, another validation presented in Figure 3.16c was conducted in order to demonstrate that the most effective traveling wave in terms of the *CF* will occur on the line shown in dark blue. This illustrates the proportionality between the frequency and phase and the color bar indicates how closely the experimental results compare with the theoretical prediction

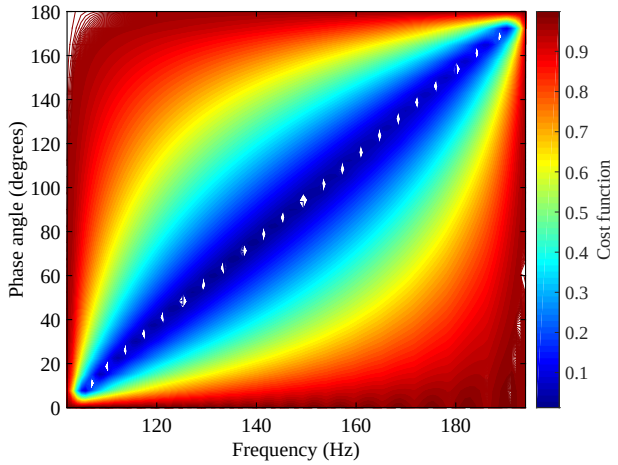

(a)

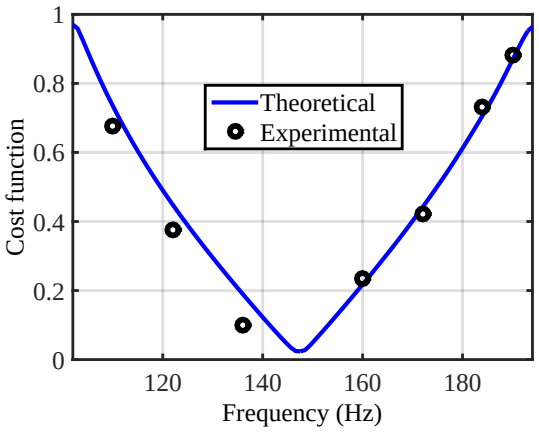

(b)

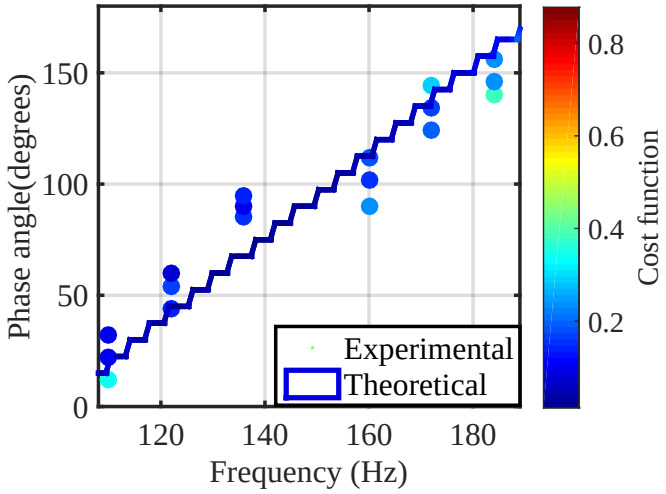

(c)

Figure 3.18: Theoretical and experimental results of the cost function of the clamped-clamped beam between the 2^{nd} and 3^{rd} mode shapes. (a) Cost Function window between two mode shapes, (b) Theoretical and experimental results of the *CF* as a function of frequency and phase angle 90°, (c) Theoretical and experimental results of the minimal *CF*.

along this line.

Similar to the free-free case, the phase is varied in the frequency range of $\omega \in (\omega_2, \omega_3)$ and $\omega \in (\omega_4, \omega_5)$ region of the clamped-clamped and clamped-free cases, as seen in Figure 3.17a and Figure 3.18a, respectively. The results clearly reflect the effect that phase has over the quality of the traveling wave and shows a trend that is analogous to Figure 3.16a. As before, these results are validated experimentally for the constant phase scenario and are compared in Figure 3.17b

and Figure 3.18b for the clamped-free and clamped-clamped cases respectively. Near the halfway between the natural frequencies Figure 3.16b and Figure 3.18b have a CF which is close to 0. However, for the clamped-free case, the curve plotted in Figure 3.17b has a minimum at a value around 0.3, higher than the other two cases. This is expected to be a result of the anti-symmetric nature of the boundary conditions of the clamped-free case. Such change in trend is also seen in the surface plots that shows the optimal phases for different frequencies. For example, the cost function is close to 1 at higher frequency ranges in Figure 3.17c. However, experimental results also show degradation of the cost function at frequencies near the 5^{th} resonant frequency. Nevertheless, the results shown in this study support the hypothesis that both frequency and phase play a crucial role in the quality of traveling waves.

Once the relationship between the phase and frequency is established through the calculation of the CF, the final investigation conducted was to compare the Hilbert approach to the Fourier approach in order to show the effectiveness of the two methods. The comparison is shown for the free-free case in Figure 3.19 for two different frequencies, $243Hz$ ($\omega \in (\omega_3, \omega_4)$) in Fig 3.19((a),(c) and (e)) and $720Hz$ ((ω_6 or ω_7)) in Fig 3.19((b),(d) and (f)). Points corresponding to the maxima, minima and arbitrary location in between the two extremes are presented on the wave envelope in Fig 3.19 ((a) and (b)). In Fig 3.19 ((c) and (d)) the amplitude and phase of these points are shown in the complex plane, while in Fig 3.19 ((e) and (f)), the amplitude of these points as a function of time is illustrated by their rotation around a circle with radius equal to their amplitudes. These plots show that, at low spatial points the Fourier approach overestimates the cost function while the Hilbert approach underestimates the cost function. As the number of spatial points increases, the cost-functions evaluated using both these methods converge to the same value.

3.7 Effect of boundary conditions

Previously, the effect of phase on the quality of traveling wave was discussed for a beam structure. In this section, the influence of boundary condition on this phase relationship is further investigated. In the earlier chapter, a theoretical framework was developed to explore the origin of traveling waves. It was shown that traveling waves are generated by simultaneously exciting a structure by two point forces. The response of a beam to two point forces is expressed as a combination of four wave components in Eq. 2.14,

$$w_{ab}^{trig.}(x,t) = \sqrt{2}C\left(C_A W_1 + C_B W_2 + C_C W_3 + C_D W_4\right), \tag{3.36}$$

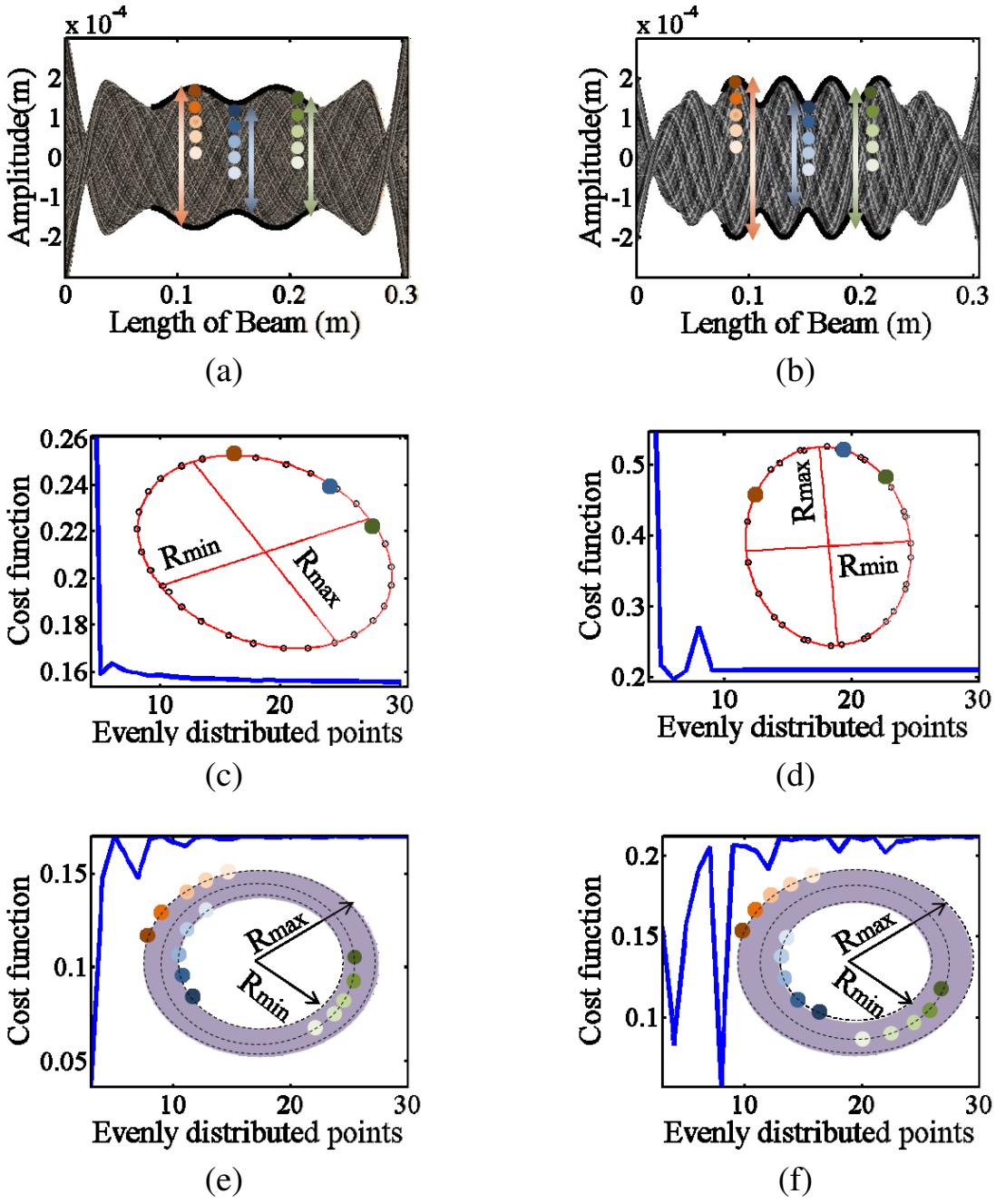

Figure 3.19: Comparison between the Hilbert's and Fourier's approach at $243Hz$ (a,c,e) and $720Hz$ (b,d,f) : (a and b) Hybrid wave waveform, (c and d) CF as a function of points taken across the structure. Points corresponding to the maxima, minima and arbitrary in between the two are presented. Fourier's approach, (e and f) CF as a function of points taken across the structure, Hilbert's approach

where the wave components are shown in Eq. 2.15 and the coefficients in Eq. 2.19. All the wave components can be represented by,

$$W_1 = X_a^{trig.}(x)cos\left(\omega_f t - \frac{\pi}{4}\right) + X_b^{trig.}(x)cos\left(\omega_f t + \frac{\pi}{4}\right). \tag{3.37}$$

In these equations, the wave components (W_i) are a linear combination of the ordinary trigonometric parts ($X^{trig.}$) of the two mode shapes. Through out this study, it is assumed that the effect of boundary conditions is reflected in the hyperbolic part ($X^{hype.}$) of the mode shapes. In the generalized theory of traveling waves section, a relationship is developed as a combination of mode shapes in Eq. 2.51. This equation is of the form,

$$w(x,y,t) = \tilde{C}_A\tilde{W}_1 + \tilde{C}_B\tilde{W}_2 + \tilde{C}_C\tilde{W}_3 + \tilde{C}_D\tilde{W}_4. \tag{3.38}$$

This relationship simulates a traveling wave that "represents" the response of the beam when simultaneously excited by two actuators. In other words, the response of the beam is simulated as the summation of the the two most dominant modes. For example, in Figure 3.20 the first five mode shapes of a free-free beam are combined to generate traveling waves. In this figure, complete mode shapes of the beam including the hyperbolic parts are used to generate one of the four wave forms (W_1). Similar wave forms are generated for the clamped-free and clamped-clamped boundary conditions. These are plotted in Figure 3.21 and Figure 3.22 respectively. These figures display the robustness of the Eq. 2.51 to simulate traveling waves for any type of boundary condition. This relationship is useful to simulate the type of the traveling wave produced in between two modes of interest. Based on this information, a design procedure that determines the frequency of excitation, the location of forces and the phase difference between forces can be developed. The waveforms in this figure represent the best traveling wave that a beam can generate by exciting the beam with two point forces with optimal phase. The amplitudes of these waves are normalized, as the amplitudes of the traveling waves are dependent on the location of forces, the position of strain-nodes of the modes of interest and the frequency of excitation. Furthermore, the influence of other modes is neglected as it is assumed these modes are sufficiently farther away from the frequency of excitation and have little effect.

Through this analysis, it is shown that based on the mode combination procedure, the shape of the traveling waves between any two modes can be simulated. However, the trigonometric term $cos(\beta_n x) - \sigma_n cos(\beta_n x)$, is present irrespective of the type of boundary condition. This oscillatory part is responsible for the traveling wave part of interest. Thus, to study the effect of boundary conditions on these traveling waves, the trigonometric part and the hyperbolic parts of the mode shapes are separated and the effect of individual parts is simulated. Figure 3.23 shows the contribution of

Free-free boundary condition

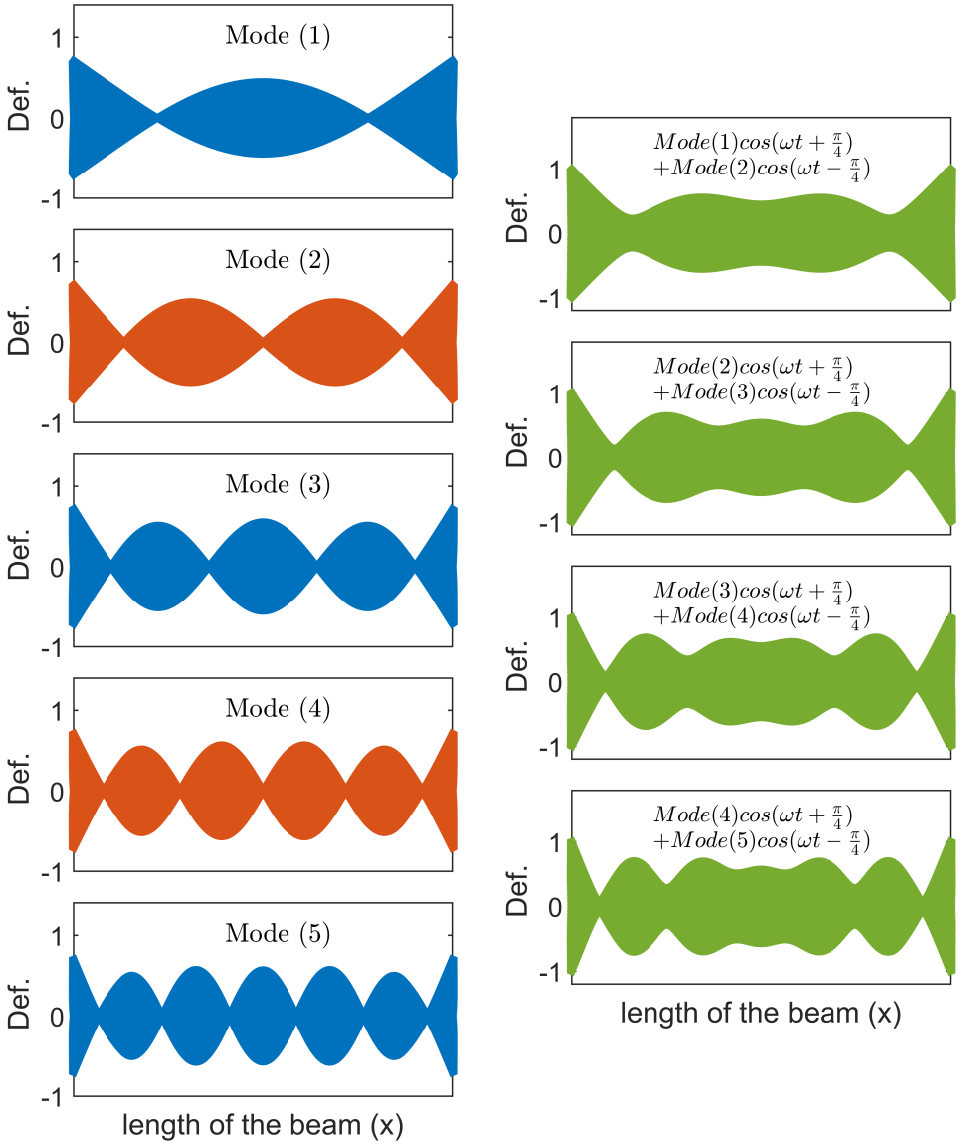

Figure 3.20: Sinusoidal combination of the ordinary trigonometric part of mode shapes of free-free beam.

Clamped-free boundary condition

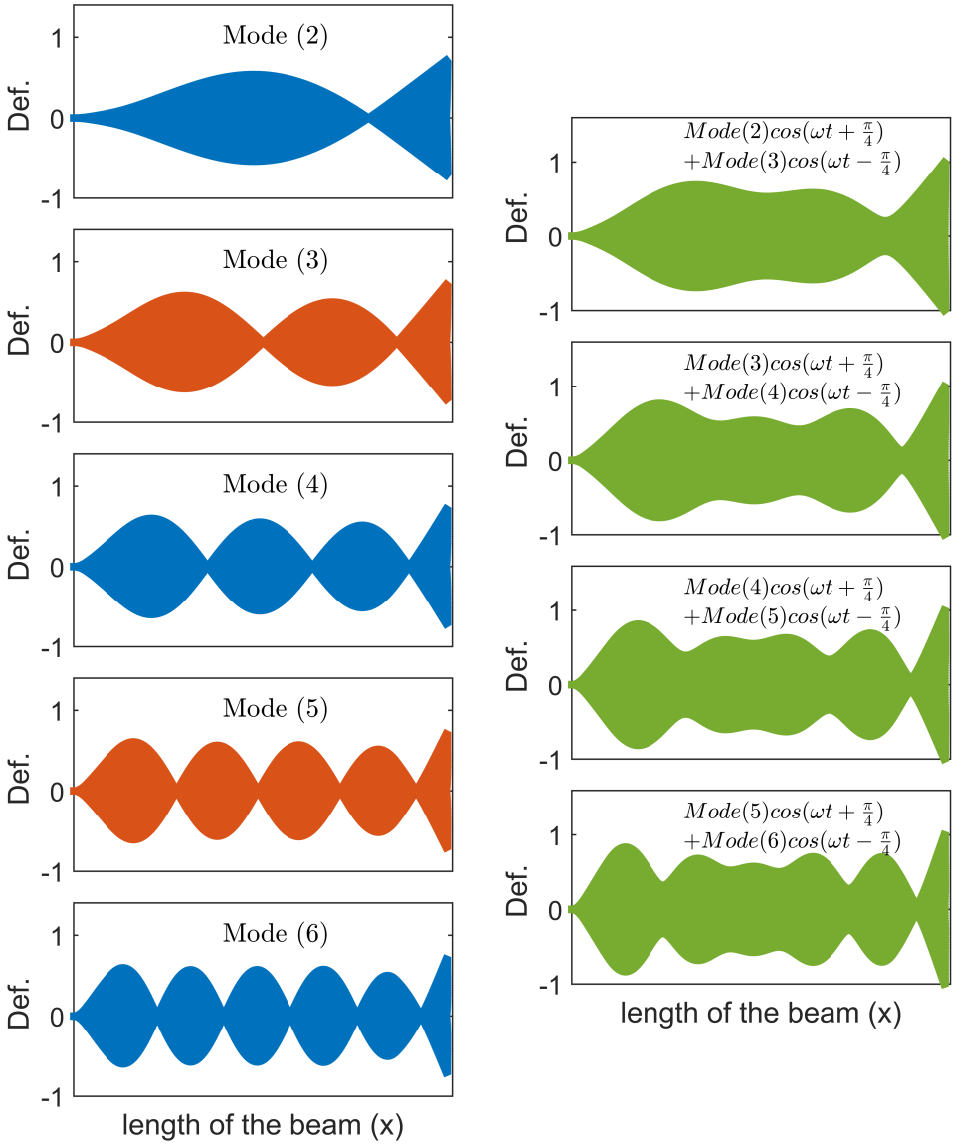

Figure 3.21: Sinusoidal combination of the ordinary trigonometric part of mode shapes of clamped-free beam.

Clamped-clamped boundary condition

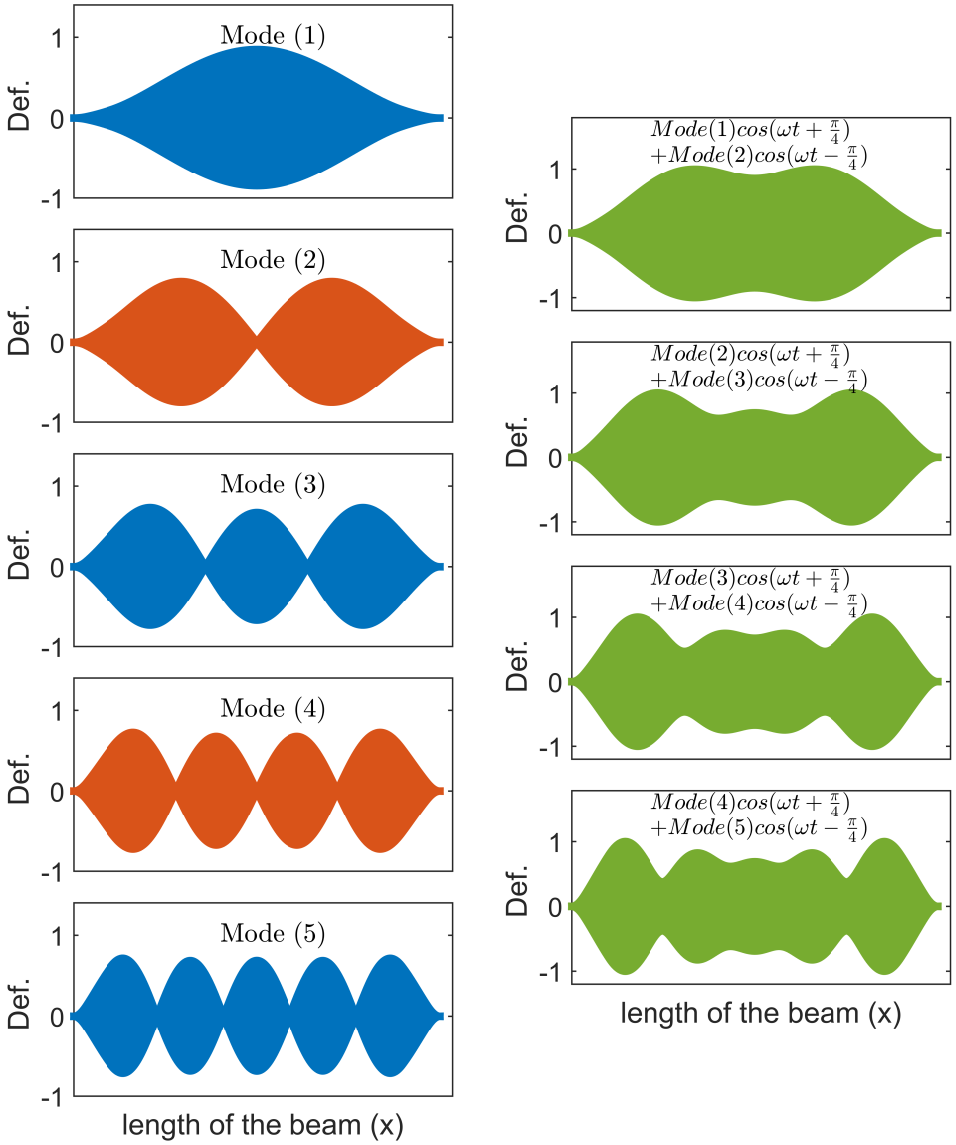

Figure 3.22: Sinusoidal combination of the ordinary trigonometric part of mode shapes of clamped-clamped beam.

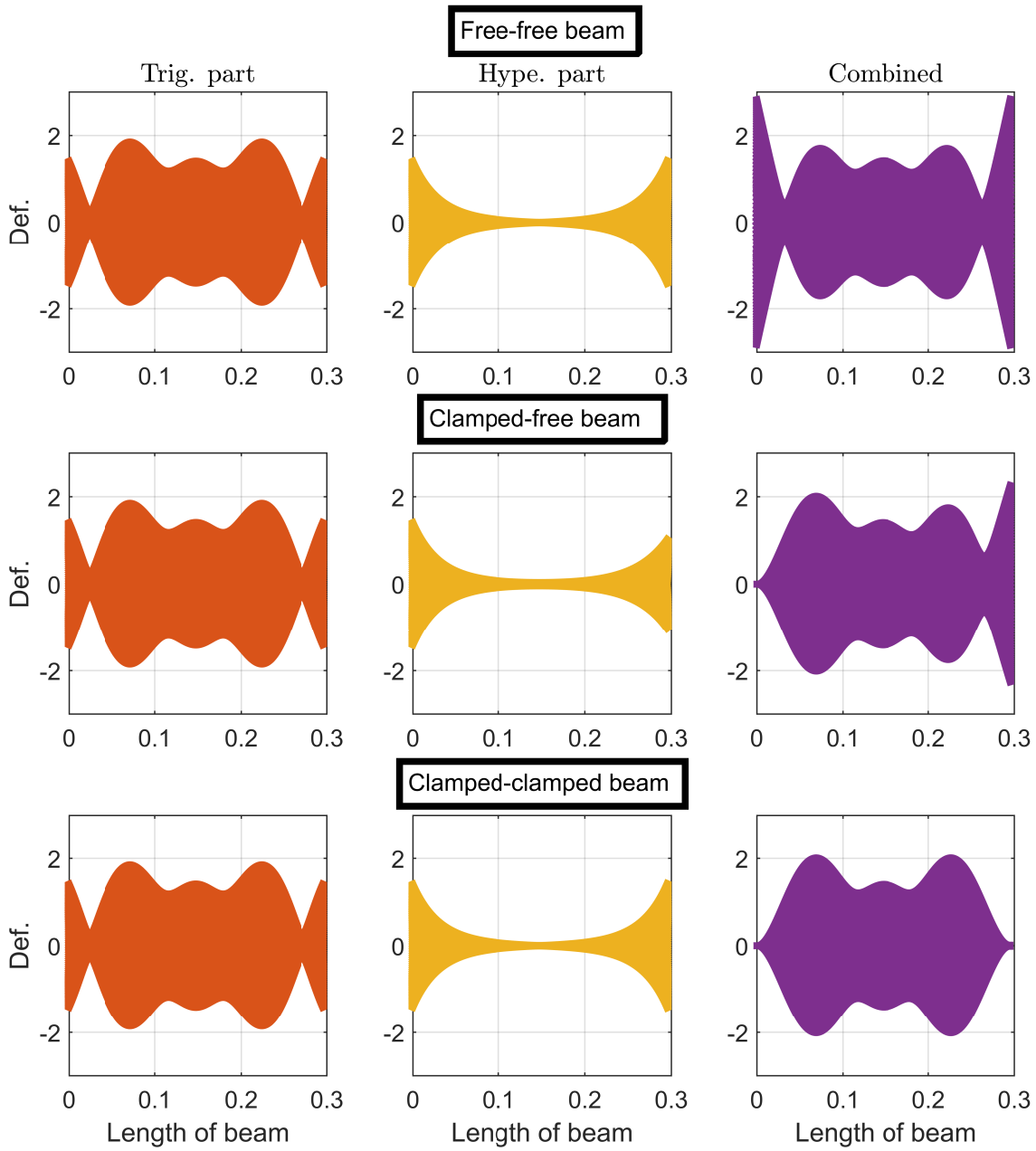

Figure 3.23: Contribution of the individual trigonometric and hyperbolic parts to generate traveling waves in free-free (between 2^{nd} and 3^{rd} modes), clamped-free (between 3^{rd} and 4^{th} modes) and clamped-clamped (between 2^{nd} and 3^{rd} modes) boundary conditions.

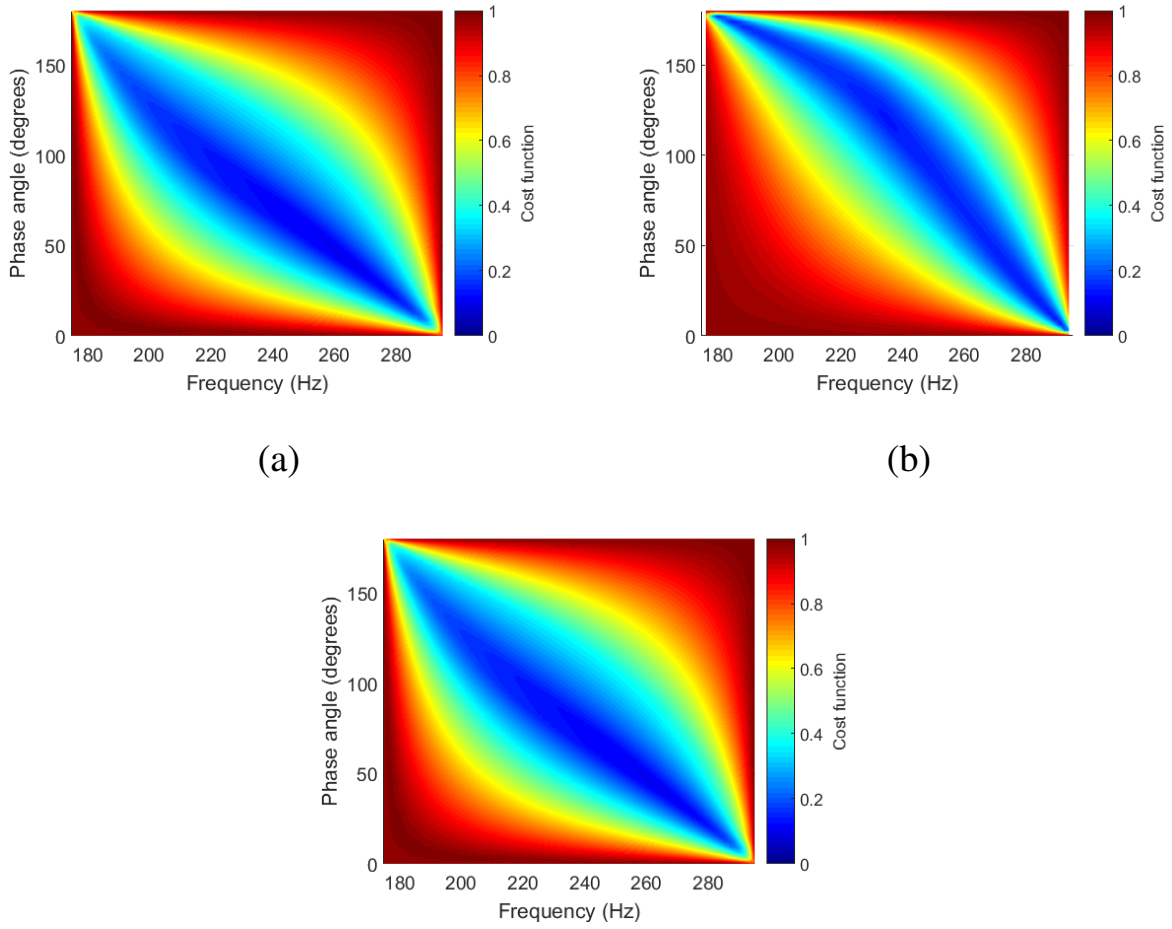

Figure 3.24: Comparison of the phase relationship of a free-free beam between 3^{rd} and 4^{th} modes using, (a) the combination of the trigonometric part of mode shapes i.e. $X_a^{trig.} cos\left(\omega_f t - \frac{\pi}{4}\right) + X_b^{trig.} cos\left(\omega_f t + \frac{\pi}{4}\right)$ (no piezoelectric), (b) the complete mode shapes of the beam including the boundary effects (no piezoelectric), (c) the full model of the beam including piezoelectric effects.

$X^{trig.}$ and $X^{hype.}$ in the combined wave form for all three boundary conditions: (i) free-free case, (ii) clamped-free case, (iii) clamped-clamped case. To compare modes of similar wavelengths, the combination of 2^{nd} and 3^{rd} modes of the free-free and the clamped-clamped cases are compared against the result of 3^{rd} and 4^{th} mode shapes of the clamped-free case. In these plots, the trigonometric part and the hyperbolic parts of all three cases are identical to each other in shape. However, there is a relative phase difference between these parts. Thus, in the clamped-free and clamped-clamped cases, the hyperbolic part is able to enforce the required boundary fixed conditions. Additionally, the hyperbolic part is only significant at the boundary conditions as compared to the trigonometric part. This is much more evident in higher modes shapes than in lower ones and this trend preserves the traveling wave behavior generated by the trigonometric part. These

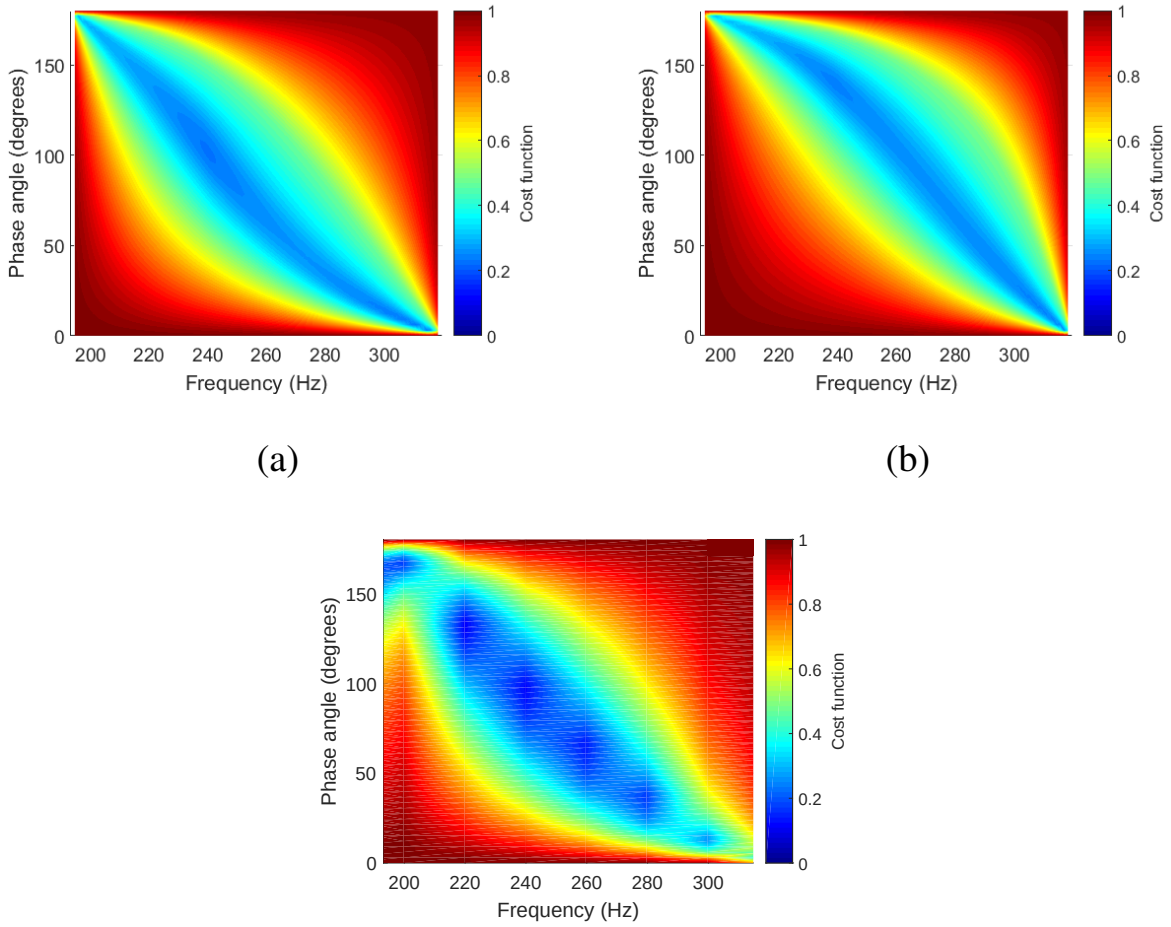

Figure 3.25: Comparison of the phase relationship of a clamped-clamped beam between 3^{rd} and 4^{th} modes using, (a) the combination of the trigonometric part of mode shapes i.e. $X_a^{trig.}cos\left(\omega_f t - \frac{\pi}{4}\right) + X_b^{trig.}cos\left(\omega_f t + \frac{\pi}{4}\right)$ (no piezoelectric), (b) the complete mode shapes of the beam including the boundary effects (no piezoelectric), (c) the full model of the beam including piezoelectric effects.

plots show that the hyperbolic part has little effect on the amplitude of the traveling waves in the central part of the beam. However, there is also a phase contribution by the hyperbolic part.

To investigate this effect, surface plots between the phase, frequency and cost function are simulated for three cases, (a) phase angle and frequencies are varied to compute the cost function from the combination of the four wave components (W_i) with just the trigonometric parts; (b) phase angle and frequencies are varied to compute the cost function from the combination of the four wave components (W_i) with both the trigonometric and hyperbolic parts; (c) phase angle and frequencies are varied in the beam model with piezoelectric patches, developed in the previous sections. In all these simulations, the location of the forces are not varied and are equidistant from

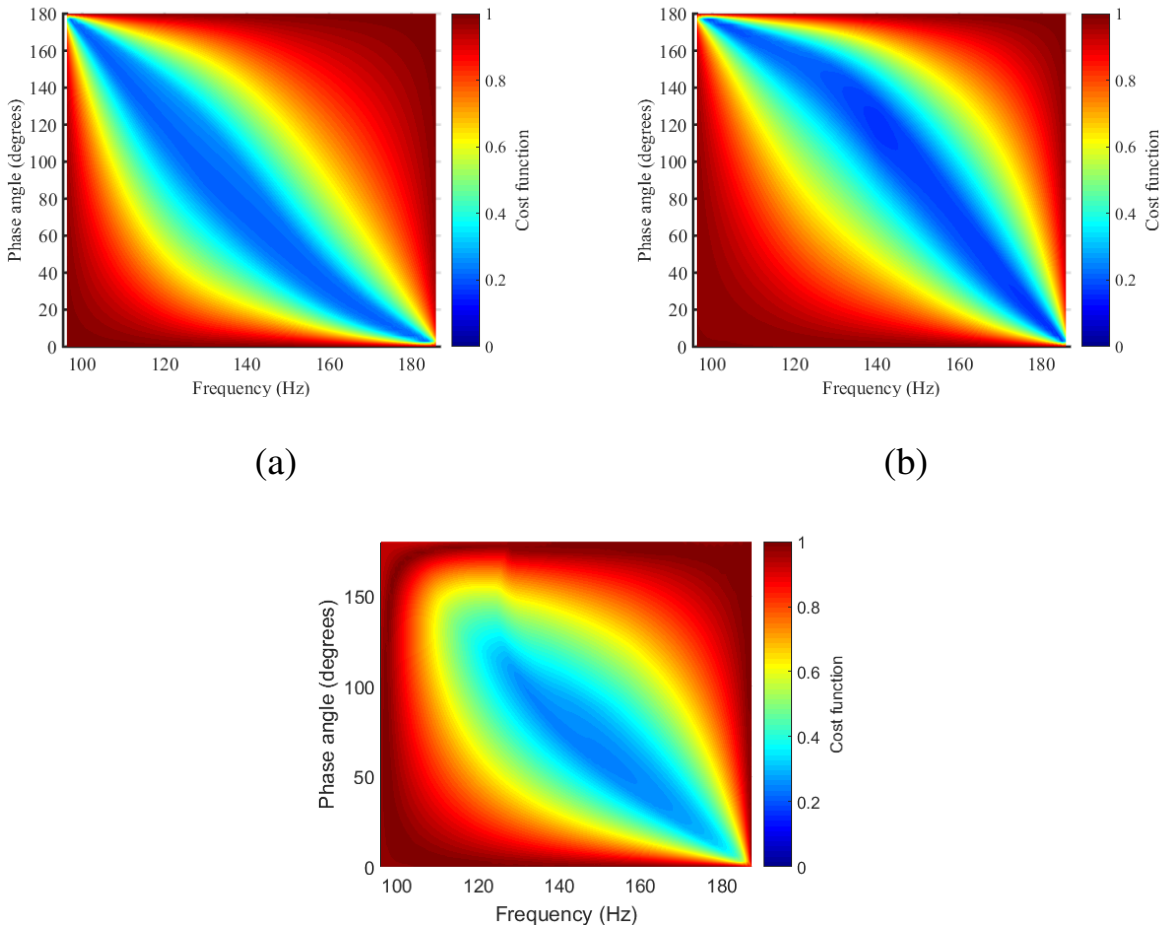

Figure 3.26: Comparison of the phase relationship of a clamped-free beam between 3^{rd} and 4^{th} modes using, (a) the combination of the trigonometric part of mode shapes i.e. $X_a^{trig.} cos\left(\omega_f t - \frac{\pi}{4}\right) + X_b^{trig.} cos\left(\omega_f t + \frac{\pi}{4}\right)$ (no piezoelectric), (b) the complete mode shapes of the beam including the boundary effects (no piezoelectric), (c) the full model of the beam including piezoelectric effects.

the edges of the beam. Figure 3.24, Figure 3.25 and Figure 3.26 display the phase relations for the free-free, clamped-clamped and clamped-free boundary conditions respectively.

For the free-free case, the overall trend between the phase vs. frequency is similar in all three cases. Near the 3^{rd} resonant frequency, the phase that results in optimal traveling wave is 180° and as the frequency increases this phase value reduces. Near the 4^{th} resonant frequency, the optimal phase value is 0°. However, by adding the boundary conditions to the free-free case, Figure 3.24a changes to Figure 3.24b. In 3.24b, at any frequency, the phase required to generate optimal traveling waves is higher than the corresponding value from 3.24a. A similar trend is also observed in the other boundary conditions, by comparing Figure 3.25a with Figure 3.25b,

and comparing Figure 3.26a with Figure 3.26b. However, if the beam structure is excited using moments, as in piezoelectric patches, instead of point forces and including all dominant modes (up to 6 modes in these cases) the phase value reduces and is similar to the trigonometric phase plot. In other words, Figure 3.24a is similar to Figure 3.24c in the free-free case, Figure 3.26a is similar to Figure 3.26c in the clamped-free case and Figure 3.25a is similar to Figure 3.25c in the clamped-clamped case. In the clamped-free scenario, the system is antisymmetric and this results in higher values for the cost function than the other two cases. Furthermore, near the natural frequencies of the clamped-free case (with piezo effects), the cost function is almost equal to 1. This is different from all other cases.

These results show that approximating the traveling wave contents as a combination of trigonometric parts is valid and is very close to the full model. The approximate shape of the traveling wave can be simulated by considering the mode shapes of the structure and then the approximate phase relationship is achieved by approximating the location of the point forces.

3.8 Multi-tone traveling waves

In earlier sections, traveling waves are generated by exciting a 1D beam structure simultaneously by two forces at a single tone. However if the structure is simultaneously actuated at two tones, two traveling waves are generated. The net response of the beam is the summation of the two traveling waves. A schematic representation of the multiple traveling wave summation is shown in Figure 3.27. In this video (digital version only), the beam response shown in blue is a summation of the low wavelength traveling wave (in red) and the high wavelength traveling wave (in green). In this example, the direction of travel of the individual traveling waves is opposite to each other and the amplitudes are significantly different. As the frequencies of the two traveling waves are different, the wave dispersion relationship results in two different wave-speeds of the traveling waves. Such differences in the individual traveling waves results in a hybrid cyclic response of the beam.

Based on this schematic, traveling wave summation is experimentally tested. The multi-tone traveling wave is generated by exiting the free-free beam at two different frequencies. One of the frequency of excitation ($130Hz$) lies between the second and third natural frequencies of the beam and the other frequency of excitation ($2584Hz$) lies between the 16^{th} and the 17^{th} natural frequency of the beam. To generate traveling waves, piezo-ceramics are exited with sinusoidal signals with a phase difference of $\pm 90^{\circ}$. Voltage signals of amplitudes 120 $Volts$ and 20 $Volts$ correspond to the frequencies of $130Hz$ and $2584Hz$ respectively. Figure 3.28a and Figure 3.28b are the experimental traveling waves at frequencies of $130Hz$ and $2584Hz$ respectively. Figure 3.28c and Figure 3.28d correspond to the summation of the individual traveling waves. While Figure 3.28d is a combination of the two traveling waves progressing in the same direction, Figure

Figure 3.27: Theoretical summation of individual traveling waves at two different tones. (Click on the picture for the video to start).

3.28c is the result of the traveling wave in opposite directions. this combination is a sample case which demonstrates the possibility of multiple traveling wave summation. The fourth and fifth modeshapes (trigonometric parts) of a free-free beam are used to generated this surface plot.

3.9 Conclusion

The focus of this thesis is to generate traveling waves on simple structures such as beams based on the two-point excitation method. To achieve this a theoretical continuous model of the composite beam is developed in this chapter. The model consists of two piezo-ceramic wafers attached to a beam, which accurately predict the response of the beam upon one point excitation and two point excitation. A comparative analysis between the theory and experiment was conducted for three different boundary conditions: clamped-clamped, clamped-free and free-free. The results demonstrated the accuracy of the theoretical model to predict the dynamics of the traveling waves. The work herein also demonstrates through experiments that net traveling waves can be generated on a beam structure by exciting it with two forces. The theoretical models have been corroborated through experimental results and then these models are further used to study the effect of phase on the quality of the traveling wave. The work also extends the concept of 90° to all frequencies for the generation of a traveling wave.

Figure 3.28: Experimental summation of individual traveling waves at two different tones (130Hz and 2584Hz). (Click on the picture for the video to start).

Chapter 4

Traveling waves in 2D plates

4.1 Introduction

The work in this chapter explores the generation of 2D flexural waves which are non-reflective on a thin rectangular plate with free boundary conditions when excited by two Macro Fiber Composites (MFCs). The voltage signals to the MFCs use a frequency lying halfway between two adjacent resonant frequencies with a phase difference of 90°. Locations of the MFCs and frequencies of actuation are varied to study the response of the plate due to these forces. A Finite Element (FE) plate model is developed and updated based on the data from an experimental modal analysis of the plate. This model is able to predict up to the 40^{th} damped eigenvalue with a maximum error of 2.5% and match mode shapes accurately, with a lowest MAC (Modal Assurance Criterion) value of 0.92. Numerical simulations of traveling waves are compared with experimental results. Preliminary results show that the location of the MFCs and the frequency of excitation have an effect on the type and the quality of the traveling waves. The work in this chapter is broadly divided into five parts. The first part discusses the modeling approach taken to simulate plate dynamics with piezoelectric patches bonded to the plate. The second part focuses on the model updating and model validation through data obtained from an experimental modal analysis. In this section, the eigenvalues and eigenvectors of the damped plate FE model are compared with experimental results. Once the plate model is validated for a single input response, traveling waves generation is addressed in the third part. Experimental and numerical responses of the plate are compared with each other when the plate is simultaneously excited with two piezo ceramic patches. Additionally, multiple approaches are developed to differentiate and categorize the plate behavior into standing or traveling waves and the effects of frequency and location on the quality of the traveling waves are discussed. The fourth part discusses the different projection based model reduction approaches used to simulate plate dynamics. The last part analyzes the experimental results with those of mode combination results.

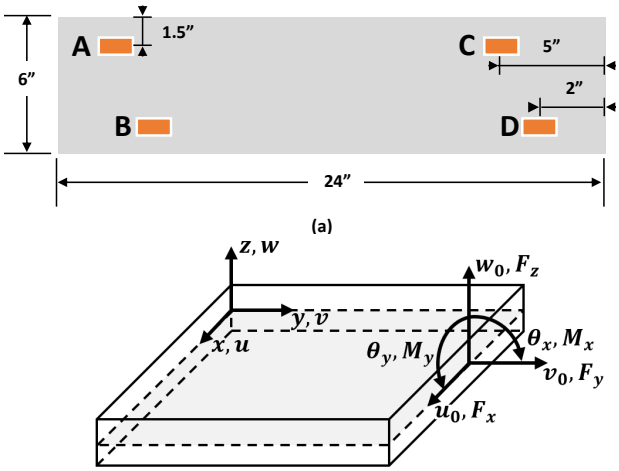

Figure 4.1: Experimental Setup: (a) rectangular plate with MFCs, (b) forces and moments acting on a plate element.

4.2 Part I: Modeling plate dynamics

Consider a homogeneous, isotropic, linear elastic plate, with four piezoelectric actuators perfectly bonded to it, as shown in Figure 4.1(a). The length, the width and the thickness of the plate are denoted by L_b, W_b, and h_b, respectively. Piezoelectric actuators dimensions are denoted by L_{pi}, W_{pi}, and h_{pi}, where $i = 1, \cdots, 4$. The mid-plane of the plate is considered as the reference plane, with the origin of the reference coordinate system (xyz) being located on this middle plane, as shown in 4.1(b).

The focus of this section is to investigate traveling waves at relatively low frequencies (up to $3000Hz$). At such frequencies the effects of the adhesive bonding layer between the plate and the piezo patches are negligible [177], and hence, those sections of the plate covered with piezo patches are considered as a composite structure. With this assumption, the classical lamination theory is adopted to obtain the equivalent material characteristics for these composite sections. Furthermore, since traveling waves are, in general, generated in thin plates, the first order shear deformation theory (FSDT) has been adopted to define the displacements in the structure. Based on the aforementioned assumptions, the displacement field in the plate is defined as,

$$\begin{aligned} u(x,y,z,t) &= u_0(x,y,t) + z\theta_y(x,y,t), \\ v(x,y,z,t) &= v_0(x,y,t) + z\theta_x(x,y,t), \\ w(x,y,z,t) &= w_0(x,y,t), \end{aligned} \tag{4.1}$$

where u_0, v_0 and w_0 are the displacements of the point (x,y) on the reference plane along the $x-$, $y-$ and $z-$ directions, respectively. θ_x and θ_y are the rotations of the normal to the reference

plane in the $yz-$ and the $xz-$planes, respectively. Translational and rotational degrees of freedom are split throughout the derivation of the governing equations and the formulation of the finite elements as follows,

$$\mathbf{d} = \mathbf{d_t} + z \begin{bmatrix} \mathbf{d_r} \\ 0 \end{bmatrix}, \tag{4.2}$$

where $\mathbf{d} = \begin{bmatrix} u & v & w \end{bmatrix}^T$, $\mathbf{d_t} = \begin{bmatrix} u_0 & v_0 & w_0 \end{bmatrix}^T$, and $\mathbf{d_r} = \begin{bmatrix} \theta_x & \theta_y \end{bmatrix}^T$. The superscript T denotes the transpose operation.

To avoid the issue of shear-lock associated with shear deformations, a reduced integration rule is used to evaluate the transverse shear strains ($\boldsymbol{\epsilon}_s$), while a full integration rule is utilized for in-plane strains ($\boldsymbol{\epsilon}_b$). Assuming small strains and deformations, $\boldsymbol{\epsilon}_b$ and $\boldsymbol{\epsilon}_s$ are defined as follows,

$$\begin{aligned} \boldsymbol{\epsilon}_b &= \begin{bmatrix} \varepsilon_{11} \\ \varepsilon_{22} \\ 2\varepsilon_{12} \end{bmatrix} = \begin{bmatrix} \frac{\partial}{\partial x} & 0 & 0 \\ 0 & \frac{\partial}{\partial y} & 0 \\ \frac{\partial}{\partial y} & \frac{\partial}{\partial x} & 0 \end{bmatrix} \begin{bmatrix} u_0 \\ v_0 \\ w_0 \end{bmatrix} + z \begin{bmatrix} \frac{\partial}{\partial x} & 0 \\ \frac{\partial}{\partial y} & 0 \\ \frac{\partial}{\partial x} & \frac{\partial}{\partial y} \end{bmatrix} \begin{bmatrix} \theta_x \\ \theta_y \end{bmatrix}, \\ &= \mathbf{L_{bt}}\mathbf{d_t} + z\mathbf{L_{br}}\mathbf{d_r}, \end{aligned} \tag{4.3}$$

$$\begin{aligned} \boldsymbol{\epsilon}_s &= \begin{bmatrix} 2\varepsilon_{13} \\ 2\varepsilon_{23} \end{bmatrix} = \begin{bmatrix} 0 & 0 & \frac{\partial}{\partial x} \\ 0 & 0 & \frac{\partial}{\partial y} \end{bmatrix} \begin{bmatrix} u_0 \\ v_0 \\ w_0 \end{bmatrix} + \begin{bmatrix} 1 & 0 \\ 0 & 1 \end{bmatrix} \begin{bmatrix} \theta_x \\ \theta_y \end{bmatrix}, \\ &= \mathbf{L_{st}}\mathbf{d_t} + \mathbf{L_{sr}}\mathbf{d_r}. \end{aligned} \tag{4.4}$$

Following the same notation, the state of the stress at any point in the plate is described by the in-plane stresses ($\boldsymbol{\sigma}_b$) and transverse shear stresses ($\boldsymbol{\sigma}_s$) as follows,

$$\boldsymbol{\sigma}_b = \begin{bmatrix} \sigma_{11} & \sigma_{22} & \sigma_{13} \end{bmatrix}^T, \qquad \boldsymbol{\sigma}_s = \begin{bmatrix} \sigma_{13} & \sigma_{23} \end{bmatrix}^T. \tag{4.5}$$

The plate is assumed to be made of homogeneous, isotropic, linear-elastic material with the following constitutive relations,

$$\boldsymbol{\sigma}_b = \boldsymbol{C}_b\boldsymbol{\epsilon}_b, \qquad \boldsymbol{\sigma}_s = \boldsymbol{C}_s\boldsymbol{\epsilon}_s. \tag{4.6}$$

where C_{ij} is the element of the reduced stiffness matrix obtained with plane-stress assumption. The relationships between these constants and the commonly used Young's modulus of elasticity and

Poisson's ratio are summarized below,

$$C_{11} = C_{22} = \frac{E}{(1-\nu^2)},$$
$$C_{12} = C_{21} = \frac{\nu E}{(1-\nu^2)},$$
$$C_{44} = C_{55} = C_{66} = \frac{E}{2(1+\nu)}.$$

For a piezoelectric actuator operating in 1-3 mode:

$$\begin{Bmatrix} \sigma_{11} \\ \sigma_{22} \\ \sigma_{12} \end{Bmatrix} = \begin{bmatrix} C_{11} & C_{12} & 0 \\ C_{12} & C_{22} & 0 \\ 0 & 0 & C_{66} \end{bmatrix}^D \begin{Bmatrix} \varepsilon_{11} \\ \varepsilon_{22} \\ 2\varepsilon_{12} \end{Bmatrix} - \begin{Bmatrix} h_{13} \\ h_{23} \\ 0 \end{Bmatrix} D_3,$$

$$\begin{Bmatrix} \sigma_{13} \\ \sigma_{23} \end{Bmatrix} = \begin{bmatrix} C_{44} & 0 \\ 0 & C_{55} \end{bmatrix}^D \begin{Bmatrix} 2\varepsilon_{13} \\ 2\varepsilon_{23} \end{Bmatrix},$$

$$E_3 = -\begin{Bmatrix} h_{13} & h_{23} & 0 \end{Bmatrix} \begin{Bmatrix} \varepsilon_{13} \\ \varepsilon_{22} \\ 2\varepsilon_{12} \end{Bmatrix} + \beta_{33}^{\varepsilon} D_3.$$

Assuming linear piezo-electricity, the constitutive equations for the piezoelectric actuators are [174],

$$\begin{aligned} \boldsymbol{\sigma}_b &= \boldsymbol{C}_b^D \boldsymbol{\epsilon}_b - \boldsymbol{h}_b \boldsymbol{D}, \\ \boldsymbol{\sigma}_s &= \boldsymbol{C}_s^D \boldsymbol{\epsilon}_s - \boldsymbol{h}_s \boldsymbol{D}. \\ \boldsymbol{E} &= -\boldsymbol{h}_b^T \boldsymbol{\epsilon}_b - \boldsymbol{h}_s^T \boldsymbol{\epsilon}_s + \boldsymbol{\beta}^{\varepsilon} \boldsymbol{D}. \end{aligned} \tag{4.7}$$

where $\boldsymbol{D}$ is the electric displacement, $\boldsymbol{E}$ is the electric field, $\boldsymbol{h}_b$ and $\boldsymbol{h}_s$ are the piezoelectric coupling matrices related to bending and shear strains, $\boldsymbol{C}_b^D$ and $\boldsymbol{C}_s^D$ are the mechanical stiffness matrices of the material measured at zero electric displacement, $\boldsymbol{\beta}^{\varepsilon}$ is the inverse permittivity matrix measured at zero strain. In this study, the piezoelectric actuators are operating in 1-3 mode. Thus, electric displacement and electric field vectors reduces to their D_3 and E_3 components, respectively.

Based on the aforementioned assumptions, the kinetic energy of the piezoelectric-plate system can be written as follows,

$$T = \frac{1}{2}\left(\iiint_{\mathcal{V}_{plt}} \rho_{plt}(\dot{\boldsymbol{d}}_{\boldsymbol{t}} + z\dot{\boldsymbol{d}}_{\boldsymbol{r}})^T(\dot{\boldsymbol{d}}_{\boldsymbol{t}} + z\dot{\boldsymbol{d}}_{\boldsymbol{r}})\, d\mathcal{V} + \iiint_{\mathcal{V}_{pzt}} \rho_{pzt}(\dot{\boldsymbol{d}}_{\boldsymbol{t}} + z\dot{\boldsymbol{d}}_{\boldsymbol{r}})^T(\dot{\boldsymbol{d}}_{\boldsymbol{t}} + z\dot{\boldsymbol{d}}_{\boldsymbol{r}})\, d\mathcal{V} \right), \quad (4.8)$$

where ρ_{plt} and ρ_{pzt} are the mass density of the plate and the piezoelectric actuators, respectively, $\mathcal{V}$ is the volume of the corresponding layer, and $(\dot{})$ denotes the first partial derivative with respect to time.

Following Helmholtz free energy definition for piezoelectric materials, the potential energy functional of the system, including the strain energy and the work done by external forces, can be expressed as,

$$\begin{aligned} U = &\frac{1}{2}\left(\iiint_{\mathcal{V}_{plt}} (\boldsymbol{\epsilon}_b^T\boldsymbol{\sigma}_b + z\boldsymbol{\epsilon}_s^T\boldsymbol{\sigma}_s)\, d\mathcal{V} + \iiint_{\mathcal{V}_{pzt}} (\boldsymbol{\epsilon}_b^T\boldsymbol{\sigma}_b + z\boldsymbol{\epsilon}_s^T\boldsymbol{\sigma}_s - 2\boldsymbol{\epsilon}_b^T\boldsymbol{h}_b\boldsymbol{D} + \boldsymbol{D}^T\boldsymbol{\beta}^{\boldsymbol{\varepsilon}}\boldsymbol{D})\, d\mathcal{V} \right) \\ &- \iint_{A_{plt}} \boldsymbol{d}^T\boldsymbol{f}\, dA - \iint_{A_{pzt}} \boldsymbol{V}(t)\boldsymbol{D}\, dA, \end{aligned} \quad (4.9)$$

where $\boldsymbol{f}$ is the externally applied surface traction vector acting over the plate's surface area A_{plt}, and $\boldsymbol{V}$ is the electric potential vector acting on the piezoelectric actuator, such that $\boldsymbol{V} = \boldsymbol{E}h_{pzt}$.

Using eight-noded isoparametric quadrilateral elements to discretize the plate, the displacement vectors, associated with the $i^{th}(i = 1,2,\ldots,8)$ node of an element are expressed as,

$$\boldsymbol{d}_{ti}^e = \begin{bmatrix} u_{0i} & v_{0i} & w_{oi} \end{bmatrix}^T, \boldsymbol{d}_{ri}^e = \begin{bmatrix} \theta_{xi} & \theta_{yi} \end{bmatrix}^T. \quad (4.10)$$

On the element level, the displacement field at any point within the element can be defined in terms of the nodal displacement vectors, $\boldsymbol{d}_t^e$ and $\boldsymbol{d}_r^e$, and shape functions matrices, $\boldsymbol{N}_t$ and $\boldsymbol{N}_r$, as follows,

$$\boldsymbol{d}_t = \boldsymbol{N}_t\boldsymbol{d}_t^e, \qquad \boldsymbol{d}_r = \boldsymbol{N}_r\boldsymbol{d}_r^e, \qquad \boldsymbol{D} = \boldsymbol{N}_t\boldsymbol{D}^e, \quad (4.11)$$

where

$$\boldsymbol{d}_t^e = \begin{bmatrix} \boldsymbol{d}_{t1}^{e\,T} & \boldsymbol{d}_{t2}^{e\,T} & \cdots & \boldsymbol{d}_{t8}^{e\,T} \end{bmatrix}^T, \qquad \boldsymbol{d}_r^e = \begin{bmatrix} \boldsymbol{d}_{r1}^{e\,T} & \boldsymbol{d}_{r2}^{e\,T} & \cdots & \boldsymbol{d}_{r8}^{e\,T} \end{bmatrix}^T,$$

$$\boldsymbol{N}_t = \begin{bmatrix} N_1 & 0 & 0 & N_2 & 0 & & 0 \\ 0 & N_1 & 0 & 0 & N_2 & \ddots & 0 \\ 0 & 0 & N_1 & 0 & 0 & & N_8 \end{bmatrix}, \qquad \boldsymbol{N}_r = \begin{bmatrix} N_1 & 0 & N_2 & 0 & & 0 \\ 0 & N_1 & 0 & N_2 & \cdots & N_8 \end{bmatrix},$$

with N_i being the second order shape function associated with the i^{th} node. Upon substitution into Eq. 4.8 and 4.9, energy functionals can be written as,

$$T = \frac{1}{2}(\dot{\boldsymbol{d}}_t^{eT}\boldsymbol{M}_{tt}^e\dot{\boldsymbol{d}}_t^e + \dot{\boldsymbol{d}}_t^{eT}\boldsymbol{M}_{tr}^e\dot{\boldsymbol{d}}_r^e + \dot{\boldsymbol{d}}_r^{eT}\boldsymbol{M}_{rt}^e\dot{\boldsymbol{d}}_t^e + \dot{\boldsymbol{d}}_r^{eT}\boldsymbol{M}_{rr}^e\dot{\boldsymbol{d}}_r^e), \tag{4.12}$$

$$\begin{aligned} U = \frac{1}{2}(&\boldsymbol{d}_t^{eT}\boldsymbol{K}_{tt}^e\boldsymbol{d}_t^e + \boldsymbol{d}_t^{eT}\boldsymbol{K}_{tr}^e\boldsymbol{d}_r^e + \boldsymbol{d}_r^{eT}\boldsymbol{K}_{rt}^e\boldsymbol{d}_t^e + \boldsymbol{d}_r^{eT}\boldsymbol{K}_{rr}^e\boldsymbol{d}_r^e + \boldsymbol{D}^{eT}\boldsymbol{K}_{dd}^e\boldsymbol{D}^e) \\ &-\boldsymbol{d}_t^{eT}\boldsymbol{K}_{td}^e\boldsymbol{D}^e - A_{pzt}\boldsymbol{V}\boldsymbol{D}^e - \boldsymbol{d}_t^{eT}\boldsymbol{F}_t^e - \boldsymbol{d}_r^{eT}\boldsymbol{F}_r^e, \end{aligned} \tag{4.13}$$

where all element matrices are defined as,

$$\boldsymbol{M}_{tt}^e = \sum_{k=1}^{2}\rho_k\iint_{A_k}\left(\int_{h_k}(\boldsymbol{N}_t^T\boldsymbol{N}_t)\,dz\right)dxdy,$$

$$\boldsymbol{M}_{tr}^e = \boldsymbol{M}_{rt}^e = \sum_{k=1}^{2}\rho_k\iint_{A_k}\left(\int_{h_k}z(\boldsymbol{N}_t^T\boldsymbol{N}_t)\,dz\right)dxdy,$$

$$\boldsymbol{M}_{rr}^e = \sum_{k=1}^{2}\rho_k\iint_{A_k}\left(\int_{h_k}z^2(\boldsymbol{N}_t^T\boldsymbol{N}_t)\,dz\right)dxdy,$$

$$\boldsymbol{K}_{tt}^e = \sum_{k=1}^{2}\iint_{A_k}\left(\int_{h_k}(\boldsymbol{B}_{bt}^T\boldsymbol{C}_b\boldsymbol{B}_{bt} + \boldsymbol{B}_{st}^T\boldsymbol{C}_s\boldsymbol{B}_{st})\,dz\right)dxdy,$$

$$\boldsymbol{K}_{tr}^e = \sum_{k=1}^{2}\iint_{A_k}\left(\int_{h_k}(z\boldsymbol{B}_{bt}^T\boldsymbol{C}_b\boldsymbol{B}_{br} + \boldsymbol{B}_{st}^T\boldsymbol{C}_s\boldsymbol{B}_{sr})\,dz\right)dxdy,$$

$$\boldsymbol{K}_{rt}^e = \sum_{k=1}^{2}\iint_{A_k}\left(\int_{h_k}(\boldsymbol{B}_{br}^T\boldsymbol{C}_b\boldsymbol{B}_{bt} + \boldsymbol{B}_{sr}^T\boldsymbol{C}_s\boldsymbol{B}_{st})\,dz\right)dxdy,$$

$$\boldsymbol{K}_{rr}^e = \sum_{k=1}^{2}\iint_{A_k}\left(\int_{h_k}(z^2\boldsymbol{B}_{br}^T\boldsymbol{C}_b\boldsymbol{B}_{br} + \boldsymbol{B}_{sr}^T\boldsymbol{C}_s\boldsymbol{B}_{sr})\,dz\right)dxdy,$$

$$\boldsymbol{K}_{dd}^e = h_{pzt}\iint_{A_{pzt}}\boldsymbol{N}_t^T\boldsymbol{\beta}^{\varepsilon}\boldsymbol{N}_t\,dxdy,$$

$$\boldsymbol{K}_{td}^e = h_{pzt}\iint_{A_{pzt}}\boldsymbol{B}_{bt}^T\boldsymbol{h}_b\boldsymbol{N}_t\,dxdy,$$

$$\boldsymbol{F}_{\boldsymbol{t}}^{\boldsymbol{e}} = \iint_A\boldsymbol{N}_t^T\boldsymbol{f}_t\,dxdy, \qquad \boldsymbol{F}_{\boldsymbol{r}}^{\boldsymbol{e}} = \iint_A\boldsymbol{N}_r^T\boldsymbol{f}_r\,dxdy,$$

$$\boldsymbol{B}_{bt} = \boldsymbol{L}_{bt}\boldsymbol{N}_t, \qquad \boldsymbol{B}_{st} = \boldsymbol{L}_{st}\boldsymbol{N}_t, \qquad \boldsymbol{B}_{br} = \boldsymbol{L}_{br}\boldsymbol{N}_r, \qquad \boldsymbol{B}_{sr} = \boldsymbol{L}_{sr}\boldsymbol{N}_r.$$

Applying Hamilton's principle, the equations of motion for the plate with the piezoelectric actuators is obtained as follows,

$$\begin{aligned} \boldsymbol{M}^e_{tt}\ddot{\boldsymbol{d}}^e_t + \boldsymbol{M}^e_{tr}\ddot{\boldsymbol{d}}^e_r + \boldsymbol{K}^e_{tt}\boldsymbol{d}^e_t + \boldsymbol{K}^e_{tr}\boldsymbol{d}^e_r &= \boldsymbol{F}^e_t + \boldsymbol{K}^e_{td}\boldsymbol{D}^e, \\ \boldsymbol{M}^e_{rt}\ddot{\boldsymbol{d}}^e_t + \boldsymbol{M}^e_{rr}\ddot{\boldsymbol{d}}^e_r + \boldsymbol{K}^e_{rt}\ddot{\boldsymbol{d}}^e_t + \boldsymbol{K}^e_{rr}\ddot{\boldsymbol{d}}^e_r &= \boldsymbol{F}^e_r. \end{aligned} \tag{4.14}$$

An additional equation can also be obtained for the elemental electric displacement degrees of freedom, $\boldsymbol{D}^e$, as follows,

$$\boldsymbol{D}^e = {\boldsymbol{K}^e_{dd}}^{-1}(A_{pzt}\boldsymbol{V} + \boldsymbol{K}_{tt}\boldsymbol{d}^e_t). \tag{4.15}$$

Substituting Eq. 4.15 into Eq. 4.14 and assembling the elemental matrices yields,

$$\begin{aligned} \boldsymbol{M}_{tt}\ddot{\boldsymbol{d}}^G_t + \boldsymbol{M}_{tr}\ddot{\boldsymbol{d}}^G_r + (\boldsymbol{I} + \boldsymbol{K}_{td}\boldsymbol{K}^{-1}_{dd})\boldsymbol{K}_{tt}\boldsymbol{d}^G_t + \boldsymbol{K}_{tr}\boldsymbol{d}^G_r &= \boldsymbol{F}_t + A_{pzt}\boldsymbol{K}_{td}\boldsymbol{K}^{-1}_{dd}\boldsymbol{V}, \\ \boldsymbol{M}_{tr}\ddot{\boldsymbol{d}}^G_t + \boldsymbol{M}_{rr}\ddot{\boldsymbol{d}}^G_r + \boldsymbol{K}_{rt}\boldsymbol{d}^G_t + \boldsymbol{K}_{rr}\boldsymbol{d}^G_r &= \boldsymbol{F}_r, \end{aligned}$$

where $\boldsymbol{M}_{tt}$, $\boldsymbol{M}_{tr}$, $\boldsymbol{M}_{rr}$, $\boldsymbol{K}_{tt}$, $\boldsymbol{K}_{tr}$, $\boldsymbol{K}_{rt}$ and $\boldsymbol{K}_{rr}$ are the global mass and stiffness matrices. The vectors $\boldsymbol{d}^G_t$ and $\boldsymbol{d}^G_r$ are the global nodal translational and rotational degrees of freedom, respectively. $\boldsymbol{F}_t$ and $\boldsymbol{F}_r$ are respectively the global force and moment vectors. In general, the thickness of the piezoelectric actuators is very small compared to the base plate thickness, thus, $\boldsymbol{M}_{tr}$ and $\boldsymbol{M}_{tr}$ can be ignored. Furthermore, for thin plates undergoing relatively low frequency excitations, the effects of rotary inertia, represented by the matrix $\boldsymbol{M}_{rr}$, are negligible. This allows solving for rotational degrees of freedom in terms of translational ones, and hence, reducing the computational cost of the model.

The steady state dynamics of this model are then validated and the FE model is updated based on experimental modal testing of a rectangular plate. The details of the experimental analysis are presented in the next section.

4.3 Part II: Modal testing of the plate

In the previous section, the dynamics of the plate are modeled through a finite element approach and this section validates the results of this model experimentally. A single-input-multi-output (SIMO) modal testing procedure is followed to extract eigenvalues and eigenvectors of the plate. Furthermore, the damping characteristics of the plate are experimentally acquired and the FE model is then updated to include damping. The various steps followed in this modal testing and

Table 4.1: Material properties for the augmented PZT-adhesive-beam system [2].

	Base Plate (Al 6061)	
E=69 GPa	ν=0.33	ρ=2700 kg$/m^3$
	PZT wafer (PZT-5A)	
E=62 GPa	ν=0.33	ρ=7800 kg/m^3
h_{13}=-8.869$\times 10^8$ V/m	h_{23}=-8.869$\times 10^8$ V/m	β_{33}=1.481$\times 10^8$ m/F

validation phases are discussed in the following sections.

4.3.1 Experimental setup

The experimental work herein uses an aluminum plate of dimensions 24"$\times$6"$\times$1/16" ($l \times w \times t$) to study 2D traveling waves. One surface of the plate is bonded with four M2814-P1 model MFCs using 3M DP460 epoxy. Material properties for the base plate and the piezoelectric actuator are summarized in Table 4.1. The MFCs (labeled A-D) are of size 1.102"$\times$0.551" and are symmetrically placed at each corner of the plate as shown in Figure 4.2 (b).

The plate is suspended in the air on two tensioned fishing lines to replicate an overall-free boundary condition (Figure 4.2 (a)). The forces on the plate on account of the support fishing lines are hence neglected in the current analysis. The strings are placed to balance the plate horizontally and at the same time not to interfere with the MFCs bonded to the bottom surface of the plate. When one or more of the MFCs are actuated, the plate is excited, and the resulting vibrations are measured by scanning the top surface of the plate using a Polytec Scanning Laser Doppler Vibrometer (SLDV). To facilitate model validation, 493 scan points are imported into Polytec SLDV software from the finite element mesh; this enables an easier and more accurate comparison of experimental and numerical results.

Firstly, a SISO modal analysis of the plate is performed through multiple frequency-sweep tests to generate Frequency Response Functions (FRFs) and experimental Operational Deflection Shapes (ODSs) [178]. In these tests, MFC A is excited with a sine-sweep signal of frequency ranging from 10 to 3000 Hz and a constant amplitude of 14 volts. The SLDV measures the out-of-plane velocity of the plate at each of these 493 scan points and computes the corresponding FRFs with respect to the input voltage supplied to the MFCs. To reduce noise effects, 20 FRFs are generated and averaged at each point. This data is further analyzed to extract experimental eigenvalues, eigenvectors, and damping parameters. These results are discussed in the next section

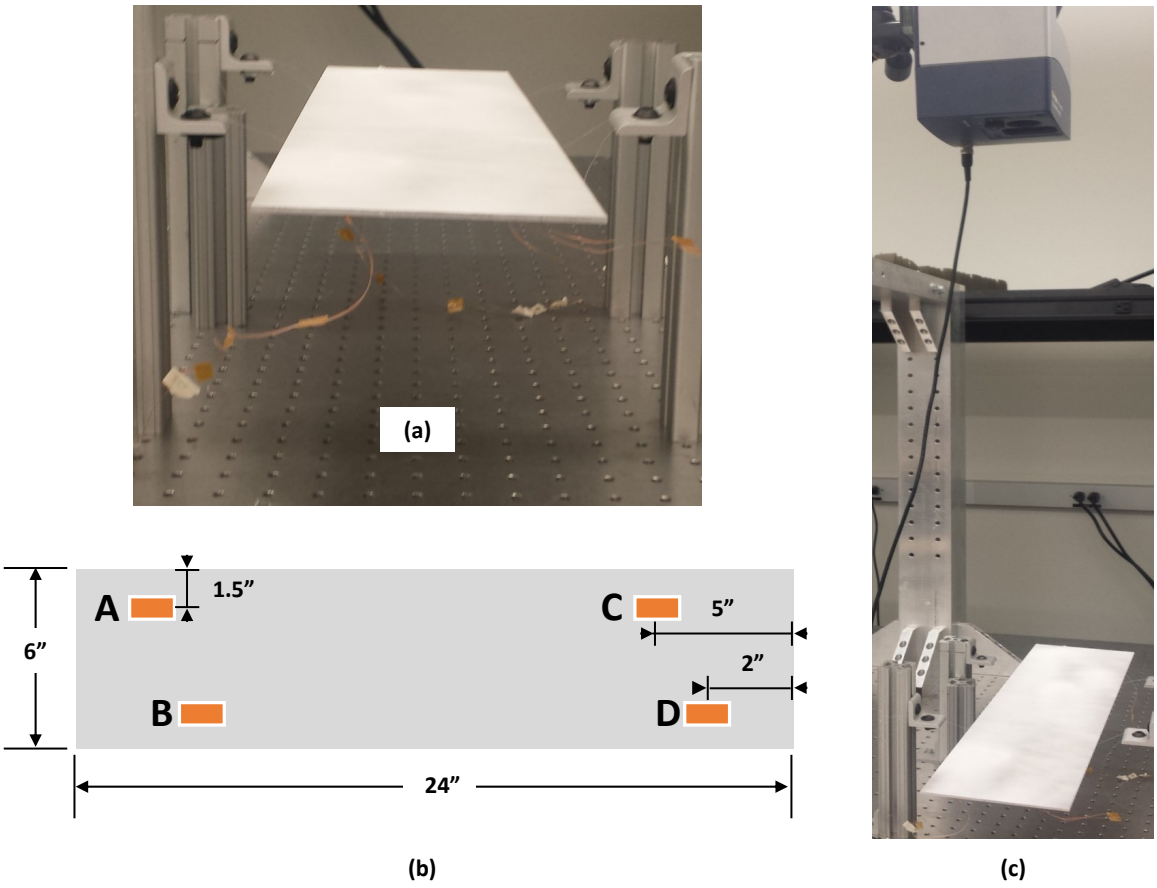

Figure 4.2: Experimental Setup: (a) a rectangular plate is suspended in air to simulate a free boundary condition, (b) locations of four MFCs bounded on to this plate are shown with respect to the plate dimensions, (c) a scanning laser vibrometer measures the response of the plate as it is excited by these MFCs.

and later this setup is used to generate traveling waves in the plate.

4.3.2 Operational deflection shapes (ODS) and eigenvectors

Polytec software processes the time-based vibration signal into the frequency domain in two ways. These are H_1 [179, 180] based FRF, which is the ratio of cross-power spectrum between input and output signals (G_{xy}) to input auto-power spectrum (G_{xx}) and the H_2 [179, 180] based FRF, defined as the ratio of output power-spectrum (G_{yy}) to cross-power spectrum (G_{xy}).

$$H_1(\omega) = \frac{G_{xy}}{G_{xx}} \quad \text{and} \quad H_2(\omega) = \frac{G_{yy}}{G_{xy}}. \tag{4.16}$$

The input and output noise effects are seen in these signals; while the H_2 based FRF performs better in capturing resonant frequencies, H_1 better predicts anti-resonant frequencies. This can

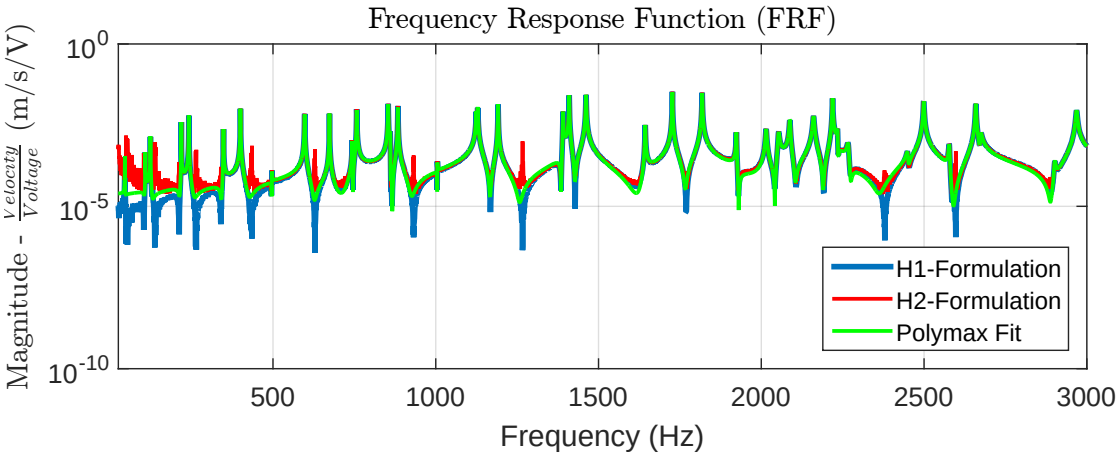

Figure 4.3: Experimental Frequency Response Functions (FRFs) are compared against the LMS polymax fit.

be seen in the Figure 4.3. The red curve (H_2-formulation) captures the peak values with a better accuracy than the blue curve (H_1-formulation). Based on these peak values, the Polytec software generates the vibratory pattern of the plate at these frequencies. These ODSs are tabulated and segregated according to the number of nodal lines in Figure 4.4. $ODS(a,b)$ denotes the number of partitions made by $a-1$ and $b-1$ nodal lines along length and width directions respectively. Figure 4.4 also shows how closely multiple ODSs occur in small frequency intervals. This renders it difficult to validate simulated undamped eigenvectors with experimental ODSs without filtering the effects of adjacent resonant frequencies, damping, noise, etc. When very close eigenvalues exist in plates, experimentally it is very difficult to isolate the dynamics of the plate at one of these frequencies from the other. The net resulting ODS has a major contribution of mode shapes from both frequencies and sometimes this results in complex ODSs.

Hence, to extract mode shapes (or eigenvectors) from these FRFs, we make use of the PolyMax algorithm in LMS TestLabs software [181] to fit frequency data. This *polyreference least-squares* approach (or PolyMax algorithm) computes a stabilization diagram based on complex frequencies, damping and participation factors obtained from the FRFs. Complex eigenvectors and eigenvalues are extracted by least-square fits of smaller frequency intervals using both H_1 and H_2 formulations. The best eigenvector at a frequency is chosen manually by identification of stable poles and the complexity of the fit. The average Polymax fit (green curves shown in Figure 4.3) is a product of the data in both H_1 and H_2 formulations.

Additionally, the experimental damping coefficients (ζ) are also estimated at all the peaks. In the next section, these estimates are used to derive a damping matrix.

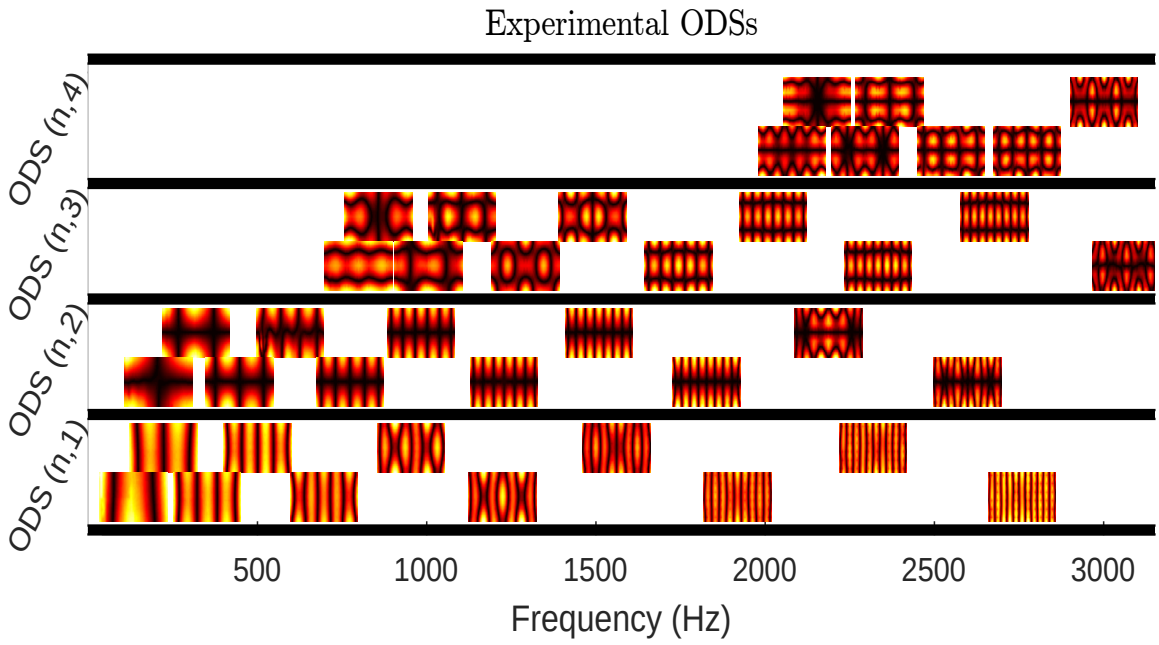

Figure 4.4: Experimental operational deflection shapes as measured by the Polytec SLDV.

4.3.3 Proportional viscous damping parameters

The earlier sections on the modeling efforts of the plate dynamics with the piezoelectric patches discussed the derivation of mass $[M]$ and stiffness $[K]$ matrices from the geometric and material properties of the structure. The model discussed in this section includes damping forces based on the approach previously developed in the literature [182]. For completeness, a brief explanation of this approach is presented.

The dynamic FE model of the plate including the effect of viscous based damping can be represented by

$$\left[s^2\boldsymbol{M} + s\boldsymbol{C} + \boldsymbol{K}\right]\boldsymbol{X}(s) = \boldsymbol{0}. \tag{4.17}$$

The non-trivial complex solution of this equation is of the form of $s = -\sigma + j\omega_d$ where $\sigma = \zeta\bar{\omega}$, $\omega_d = \bar{\omega}\sqrt{1-\zeta^2}$, ω_d and $\bar{\omega}$ are the damped and undamped natural frequencies, and ζ is the damping coefficient. In the present work, viscous based damping matrix $\boldsymbol{C}$ is assumed to be proportional to both mass $(\boldsymbol{M})$ and stiffness $(\boldsymbol{K})$ matrices,

$$\boldsymbol{C} = \alpha\boldsymbol{M} + \beta\boldsymbol{K}. \tag{4.18}$$

The unknown parameters α and β are estimated from the experimental data. Eq 4.18 is substituted

into Eq 4.17 and when simplified results in

$$\left\{ \begin{array}{c} \Big((\sigma^2 - \omega_d - \alpha\sigma) + i(-2\sigma\omega_d + \alpha\omega_d)\Big)\boldsymbol{M} \\ \\ +\Big((-\sigma\beta + 1) + i\beta\omega_d\Big)\boldsymbol{K} \end{array} \right\} \boldsymbol{X}(s) = \boldsymbol{0}. \tag{4.19}$$

As the mode shapes of this system are real-valued, the real and imaginary components of this equation are uncoupled and can be rewritten as

$$\begin{aligned} \left(\frac{\sigma^2 - \omega_d^2 - \alpha\sigma}{-\sigma\beta + 1}\boldsymbol{M} + \boldsymbol{K}\right)\boldsymbol{X}(s) = \boldsymbol{0}, \\ \left(\frac{-2\sigma + \alpha}{\beta}\boldsymbol{M} + \boldsymbol{K}\right)\boldsymbol{X}(s) = \boldsymbol{0}. \end{aligned} \tag{4.20}$$

Both of these equations, which are in the form of a generalized undamped eigenvalue problem, should be satisfied simultaneously; the coefficients of the mass matrices are simultaneously equal to the undamped natural frequency,

$$\frac{\sigma^2 - \omega_d^2 - \alpha\sigma}{-\sigma\beta + 1} \quad = \quad \frac{-2\sigma + \alpha}{\beta} = -\bar{\omega}^2 \left(= -\frac{\omega_d^2}{1 - \zeta^2} \right). \tag{4.21}$$

With the help of these two relationships, the undamped natural frequencies ($\bar{\omega}$) and the experimental damping coefficients (ζ), the two unknown parameters α and β can be estimated using a least square approach;

$$2 \begin{Bmatrix} \sigma_1 \\ \sigma_2 \\ \vdots \\ \sigma_N \end{Bmatrix} = \begin{bmatrix} 1 & \bar{\omega_1}^2 \\ 1 & \bar{\omega_2}^2 \\ \vdots & \vdots \\ 1 & \bar{\omega_N}^2 \end{bmatrix} \begin{Bmatrix} \alpha \\ \beta \end{Bmatrix}. \tag{4.22}$$

This equation has two known quantities ζ_i and $\bar{\omega}_i$, while the damping coefficients (ζ_i) are determined through experiments (half-power method). The undamped natural frequency can be determined in two ways: (Case 1) through experimental data ($\omega_d \Big/ \sqrt{1 - \zeta^2}$), (Case 2) through the theoretical eigenvalue problem ($|\boldsymbol{K} - \boldsymbol{M}\bar{\omega}^2| = 0$). When both approaches are considered, there are two estimates of (α, β): Case 1 results in (1.0793, 7.317×10^{-8}) and Case 2 results in (1.1074,

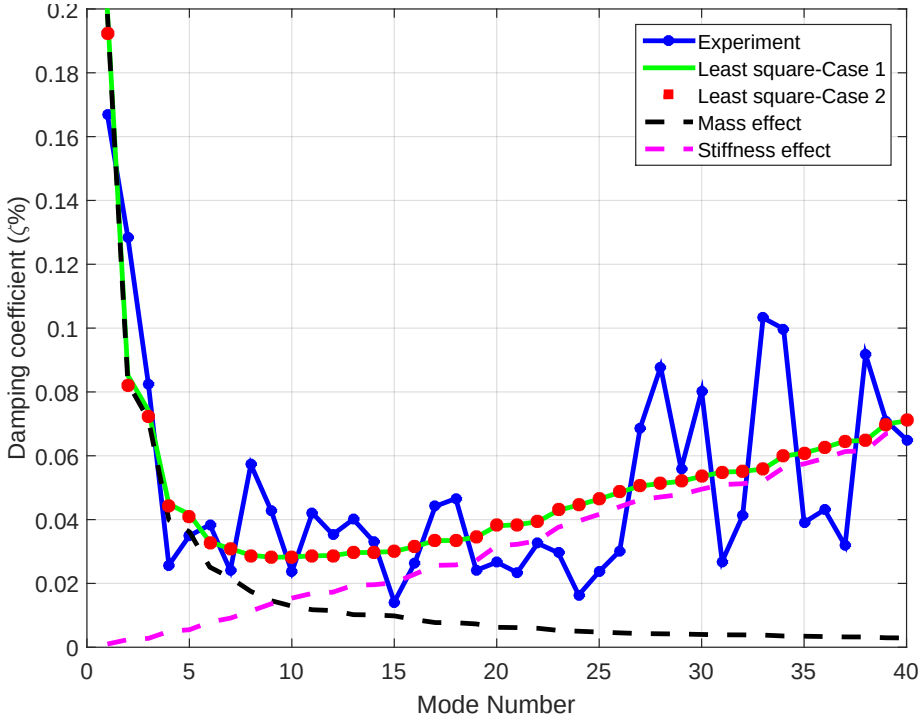

Figure 4.5: Experimental damping estimates based on H1 formulation .

7.1687×10^{-8}). Each of these least-square coefficients predict ζ with an RMS error of 2.09×10^{-4} and 2.101×10^{-4}, respectively. Figure 4.5 shows the experimental damping coefficient values for the first 40 plate modes along with the least square predictions. The high damping values near lower modes are due to the mass matrix ($\boldsymbol{M}$) and the gradual increase in damping values with higher modes are due to the stiffness matrix ($\boldsymbol{K}$) as seen in this figure.

As the proportional damping coefficients estimated through both cases are very close to each other, the coefficients estimated in case 1 are used in the rest of the chapter. Based on these values the complex eigenvalue problem is solved in the next section.

4.3.4 Complex eigenvalue problem

The previously developed finite element formulation of the plate is updated with the proportional damping values computed in the previous section and this results in:

$$\boldsymbol{M}\ddot{x}(t) + \Big(\alpha \boldsymbol{M} + \beta \boldsymbol{K}\Big)\dot{x}(t) + \boldsymbol{K}x(t) = 0.$$

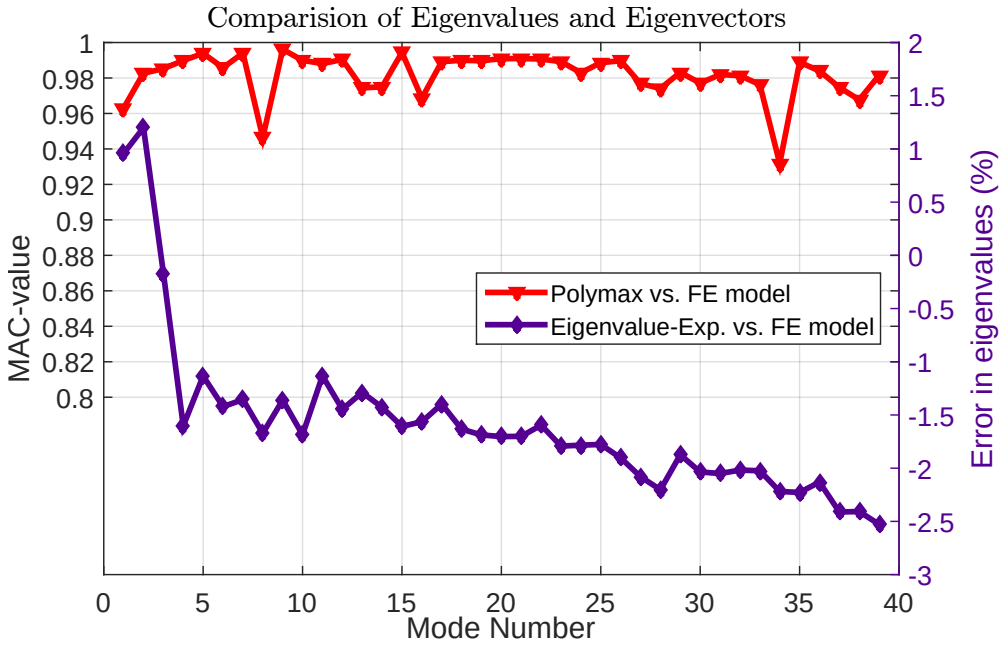

Figure 4.6: Simulated eigenvalues and eigenvectors of the damped plate model are compared against corresponding experimental values through the % error in eigenvalue prediction (purple) and MAC (red) respectively .

The eigenvalue problem arising from these set of equations is a complex equation and can be observed when $x(t)$ is assumed to be in the form of $Xe^{j\lambda t}$:

$$\Big(\boldsymbol{K}+i\Big(\alpha\boldsymbol{M}+\beta\boldsymbol{K}\Big)\lambda-\lambda^2\boldsymbol{M}\Big)x(t)=0.$$

This equation results in complex eigenvalues and complex eigenvectors which are solved in Matlab using the *polyeig* command. The damped natural frequency and complex mode shapes are then compared with the experimental natural frequencies and mode shapes extracted using the PolyMax algorithm and are plotted in Figure 4.6.

The updated FE model is able to predict eigenvalues with a maximum error of 2.5% for the entire bandwidth. Other than the first two eigenvalues, the FE model eigenvalues are in general larger than that of the experimental, and the error gradually increases with modes. Such a trend is expected, as the FE model has a higher stiffness as compared to the actual setup. Experimental (${}^1\Psi_i$) and theoretical (${}^2\Psi_j$) mode shapes are compared by using the Modal Assurance Criterion (MAC) [176, 180] values which is given by

$$MAC({}^1\Psi_i,{}^2\Psi_j)=\left(\frac{{}^1\Psi_i^T\,.{}^2\Psi_j}{\|{}^1\Psi_i\|\,\|{}^2\Psi_j\|}\right)^2. \tag{4.23}$$

Higher MAC values (close to 1) imply a higher correlation in the mode shapes. In the present scenario, all mac values are greater than 0.92, which shows a very good correlation between the experiment and finite element model. Thus, in this part of the thesis, the FE plate model is validated through SISO modal analysis and it predicts the steady state dynamic response with very high accuracy. In the next part, the steady state time response of the plate under multiple inputs is studied.

4.4 Part III: Traveling Waves

The traveling wave generation approach in this chapter is an extension of the two-mode excitation technique [59, 118, 118] or the impedance matching efforts [41, 172] previously carried out in 1-D systems. In these previous studies, a string or a beam is excited simultaneously by two actuators at a frequency halfway between two adjacent natural frequencies with a phase difference of 90°. In impedance matching literature, this phase difference is achieved by leading or lagging the voltage signal through electronic circuits. Further, our previous work in [70, 183, 184] and also described in previous chapter, has shown experimentally that traveling waves are achievable at any frequency in beams by varying the phase difference between the input voltage signals to an optimal value. However, it is easier to generate 1D waves as the number of parameters influencing the dynamics of symmetrically actuated systems are limited to the frequency of actuation and phase change. In 2D systems, such as plates [185, 186] and cylinders [187] it is much more complex to generate traveling waves.

4.4.1 Traveling wave generation

In this section the theoretical plate model, previously validated for steady state response, is used to study the behavior of the plate when excited by two MFCs in order to induce traveling waves. Earlier research [184] on 1-D traveling wave generation in beams suggests that the phase difference between the two actuators is dependent on the placement of the actuators and the driving frequency. This concept is extended and applied in the present work for 2D plates. For example, the model predicts the 9^{th} and 10^{th} natural frequencies of the plate to be at $504Hz$ and $606Hz$ respectively; the two-mode excitation theory suggests that if the plate is excited at the halfway frequency, i.e. at $555Hz$, with a phase difference of 90° between the two MFCs, this will result in a traveling wave response. This concept is tested in this section by choosing three MFC configurations to actuate the plate at eight such "*halfway*" frequencies. If the halfway frequency is ω_h rad/s, the response of

the plate is given by solving the forced system of equations given by

$$\boldsymbol{M}\ddot{x}(t) + \boldsymbol{C}\dot{x}(t) + \boldsymbol{K}x(t) = F_1(x_1, y_1, t) + F_2(x_2, y_2, t),$$

where $F_1(x_1, y_1, t)$ and $F_2(x_2, y_2, t)$ are the forces due to the two MFCs at two different locations. These forces are estimated by using the piezo control influence matrices $\{[\boldsymbol{K}_{td}\boldsymbol{K}_{dd}]_1\}$ and $\{[\boldsymbol{K}_{td}\boldsymbol{K}_{dd}]_2\}$ and the voltage signal $(V(t))$ for both piezos, respectively. The plate velocity response $(\bar{\mathcal{V}})$ due to these two forces $(\boldsymbol{F} = F_1(x_1, y_1, t) + F_2(x_2, y_2, t))$ is computed using the superposition theorem as

$$\bar{\mathcal{V}} = \left[\boldsymbol{K} + j.\omega_h \boldsymbol{C} - \omega_h^2 \boldsymbol{M}\right]^{-1} \boldsymbol{F}, \tag{4.24}$$

where

$$\boldsymbol{F} = \left([\boldsymbol{K}_{td}\boldsymbol{K}_{dd}]_1 + [\boldsymbol{K}_{td}\boldsymbol{K}_{dd}]_2 e^{j.\pi/2}\right) V e^{j.\omega_h t}. \tag{4.25}$$

Experimentally, this halfway frequency is chosen based on experimental resonant frequencies, i.e. in the previous case this halfway experimental frequency is at $546Hz$, as the nearest two resonant frequencies are at $496Hz$ and $596Hz$ respectively. At this frequency, the plate is excited simultaneously by two of the four MFCs attached to the plate. Three combinations of MFC pairs are used to actuate the plate (refer to Figure 4.1): (1) MFC A and B, (2) MFC A and C, and (3) MFC A and D. In each of these actuation scenarios, the phase is maintained at 90° and input voltage amplitude at 14 Volts. As the plate is excited, the top face of the plate is scanned in the time-domain at all 493 points by the Polytec SLDV. One of the tasks in analyzing these results is to differentiate between 2D traveling and standing waves; this is further discussed in the next section.

4.4.2 Standing vs. Traveling waves

To distinguish between traveling waves and standing waves, the features of these waves have to be revisited [184]. In 1-D or 2-D flexural waves, all material particles of the structure vibrate sinusoidally with a constant phase difference between them. In standing waves, when there is no damping, this phase difference is either 0° or 180° and the transition between these phases is due to the presence of strain nodes i.e. points with no displacement. In traveling waves, although the phase difference between any two points is fixed in time, this value changes spatially and gradually increases from 0° to 180° over a given wavelength. Hence there are no strain nodes in traveling waves. This is the striking feature of traveling waves that separate them from standing waves. The

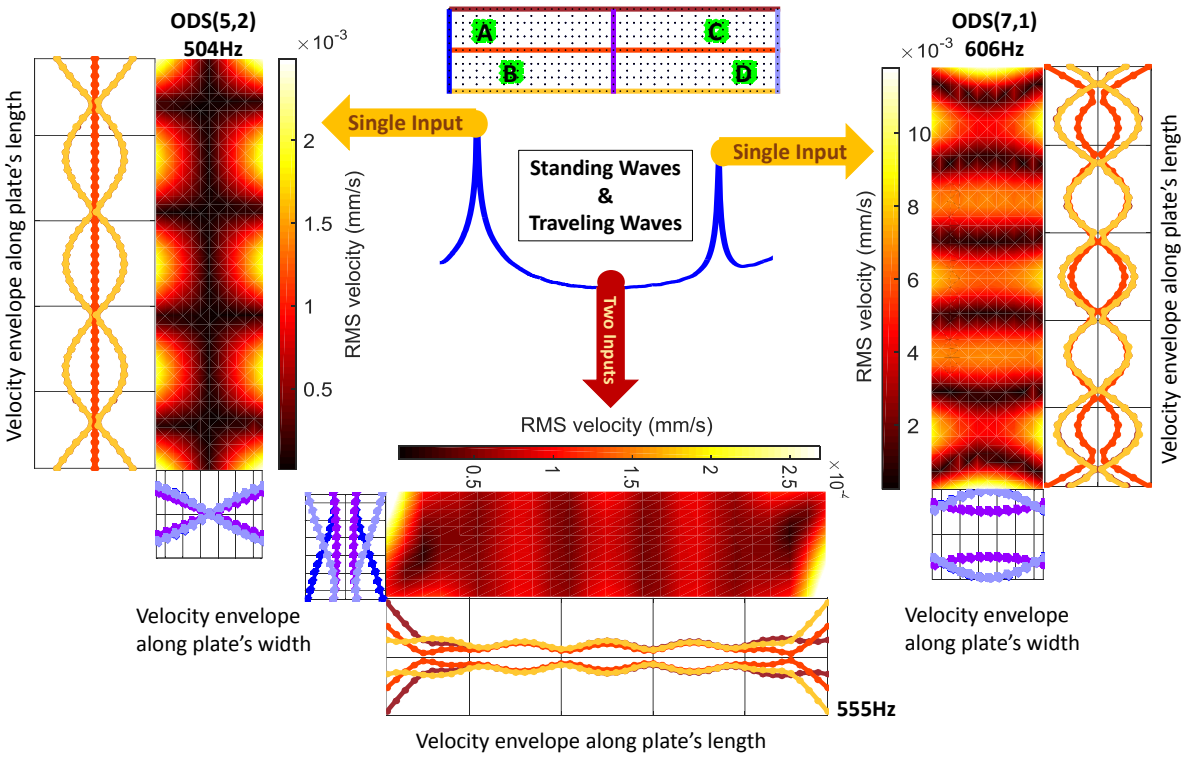

Figure 4.7: RMS contour plot and wave envelope plot for standing and traveling waves.

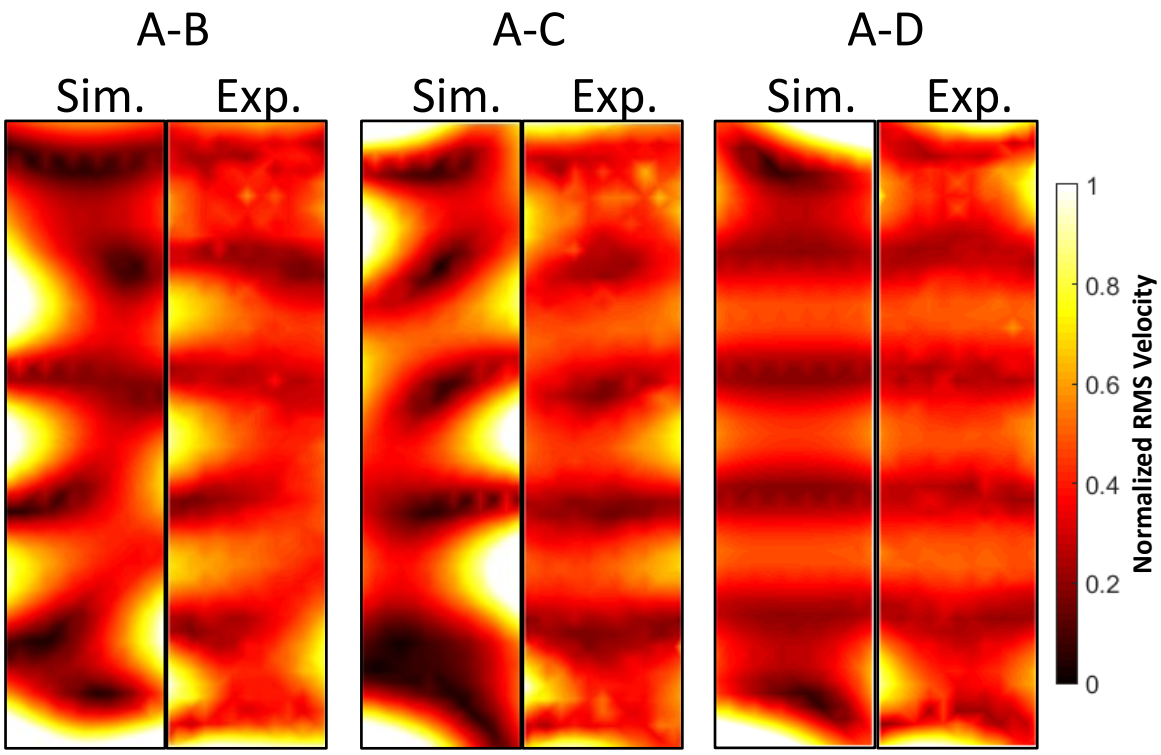

Figure 4.8: Comparing experimental and simulated RMS velocity contours of the plate at 546Hz and 555Hz respectively.

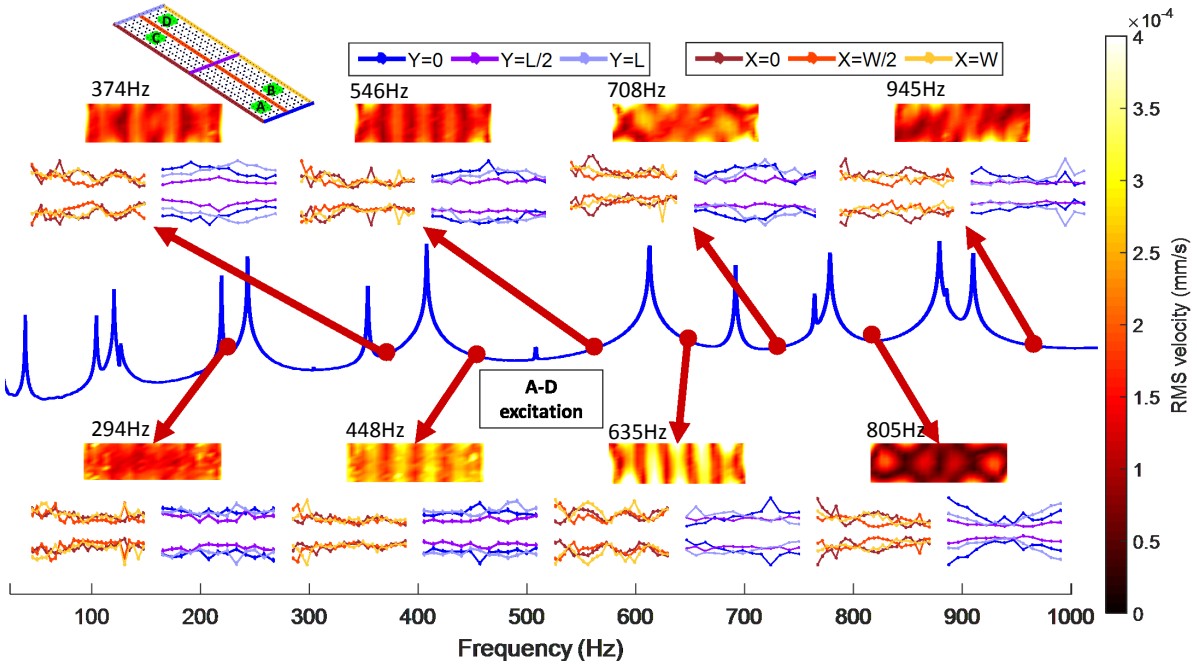

Figure 4.9: Experimental results of plate when excited at with MFCs A and D.

work presented in this chapter develops continuous traveling waves such that there are no effective reflections at the plate boundaries.

In the rest of the chapter, the presence or absence of strain nodes is used as a primary indicator to judge the quality of the traveling waves. The contour plots in this figure map the root-mean-squared (RMS) velocity of the plate. Contour plots and envelope plots, shown in Figure 4.7, can also used to study plate dynamics. This figure presents simulated data of the plate response when actuated by a single piezo at $504Hz$ and $606Hz$ and also when excited by two piezo patches at $555Hz$ (bottom plot). While the darker regions of such plots correspond to the region with little or no particle velocity (or nodal lines), the brighter regions correspond to the high particle velocity. In the contours of standing waves, there are both dark and bright regions and these correspond to the strain nodes and spatial anti-nodes. However, a contour of a pure traveling wave has uniform contrast throughout the plot.

For example, either of the single input actuation scenarios shown in this figure have clear nodal lines in the contour plots. Dark regions are parallel to both length and width of the plate in the case corresponding to 9^{th} resonant frequency (i.e ODS(5,2)) and only parallel to width when the plate is excited at the 10^{th} resonant frequency (i.e ODS(7,1)). Furthermore, the scenario where the plate is excited by two forces which are separated by a phase difference of 90° results in a contour which has an almost uniform contrast throughout.

Additionally, envelope plots along the length and the width of the plate are also provided for all cases. Three locations along the length ($Y = 0$, $Y = L/2$ and $Y = L$) and three along the width

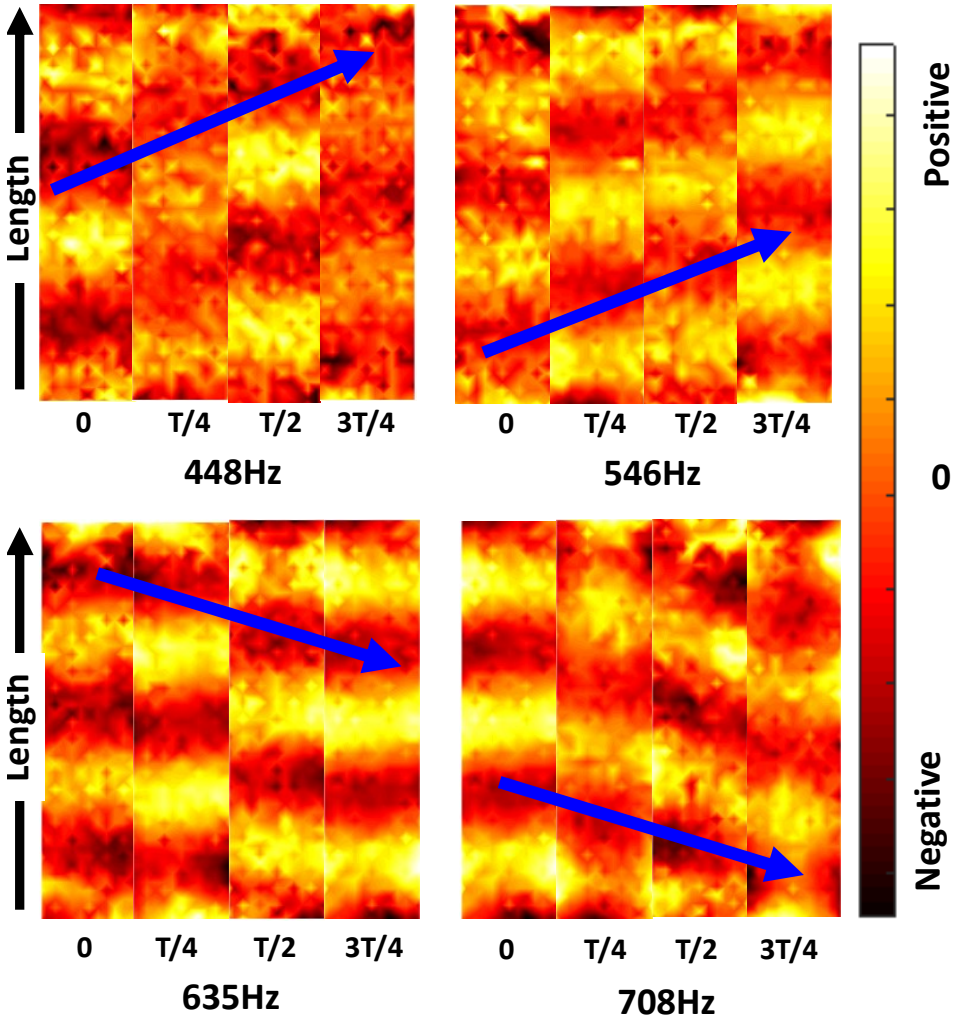

Figure 4.10: Time frames of wave progression along length of the plate at times $=\{0, T/4, T/2, 3T/4\}$ for 448Hz, 546Hz, 635Hz, and 708Hz based on experimental data obtained when the plate is excited by MFC A and D. (T is the time period of the wave at each respective frequencies.)

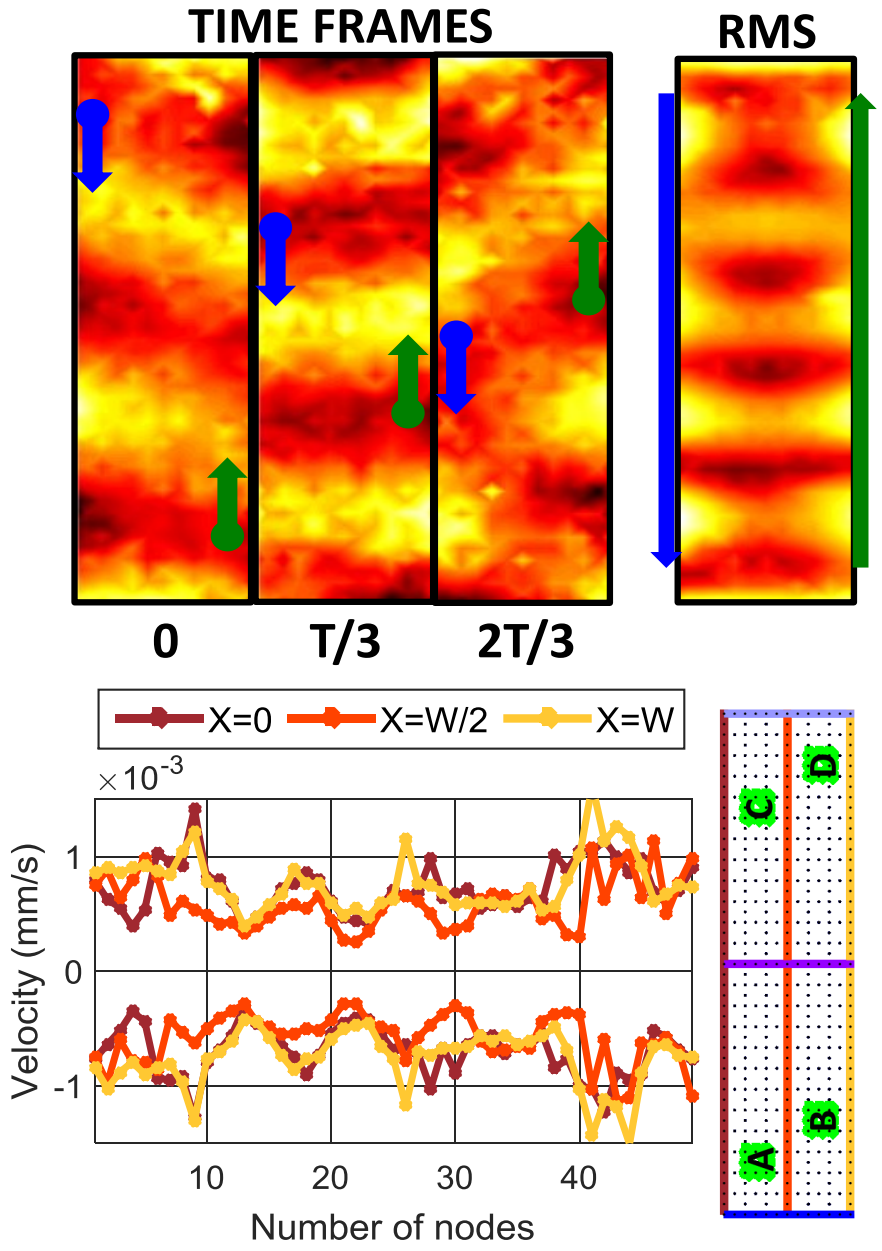

Figure 4.11: Experimental traveling wave phenomenon in the plate when excited by MFC A and B at 635Hz.

($X = 0$, $X = W/2$ and $X = W$) are chosen to study these maximum and minimum envelopes. Similar to the contour plots, these envelope plots provide information related to the maximum and minimum velocity of points along discrete locations along the length and the width of the plate. In the presence of strain nodes, the maximum and minimum displacement/velocity of the particles are equal to zero and this is visible through these plots. Care should be taken in assuming the presence of traveling waves based on just these envelope plots, as nodal lines may be present only in one direction. For example, in the standing wave case of $606Hz$, nodal lines occur parallel to the width of the plate and hence can only be seen in the envelop plot which presents data along the length of the plate.

4.4.3 Effects of actuation locations

This section discusses the role played by MFC placement in determining the type of resulting 2D planar wave, by changing the actuator pair used to excite the plate. The RMS contour plots in Figure 4.8 show plate responses when it is excited by three different MFC pairs: A-B, A-C, and A-D. To compare similar plate effects at halfway frequencies, the experimental data at $546Hz$ is compared with $555Hz$ in simulations for all three scenarios. Contour patterns in all three cases are significantly different from each other, revealing that actuation location plays a significant role when the driving frequency is kept constant. In all three cases, the MFC pairs that are actuated can be easily located in the corners of the plate by identifying areas which are white in color; these areas have particles which have much higher velocities as compared to the rest of the plate, as expected. In cases where the plate is excited using A-B and A-C pairs, there are areas (dark or black in color) where the velocities of the points on the plate are much smaller than the rest of the plate. Although these two scenarios result in complex standing wave patterns, the third case where the plate is excited by the A-D MFC pair, has a recognizable traveling wave pattern. In this case, it is observed that there is a wave which starts at MFC A and travels along the longer side of the plate to reach the other MFC (D). These patterns generated by the FE model closely follow the patterns observed experimentally, which confirms that the excitation locations of the MFC's bonded to the plate play an important role in traveling waves generation. Although, only one of the eight halfway frequencies ($294Hz$, $374Hz$, $448Hz$, $546Hz$, $635Hz$, $708Hz$, $805Hz$, $945Hz$) experimentally tested is presented here, a similar trend is observed in most of the cases wherein MFC pairs A-B and A-C generate patterns that are not as good as the wave generated in the A-D pair. Furthermore, in all cases where the plate is excited with the MFC A-D pair (except for the $805Hz$), a traveling wave with varying wavelengths is observed. At $805Hz$, a complex standing wave is observed. The experimental RMS contours and wave envelopes for all these cases are plotted along with the averaged frequency response function in Figure 4.9.

In the frequency range tested, traveling waves are always found to travel along the length of the plate when the plate is excited using the MFC A-D pair. The direction and the wavelength of these waves vary from case-to-case as shown in Figure 4.10. In this figure, the time trace contours of the wave progression are presented at four time-stamps: 0, $T/4$, $T/2$, $3T/4$; where T is the time-period of the wave at the frequency of excitation. As these contours display the instantaneous velocity profile of the plate at various time stamps, the scale of the contour ranges from a negative minimum value to a positive maximum value as opposed to the RMS contours previously discussed. The blue arrows shown in this figure follow the direction of wave propagation in the plate. Although, in all of these cases the phase difference between the MFC pair A-D is 90°, the direction of the wave is not the same. While, in the $448Hz$ and $546Hz$ cases, the wave starts from A and ends at D, the trend is opposite at the other two frequencies where the wave starts at D and ends at A. A similar phenomenon is also observed in beams where the direction of the waves changes [184] and Chapter 3. Although, there is a specific pattern in beams where the direction of the traveling waves alternates after each resonant frequency, such a trend is not observed in plates. For example, the frequency pairs ($448Hz$ & $546Hz$) and ($635Hz$ & $708Hz$) have only one resonant frequency between them, there is no change in the direction of the traveling waves. However, there is a reversal of direction when the frequency of excitation changes from $546Hz$ to $635Hz$. A more detailed study is required to understand this phenomenon, but it is presumed to be due to the presence of nodes in both directions (width and length) which is not present in beams. Furthermore, as the frequency increases, the wavelength decreases as predicted by the dispersion relation of the plate, and this trend is also visible in the contour plot.

4.5 Part IV: Reduction of FE plate model

As analytical solutions to 2D plates are complex to analyze, a FE approach, supported by experimental results. However, a comprehensive analysis requires simulating the FE model for various cases: varying the locations of forces, the phase timing between forces, the amplitude of these forces and the frequency of excitation. Such simulations on the plate model are computationally intensive.

The present section attempts to scale-down these large FE models into reduced order models (ROMs) that are still representative of the dynamics of the system under study. The importance of model reduction of complex dynamical systems arises from the need for reducing the computational cost of numerical simulations, which can put overwhelming burden on computational resources. The need for model reduction becomes even more substantial when a large number of full-system evaluations or real-time (or near real-time) responses are required. Computational mechanics based optimization, statistical analysis, parametric studies and optimal control, analysis

of nonlinear phenomena, such as turbulence, large deformations, plasticity and contact mechanics are few examples where model reduction techniques are heavily used. We refer the reader to the following monographs and survey papers [188–194] for a description and analysis of various model reduction techniques in additions to examples of model reduction in action.

In this chapter, the limits and capabilities of some model reduction techniques to capture the dynamics of an aluminum thin plate are studied. The next section, '*Projection-based model reduction techniques*' features the concepts behind the various model reduction techniques to develop a reduced-order model to approximate the full system. Furthermore, the issues of reducing an unconstrained plate model especially due to the rigid-body modes are discussed. Various reduction techniques based on the concepts of reachability, observability, balanced truncation and Iterative Rational Krylov Algorithm are also presented. The theoretical background of these techniques used in this chapter are well developed in the literature; [188, 189, 194–196] and have been presented here only briefly.

4.5.1 Projection-based model reduction

Simulations of complex engineering problems such as dynamic structures, fluid systems, and material models make use of fine-scaled finite element models with huge dimensions. Computational burden, conditioning and numerical stability, and data storage are challenging factors for such finite element formulations. To obviate the aforementioned challenges, the full scale finite element model can be scaled down to an approximate reduced-order-model (ROM), preserving the needed input-output characteristics. The present work considers four model reduction approaches based on projections to scale-down the finite element model developed in the earlier section. The steady state frequency and time response of the ROM is then compared with the full FE model. The plate FE model can be represented in a generalized second-order differential equation as

$$\begin{aligned} \boldsymbol{M}\ddot{\boldsymbol{q}}(t) + \mathcal{G}\dot{\boldsymbol{q}}(t) + \boldsymbol{K}\boldsymbol{q}(t) &= \boldsymbol{F}\boldsymbol{u}(t) \\ \boldsymbol{y} &= \boldsymbol{c}\dot{\boldsymbol{q}}(t), \end{aligned}$$

which can be rewritten in the state-space representation as

$$\begin{aligned} \dot{\boldsymbol{x}} &= \begin{bmatrix} \boldsymbol{0} & \boldsymbol{I} \\ -\boldsymbol{M}^{-1}\boldsymbol{K} & -\boldsymbol{M}^{-1}\mathcal{G} \end{bmatrix} \boldsymbol{x} + \begin{bmatrix} \boldsymbol{0} \\ -\boldsymbol{M}^{-1}\boldsymbol{F} \end{bmatrix} \boldsymbol{u}, \\ \boldsymbol{y} &= \begin{bmatrix} \boldsymbol{0} & \boldsymbol{c} \end{bmatrix} \boldsymbol{x}, \end{aligned} \tag{4.26}$$

where $\boldsymbol{x} = \begin{bmatrix} \boldsymbol{q} \\ \dot{\boldsymbol{q}} \end{bmatrix}$. Note that except for the special cases such as when the mass matrix $\boldsymbol{M}$ is diagonal and well-conditioned, one avoids inverting $\boldsymbol{M}$, as this operation will be too costly and will destroy the sparsity. In that case, a block diagonal matrix will multiply the state-vector $\boldsymbol{x}$ leading to a generalized state-space system. In this chapter, to keep the notation simpler, we use the state-space representation in (4.26). All the discussion that follows directly extends to the generalized state-space case. We will denote the state-space representation in (4.26) by

$$\begin{aligned} \dot{\boldsymbol{x}}(t) &= \boldsymbol{A}\boldsymbol{x}(t) + \boldsymbol{B}\boldsymbol{u}(t), \\ \boldsymbol{y}(t) &= \boldsymbol{C}\boldsymbol{x}(t) + \boldsymbol{D}\boldsymbol{u}(t), \end{aligned} \tag{4.27}$$

where the first equation describes the internal dynamics, illustrating how the internal state variable $\boldsymbol{x}(t) \in \mathbb{R}^n$ changes in response to the input $\boldsymbol{u}(t) \in \mathbb{R}^m$ applied to the system. The state variable $\boldsymbol{x}(t)$ contains the plate displacements and velocities discretized at all finite element nodes, in all three directions x, y and z. The input $\boldsymbol{u}(t)$ is a vector of voltage signals applied to the four piezo-ceramics bonded to the plate. The output variable $\boldsymbol{y}(t) \in \mathbb{R}^p$ is the desired out-of-plane velocities (i.e., in the z-direction) of the plate meshed at 493 locations. Therefore the dimensions of the state space matrices of the full-order system are $\boldsymbol{A} \in \mathbb{R}^{n\times n}$, $\boldsymbol{B} \in \mathbb{R}^{n\times m}$, $\boldsymbol{C} \in \mathbb{R}^{p\times n}$, and $\boldsymbol{D} \in \mathbb{R}^{p\times m}$. For the full plate model we consider here, $n = 2956$, $m = 4$, and $p = 493$.

For linear dynamical systems such as the FE plate model considered here, the model reduction framework and the error analysis is best understood in the frequency domain. Then, by taking the Laplace transform of (4.27), we obtain the transfer function $G(s)$ of the underlying model, given by

$$\begin{aligned} G(s) &:= \left[\begin{array}{c|c} \boldsymbol{A} & \boldsymbol{B} \\ \hline \boldsymbol{C} & \boldsymbol{D} \end{array}\right], \\ &:= \boldsymbol{C}(s\boldsymbol{I} - \boldsymbol{A})^{-1}\boldsymbol{B} + \boldsymbol{D}. \end{aligned} \tag{4.28}$$

Note that the transfer function $G(s)$ is a matrix-valued rational function of degree-n. Then, the purpose of model reduction is to construct a reduced-order rational function (i.e., a reduced-order transfer function) $G_r(s)$ of degree $r \ll n$ such that $G_r(s)$ is a good approximation to $G(s)$ in an appropriate norm. This is achieved by projecting the full state-space onto a lower dimensional one using Petrov-Galerkin projection. To achieve this goal, we construct two model reduction bases $\boldsymbol{V} \in \mathbb{R}^{n\times r}$ and $\boldsymbol{W} \in \mathbb{R}^{n\times r}$ where r is the desired reduced-order. Without loss of generality, assume that $\boldsymbol{V}$ and $\boldsymbol{W}$ are bi-orthogonal, i.e., $\boldsymbol{W}^T\boldsymbol{V} = \boldsymbol{I}_r$. Then, we approximate the full-state

as $\boldsymbol{x} \approx \boldsymbol{V}\boldsymbol{x}_r$, where $\boldsymbol{x}_r \in \mathbb{R}^r$ is the reduced state, and enforce a Petrov-Galerkin condition on the error

$$\boldsymbol{W}^T\left(\boldsymbol{V}\dot{\boldsymbol{x}}_r - \boldsymbol{A}\boldsymbol{V}\boldsymbol{x}_r - \boldsymbol{B}\boldsymbol{u}(t)\right) = \boldsymbol{0}$$

to obtain the reduced-order model (ROM) given by

$$\begin{aligned} \dot{\boldsymbol{x}}_r(t) &= \boldsymbol{W}^T A\boldsymbol{V}\boldsymbol{x}_r(t) + \boldsymbol{W}^T\boldsymbol{B}\boldsymbol{u}(t), \\ \boldsymbol{y}_r(t) &= \boldsymbol{C}\boldsymbol{V}\boldsymbol{x}_r(t) + \boldsymbol{D}\boldsymbol{u}(t), \end{aligned} \tag{4.29}$$

or, equivalently in the frequency domain,

$$\begin{aligned} G_r(s) &:= \left.\begin{array}{c|c} \boldsymbol{W^T A V} & \boldsymbol{W^T B} \\ \hline \boldsymbol{CV} & \boldsymbol{D} \end{array}\right. = \left.\begin{array}{c|c} \boldsymbol{A_r} & \boldsymbol{B_r} \\ \hline \boldsymbol{C_r} & \boldsymbol{d_r} \end{array}\right., \\ &:= \boldsymbol{C_r}(s\boldsymbol{I} - \boldsymbol{A_r})^{-1}\boldsymbol{B_r} + \boldsymbol{D}. \end{aligned} \tag{4.30}$$

Note that in the projected space, the dimensions of the state space matrices are $\boldsymbol{x_r}(t) \in \mathbb{R}^r$, $\boldsymbol{A_r} \in \mathbb{R}^{r\times r}$, $\boldsymbol{B_r} \in \mathbb{R}^{r\times m}$, $\boldsymbol{C_r} \in \mathbb{R}^{p\times r}$, and $\boldsymbol{D} \in \mathbb{R}^{p\times m}$. In other words, while the internal state dimension is reduced from n to r, the number of input and output dimensions are kept the same. Therefore, while $G(s)$ is a $p \times m$ matrix valued rational function of degree-n, $G(s)$ is a $p \times m$ matrix valued rational function of degree-r. There are many approaches to construct the model reduction bases $\boldsymbol{V}$ and $\boldsymbol{W}$; the underlying concept of Petrov-Galerkin projection remains same. The later sections of this chapter discuss various techniques to construct these bases. Before delving into these details, the approach we take to compare reduced models with full order models is first discussed in the next section.

4.5.2 Ellipse fits to detect traveling waves in 2D plates

Although, as previously stated, most of the experiments actuating MFC pair A-B have not resulted in linear traveling waves, there is one frequency at which this pair exhibits traveling waves. The experimental plate response at frequency $635Hz$ is shown in Figure 4.11. While this wave travels along the length of the plate similar to the previously discussed results, it propagates near its long edges and is a combination of waves in both directions. It is easier to visualize this as a traveling wave which is rotating clockwise along the circumference of the plate. As the length of the plate under consideration dominates over its width, this traveling wave appears to be two separate traveling waves progressing in opposite directions. It is quite interesting to note that by changing the location of the forces, at least two different types of traveling waves can exist at a given frequency. This shows the potential to generate multiple traveling waves by changing the

location, the frequency of operation and other parameters such as phase and amplitude.

In our previous research [69, 70, 183, 184], 1D traveling waves were generated in beams by simultaneously exciting two MFCs with a phase difference. The present work extends the prior excitation methodology to plates. So, two sinusoidal voltage signals, with a phase difference of 90°, are applied to two MFCs at a time. Although, four MFCs are bonded to the present structure, only two of these, namely MFC A and D are used to excite the plate. The frequency of excitation is chosen to be a value halfway between the eight and the ninth natural frequency. In experiments, this frequency is $546Hz$ and in simulations, this is $555Hz$.

The time responses of the plate, i.e. the out-of-plane velocities are collected at all 493 points as seen in Figure 4.12 and the root-mean-squared values are plotted as a contour in the Figure 4.13. Based on this figure, we can detect if the resulting wave is a standing or a traveling wave by observing the presence or the absence of strain nodes. Although there are no strain nodes in this figure, the amplitude changes along the longer side of the plate. However, in later sections, it is difficult to compare such details in two contour plots from the full and the reduced models and appraise the reduced model. Thus, a basic and visual detection technique is derived from the 1D Fourier analysis and adapted to the present 2D case. In the 1D beam case, the first step is to compute the FFT of the velocity responses at all points. Then, the complex values of the Fourier transformed signals at the excitation frequency are collected. Then the complex FFT values of these points are plotted in the complex plane. If the resulting curve is a circle, then the beam response is a pure traveling wave as the phase difference between adjacent points along the beam's length is constant and varies from 0° to 180° over a wavelength. However, if they form a straight line, then the response is a pure standing wave as the phase difference between adjacent points along the beam's length is either 0° or 180°. But, if they result in an elliptical curve, then the beam has a mixture of both pure standing and pure traveling waves (as seen in Figure 4.14).

This concept is adapted to the 2D plate case by discretizing the plate into multiple 1D 'beam' sections. Each 1D beam results in one curve. To avoid confusion, only the relevant sections of 7 curves, at equally spaced locations along the width of the plate are plotted in Figure 4.13 and Figure 4.14. In Figure 4.13 the 7 locations where the plate is discretized into 1D beams is also plotted. In the present work, we deal with the plate response at $555Hz$. We frequently refer back to this ellipse and check if the reduced model is able to simulate similar elliptical curves.

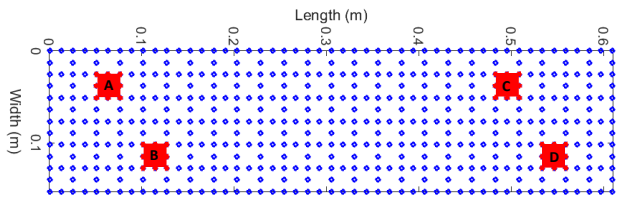

Figure 4.12: FE nodes of the plate and the location of the piezo-patches.

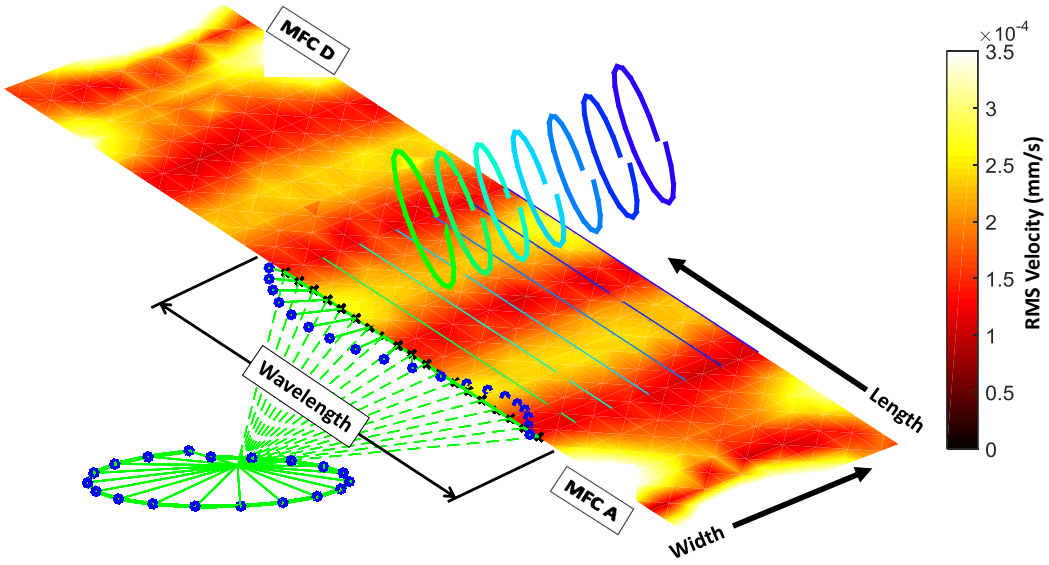

Figure 4.13: Contour plot represents the RMS velocity profile of the plate at $546Hz$ when actuated by two MFCs. Multiple ellipses are generated from the velocity of different points.

4.5.3 Rigid-body modes and instability

The present work attempts to simulate the dynamics of a plate with unconstrained boundary conditions. Such unconstrained model will allow the plate to respond freely to any force in all six degrees-of-freedom as a rigid body [1]. In the modal analysis of unconstrained systems, such flexible movements of the structures appear as rigid-body modes with zero valued resonant frequencies [8]. As these modes have no vibratory deformations that contribute to the dynamic analysis, several studies tend to ignore these rigid body modes. However, in system modeling applications, these modes play an important role in component mode synthesis, as they contain inertia and stiffness characteristics [197–200].

In the present finite-element model, the second-order matrix differential equation has discretized the plate with 493 nodes or 1479 DOF. In the rest of the model reduction sections, the column space spanned by the eigenvectors of this finite-element model are referred to as modal space. This results in 1479 eigenvalues, out of which the first six eigenvalues correspond to the rigid-body modes. The state-space formulation of this model has twice the number of degrees of freedom (i.e 2958 DOF) and twice the number of eigenvalues which appear as complex conjugate pairs. The i^{th} state-space eigenvalue (s_i) of a damped structure is of the form $s_i = -\zeta\omega_i \pm i\omega_i\sqrt{1-\zeta_i^2}$; where ω_i and ζ_i are the i^{th} undamped natural frequency and modal damping coefficient, respectively. In theory, as the undamped natural frequencies of rigid-body modes are of zero value [8], both the real and imaginary parts of the state-space eigenvalues are also of a zero value. Such a system

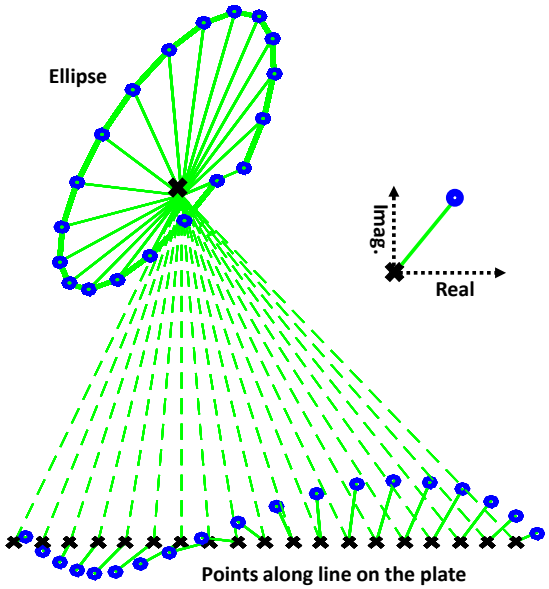

Figure 4.14: A schematic representation of generation of an ellipse from the complex magnitude of the points along a line on the plate.

is critically stable. However, due to numerical issues of ill-conditioned state-space matrices, the eigenvalue problem can result in rigid-body eigenvalues with very small positive real parts resulting in numerically unstable models. To avoid such issues, the 12 rigid-body modes present in the state-space model are first decoupled from the full model and the remaining asymptotically stable part is scaled-down in later sections using model reduction techniques.

We achieve this decoupling by employing the ordered real Schur decomposition algorithm; see, e.g., [201, 202] and the references therein. We briefly mention the details here to make the chapter self-contained. The real Schur decomposition [203] transforms the state matrix $\boldsymbol{A}$ into a quasi upper-triangular matrix $\boldsymbol{T}$ and an orthogonal matrix $\boldsymbol{U}$ such that $\boldsymbol{A} = \boldsymbol{U}\boldsymbol{T}\boldsymbol{U}^{\boldsymbol{T}}$ and $\boldsymbol{U}^{\boldsymbol{T}}\boldsymbol{U} = \boldsymbol{I}$ where the eigenvalues of the state matrix $\boldsymbol{A}$ appear along the diagonal blocks of the Schur matrix $\boldsymbol{T}$. This Schur matrix is then reordered to separate the rigid-body modes. The numerically unstable rigid-body eigenvalues are placed in the lower right diagonal block of the quasi-triangular Schur

matrix $\boldsymbol{T}$. The corresponding state-space transformation to the full-order model is

$$
\begin{aligned}
G(s) := \left[\begin{array}{c|c} \boldsymbol{A}_T & \boldsymbol{B}_T \\ \hline \boldsymbol{C}_T & \boldsymbol{D} \end{array}\right] &= \left[\begin{array}{c|c} \boldsymbol{U}^T\boldsymbol{A}\boldsymbol{U} & \boldsymbol{U}^T\boldsymbol{B} \\ \hline \boldsymbol{C}\boldsymbol{U} & \boldsymbol{D} \end{array}\right], \\
&= \left[\begin{array}{cc|c} \boldsymbol{A}_{T11} & \boldsymbol{A}_{T12} & \boldsymbol{B}_{T11} \\ \boldsymbol{0} & \boldsymbol{A}_{T22} & \boldsymbol{B}_{T21} \\ \hline \boldsymbol{C}_{T11} & \boldsymbol{C}_{T12} & \boldsymbol{D} \end{array}\right],
\end{aligned}
\tag{4.31}
$$

where $\boldsymbol{A}_{T11} \in \mathbb{R}^{n-12\times n-12}$, $\boldsymbol{A}_{T12} \in \mathbb{R}^{n-12\times 12}$, $\boldsymbol{A}_{T22} \in \mathbb{R}^{12\times 12}$ correspond to the stable part, the coupled part and the numerically unstable part, respectively. Another state transformation is required to decouple stable and unstable parts completely. This is achieved by using

$$
\begin{aligned}
\boldsymbol{V} &:= \begin{bmatrix} \boldsymbol{I}_{n-12\times n-12} & \boldsymbol{R}_{n-12\times 12} \\ \boldsymbol{0} & \boldsymbol{I}_{12\times 12} \end{bmatrix}, \\
\boldsymbol{W} &:= \begin{bmatrix} \boldsymbol{I}_{n-12\times n-12} & -\boldsymbol{R}_{n-12\times 12} \\ \boldsymbol{0} & \boldsymbol{I}_{12\times 12} \end{bmatrix},
\end{aligned}
\tag{4.32}
$$

where the matrix $\boldsymbol{I}$ is an identity matix and $\boldsymbol{R}$ is a rectangular matrix that will be selected below to decouple the state space equations. By using these bases transformation matrices, we obtain

$$
\boldsymbol{W}^T\boldsymbol{A}_T\boldsymbol{V} := \begin{bmatrix} \boldsymbol{A}_{T11} & \boldsymbol{A}_{T11}\boldsymbol{R} - \boldsymbol{R}\boldsymbol{A}_{T22} + \boldsymbol{A}_{T12} \\ \boldsymbol{0} & \boldsymbol{A}_{T22} \end{bmatrix}.
$$

Then, the decoupling is completed by choosing the matrix $\boldsymbol{R}$ such that the off-diagonal term is zero. This results in the Sylvester equation [201], $\boldsymbol{A}_{T11}\boldsymbol{R} - \boldsymbol{R}\boldsymbol{A}_{T22} + \boldsymbol{A}_{T12} = 0$ for $\boldsymbol{R}$. These

bases completely separate the full model ($G(s)$) into stable ($G_s(s)$) and the unstable part ($G_u(s)$),

$$
\begin{aligned}
G(s) &:= \left.\begin{array}{c|c} \boldsymbol{W}^T\boldsymbol{U}^T\boldsymbol{A}\boldsymbol{U}\boldsymbol{V} & \boldsymbol{W}^T\boldsymbol{U}^T\boldsymbol{B} \\ \hline \boldsymbol{C}_{T1} & \boldsymbol{D} \end{array}\right., \\
&= \left.\begin{array}{c|c} \boldsymbol{A}_{T11} & \boldsymbol{B}_{T11} \\ \hline \boldsymbol{C}_{T11} & \boldsymbol{D} \end{array}\right. + \left.\begin{array}{c|c} \boldsymbol{A}_{T22} & \boldsymbol{B}_{T21}-\boldsymbol{R}\boldsymbol{B}_{T11} \\ \hline \boldsymbol{C}_{T12}+\boldsymbol{R}\boldsymbol{C}_{T1} & \boldsymbol{D} \end{array}\right., \\
&= \left.\begin{array}{c|c} \boldsymbol{A}_s & \boldsymbol{B}_s \\ \hline \boldsymbol{C}_s & \boldsymbol{D}_s \end{array}\right. + \left.\begin{array}{c|c} \boldsymbol{A}_u & \boldsymbol{B}_u \\ \hline \boldsymbol{C}_u & \boldsymbol{D}_{\boldsymbol{u}} \end{array}\right..
\end{aligned}
\tag{4.33}
$$

$$G(s) = G_s(s) + G_u(s).$$

The dimensions of the state matrices of the stable and unstable components are $A_s \in \mathbb{R}^{2946\times 2946}$ and $A_u \in \mathbb{R}^{12\times 12}$ respectively.

4.5.4 Model validation and error prediction

When we project the full-model ($G_s(s)$) onto a lower dimensional space, we need appropriate error measures to evaluate the performance of the reduced model ($G_r(s)$). It is convenient to define error measures ${}_{rel}\mathcal{H}_2$ and ${}_{rel}\mathcal{H}_\infty$ norms to show how close $G_s(s)$ and $G_r(s)$ are over the entire frequency spectrum [188]:

$$
\begin{aligned}
{}_{rel}\mathcal{H}_2 &= \frac{\|G_s - G_r\|_{\mathcal{H}_2}}{\|G_s\|_{\mathcal{H}_2}}, \\
{}_{rel}\mathcal{H}_\infty &= \frac{\|G_s - G_r\|_{\mathcal{H}_\infty}}{\|G_s\|_{\mathcal{H}_\infty}}.
\end{aligned}
\tag{4.34}
$$

where the $\mathcal{H}_2$ and $\mathcal{H}_\infty$ norms of a stable transfer function $H(s)$ are defined as

$$\|H\|_{\mathcal{H}_2} = \left(\frac{1}{2\pi}\int_{-\infty}^{\infty}\|H(\imath\omega)\|_F^2 d\omega\right)^{1/2}, \tag{4.35}$$

and

$$\|H\|_{\mathcal{H}_\infty} = \sup_{w\in\mathbb{R}}\|H(\imath\omega)\|_2 \tag{4.36}$$

where $\|\boldsymbol{N}\|_F$ and $\|\boldsymbol{N}\|_2$ denote, respectively, the Frobenius norm and 2-norm of the matrix $\boldsymbol{N}$.

In addition, one sometimes is interested in comparing the two models only over a specific frequency range. One can achieve this by using the corresponding weighted-$\mathcal{H}_2$ and weighted-$\mathcal{H}_\infty$ norms. However, these measures still require that both systems be asymptotically stable. In our case, we would like to be able to measure, or at least approximate, the distance of the reduced model from the original model $G(s)$, which theoretically has poles on the imaginary axis. Therefore, we will approximate the distance from $G(s)$ using a sampling approach, leading to two error measures ${}_{rel}\mathcal{E}_F$ and ${}_{rel}\mathcal{E}_2$. These measures compare the input-output mapping between one of the inputs ($\boldsymbol{u_1}$) and the outputs ($\boldsymbol{y}_i$) for the two models. In this study, it is defined as the error between the frequency response functions (FRFs) generated between the out-of-plane plate velocities at all 493 points (y_i) and the input voltage signal supplied to the MFC A (refer to Figure 4.12). This transfer function is similar to the mobility FRF ($\mathcal{Y}_{k1}$) of a point (y_k) on the plate due to the input signal u_1 at a frequency ω_i, which is,

$$\mathcal{Y}_{k1}(\omega_i) = \boldsymbol{C}[(j\omega_i)\boldsymbol{I} - \boldsymbol{A}]^{-1}\boldsymbol{B} + \boldsymbol{D}. \tag{4.37}$$

A transfer function matrix ($\mathcal{Y}_1$) is generated by evaluating the above equation at various frequencies, $\{\omega_1, \ldots, \omega_N\}$, and locations. Define

$$\mathcal{Y}_1(\Omega) = [\, \mathcal{Y}_1(\omega_1),\ \mathcal{Y}_1(\omega_2), \ldots, \mathcal{Y}_1(\omega_N)\,].$$

Then, the approximate error measures ${}_{rel}\mathcal{E}_F$ and ${}_{rel}\mathcal{E}_2$, are calculated by

$${}_{rel}\mathcal{E}_F = \frac{\|\mathcal{Y}_1(\Omega) - \mathcal{Y}_{1,r}(\Omega)\|_F}{\|\mathcal{Y}_1(\Omega)\|_F}, \tag{4.38}$$

and

$${}_{rel}\mathcal{E}_2 = \frac{\max_{\omega_i}\|\mathcal{Y}_1(\omega_i) - \mathcal{Y}_{1,r}(\omega_i)\|_2}{\max_{\omega_i}\|\mathcal{Y}_1(\omega_i)\|_2}. \tag{4.39}$$

Based on these definitions, the approximate distance between the stable model ($G_s(s)$) and the full FE model ($G(s)$) is given in Table 4.2. The error measures ${}_{rel}\mathcal{E}_F$ and ${}_{rel}\mathcal{E}_2$ are estimated at 1000 equally spaced frequency points between $1Hz$ and $3200Hz$. Figure 4.15 shows the mobility Bode plots for different cases: the full model-$G(s)$, the stable model - $G_s(s)$, the antistable model - $G_u(s)$ and $G_s(s) + G_u(s)$. The 'green' curve shows the effect of the rigid-body modes on the dynamics of the plate. As expected, there is only one peak in this bode plot (green) at the rigid-body eigenvalue ($0Hz$). These rigid body modes influence the presence of anti-resonant peaks at lower frequency ranges and also slightly change the magnitude of the resonant peaks.

Additionally, a chirp input signal is used to establish the frequency response functions of the

Table 4.2: Error between the full FE model- $G(s)$ and the stable model- $G_s(s)$.

${}_{rel}\mathcal{E}_F = 2.60 \times 10^{-1}$	${}_{rel}\mathcal{E}_2 = 3.614 \times 10^{-1}$

plate. In the present work, experimental resonance frequencies and operational deflection shapes are generated through chirp excitation. Therefore, we first simulate the plate response to the same excitation and then establish the input-output relationship. The frequency response function of the plate excited with a chirp input is the ratio of the cross-power spectrum (P_{yu}) between the chirp input and the output signal to the auto-power spectrum of the input (P_{uu}) [180], i.e.,

$$H_1(\omega_i) = \frac{P_{yu}(\omega_i)}{P_{uu}(\omega_i)}.$$

The frequency response functions with both the approaches match along most of the frequency range as observed in Figure 4.16. These plots differ at higher frequencies where there is a reduction in the power of the input signal. Out of the 41 eigenvalues of the plate model, between $0Hz$ and $3200Hz$, 40 eigenvalues are the out-of-plane eigenvalues and one is the in-plane eigenvalue. In the present study, as we are only interested in the out-of-plane plate response, we compare the first 40 out-of-plane simulated natural frequencies with the corresponding experimental values. The maximum error between these values is 2.2% at the 39^{th} mode. Further, the operational deflection shapes at these 40 peaks are extracted from the FRFs and are compared with the experimental values using the Modal Assurance Criterion (MAC) [180, 204]. Figure 4.17 displays the MAC values between the stable and the experimental ODSs. The high diagonal values of the MAC matrix represent the similarity in the eigenspace of the experiments and the FE model. The presence of some off-diagonal MAC values is due to the presence of cross-coupling between adjacent ODSs. Usually, to avoid this problem, we extract and compare the mode shapes of the plate instead of ODSs [178, 180]. However, the present study does not consider the comprehensive modal analysis of the plate .

Time domain is another area to test the quality of the state-space model. Specifically, the response of the plate when excited by two inputs is of interest. Although there are four inputs to the original model, two inputs (MFC A and D) are chosen to simultaneously excite the plate to generate traveling waves. Two sinusoidal voltage signals of amplitude $V = 10Volts$ and frequency $f_s = 555Hz$ are applied to these MFCs. There is a 90° phase difference between these voltage

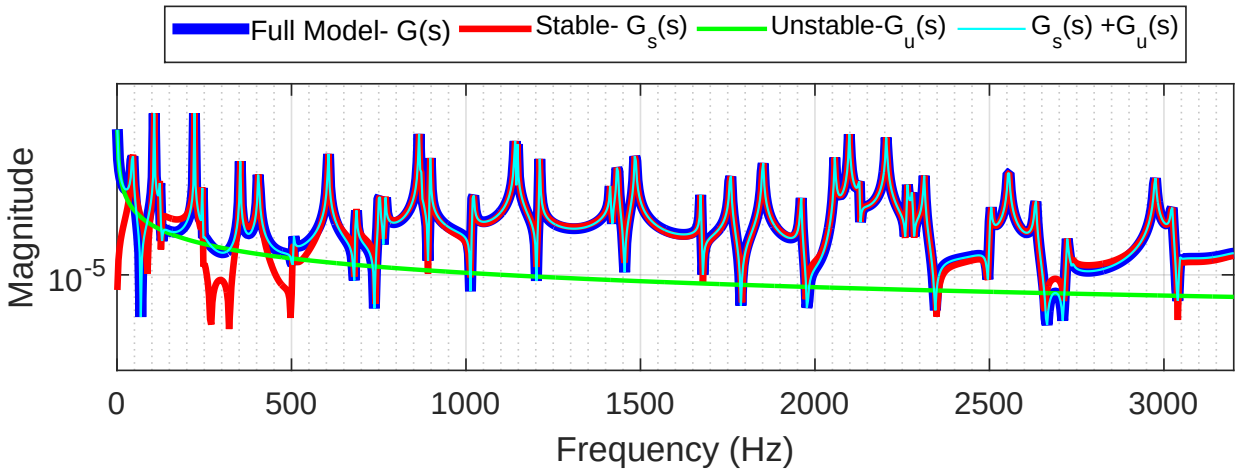

Figure 4.15: Bode plot comparison between the full FE mode, the stable and the unstable parts.

signals. At a time instant t, the plate response ($y_f(t)$) is given by

$$y_f(t) = C_r[i2\pi f_s I - A_r]^{-1} B_r . V e^{j.2\pi f_s . t} \begin{bmatrix} 1 \\ 0 \\ 0 \\ e^{j.\pi/2} \end{bmatrix}. \tag{4.40}$$

The time domain response ($y_f(t)$) is then converted to the frequency domain by applying the Fast Fourier Transform. The complex response of all points on the plate at the excitation frequency are collected and plotted in the complex plane, as shown in Figure 4.18. This results in multiple elliptical curves as previously observed in Figure 4.14 of the section 4.5.2.

In the next few sections, model reduction techniques are applied on the stable part of the full model, i.e., $G_s(s)$. Similar steady-state frequency and time domain analysis are performed to test the reduced models.

4.5.5 Reachability-based model reduction

Reachability quantifies the '*ease*' of reaching a final state $\boldsymbol{X_R}$ from the zero initial state $X_0 = 0$ in finite time T by spending finite energy ($\xi^{reach}_{\boldsymbol{X_R}}$) [205]. States that correspond to small reachability energy are easier to reach. The concept of reachability only depends on the state matrices (A, B). Assuming that the system is completely reachable, the reachability energy can be computed as

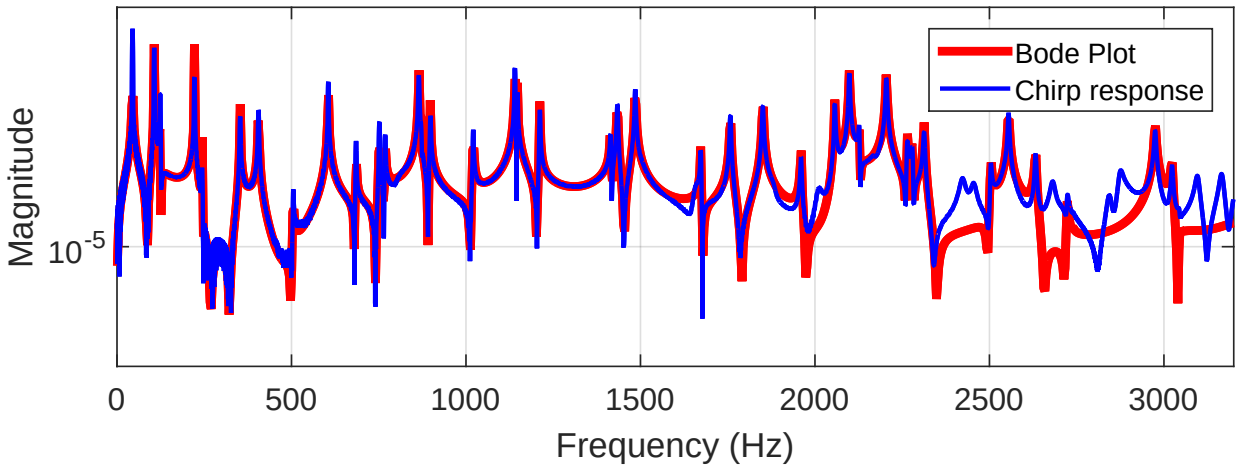

Figure 4.16: Comparison between the bode plot and frequency response of the plate due to chirp voltage input.

[188],

$$\xi_{\boldsymbol{X_R}}^{reach} = \boldsymbol{X_R^T} \mathcal{P}(T)^{-1} \boldsymbol{X_R}, \tag{4.41}$$

where $\mathcal{P}$ is the finite-time reachability gramian and defined as

$$\mathcal{P}(T) = \int_0^T e^{\boldsymbol{A}t} \boldsymbol{B}\boldsymbol{B}^T e^{\boldsymbol{A}^T t} \mathrm{d}t. \tag{4.42}$$

For asymptotically stable dynamical systems, we let $T \to \infty$ in (4.42) to obtain the infinite reachability gramian $\mathcal{P}$, which we will simply call the reachability gramian. One does not evaluate the integral (4.42) to compute $\mathcal{P}$; instead $\mathcal{P}$ is computed by solving the reachability Lyapunov equation

$$\boldsymbol{A}\mathcal{P} + \mathcal{P}\boldsymbol{A}^T + \boldsymbol{B}\boldsymbol{B}^T = 0. \tag{4.43}$$

In a physical sense, a state X_R is easier to reach when the corresponding reachability energy in (4.41) is small. From the definition of the reachability energy, such states are spanned by the left singular vectors of $\mathcal{P}$ corresponding to the largest singular values, as plotted in Figure 4.19 in decreasing order. The hard-to-reach states, on the other hand, correspond to the smallest singular values of $\mathcal{P}$; thus, they can be truncated by choosing $\boldsymbol{V} = \boldsymbol{W}$ in (4.29) as the leading dominant left singular vectors of $\mathcal{P}$. In this plate state space model, there are 493 outputs and four inputs; therefore, the output space is dominant; however the reachability-based reduction approach completely ignores this. This is evident in the reachability energy plot shown in Figure 4.20. The reachability energy of a particular state is calculated by substituting the eigenvector ($\mathcal{V}_i$) of that

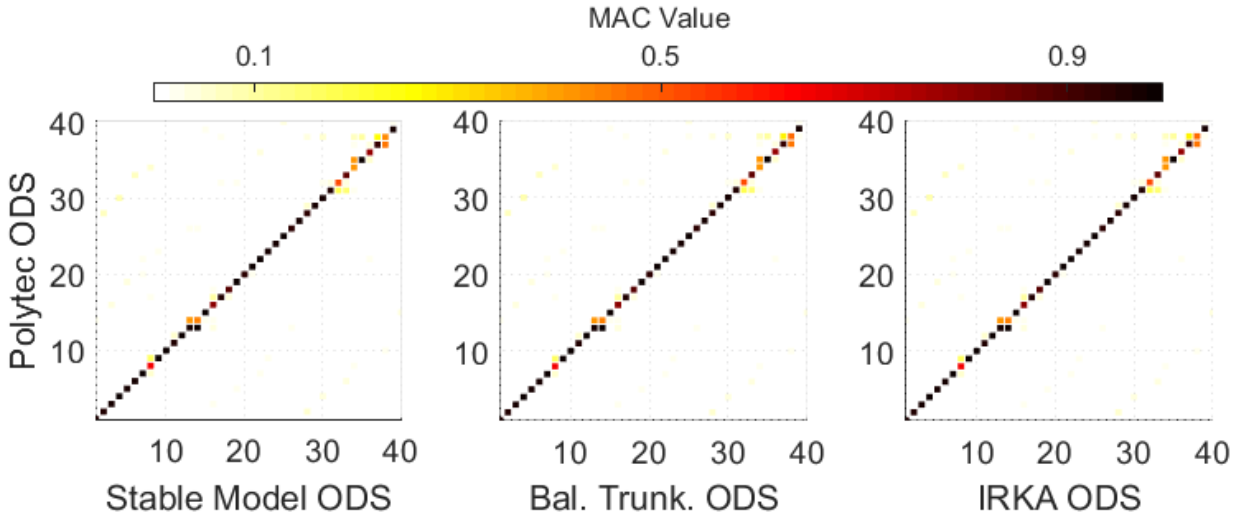

Figure 4.17: Comparison of experimental and simulated operational deflection shapes due to chirp input.

state into $\xi_{\mathcal{V}_i}^{reach} = \mathcal{V}_i^T \mathcal{P}^{-1} \mathcal{V}_i$. The reachability energies of the first 40 out-of-plane eigenvectors are highlighted in this plot. Based on this plot, at least 429 leading singular values are required to span the reduced space with the 40 desired eigenvectors. Although a reduced model of this size has the required eigenvectors spanning its column space, the eigenvalues do not match those of the full model. A much higher order model ($r = 900$) is required for the first 40 eigenvalues to converge to the desired values. Table 4.3 presents the errors corresponding to this reachability-based ROM. As reachability-based truncation of high-energy states resulted in a relatively large state-space model, further analysis in the time domain is not performed. The observability-based model reduction is explored in the next section.

Table 4.3: Error between the stable model- $G_s(s)$ and the reachability based ROM- $G_r(s)$ (r=900).

${}_{rel}\mathcal{H}_2$	1.551×10^{-1}	${}_{rel}\mathcal{H}_\infty$	1.361×10^{-1}
${}_{rel}\mathcal{E}_F$	1.353×10^{-1}	${}_{rel}\mathcal{E}_2$	1.209×10^{-1}

4.5.6 Observability-based model reduction

Observability is the dual-concept of reachability. Here, the observability of an initial state $\boldsymbol{X_O}$ means that it can be distinguished from the zero state by observing the output signal $\boldsymbol{y(t)}$ over a finite time interval in the case of zero input, i.e., $\boldsymbol{u}(t) = 0$. Therefore, only the matrices $\boldsymbol{A}$ and $\boldsymbol{C}$ play a role in the concept of observability. Similar to the case of reachability, here by observing the

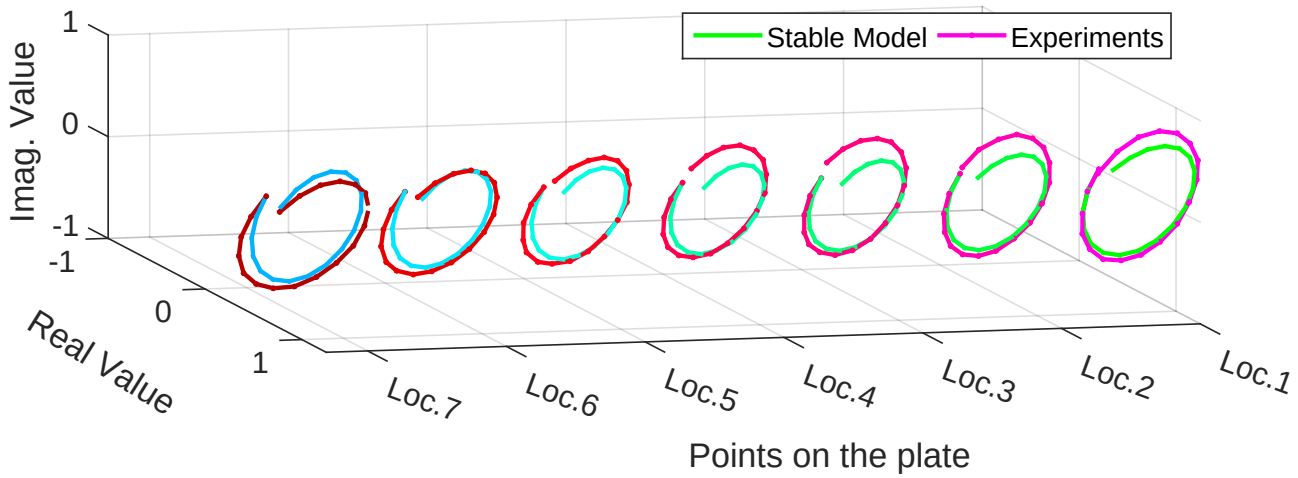

Figure 4.18: Comparison between the ellipse fits generated experimentally and simulations.

energy of the output signal $\boldsymbol{y(t)}$, over a finite time interval T with $\boldsymbol{u}(t) = 0$, we can quantify the '*ease*' of observing an initial state $\boldsymbol{X_O}$. The energy of the output signal is called the observability energy ($\xi^{obs}_{\boldsymbol{X_O}}$) and is given by,

$$\xi^{obs}_{\boldsymbol{X_O}} = \boldsymbol{X_O}^T \mathcal{Q}(T) \boldsymbol{X_O}, \tag{4.44}$$

where the finite-time observability gramian is defined as,

$$\mathcal{Q}(T) = \int_0^T e^{\boldsymbol{A}^T t} \boldsymbol{C}^T \boldsymbol{C} e^{\boldsymbol{A}t} \mathrm{d}t. \tag{4.45}$$

For asymptotically dynamical systems, we let $T \to \infty$ in (4.45) to obtain the infinite observability gramian $\mathcal{Q}$, which we will simply call the observability gramian. As in the reachability case, the observability gramian satisfies the following Lyapunov equation:

$$\boldsymbol{A}^T \mathcal{Q} + \mathcal{Q} \boldsymbol{A} + \boldsymbol{C}^T \boldsymbol{C} = 0. \tag{4.46}$$

In a physical sense, a state is unobservable when its energy is equal to that of the zero state. A state is easier to observe if it leads to higher observability energy. From the definition in (4.44) these are the states spanned by the dominant left singular vectors of $\mathcal{Q}$. Figure 4.19 shows the singular values of $\mathcal{Q}$ in descending order. The hard-to-observe states, i.e., those corresponding to the smallest singular values of $\mathcal{Q}$, can be truncated by choosing $\boldsymbol{V} = \boldsymbol{W}$ in (4.29) as the leading dominant left singular vectors of $\mathcal{Q}$. Figure 4.21 shows the observability energies of all states in the state-space. This figure also highlights the observability energies corresponding to the first 40 out-of-plane eigenvectors, which in-turn gives an estimate of the size of the reduced model with the

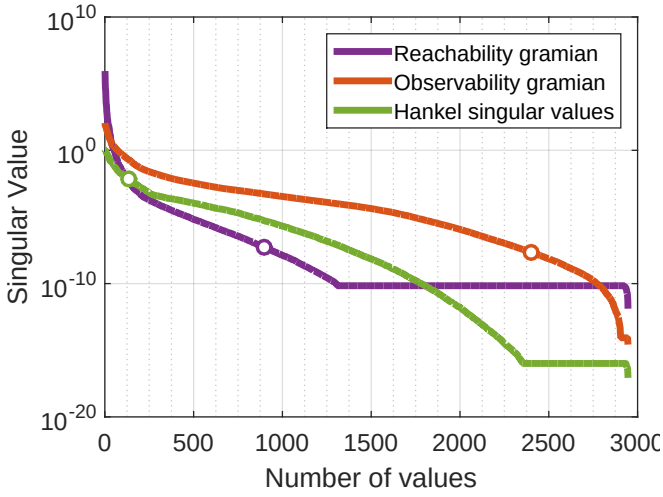

Figure 4.19: Singular values of Reachability and Observability gramians, and Hankel singular values.

required column space. The observability energy of a particular state is calculated by substituting the eigenvector (V_i) into $\xi_{\boldsymbol{V_i}}^{obs} = \boldsymbol{V_i}^T \mathcal{Q}(T) \boldsymbol{V_i}$. Based on this plot, a reduced model needs at least 2400 leading eigenvectors to span its column space; this suggests that there are many eigenvectors in the first 40 modes which are difficult to observe. Hence, observability-based truncation cannot drastically reduce the full system.

However, the concept of reachability and observability depend on the basis of the state space matrices. To put it differently, a change of basis results in the change of reachability and observability energies and, thus different model reduction bases. The following section discusses the choice of one such basis called the 'balanced' basis.

Table 4.4: Error between the stable model- $G_s(s)$ and the observability based ROM- $G_r(s)$ (r=2300).

${}_{rel}\mathcal{H}_2$	1.5633×10^{-1}	${}_{rel}\mathcal{H}_\infty$	3.1171×10^{-1}
${}_{rel}\mathcal{E}_F$	1.4735×10^{-1}	${}_{rel}\mathcal{E}_2$	1.2113×10^{-1}

4.5.7 Balanced truncation

In the reachability and the observability based reduction approaches, the states which are easy-to-reach need not match the states which are easy-to-observe. Balanced truncation ([205, 206]) resolves this issue: It transforms the states into a new basis, called the balanced basis, so that in this

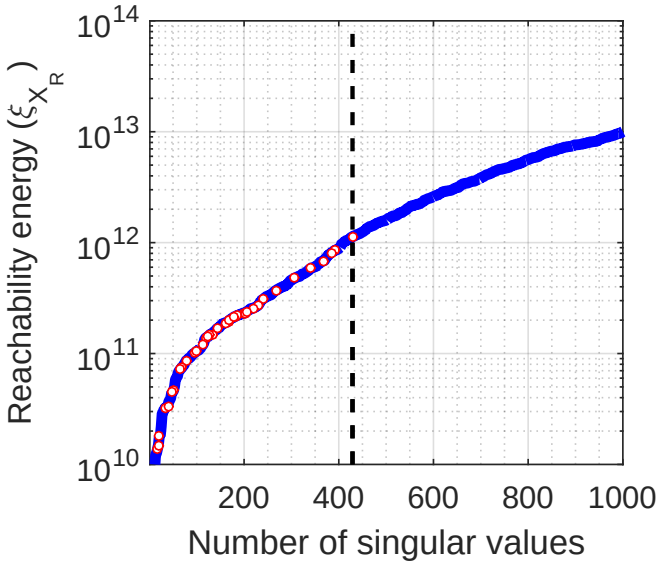

Figure 4.20: Ranking of the reachability energy of the first 40 states among the whole spectrum.

new basis the new gramians are equal, and thus the states which are easy-to-reach are also easy-to-observe . Let $\mathcal{P} = \mathcal{U}\mathcal{U}^{\mathcal{T}}$ be the Cholesky decomposition of $\mathcal{P}$. Moreover, let $\mathcal{U}^T\mathcal{Q}\mathcal{U} = \mathcal{K}\Sigma^2\mathcal{K}^T$ be the eigen decomposition of $\mathcal{U}^{\mathcal{T}}\mathcal{Q}\mathcal{U}$. Then the transformation that 'balances' the gramians is given by $\mathcal{T} = \Sigma^{1/2}\mathcal{K}^T\mathcal{U}^{-1}$. The diagonal elements of the diagonal matrix Σ, which are also equal to the square root of the eigenvalues of $\mathcal{P}\mathcal{Q}$, are called the Hankel singular values of the system $G_s(s)$. These singular values are input-output invariants i.e. they do not change with changing the basis. This transformation results in new reachability and observability gramians $\tilde{\mathcal{P}}$ and $\tilde{\mathcal{Q}}$ which are diagonal and satisfy $\tilde{\mathcal{P}} = \tilde{\mathcal{Q}} = \Sigma$. The corresponding observability and reachability energies for the transformed state ($\tilde{\boldsymbol{x}}$) can be computed using $\xi_{\tilde{\boldsymbol{x}}}^{reach} = \tilde{\boldsymbol{x}}^T\Sigma^{-1}\tilde{x}$ and $\xi_{\tilde{\boldsymbol{x}}}^{obs} = \tilde{\boldsymbol{x}}^T\Sigma\tilde{x}$.

We would like to emphasize that in practice one computes balanced truncation in a numerically robust way using the square-root balancing approach. Let $\mathcal{P} = \mathcal{U}\mathcal{U}^T$ and $\mathcal{Q} = \mathcal{L}\mathcal{L}^T$ be factorizations of $\mathcal{P}$ and $\mathcal{Q}$, respectively. In practice, one never computes the full $\mathcal{P}$ and $\mathcal{Q}$ matrices; instead $\mathcal{U}$ and $\mathcal{L}$ are computed directly without forming $\mathcal{P}$ and $\mathcal{Q}$, see, e.g., [207, 208]. Compute the singular value decomposition of $\mathcal{U}^T\mathcal{L} = \mathcal{Z}\Sigma\mathcal{Y}^T$ where $\Sigma = \mathrm{diag}(\sigma_1, \sigma_2, \ldots, \sigma_n)$. The $\{\sigma_i\}$ are the Hankel singular values. Assume that $\sigma_r > \sigma_{r+1}$. Then, the degree-r reduced model by balanced truncation is computed by a Petrov-Galerkin projection as in (4.29) with

$$\boldsymbol{V} = \mathcal{U}\mathcal{Z}_r\Sigma_r^{-1/2} \quad \text{and} \quad \boldsymbol{W} = \mathcal{L}\mathcal{Y}_r\Sigma_r^{-1/2}, \tag{4.47}$$

where $\mathcal{Z}_r$ and $\mathcal{Y}_r$ denote the leading r columns of $\mathcal{Z}$, and $\mathcal{Y}$, respectively, and $\Sigma_r = \mathrm{diag}(\sigma_1, \sigma_2, \ldots, \sigma_r)$. The reduced model $G_r(s)$ of $G_s(s)$ due to balanced truncation is asymptotically stable and the error

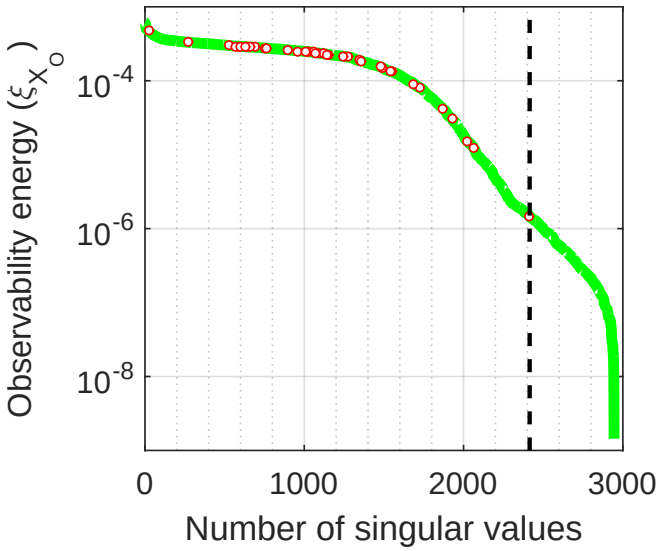

Figure 4.21: Ranking of the observability energy of the first 40 states among the whole spectrum.

satisfies $\|G_s - G_r\|_{\mathcal{H}_\infty} \leq 2(\sigma_{r+1} + \cdots + \sigma_n)$.

The balancing transformation also projects the eigenvectors into the balanced basis. First we compute the corresponding reachability and observability energies in this new basis and plot them in Figure 4.22. Earlier, in the reachability and observability sections, the energies of the first 40 eigenvectors spanned a wide range of values which resulted in a large size of the reduced model. However, when the state-space is balanced, states which are easy-to-reach are also easy-to-observe. This is evident from the change in rank of the reachability and observability energies of the desired 40 eigen solutions in the unbalanced basis, (Figure 4.20 and Figure 4.21) to the balanced basis (Figure 4.22). All in all, a balanced and reduced model of order 132 has the same column space as that of a full model, in the frequency range of interest. This is a 95.5% reduction in size.

Figure 4.24 plots the relative error in eigenvalues of this reduced model to that of the full model. As expected, the relative error increases with frequency. Similarly, the eigenvectors of the reduced model are compared with the experimental values in Figure 4.17 and the trend of MAC values of the balanced model is similar to that of the full model.

In a similar fashion, the balanced truncation approach can reduce the full model if the first 10, 20 or 30 eigen solutions are more significant than the rest of the frequency spectrum. Observability and reachability energies in the balanced space are useful to estimate the minimum sizes of the balanced ROMs. Table 4.5 presents the sizes of these ROMs and useful frequency ranges for these scenarios. Additionally, the error measures, ${}_{rel}\mathcal{H}_2$ and ${}_{rel}\mathcal{H}_\infty$ errors, decrease with the increase in the size of the ROM. This is expected as these error indicators consider the total frequency spectrum. In contrast, the ${}_{rel}\mathcal{E}_F$ and ${}_{rel}\mathcal{E}_2$ errors, which are defined over their specific frequency

ranges and for one of the four inputs, do not have any specific trend.

It is also interesting to note that in the case of 10 eigensolutions, the size of the ROM is 20. This reduced model has 10 pairs of complex conjugate eigenvectors, all of which are part of the desired modal space (or eigenspace). In contrast, all other balanced ROMs have eigenspaces which are larger than the corresponding desired modal space. This shows that there are some eigensolutions, which are out of the desired frequency range, which have higher total 'energy' than those eigensolutions within the desired frequency range. The influence of the out-of-range eigensolutions in the frequency range of interest is shown in the Figure 4.23. Although the out-of-range eigensolutions have higher Hankel singular values than some in-range eigensolutions, the effect of all these states is not the same in the frequency range of interest. For instance, an out-of-range state with an eigenvalue of $4969Hz$ has a Hankel singular value of 2.04×10^{-2} might be less influential than a much closer state of $3777Hz$ with a Hankel singular value of 1.95×10^{-2}. Therefore, a frequency weighted version of balanced truncation (see, e.g., [188, 209, 210] and the references therein) has a potential to achieve a ROM with lower size. However, in this chapter we focus on the global error measures. The frequency limited implementations are to be further investigated.

The steady state frequency responses of the balanced ROM and the full model are compared previously. Now, the steady state time responses of the full model and balanced ROM ($r = 132$) are compared. The plate is excited by two of the four inputs with a phase difference of 90°. As explained earlier, we generate and then compare the elliptical curves for both the full model and the reduced model. The curves in Figure 4.25 show the ability of these models to generate 2D traveling waves in the plate. The two elliptical curves lie on each other. This shows that the reduction of the full model preserved the amplitude and the phase properties of all the points on the plate. A quantitative comparison of the quality of the traveling waves requires a full-fledged indicator, similar to the cost-function in 1D waves [184].

To summarize, the frequency and the time domain responses of the ROM are simulated and compared to the full scale model. Nevertheless, the analysis so far does not include the rigid-body modes of the original system. As stated earlier, the rigid-body dynamics are important in many applications. Therefore, it is important to contain these dynamics in the reduced model. Recall that we only have 12 modes corresponding to the rigid-body dynamics. The Hankel singular values of the unstable part are the square root of the eigenvalues of $\mathcal{P}_u\mathcal{Q}_u$. These values are also ranked along with the Hankel singular values of the stable part, and the hybrid reduced model is computed. However, theoretically, all rigid-body eigenvalues have a zero value. But due to numerical issues, the real part of some of these eigenvalues tend to be positive, some negative and others zero. In such cases, it is not possible to directly compute gramians for the unstable part. We also have a similar situation where some of the real parts are positive and others are negative. Thus, it is not straight forward to apply reduction techniques to the unstable part. To make sure that the rigid-

body dynamics are matched, we have simply attached the 12-dimensional dynamics of the rigid body modes to the reduced matrices. The new set of reduced state space matrices is the given by,

$$
\begin{aligned}
G_d(s) &= G_r(s) + G_u(s), \\
&= \left[\begin{array}{cc|c} \boldsymbol{A}_r & \boldsymbol{0} & \boldsymbol{B}_r \\ \boldsymbol{0} & \boldsymbol{A}_u & \boldsymbol{B}_u \\ \hline \boldsymbol{C}_r & \boldsymbol{C}_u & \boldsymbol{D} \end{array}\right] = \left[\begin{array}{c|c} \boldsymbol{A}_d & \boldsymbol{B}_d \\ \hline \boldsymbol{C}_d & \boldsymbol{D} \end{array}\right].
\end{aligned} \tag{4.48}
$$

where $G_d(s)$ is the reduced state space equations with the rigid body modes and $\boldsymbol{A}_d \in \mathbb{R}^{144\times144}$, $\boldsymbol{B}_d \in \mathbb{R}^{144\times4}$ and $\boldsymbol{C}_d \in \mathbb{R}^{493\times144}$. The relative errors ${}_{rel}\mathcal{E}_F$ and ${}_{rel}\mathcal{E}_2$ between the full model $G(s)$ and the reduced model ($G_d(s)$) based on balanced truncation are

$$
{}_{rel}\mathcal{E}_F = 9.3646 \times 10^{-4} \text{ and } {}_{rel}\mathcal{E}_2 = 6.0461 \times 10^{-4};
$$

once again clearly illustrating the accuracy of the reduced model.

Even though the balanced truncation technique is able to simulate the transient and steady-state response of the full-plate model, for large-scale models, computing the exact gramians $\mathcal{P}$ and $\mathcal{Q}$ is a computationally challenging task. For effective iterative approximate solutions of Lyapunov equations in large-scale settings, see, e.g., [211–217], and the references therein. Next we discuss an interpolation-based model reduction technique which does not require solving large-scale Lyapunov equations.

Table 4.5: Error between the stable model- $G_s(s)$ and the balanced truncation based ROM- $G_r(s)$.

Number of eigenvalues	Freq. range	Size of ROM	**Balanced Truncation**			
			${}_{rel}\mathcal{H}_2$	${}_{rel}\mathcal{H}_\infty$	${}_{rel}\mathcal{E}_F$	${}_{rel}\mathcal{E}_2$
10	$\leq 700Hz$	20	2.4706×10^{-1}	5.7055×10^{-1}	6.7014×10^{-3}	1.0157×10^{-3}
20	$\leq 1450Hz$	60	2.0979×10^{-1}	1.8366×10^{-2}	9.7321×10^{-4}	8.6831×10^{-5}
30	$\leq 2350Hz$	102	1.6186×10^{-1}	1.1487×10^{-2}	2.3231×10^{-2}	1.9096×10^{-2}
40	$\leq 3200Hz$	132	1.1968×10^{-1}	5.9955×10^{-3}	9.6981×10^{-4}	6.0461×10^{-4}

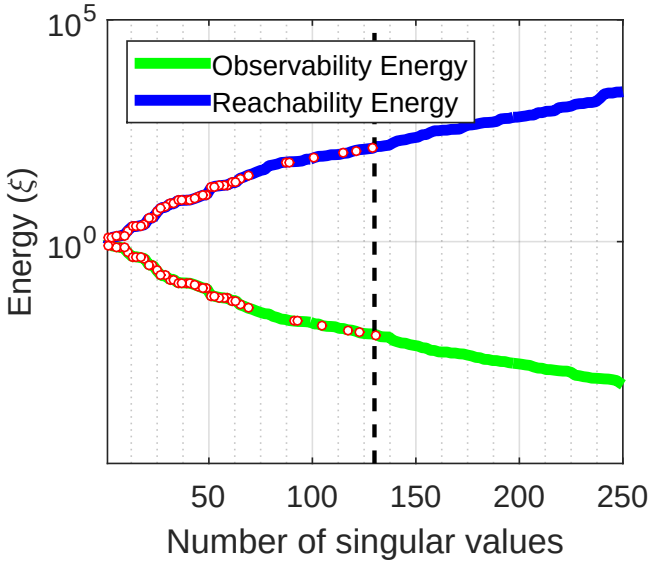

Figure 4.22: Ranking of the reachability and observability energies of the first 40 states on a balanced basis.

4.5.8 Iterative Rational Krylov Algorithm (IRKA)

The Iterative Rational Krylov Algorithm [218] is an interpolation based model reduction technique which yields a reduced model $G_r(s)$ that minimizes the $\mathcal{H}_2$ model reduction error, i.e. $\|G_s - G_r\|_{\mathcal{H}_2}$, at least locally.

Interpolatory model reduction constructs a reduced model whose transfer function interpolates that of the full-model at selected directions in the complex domain. Assume that one has chosen the r interpolation points $\{s_i\}_{k=1}^r \in \mathbb{C}$, the r right-tangential directions $\{\tilde{\boldsymbol{b}}_k\}_{k=1}^r \in \mathbb{C}^m$ and the r left-tangential directions $\{\tilde{\boldsymbol{c}}_k\}_{k=1}^r \in \mathbb{C}^p$. Then, the goal is to construct a reduced-model $G_r(s)$ that tangentially interpolates $G(s)$ at these selected points along the selected directions, i.e, the goal is to satisfy, for $k = 1, 2, \ldots, r$,

$$\begin{aligned} G(s_k)\tilde{\boldsymbol{b}}_k &= G_r(s_k)\tilde{\boldsymbol{b}}_k, \\ \tilde{\boldsymbol{c}}_k^T G(s_k) &= \tilde{\boldsymbol{c}}_k^T G_r(s_k), \\ \tilde{\boldsymbol{c}}_k^T G'(s_k)\tilde{\boldsymbol{b}}_k &= \tilde{\boldsymbol{c}}_k^T G_r'(s_k)\tilde{\boldsymbol{b}}_k, \end{aligned} \tag{4.49}$$

where $G'(s)$ is the derivative of $G(s)$. Then the question is, how to construct the model reduction bases $\boldsymbol{V}$ and $\boldsymbol{W}$ so that the interpolation conditions (4.49) are met. To achieve this, one simply

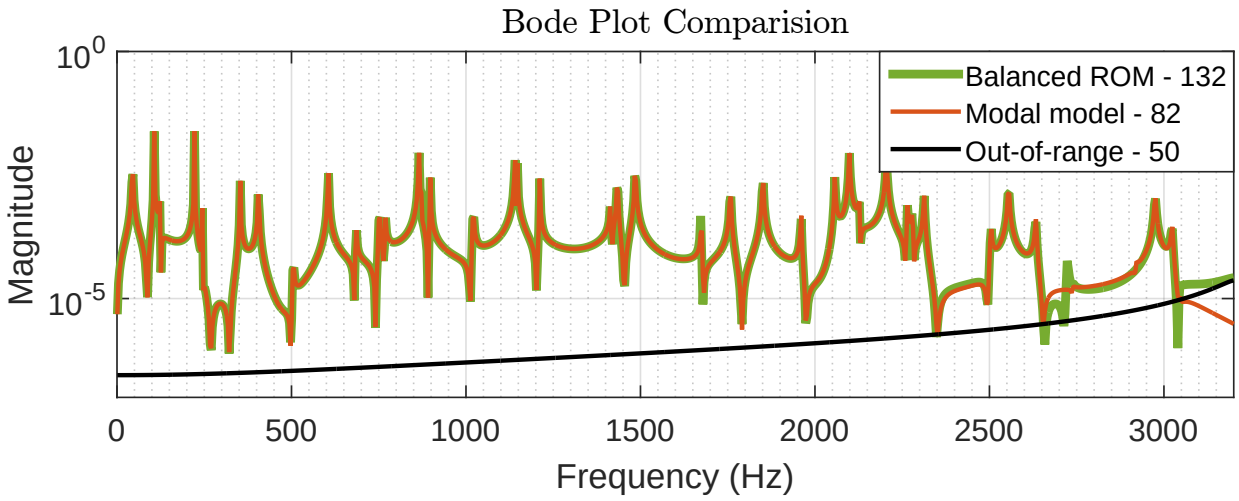

Figure 4.23: Effect of in-range and out-of-range eigen-solutions in a ROM of size 132 in the frequency range up to $3200Hz$.

constructs $\boldsymbol{V}$ and $\boldsymbol{W}$ as

$$\begin{aligned} \boldsymbol{V_r} &= [(s_1\boldsymbol{I}-\boldsymbol{A}_s)^{-1}\boldsymbol{B}\tilde{\boldsymbol{b}}_1 \cdots (s_r\boldsymbol{I}-\boldsymbol{A}_s)^{-1}\boldsymbol{B}\tilde{\boldsymbol{b}}_r], \\ \boldsymbol{W_r} &= [(s_1\boldsymbol{I}-\boldsymbol{A}_s)^{-T}\boldsymbol{C}^T\tilde{\boldsymbol{c}}_1 \cdots (s_r\boldsymbol{I}-\boldsymbol{A}_s)^{-T}\boldsymbol{C}^T\tilde{\boldsymbol{c}}_r]. \end{aligned} \tag{4.50}$$

Then, the reduced model obtained by projection as (4.29) satisfies the interpolation conditions (4.49). Here we focus only on the Hermite interpolation as this is what optimality requires. The results can be easily extended to higher-order derivatives if needed. For details, we refer the reader to [195, 219].

Even though this construction tells how to achieve interpolation, it does not reveal anything about how to choose the interpolation points (optimally). This questions can, fortunately, be answered in the case of the $\mathcal{H}_2$ norm. To be able to answer this questions, we write the reduced-model $G_r(s)$ in the pole-residue form:

$$G_r(s) = \boldsymbol{C}_r(s\boldsymbol{I}-\boldsymbol{A}_r)^{-1}\boldsymbol{B}_r = \sum_{j=1}^{n} \frac{\hat{\boldsymbol{c}}_j\hat{\boldsymbol{b}}_j^T}{s-\hat{\lambda}_j}, \tag{4.51}$$

where $\hat{\lambda}_j$ are the eigenvalues of $\boldsymbol{A_r}$, and $\hat{\boldsymbol{b}} \in \mathbb{C}^m$ and $\hat{\boldsymbol{c}} \in \mathbb{C}^p$ are called, respectively, the right and left residue directions, and $\Phi_j = \hat{\boldsymbol{c}}_j\hat{\boldsymbol{b}}_j^T$ is the residue of $G_r(s)$ at the pole $\hat{\lambda}_i$. Here, for simplicity, we assume that the reduced poles are distinct. Then, if $G_r(s)$ is an $\mathcal{H}_2$-optimal approximation to

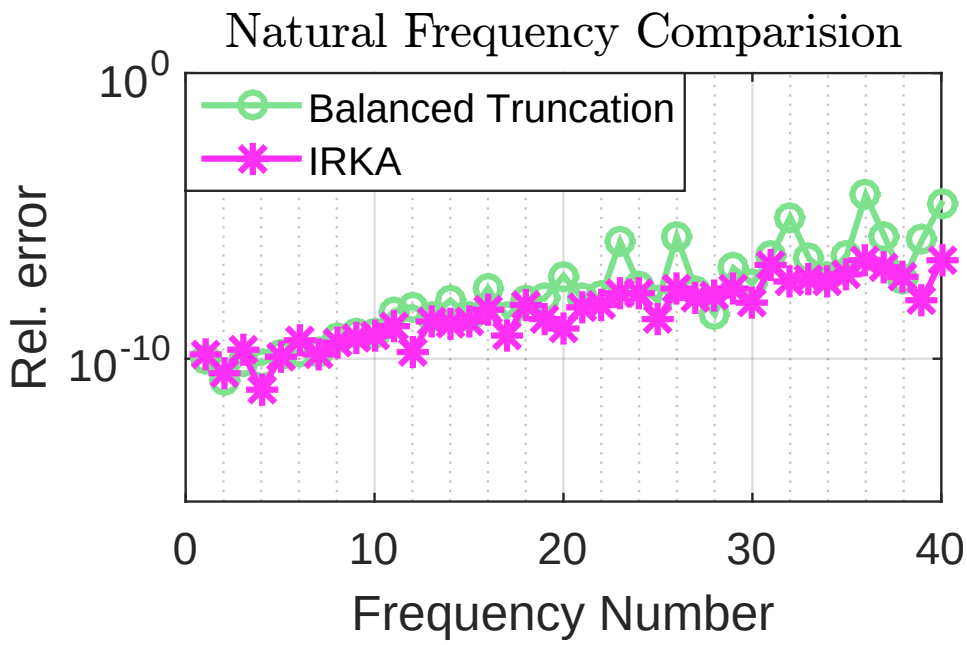

Figure 4.24: Relative errors in eigenvalues models reduced through Balanced truncation and IRKA against the stable model.

$G(s)$, then it satisfies the following interpolatory first-order necessary conditions:

$$\begin{aligned} G(-\hat{\lambda}_j)\hat{\boldsymbol{b}}_k &= G_r(-\hat{\lambda}_j)\hat{\boldsymbol{b}}_k, \\ \hat{\boldsymbol{c}}_k^T G(-\hat{\lambda}_j) &= \hat{\boldsymbol{c}}_k^T G_r(-\hat{\lambda}_j), \\ \hat{\boldsymbol{c}}_k^T G'(-\hat{\lambda}_j)\hat{\boldsymbol{b}}_k &= \hat{\boldsymbol{c}}_k^T G_r'(-\hat{\lambda}_j)\hat{\boldsymbol{b}}_k. \end{aligned} \tag{4.52}$$

In other words, the $\mathcal{H}_2$-optimal approximation $G_r(s)$ to $G(s)$ is a tangential Hermite interpolant to $G(s)$, where the optimal interpolation points are the mirror images of the poles of $G_r(s)$ and the optimal tangential directions are determined by its corresponding residues. This result is the link between $\mathcal{H}_2$-optimal model reduction and interpolation. For the single-input single-output dynamical systems, these are called the Meier-Luenberger conditions; see [220]. For the general case of multi-input/multi-output systems that we consider here, we refer the reader to [195, 218, 221–223] and the references therein.

The optimality conditions (4.52) reveal that the optimal interpolation points and tangential directions depend on the reduced model $G_r(s)$ to be constructed and thus cannot be computed a priori. Thus, an iterative scheme is needed to satisfy these conditions. This is exactly what the Iterative Rational Krylov Algorithm (IRKA) of [218] achieves. To start IRKA, the interpolation points $\{s_j\}_{j=1}^r$, and the tangential directions $\{\tilde{\boldsymbol{b}}_j\}_{j=1}^r$ and $\{\tilde{\boldsymbol{c}}_j\}_{j=1}^r$ are assigned initial values. Then, the model reduction bases $\boldsymbol{V}$ and $\boldsymbol{W}$ are constructed as in (Eq. 4.50) and the intermediate reduced model, and thus the reduced state-spaces matrices are generated via $\boldsymbol{A}_r = \boldsymbol{W}^T\boldsymbol{A}\boldsymbol{V}, \boldsymbol{B}_r = \boldsymbol{W}^T\boldsymbol{B}_s$

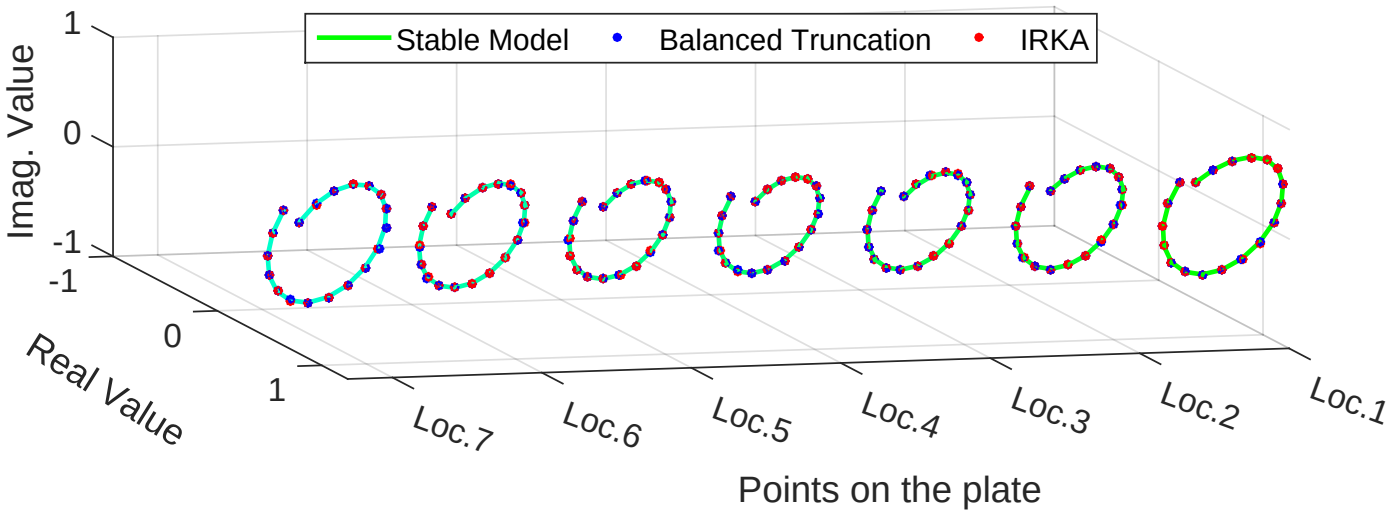

Figure 4.25: Comparison between the ellipse fits generated through full stable model and models reduced through Balanced truncation and IRKA.

and $\boldsymbol{C}_r = \boldsymbol{C}_s \boldsymbol{V}$. A pole-residue decomposition of this intermediate reduced model $G_r(s)$ as in (4.51) is computed. Note that this computation is trivial since $G_r(s)$ has only degree-r. Then, using the pole-residue expansion of $G_r(s)$, the interpolation points and tangential directions are updated based on the optimality conditions as $s_j \leftarrow -\hat{\lambda}_j$, $\tilde{\boldsymbol{b}}_j \leftarrow \hat{\boldsymbol{b}}_j$, and $\tilde{\boldsymbol{c}}_j \leftarrow \hat{\boldsymbol{c}}_j$, for $j = 1, \ldots, r$. The procedure is repeated until convergence. Upon convergence, the reduced model $G_r(s)$ satisfies the optimal interpolation conditions (4.52) for $\mathcal{H}_2$ optimal model reduction. For details regarding the implementation details of IRKA, including convergence speed, initialization, stopping criterion, we refer the reader to the original resource [218].

Similar to the balanced truncation approach, ROMs of multiple sizes are developed and compared. The error measures comparing the full model with the IRKA based ROMs are tabulated in Table 4.6. Compared to the balanced truncation error measures, ${}_{rel}\mathcal{H}_2$ are slightly lower in IRKA models. This reduction is expected as the IRKA algorithm optimizes the $\mathcal{H}_2$ error locally. The ranges of the other error measures are of the same order of magnitude as that of the balanced-truncation.

The errors in the eigenvalues are plotted in Figure 4.24. This figure also displays the results of the balanced truncation based ROM of the same order. In general, both balanced truncation based ROM and IRKA based ROM accurately predict the eigenvalues of the plate model. Furthermore, the IRKA based ROM has slightly less error than the balanced truncation based ROM. The ODSs of the ROM are compared with the experimental ones and are plotted in Figure 4.17. All three MAC plots displayed in this figure have similar pattens. Similarly, the IRKA based ROM is able to generate traveling waves; as suggested by the elliptical curves are plotted in Figure 4.25. These re-

sults show that both the balanced truncation based ROM and IRKA based ROM accurately capture the dynamics of the original stable part of the plate model. The elliptical curves in Figure 4.25 and the bode plots in Figure 4.26 convey the agreement of these ROMs with the full model in steady state time and frequency domains respectively. As we did earlier for balanced truncation, we attach the 12-dimensional rigid-body dynamics to the IRKA-based ROM and compute the approximate relative distance from the model $G(s)$. The resulting model is of size 144 and have the relative error measures

$$_{rel}\mathcal{E}_F = 7.5838 \times 10^{-4} \text{ and } _{rel}\mathcal{E}_2 = 9.8106 \times 10^{-5};$$

illustrating a high-fidelity reduced model as in the balanced truncation case.

Table 4.6: Error between the stable model- $G_s(s)$ and the IRKA based ROM- $G_r(s)$ after 20 iterations.

Number of eigenvalues	Freq. range	Size of ROM	**IRKA**			
			$_{rel}\mathcal{H}_2$	$_{rel}\mathcal{H}_\infty$	$_{rel}\mathcal{E}_F$	$_{rel}\mathcal{E}_2$
10	$\leq 700Hz$	20	5.7055×10^{-1}	2.4706×10^{-1}	6.6954×10^{-3}	1.0157×10^{-3}
20	$\leq 1450Hz$	60	2.0711×10^{-1}	1.8377×10^{-2}	9.1982×10^{-4}	8.3455×10^{-5}
30	$\leq 2350Hz$	102	1.5946×10^{-1}	1.1608×10^{-2}	2.3227×10^{-2}	1.9098×10^{-2}
40	$\leq 3200Hz$	132	1.1765×10^{-1}	6.0133×10^{-3}	7.8539×10^{-4}	9.8106×10^{-5}

Table 4.7: Error of IRKA based ROMs of size 132, initiated by different approaches and after 50 iterations.

Freq. range	Errors	Reachability	Observability	Balanced truncation	Eigenvectors
$\leq 3200Hz$	$_{rel}\mathcal{E}_F$	6.4491×10^{-3}	2.1722×10^{-2}	7.8539×10^{-4}	8.6683×10^{-4}
$\leq 3200Hz$	$_{rel}\mathcal{E}_2$	4.3910×10^{-4}	1.3905×10^{-2}	$9.8106e \times 10^{-5}$	7.7280×10^{-5}

The IRKA based ROM developed so far was initialized by the ROM developed through balanced truncation. But, this is not practical as IRKA is developed to be an alternative to the need for solving large-scale Lyapunov equations. IRKA can be initialized effectively and cheaply in many ways using only a restricted amount of information on the full model. Moreover, as shown via numerous examples, IRKA is not very sensitive to the initialization unless a very poor initialization is made. Once again, we refer to the original resources [195, 218] for details. One can initialize IRKA using ROMs based on other approaches, a coarser FE mesh or even some subset of the

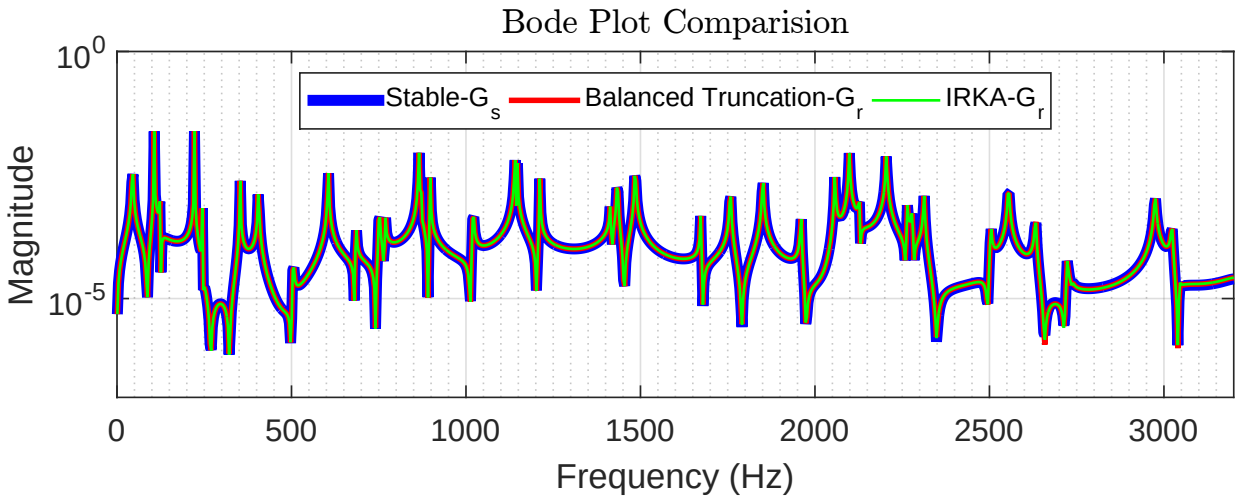

Figure 4.26: Comparison of FRFs generated by the full stable model (size:4946), Balanced truncation based ROM (size:132) and IRKA based ROM (size:132).

eigenvalues of the full model. Even though, these different initializations might not result in the same final ROM or might not converge after the same number of iterations, the experience shows that the resulting ROMs mostly have the same level of accuracy [218]. To further study the effect of these initializations for the FE plate model under investigation, four initial ROMs of size 132 are chosen. Three of the four ROMs are based on the previously discussed concepts of reachability, observability and balanced truncation. The fourth ROM is based on the first 132 eigenvectors of the full model. All the models are iterated 50 times and the iterative errors are plotted in Figure 4.27. As IRKA iterations proceeds, each of these initializations results in a different ROMs. Among all these initial interpolation points and directions, the balanced truncation based ROM has plateaued after just 12 iterations, followed by the observability and the eigenvectors based ROM. However, the reachability based ROM did not converge after 50 iterations. This is expected since the reachability-based ROM is a rather poor ROM making it a poor initialization. The errors of the models after 50 iterations are presented in Table 4.7 and the corresponding FRFs are shown in Figure 4.28. From these results it can be inferred that irrespective of the type of initialization, the error measures in the frequency range of interest are in the same order of magnitude, confirming the general behavior of IRKA observed in the literature. It is important to mention that, that while the reachability based ROM has less than 50% of the desired eigen solutions, the observability based ROM has just one desired eigen solution (Figure 4.20 and Figure 4.21). Despite this, all the IRKA based ROMs have accurately captured the required dynamics. In conclusion, IRKA based model reduction is able to successfully scale-down the full-scale FE plate model.

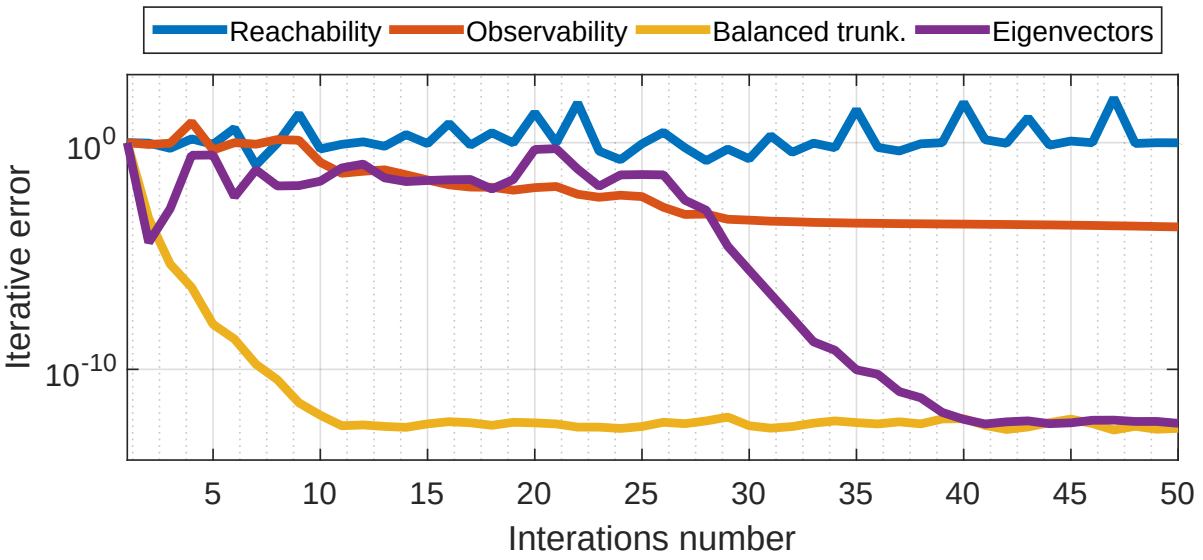

Figure 4.27: Change in iterative error over iterations of differently initialized IRKA plots of size 132.

4.6 Part V: Combination of 2D plate modes

In this section, the 2D traveling waves of the plate are expressed as a combination of 2D mode shapes of the plates. Based on the generalized theory of traveling waves, traveling waves are simulated as a combination of the 2D plate modes. The governing equation that simulates the response of a plate is given in Eq.2.51,

$$w(x,y,t) = \tilde{C}_A\tilde{W}_1 + \tilde{C}_B\tilde{W}_2 + \tilde{C}_C\tilde{W}_3 + \tilde{C}_D\tilde{W}_4. \tag{4.53}$$

This equation is a summation of multiple 2D wave forms $\tilde{W}_i(x,y)$ which are of the form,

$$\tilde{W}_1 = \frac{1}{2\sqrt{2}}\left(\Phi_a(x,y)cos\left(\omega_f t - \frac{\pi}{4}\right) + \Phi_b(x,y)cos\left(\omega_f t + \frac{\pi}{4}\right)\right). \tag{4.54}$$

This assumption is validated at three different frequencies of excitation $546Hz$, $635Hz$ and $708Hz$. In each of these case, the location of excitation is chosen to be either the pair A and B or the pair A and C. Consider the scenario where the frequency of excitation is $635Hz$. This frequency is half-way between the 9^{th} and 10^{th} resonant frequencies of the plate and the corresponding mode-shapes are plotted in Figure 4.29. This figure clearly shows the locations of the mode shapes which are in-phase with each other and locations that are out-of-phase which each other. Assuming that the piezo-ceramics are bonded to the plate at all four corners, the symmetry of the excitation is assumed throughout this section. Experimental results and FE results are based on the case where the piezo-ceramics are slightly asymmetric as seen in Figure 4.1. However, the mode combination

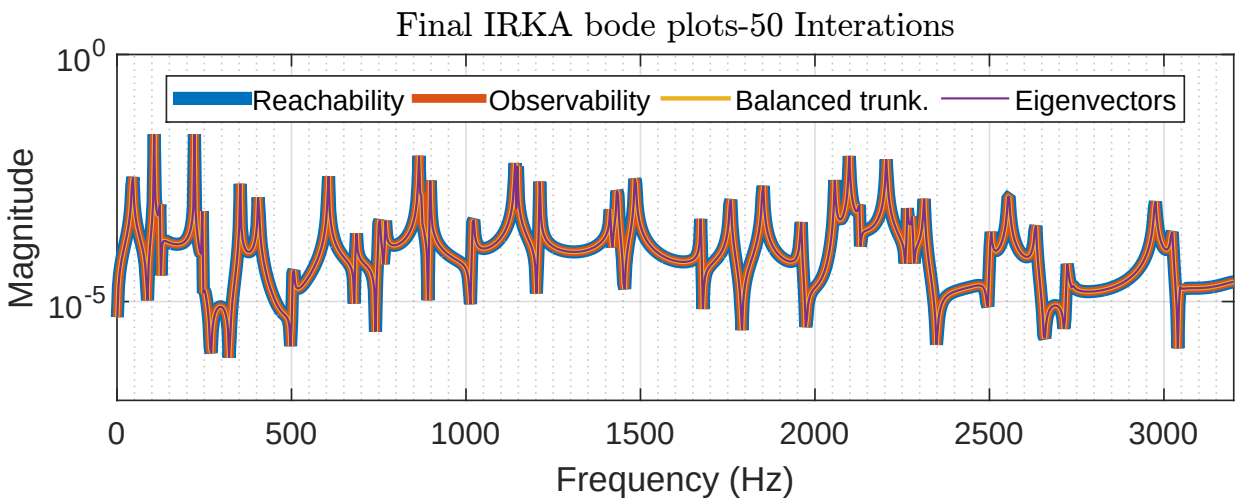

Figure 4.28: Bode plots of differently initialized IRKA plots of size 132 in the frequency range up to $3200Hz$.

results (which assume symmetry) are compared against the available experimental and FE results. This assumption is validated at three different frequencies of excitation $546Hz$, $635Hz$ and $708Hz$. In each of these case, the location of excitation is chosen to be either the pair A and B or the pair A and C. Consider the scenario where the frequency of excitation is $635Hz$. This frequency is half-way between the 9^{th} and 10^{th} resonant frequencies of the plate and the corresponding mode-shapes are plotted in Figure 4.29. This figure clearly shows the locations of the mode shapes which are in-phase with each other and locations that are out-of-phase which each other. Assuming that the piezo-ceramics are bonded to the plate at all four corners, the symmetry of the excitation is assumed throughout this section. Experimental results and FE results are based on the case where the piezo-ceramics are slightly asymmetric as seen in Figure 4.1. However, the mode combination results (which assume symmetry) are compared against the available experimental and FE results.

Figure 4.29 shows that mode 9 is symmetric for both cases of excitation (pair [A B] and pair [A C]). In contrast, the 10^{th} mode is antisymmetric for both locations of excitation. As one mode is symmetric and other is anti-symmetric, the wave combination approach is valid. A video which compares experimental results with FE model and mode combination results are shown in Figure 4.30 for locations A and B and in Figure 4.30 for locations A and C. The amplitudes of all these figures are normalized and all the responses are manually time-synced. For the ease of studying these figures, only the positive amplitudes of the traveling waves are plotted in these videos. For the mode combination videos, only the case (one of the four waveforms $\tilde{W}_i$) that closely resembles the experimental plate response is plotted. The other phase forms lag this result by a phase of $90°$.

Figure 4.30 (a) and Figure 4.31 (a) show this experimental velocity profile of the plate when actuated at $635Hz$. The experimental noise in these profiles is filtered with the help of a Butterworth

bandpass filter and the filtered experimental profiles are shown in Figure 4.30 (b) and Figure 4.31 (b). These plate responses are then compared with the corresponding FE model results in Figure 4.30 (c) and Figure 4.31 (c). The mode combination results are plotted in the last two part of these videos. While the (d) part shows the surface videos which are a combination of FE modes, the (e) combines the experimentally extracted mode shapes. The waveforms ($\tilde{W}_i$) which are the combination of 2D plate modes are independent of the frequency of excitation and location of excitation. Therefore, Figure 4.30 (d) and Figure 4.31 (d) are the same video and Figure 4.30 (e) and Figure 4.31 (e) are one and the same. By closely observing the wave forms in all these cases, we can infer that the basic traveling wave in all these scenarios is the same. In other words, the traveling wave which is a result of the mode combination of the two modes is matching the experimental plate response and the FE simulation. Although, there are inherent differences between each of these videos, the general wave trend is the same for all these cases. For both Figures 4.30 and 4.31, the waveform travels along the circumference of the plate. One of the interesting results of these plots is that the traveling waveform is similar when the plate is exited at different locations. This follows the results of the generalized theory of traveling waves.

The plate response at another frequency of excitation, $708Hz$, is also discussed in this section. This frequency is halfway between the 10^{th} and 11^{th} resonant frequencies of the plate. The mode shapes and their symmetry are shown in Figure 4.32. Similar to the previous frequency of excitation, the conditions for the mode combination theory are satisfied for this case. The videos comparing the experimental results, the FE simulations and the mode combinations are plotted in Figure 4.33 and Figure 4.34 for both locations of excitation. The traveling wave is found in three interconnected pockets where the waveform rotates in clockwise or counter-clockwise directions. Such a behavior is also observed when the plate is actuated from both locations of excitations. Although, there are much larger deviations between different models, the broader mode combination approach is still valid for this frequency of excitation.

The last frequency studied for traveling waves is $546Hz$. This frequency lies between the 8^{th} and the 9^{th} resonant frequency. The corresponding modeshapes are plotted in Figure 4.35. As seen in this figure, the ninth mode shape is symmetric in both directions i.e along the length and width of the plate, and the eighth mode shape is only symmetric along the length of the plate. Therefore the scenario where the plate is excited in the locations A and B satisfies the conditions for the theory of mode combinations. As before, the experimental response of the plate is compared against the FE model and the mode combination results for the location pair A and B in Figure 4.36. As expected, the mode combination wave profile follows the experimental plate response. The traveling wave is a combination of the rotational and translation motion. In this video, the experimental velocity profile near the width of the plate (shorter edge) is more similar to the mode combination waveform than the FE model.

Additionally, in the scenario where the plate is excited at the location A and C, the conditions for the theory of mode combination are not satisfied. Therefore the mode combination theory, do not predict the plate response in this scenario. However, to test the limits of the proposed theory of traveling waves, the experimental results are compared against the mode combination waveforms ($\tilde{W}_i$). The different traveling waves are shown in Figure 4.37. The mode combination videos in this figure are similar to those from the previous location, shown in Figure 4.36. Although there are many differences between the traveling waveforms between the experimental and theoretical results, the overarching traveling waveform is of the same form as that of the mode combination wave. One of the possible explanations is that the conditions stated in the generalized theory section are sufficient conditions to generate traveling waves and not necessary conditions. At least, this is true in the case of complex 2D structures such as plates. A further, in-depth analysis on 2D waveforms is required to further understand these differences.

4.7 Conclusion

The work presented in this chapter is the basis for investigating 2D bending waves in plates. Initially, a finite element model is formulated to simulate the dynamics of the plate when actuated by multiple piezo-ceramics. The model is validated through experimental modal tests wherein a rectangular plate is actuated by an MFC and frequency response characteristics such as mode shapes, natural-frequencies and damping coefficients are estimated. The FE model is updated by evaluating the proportional damping constants through experimental results. This updated model is able to predict up to the 40^{th} damped eigenvalue with a maximum error of 2.5% and match mode shapes accurately, with a lowest MAC value of 0.92. The FE model is used to generate traveling waves by exciting the plate at multiple locations and at multiple frequencies of excitation. These results are later validated through experiments.

Based on the FE model developed in the earlier sections of this chapter, projection based reduced models are developed in a later section of this chapter. The plate dynamics are simulated in the state-space domain, and reduced models are tested for steady state frequency and time responses. The unconstrained boundary conditions of this plate resulted in 12 eigenvalues, corresponding to the rigid-body modes of the plate. These 12-dimensional rigid-body dynamics are decoupled from the full-order dynamics via Schur decomposition technique, and projection-based reduced order models are developed by reducing the asymptotically stable 2946-dimensional state-space. Once the ROMs are computed, the separated rigid-body dynamics are later attached to the these scaled-down models to form the final reduced model. In the present work four ROMs are developed based on the concepts of reachability, observability, balanced truncation and IRKA. In the first three approaches, the criteria for determining the smallest order of the reduced models are

presented. Among these, the balanced truncation based ROM has a size of 5% of the full model, and it is able to accurately capture the frequency and time domain responses in the frequency range of interest with a relative error in the order of 10^{-4}. IRKA is also able to generate a ROM with the same size and with similar error measures. IRKA has the computational advantage that the model reduction process does not require solving large scale Lyapunov equations as required in balanced truncation. However, for the model dimension we considered here, solving these Lyapunov equations does not incur too much computational burden.

The previous section discusses the capabilities of the mode combination approach to replicate the traveling waves developed in plates. The experimental results are compared against the plate response simulations of the finite element model and the mode combination waveforms. The effect of variation of location is studied by varying the excitation location from the pair [A, B] to [A, C] for three frequencies of excitation. Out of the six cases discussed in that section, five cases satisfy the initial symmetry conditions of the mode shapes. However, in all cases, the mode combination approach is able to replicate the response of the plate to multiple inputs. The results presented show the need for further analysis of wave generation in complex 2D structures.

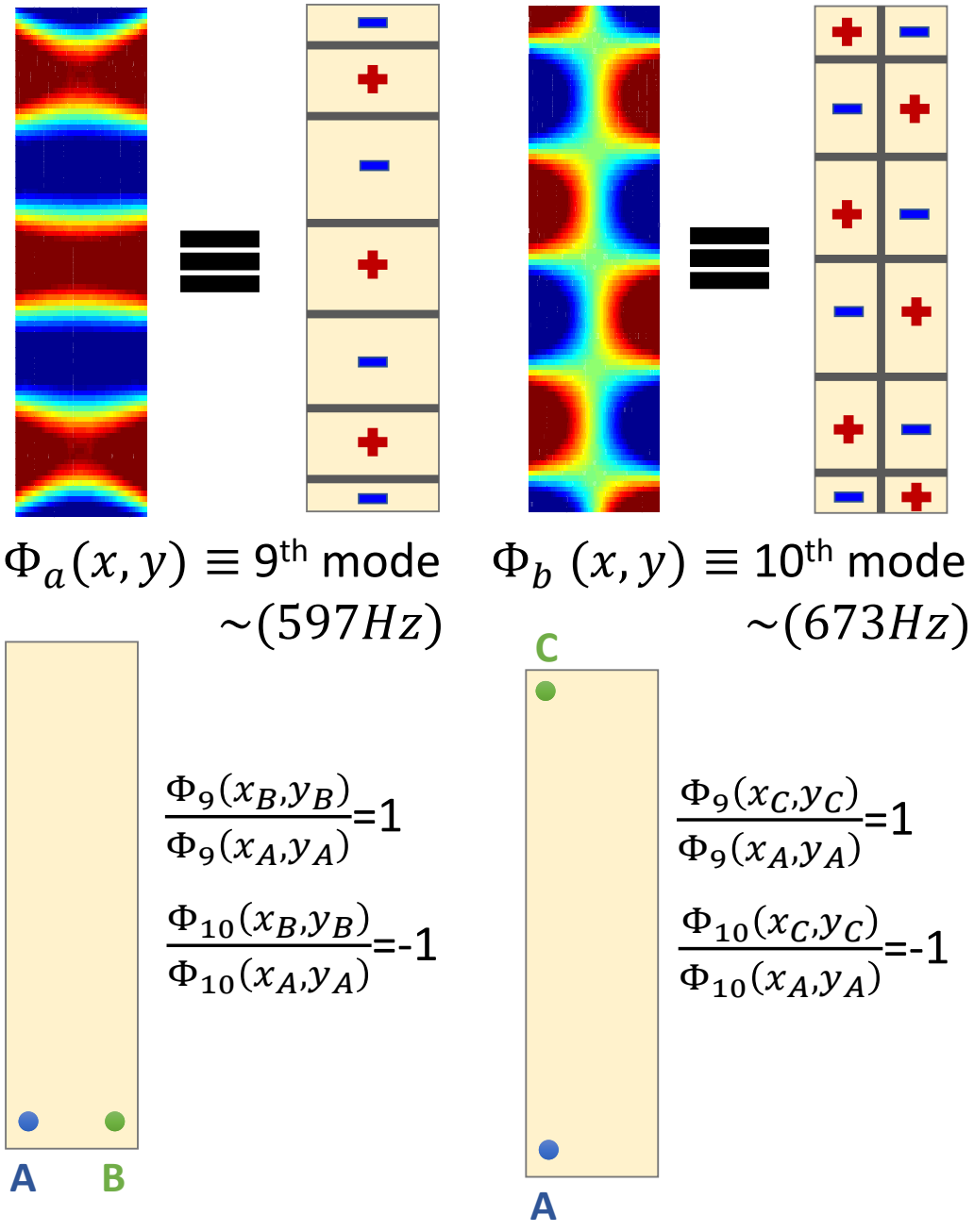

Figure 4.29: The modeshapes of the 9^{th} and the 10^{th} resonant frequencies of the plate. The spatial assumptions that support the generalized theory of traveling waves is also shown.

Figure 4.30: Plate response when excited at location A and B with a $635Hz$ signal (Click on the picture for the video to start).

Figure 4.31: Plate response when excited at location A and C with a $635Hz$ signal (Click on the picture for the video to start).

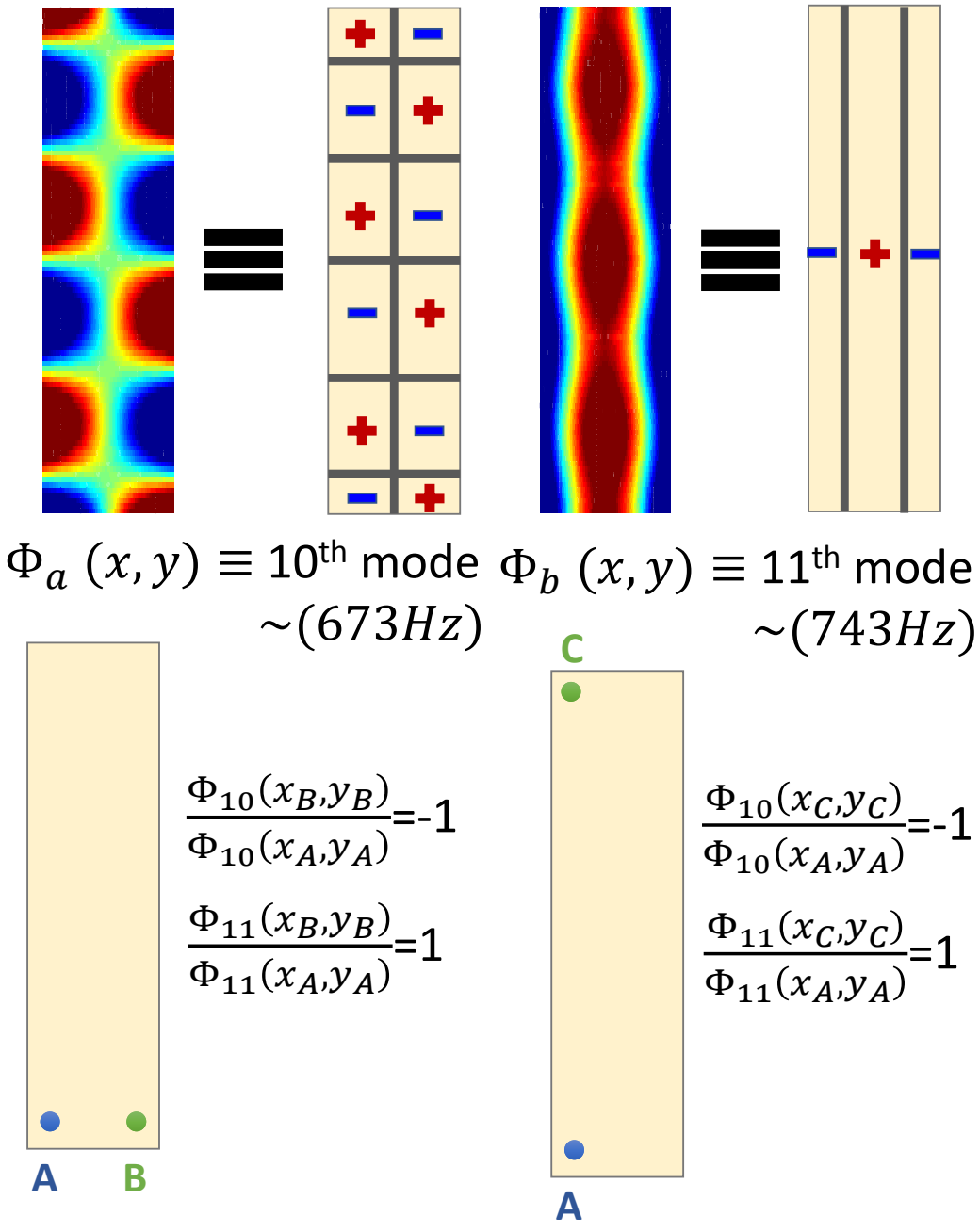

Figure 4.32: The modeshapes of the 10^{th} and the 11^{th} resonant frequencies of the plate. The spatial assumptions that support the generalized theory of traveling waves is also shown.

Figure 4.33: Plate response when excited at location A and B with a 708Hz signal (Click on the picture for the video to start).

Figure 4.34: Plate response when excited at location A and C with a 708Hz signal (Click on the picture for the video to start) .

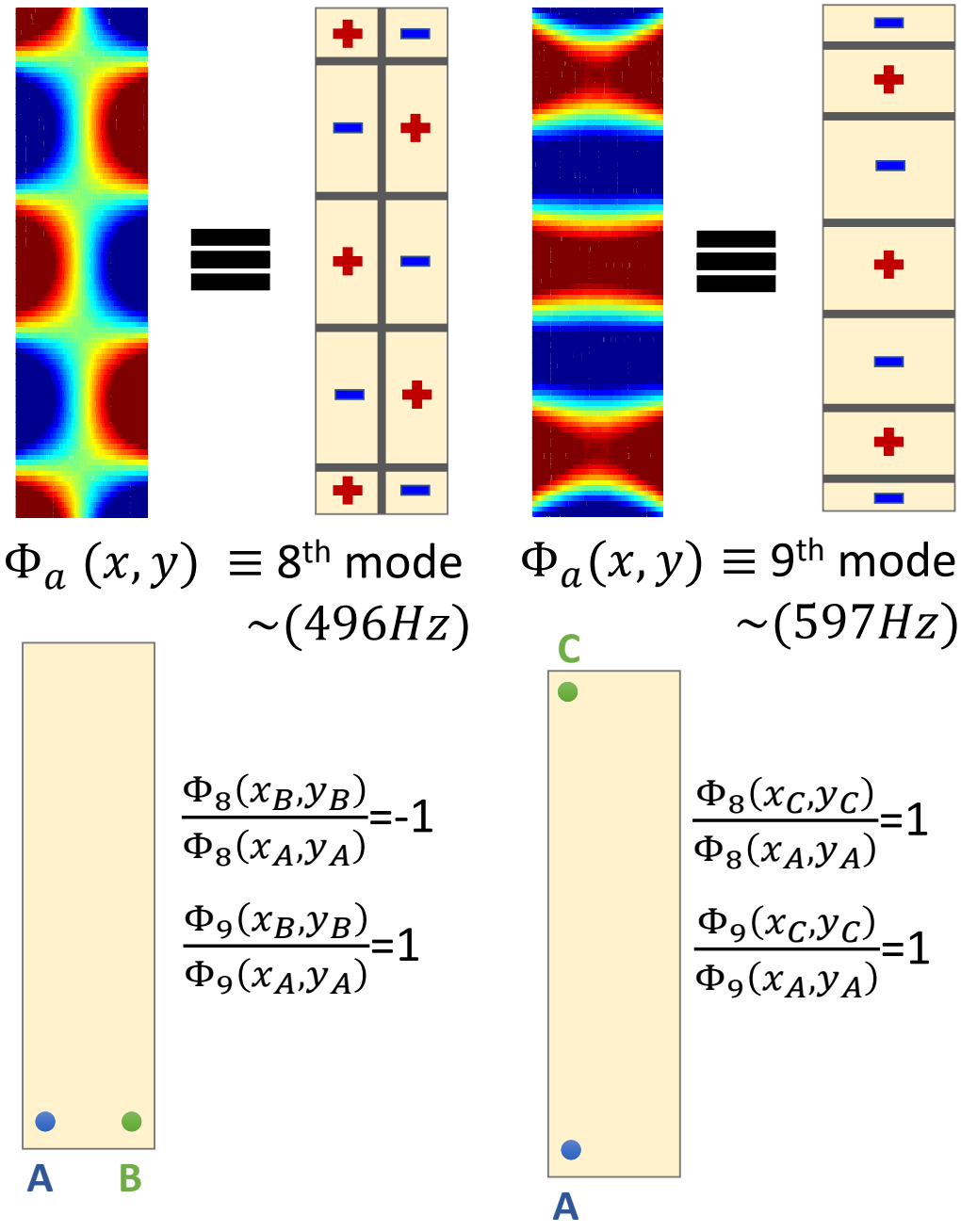

Figure 4.35: The modeshapes of the 8^{th} and the 9^{th} resonant frequencies of the plate. The spatial assumptions that support the generalized theory of traveling waves is also shown.

Figure 4.36: Plate response when excited at location A and B with a $546Hz$ signal (Click on the picture for the video to start).

Figure 4.37: Plate response when excited at location A and C with a $546Hz$ signal (Click on the picture for the video to start).

Chapter 5

Traveling waves in cylinders

5.1 Introduction

The previous work has demonstrated that piezo-ceramics are capable of generating net wave propagation in one-dimensional structures such as beams and 2D structures such as plates. In this chapter cylindrical traveling waves are investigated. Cylinders provide insight into unique dynamics (i.e., symmetric and non-symmetric modes) that have yet to be fully defined for two and three dimensional systems. This chapter extends the research findings of 1D beam structures and applies it to 2D traveling waves in a symmetric cylindrical structure. The work herein will focus on the generation and characterization of traveling waves that propagate along the circumferential direction. The coupled system, given by a free-free cylinder with multiple piezoelectric actuator (PZT) patches, is used to evaluate several traveling wave modes in the cylinder. Finite Element Modeling (FEM), in conjunction with experiments, were conducted to provide a comprehensive understanding of the generation and propagation behavior of the traveling wave modes in a thin walled cylinder. These waves provide interesting pumping and mixing applications beyond the 1D traveling wave capability. The work provides an initial study that could lead to several fluid-structural interaction applications.

For example, cylindrical traveling wave applications have the potential to increase propulsive capability compared to prior work, by introducing additional control capability and system coupling. The circumferential traveling wave provides unique mixing capability for static and dynamic flows, active flow control, and other piping applications [27, 29, 65]. This methodology also has the potential to provide efficient solid state pumping capability where pumping is impractical or impossible before. In this work, two PZT patches are used to excite a cylinder between the first and second breathing modes. The present work discusses the method used to verify the dynamics of circumferential traveling waves through testing and modeling. The hardware and test setup plan is discussed in later sections of this chapter, the FEM development and verification, as well as the

results from the standing and traveling wave tests. The phase shifts effect on the type of generated wave and a study into repeated modes traveling waves is also addressed.

5.2 Test description

One of the significant differences in analyzing cylindrical waves against planar waves is differentiation of traveling waves with standing waves. The time-based data is evaluated in two ways as demonstrated in Figure 5.1. The first method evaluates the quality of the traveling waves using the Fourier's approach [65]. This method evaluates the maximum real and imaginary displacement values of the Fast Fourier Transform (FFT) for every location around the circumference of the cylinder. Using this method, a purely traveling wave will result in a circle (or an ellipse) and a standing wave will produce a linear plot, as seen in Figure 5.1. The second method uses the time response data plotted on the original cylindrical geometry to generate a snapshot of the displacement data. In the case of pure standing waves, there are locations along the circumference of the tube where there is no displacement; such points are also called strain nodes. In contrast, in the case of pure traveling waves, the displacement of all the points along the circumference of the tube have equal and non-zero displacement. As seen in Figure 5.1, for a standing wave, there are locations of no displacement, while in the pure traveling wave, the maximum and minimum displacements on the plot are constant for every point along the circumference. In the succeeding sections of this chapter, these methods are used to evaluate the quality of the wave and determine if the response is traveling, stationary, or a combination of the two.

In the present work, a free-free boundary condition is experimentally simulated by hanging the cylinder from the ceiling as seen in Figure 5.2. The tested hardware is extruded aluminum measuring 50 $^{3}/_{8}$ inches long with an outer diameter of 10 inches and a wall thickness of 0.1 inches. The tube and PZT setup is used because of its well understood dynamics and the ease of testing [224].

The cylindrical tube considered for experimentation is mounted with 36 piezo-ceramic wafers, shown in Figure 5.2. Each of the three rows consists of 12 piezoelectric actuators that are positioned every 30° around the circumference. The rows are placed at heights of 4 inches, 25 $^{3}/_{16}$ inches, and finally 46 $^{3}/_{8}$ inches. The two PZTs used to excite the structure were located in the first row, 4 inches from the bottom and 180° apart.

In the development of the test setup 12 single axis PCB 352C67 shear accelerometers were placed around the circumference of the tube 3 inches above the active piezoelectric actuators as seen in Figure 5.2 (B). They are oriented to measure the radial (R) response of the cylinder. The accelerometers were placed at intervals of 30° for the first test configuration.

As this configuration allows the detection of traveling waves along the circumference of the

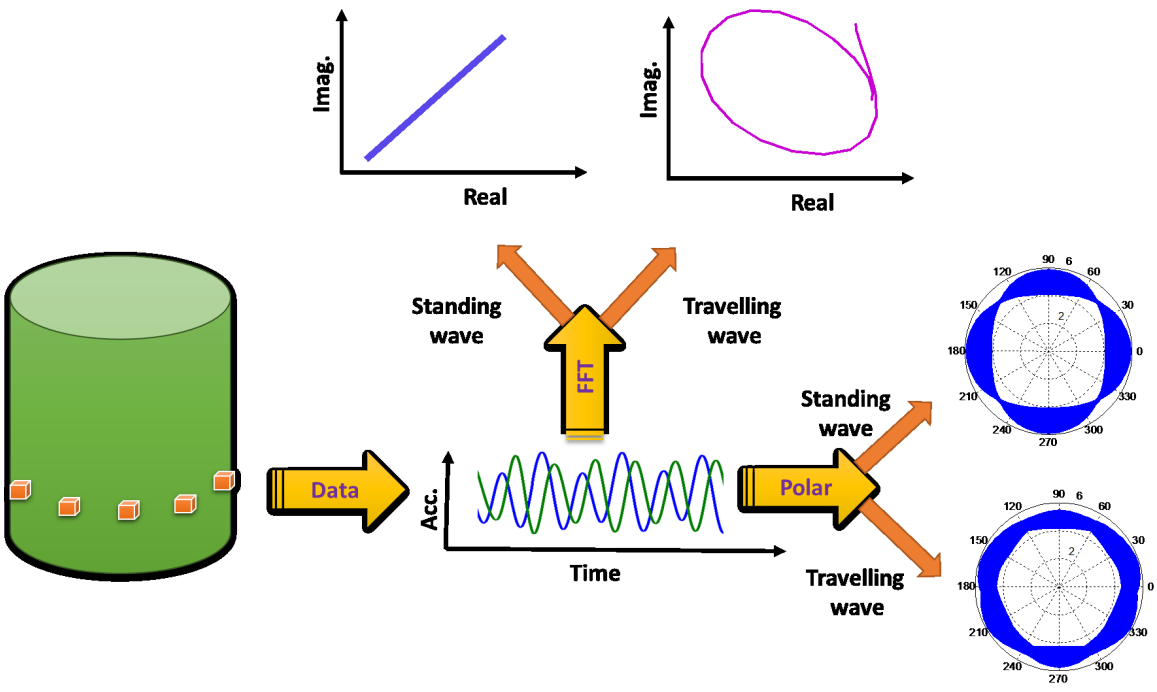

Figure 5.1: Method for determining the nature of the traveling wave in the time and frequency domain.

cylinder and neglects its longitudinal direction, additional test data is recorded by a linear sensor pattern. For this test, the accelerometers were placed along the length of the tube at intervals of 3 inches as seen in Figure 5.2 (C). This data provided the necessary information in order to identify if a wave is propagating along the length of the cylinder (Z direction).

First, the cylindrical structure is excited by a single PZT element by actuating it with a sinusoidal voltage sweep signal. The frequency is varied from $20Hz$ to $2000Hz$ and its response is measured with several of the accelerometers. The frequency response and modes obtained where used to validate the FEA model (described in the next section), and define the excitation frequency required to generate a traveling wave. The measured response is compared against the FEM predicted FRF to ensure the modeled dynamics are accurate within the frequencies of interest.

The second set of experiments focus on the generation of traveling waves with the help of multiple PZT excitation. In the previous works [70] it is shown that 1D traveling waves are obtained when two separate PZTs, with a phase shift of 90°, are actuated at a frequency which is located directly in between the two modes of interest. In this case, the two modes of interest are the first (with one axial strain nodal line) and second breathing modes (with not axial nodal lines) at $107Hz$ and $300Hz$, respectively. For this system, the excitation is applied at $203Hz$ by PZTs located 180° apart. The traveling wave dynamics are a function of the chosen excitation points, but no further investigation is done on alternative excitation locations.

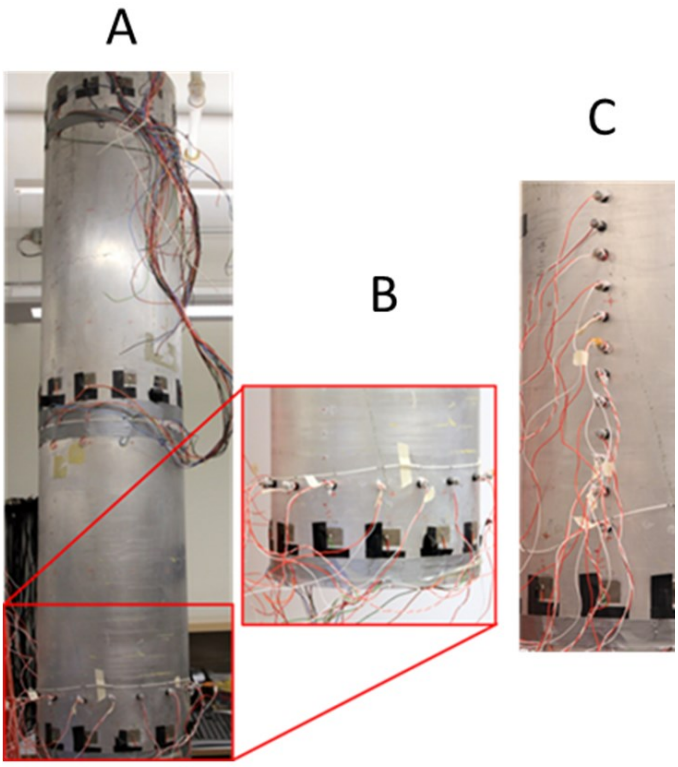

Figure 5.2: (A) Test hardware with PZT elements and Accelerometer placement is shown with (B) a detailed view and (C) a view of the vertical test configuration.

5.3 Finite element model

A FEM of the cylinder is developed using the MSC Nastran software as shown in shown in Figure 5.3a. The cylinder is modeled with 48 linear *CQUAD*4 shell elements around the circumference and 25 elements along the height of the cylinder. The FEM uses 1152 shell elements with 1200 fe nodes and a resulting 7200 total degrees of freedom. The first 50 modes are evaluated in this model resulting in full modal content below 550 Hz. This ensures an accurate representation of the dynamics up to at least 360 Hz. The first (with an axial strain node) and second breathing modes were predicted to be at 107 Hz and 302 Hz as compared to measured frequencies of 104 Hz and 296 Hz with a respective 1.9% and 2% error. This yields a very satisfactory correlation between the model and the test specimen for the dynamics of interest for this problem. Further, the response of the cylinder at these frequencies is evaluated and the standing wave characteristics using the Fourier and envelop approaches, discussed earlier, is studied.

The piezoelectric actuation is modeled in the FEM as an out of plane unit point load applied at the center of the PZT patch. The nodal output coordinate system is defined in cylindrical coordinates to ensure that the radial displacements and the phase differences match the 1D beam case.

The phase relationship is defined with the load applied in the positive radial direction as seen in Figure 5.3b. The MSC Nastran solution 112, the Modal Transient Response Analysis, is employed to model the traveling wave with 501 time steps of 2×10^{-4} seconds to model the system from 0 to 0.1 seconds.

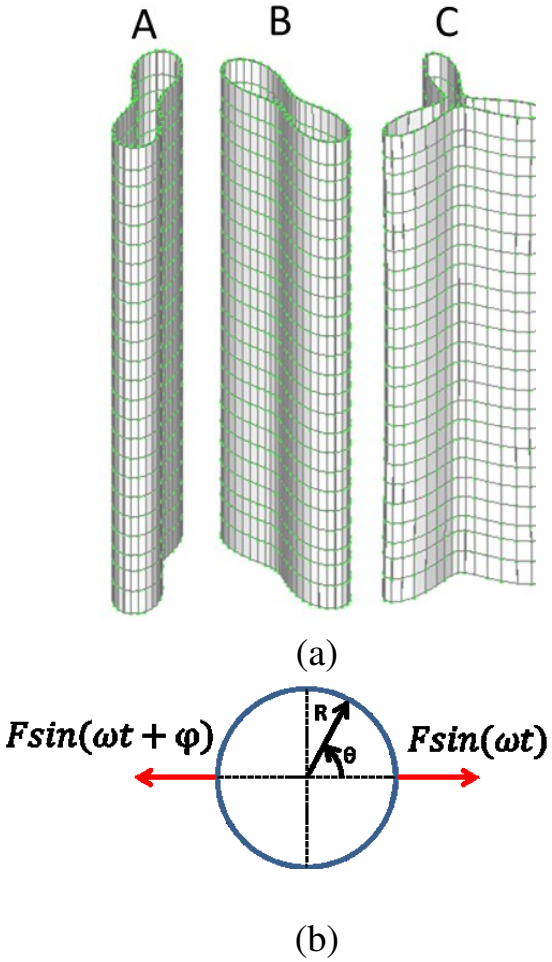

Figure 5.3: (a) (A) Finite Element Model of the Cylinder with (B) Mode one at 107 Hz and (C) Mode two 300 Hz; (b) FEA loading applied at a frequency of (ω) with a phase shift (ϕ) of 0° in the cylindrical coordinate system.

5.4 Results and discussion

The model previously described is used to predict the wave response and identify the nature of the wave. To develop a standing wave baseline, a single frequency sine wave is applied to the cylinder at the resonant frequencies of 106Hz and 300Hz modes separately. This will yield a baseline to compare the wave dynamics of future tests.

5.4.1 Cylindrical standing waves

The standing wave time-history displacements in Figure 5.4 are plotted on the original geometry and amplified to allow for easier viewing of the displaced pattern. The $100Hz$ standing mode time history seen in Figure 5.4a replicates the first breathing mode of the cylindrical tube. The mode shape has four FE-nodes as was expected from the first mode shape seen in Figure 5.3a(B). The $300Hz$ second breathing mode seen in Figure 5.4b, has six nodes as expected.

FFT is applied on the time-history data of the standing waves data at different locations and the Fourier approach is tested. The FFTs of the simulated time data is plotted in Figure 5.4c and Figure 5.4d for $106Hz$ and $300Hz$ respectively and the corresponding Fourier curves are plotted in Figure 5.4e and Figure 5.4f for $106Hz$ and $300Hz$ respectively. As expected the standing wave has a linear response, as every FE-node's relative amplitude and phase are linearly correlated. Additionally, the response is symmetric around the origin $(0,0)$, corresponding to the nodes in the excited mode. This response is a strong representation of the standing wave dynamics of the system.

5.4.2 Cylindrical traveling waves

In earlier section it was mentioned that the optimal case for a traveling wave is to excite the structure 90° out of phase at a frequency value between the first two modes (i.e., in this case $203Hz$). By doing this and following the same response analysis as before, the responses for a traveling wave show significant variation from the standing wave case. The first thing to notice is that the excitation at $203Hz$ excites both the first and second breathing mode. Secondly, it can be seen in Figure 5.5c that there is a phase shift for each of the FE-nodes along the circumference. This is indicative of a traveling wave that has a corresponding phase shift for the peak response for each node in the circumferential direction.

A secondary check that provides insight into the nature of the traveling wave is an investigation into the time history of the response. The time response in Figure 5.5a shows that the wave moves around the circumference and no nodal points or zero excitation points exist (as seen in Figure 5.4). As is expected, the wave can also be seen to have a nearly constant maximum and minimum displacement indicating that a constant amplitude wave is traveling along the circumference.

5.5 Effect of phase in cylindrical waves

To better understand the effect phase has on the quality of the traveling waves, the phase was swept from 0° to 180° and the Fourier approach was applied for each of these cases. As stated before, if the system has a pure traveling wave, the resulting plots in Figure 5.6a would be perfect circles. The best case observed, in the modeling efforts, can be seen for the 90° case. These cases with the

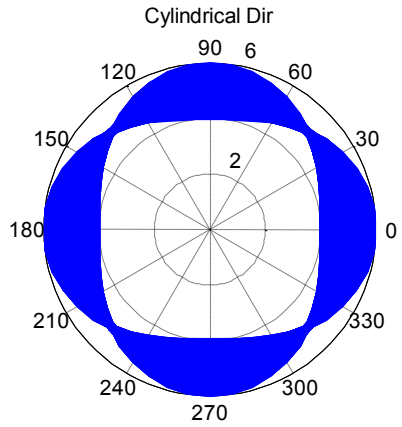

(a)

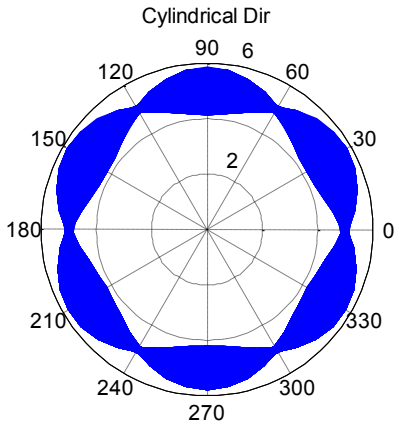

(b)

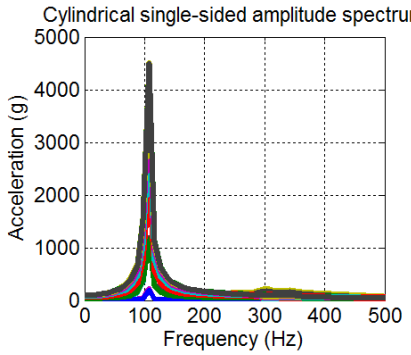

(c)

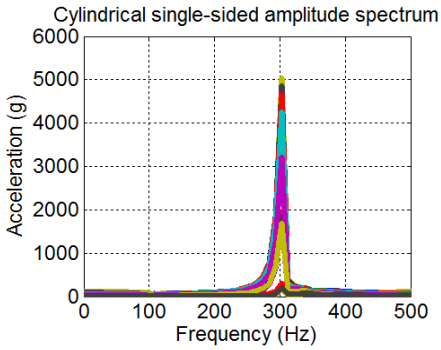

(d)

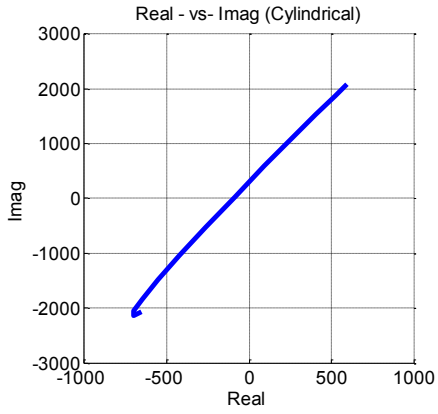

(e)

(f)

Figure 5.4: Time data response of the standing wave excitation at the first two breathing modes at (a) 106Hz and, (b) 300Hz from FE model, Frequency Response spectrum at (c) 106Hz and, (d) 300Hz and the real and imaginary elliptical curves at the peak response for every FE-node using the simulated time data at (e) 106Hz and, (f) 300Hz .

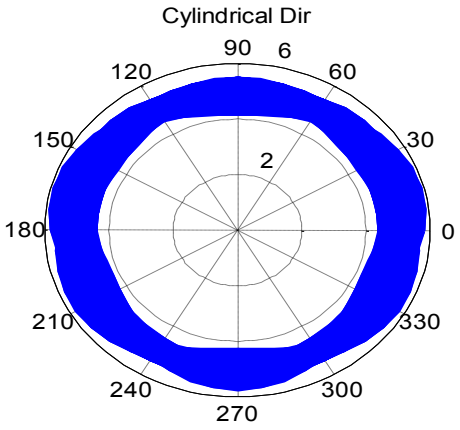

(a)

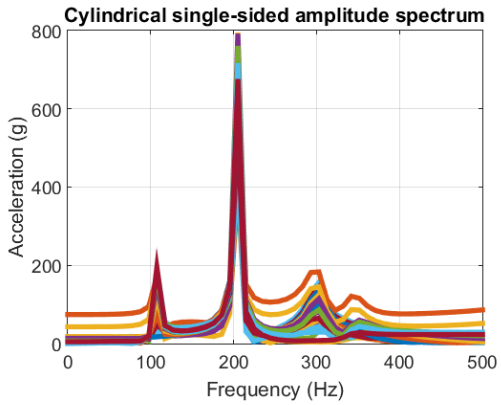

(b)

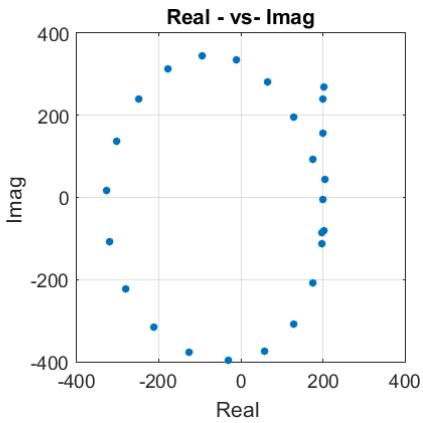

(c)

Figure 5.5: (a) Simulated time data response of the traveling wave excitation at 200 Hz, (b) Frequency Response for the traveling wave at 200 Hz as well as the magnitude and phase of the peak response (c).

exception of 0° and 180° exhibit a traveling wave behavior as expected with diminishing level of performance as the phase moves away from the ideal 90°. On the contrary, Figure 5.6b demonstrates that the longitudinal direction exhibits a strongly linear response, indicating no traveling wave in this direction. Knowing the longitudinal direction shows no traveling waves along that axis; it can be confidently stated that a purely circumferential traveling wave is achieved.

Figure 5.7 demonstrates how the response changes as the system is excited at $203Hz$ and the phase is varied from 0° to 180°. As the phase is swept from 0° to 90° the response shape slowly transitions from a standing wave with 4 nodal points 5.7a to a fully traveling wave 5.7c. As the phase is swept from 90° to 180° the response shape slowly transitions from a traveling wave to a standing wave with 6 nodal points 5.7g. This plot shows that the phase shift at 0° fully excites the $106Hz$ standing mode dynamics and a phase shift at 180° fully excites the $300Hz$ mode. Between

these values the traveling wave begins to develop.

To fully compare the FE system with the experimental data, the Fourier curves are plotted in Figure 5.8, respectively. The resulting test data and FEM predictions accurately predict the wave dynamics, but do not accurately predict the specific nodal responses. The arbitrary direction for the FEM mode shapes complicates the phase comparison between the FEM and test results. Further work will be done to investigate these phase relationships and how to better match the FEM results with the test data.

The traveling waves generated show significant promise for pumping and mixing applications, but no work has been done to evaluate this system's pumping capability. To better understand the capability of these systems future work is required to evaluate the fluid structural energy transfer capability and the overall efficiency of the system.

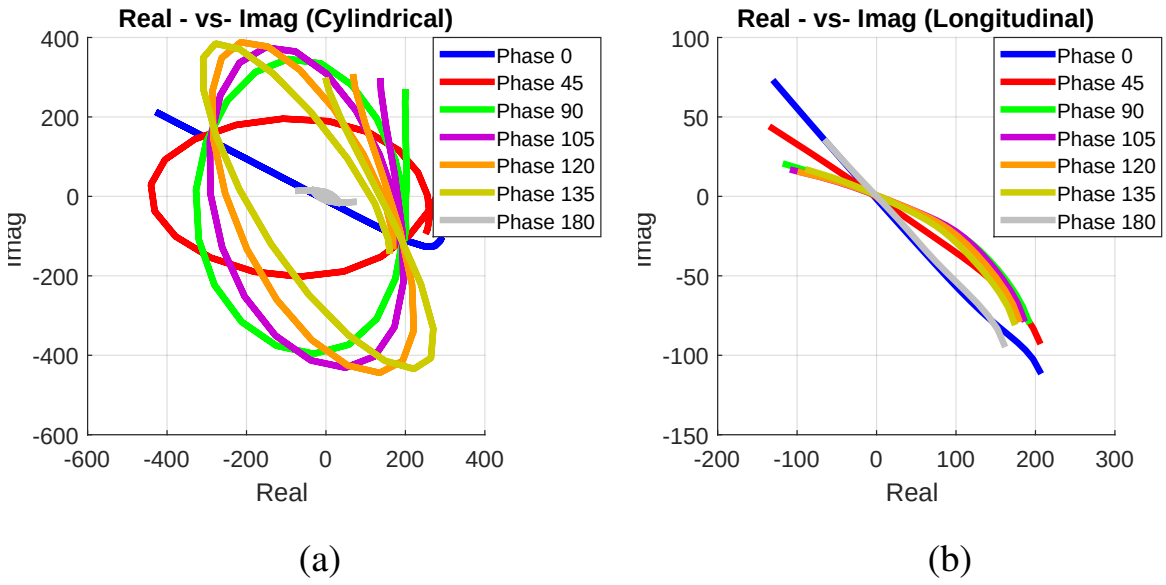

(a) (b)

Figure 5.6: Simulated ellipses of the response at the peak excitation at $200Hz$ in the (a) cylindrical direction and (b) longitudinal direction.

5.6 Study of traveling waves using repeated modes

Symmetrical systems exhibit repeated modes that are examined here as a possible candidate for wave propagation. In the case of 1D systems, traveling waves have been observed when excited at the natural frequencies with a phase of 0° or 180°. To better evaluate the dynamics of symmetrical systems, the cylindrical structure studied here was driven at the first and second natural frequency with a variety of phase shifts. This was done to evaluate the ability to excite traveling waves

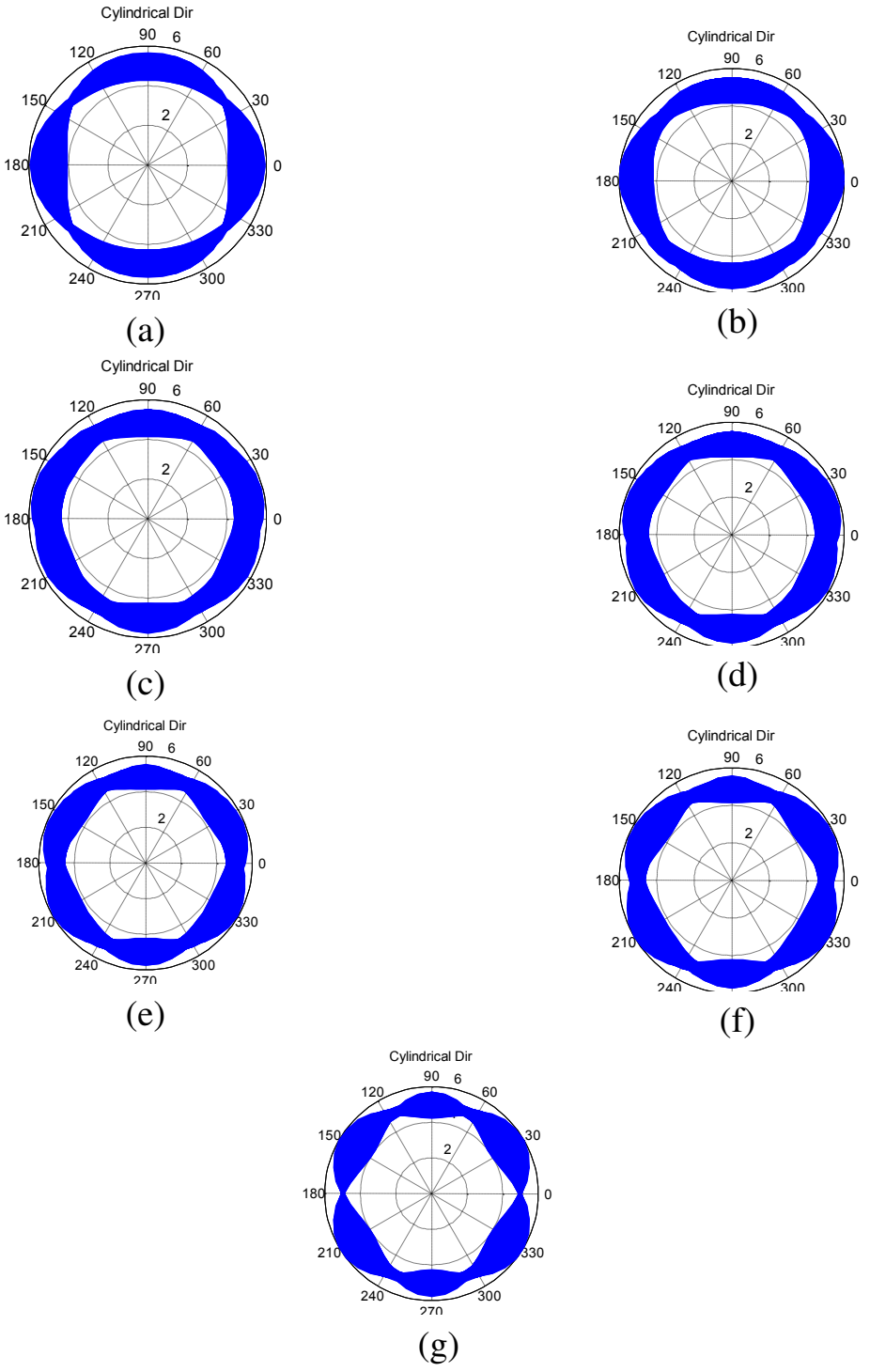

Figure 5.7: Fe model based time history responses at $203Hz$ with a phase difference of (a) 0°, (b) 45°, (c) 90°, (d) 105°, (e) 120°, (f) 135°, and (g) 180°.

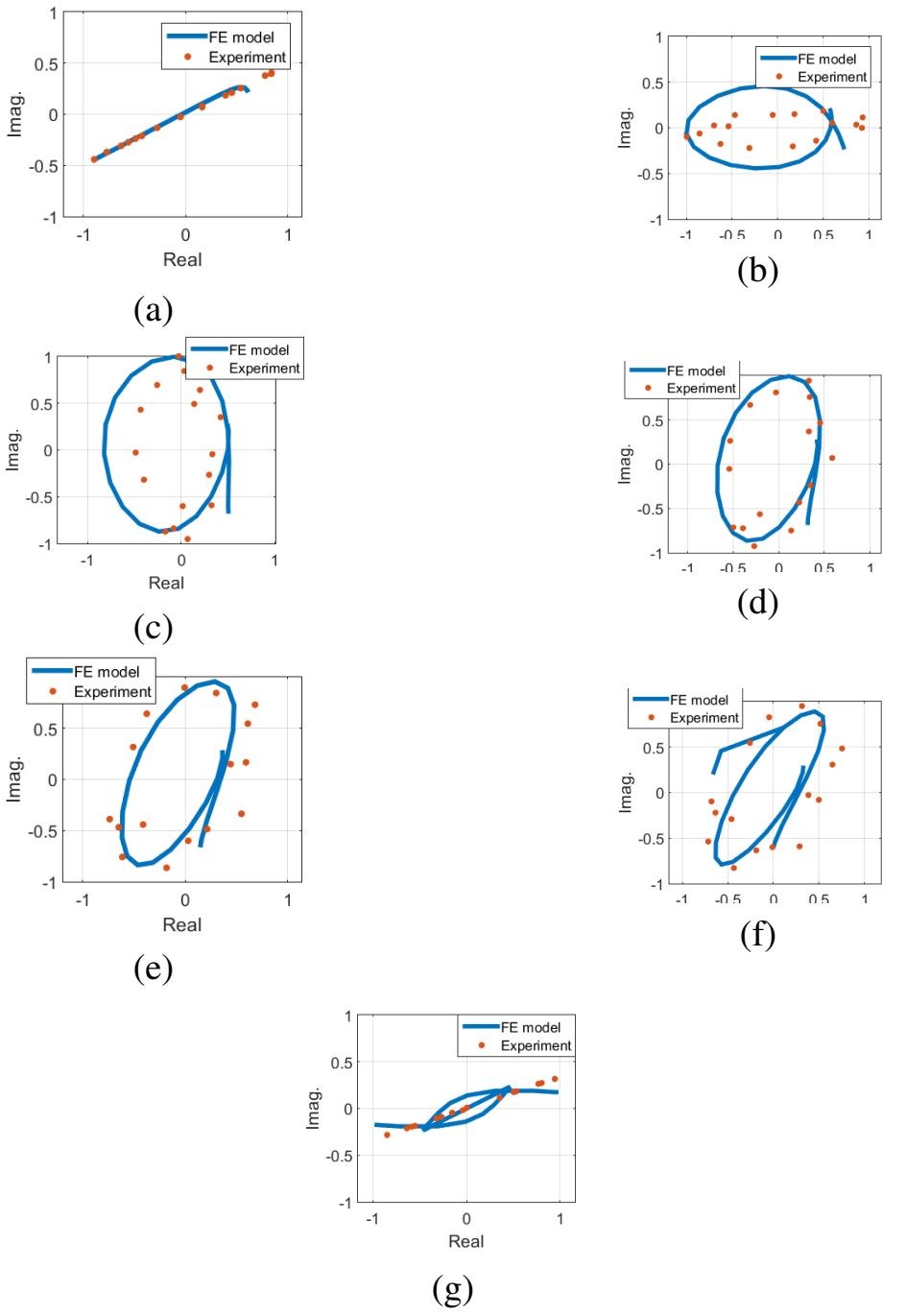

Figure 5.8: Normalized ellipse comparison between experiments and FE simulations at 203Hz with a phase difference of (a) 0°, (b) 45°, (c) 90°, (d) 105°, (e) 120°, (f) 135°, and (g) 180°.

using the repeated modes seen in Figure 16. As can be seen at the same frequency value there are repeated eigenvalue roots for each of the breathing modes. This results in identical mode shapes with a rotation about the longitudinal axis. These repeated modes were excited with the intent of producing additional traveling modes using the same two PZT excitations and phase shift convention used previously.

The $106Hz$ excitation results in pure standing waves in both the cylindrical and the circumferential directions as seen in Figure 5.9a and Figure 5.9b, respectively. The plots in Figure 5.10a and Figure 5.10b exhibit the same behavior for the $300Hz$ case with no traveling waves observed. The development of traveling waves at these frequencies was not successful for the given excitation points. Further investigation is needed to evaluate if repeated roots could be used to generate traveling waves given different conditions.

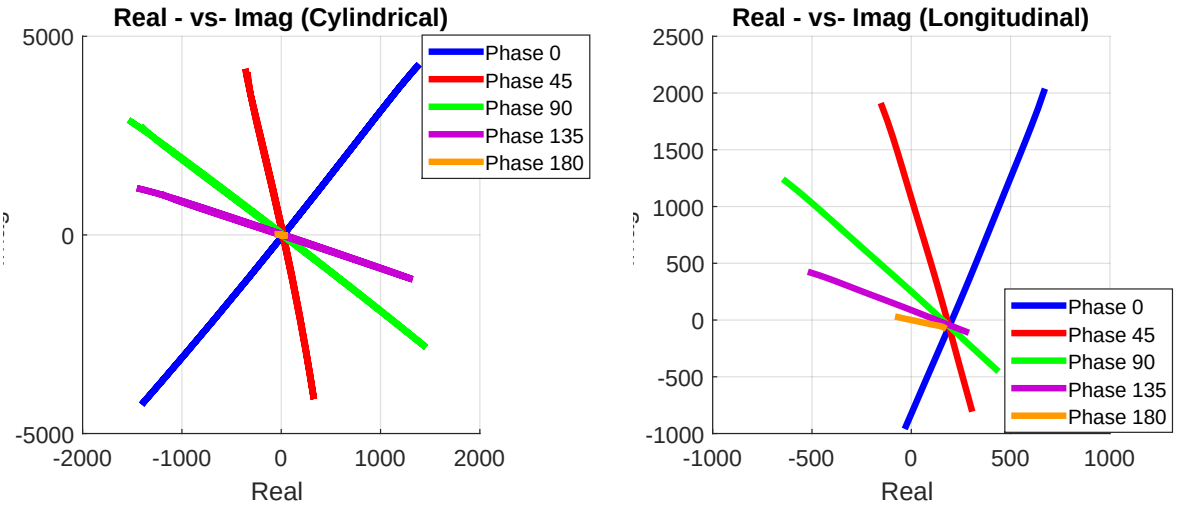

(a) (b)

Figure 5.9: Simulated ellipses of the response at the peak excitation at $105Hz$ in the (a) cylindrical direction and (b) longitudinal direction.

5.7 Cylindrical mode combination

In earlier chapters, traveling waves are simulated as a combination of two mode shapes. In this section a similar approach is taken to predict the response of the cylindrical structures when excited at the optimal conditions. Figure 5.11 present the simulated cylindrical traveling waves. Each traveling wave video is a result of the summation of two mode shapes. All the animations are

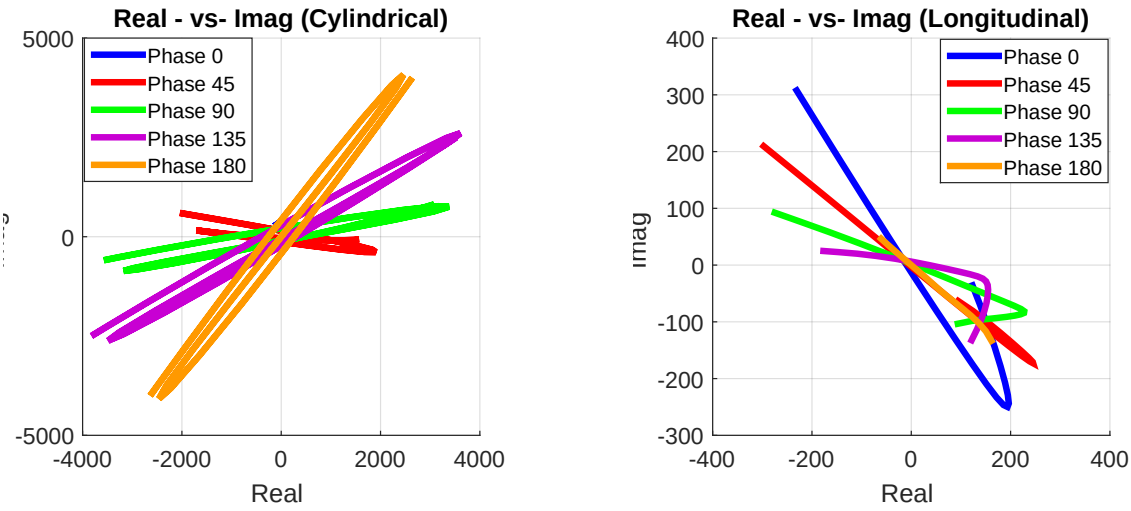

(a) (b)

Figure 5.10: Simulated ellipses of the response at the peak excitation at $105Hz$ in the (a) cylindrical direction and (b) longitudinal direction.

generated based on the FE based mode shapes and the traveling wave forms are obtained by using,

$$W_{AB} = X_A(x,y,z)cos\left(\omega t + \frac{\pi}{4}\right) + X_B(x,y,z)cos\left(\omega t - \frac{\pi}{4}\right). \tag{5.1}$$

While the value of A varies from 1 to 7, B is the next higher mode shape i.e. $B = A + 1$. As in previous sections it was found that repeated modes do not result in traveling waves, only non-repeated mode shapes are considered for this simulation (mode numbering in this video is based on the total number of modes considered for this study). Furthermore, as the frequency of excitation does not effect the animation, ω is kept constant at $100Hz$.

Consider the case of mode 1 and mode 2. While in the radial direction both these modes have the same first breathing mode, in the longitudinal direction they have different behaviors. Mode 2 has a axial strain nodal line. This difference in characteristics resulted in a longitudinal traveling wave. However, when mode 2 is compared against mode 3, there are differences in both radial and longitudinal directions. This resulted in a traveling wave along the circumferential direction and also the longitudinal direction. Similarly, the combination of higher modes results in directions which have differences between the mode shapes.

As cylindrical structures are experimentally difficult to test and study, such predictive wave forms are highly useful in the planning stage. However, in such symmetric structures that have multiple repeated modes, the resonant frequencies of some modes are very close to each other. For example, there are two different eigenvalues between $106Hz$ and $108Hz$ and two between $300Hz$

and $303Hz$. If we are trying to generate a traveling wave at $200Hz$, four modes will have the significant contribution. To simulate such scenarios is highly complex and can be a combination of multiple traveling waves. In future studies a more detailed analysis will be carried out to further study this phenomenon.

Figure 5.11: Traveling waves expressed as a summation of pairs of mode shapes. (Click on the picture for the video to start).

5.8 Conclusion

This chapter details the work to date on circumferential traveling waves and an approach for modeling and evaluating the resulting dynamics. The FEM developed has been shown capable of predicting the onset and behavior of these traveling waves. This FEM was used to gain a more complete understanding of the 2D circumferential traveling waves in cylindrical system.

This chapter evaluated the various frequencies of excitation and the phase shifts required to generate a 2D cylindrical traveling wave. It was shown that with the given loading positions, the traveling waves with the most energy were generated at $203Hz$ with a phase shift of 90°. Furthermore, the work herein attempted to generate traveling waves given symmetrical repeated

roots present in the system. The current approach proved to be unsuccessful in generating traveling waves at these repeated roots corresponding to symmetrical modes. Further analysis is needed in order to fully evaluate this potential.

Using the technique detailed in this chapter, circumferential traveling waves were successfully generated experimentally and modeled using a FEM. Circumferential traveling waves such as these provide a novel method for mixing, fluid flow optimization, and propulsion. Further experimentation and modeling is required to fully evaluate the potential of the proposed system. Using the technique detailed in this paper, circumferential traveling waves were successfully generated experimentally and modeled using a FEM. Circumferential traveling waves such as these may provide a novel method for mixing, fluid flow optimization, and propulsion. Further experimentation and modeling is required to fully evaluate the potential of the proposed system. This work provides a novel approach for this field of structure-fluid coupling.

Chapter 6

Conclusions and future work

6.1 Conclusions

The major contributions and results presented in this thesis are summarized below,

Theoretical analysis of traveling waves

(a) The feasibility of generating traveling waves in finite structures is investigated in this chapter. A simplified model of a free-free beam is developed to study the response of a beam when excited by two point forces. The contribution of the trigonometric and hyperbolic parts of the mode shapes are separately investigated to understand the effect of boundary conditions of the beam dynamics.

(b) Theoretically, a phase relationship is established that governs the quality of traveling wave. The traveling wave is represented as the combination of trigonometric parts of the mode shapes. The phase relationship manipulates the amplitudes of the individual waveforms and thus resulting in an optimal traveling waves at any frequency.

(c) The role of the frequency of excitation and the location of forces on the amplitude of the traveling wave is investigated. This study also establishes the conditions on the spatial locations where the forces are applied on the beam to generate traveling waves. Through multiple examples, the influence of location of the point forces and the frequency of excitation on the amplitude and quality of traveling wave is discussed.

(d) The 1D theory of traveling waves is extended to a generalized case which is independent of the dimensionality or the boundary condition of the structure under study. This study paves the way to predict the type of traveling wave as a combination of mode summation for any structure. This theory is later validated through experiments and simulations.

Traveling waves in 1D beams

(e) Traveling wave generation is studied in 1D beams through simulations and experiments. A theoretical model of the beam bonded with two piezo-ceramics is developed based on the mode summation approach. The steady state frequency response of this beam model is compared against experimental results.

(f) The study demonstrates through experiments that net traveling waves can be generated on a beam structure by exciting it with multiple forces. The dynamics of the beam when simultaneously actuated with two inputs is the focus of the study in the initial part of this work. It is shown that such an actuation results in a mixture of pure standing waves and traveling waves. The relative ratio of these wave content is quantified by defining cost-functions. The cost-functions presented in this study demonstrates the capabilities of two approaches, Hilbert and Fourier, to accurately predict and represent the quality of the mechanical waves being generated.

(g) A comparative analysis between the theory and experiment was conducted for three different boundary conditions: clamped-clamped, clamped-free and free-free. The results demonstrated the accuracy of the theoretical model to predict the dynamics of the traveling waves.

(h) The beam models are further used to study the effect of phase on the quality of the traveling wave. The phase relationship obtained through these simulations match the theoretical findings of the previous chapter. Experimental test results were also used to validate the accuracy of these results. It has been further shown that by changing the sign of the phase results in a wave changing its direction of travel.

(i) Based on the theoretical formulations developed in the earlier chapter, the two-mode combination approach is also used to generate 1D traveling waves. These results are compared against simulations and experiments. The effect of boundary conditions on the phase relationship is also discussed in this chapter.

Traveling waves in 2D plates

(j) The work presented in this chapter is the basis for investigating 2D bending waves in plates. Initially, a finite element model is formulated to simulate the dynamics of the plate when actuated by multiple piezo-ceramics. The model is validated through experimental modal tests wherein a rectangular plate is actuated by an MFC and frequency response characteristics such as mode shapes, natural-frequencies and damping coefficients are estimated.

(k) The FE model is updated by evaluating the proportional damping constants through experimental results. This updated model is able to predict up to the 40^{th} damped eigenvalue with a maximum error of 2.5% and match mode shapes accurately, with a lowest MAC value of 0.92. The FE model is used to generate traveling waves by exciting the plate at multiple locations and at multiple frequencies of excitation. These results are later validated through experiments.

(l) Based on the FE model, projection based reduced models are developed in this chapter. The plate dynamics are simulated in the state-space domain, and the reduced models are tested for steady state frequency and time responses. The unconstrained boundary conditions of this plate resulted in 12 eigenvalues, corresponding to the rigid-body modes of the plate. These 12-dimensional rigid-body dynamics are decoupled from the full-order dynamics via Schur decomposition technique, and projection-based reduced order models are developed by reducing the asymptotically stable 2946-dimensional state-space.

(m) Once the ROMs are computed, the separated rigid-body dynamics are later attached to the these scaled-down models to form the final reduced model. In the present work four ROMs are developed based on the concepts of reachability, observability, balanced truncation and IRKA. In the first three approaches, the criteria for determining the smallest order of the reduced models are presented. Among these, the balanced truncation based ROM has a size of 5% of the full model, and it is able to accurately capture the frequency and time domain responses in the frequency range of interest with a relative error (H_2) in the order of 10^{-4}. IRKA is also able to generate a ROM with the same size and with similar error measures. IRKA has the computational advantage that the model reduction process does not require solving large scale Lyapunov equations as required in balanced truncation. However, for the model dimension we considered here, solving these Lyapunov equations does not incur in significant computational burden.

(n) The last section of this chapter discusses the capabilities of the mode combination approach to replicate the traveling waves developed in plates. The experimental results are compared against the plate response simulations of the finite element model and the mode combination waveforms. The effect of variation of location is studied by varying the excitation location from the pair [A, B] to [A, C] for three frequencies of excitation. Out of the six cases discussed, five cases satisfy the initial symmetry conditions of the mode shapes. However, in all cases, the mode combination approach is able to replicate the response of the plate to multiple inputs. The results presented show the need for further analysis of wave generation in complex 2D structures.

Traveling waves in cylinders

(o) This chapter details the work to date on circumferential traveling waves and an approach for modeling and evaluating the resulting dynamics. The FEM developed has been shown capable of predicting the onset and behavior of these traveling waves. This FEM was used to gain a more complete understanding of the 2D circumferential traveling waves in this system.

(p) This chapter evaluated the various frequencies of excitation and the phase shifts required to generate a 2D cylindrical traveling wave. It was shown that with the given loading positions, the traveling waves with the most energy were generated at $203Hz$ with a phase shift of 90°. Furthermore the work herein attempted to generate traveling waves given symmetrical repeated roots present in the system. The current approach proved to be unsuccessful in generating traveling waves at these repeated roots corresponding to symmetrical modes. Further analysis is needed in order to fully evaluate this potential.

(q) Using the technique detailed in this chapter, circumferential traveling waves were successfully generated experimentally and modeled using a FEA. Circumferential traveling waves such as these provide a novel method for mixing, fluid flow optimization, and propulsion. Further experimentation and modeling is required to fully evaluate the potential of the proposed system. Using the technique detailed in this chapter, circumferential traveling waves were successfully generated experimentally and modeled using a FEA.

6.2 Future work

6.2.1 Propulsion

In a 1D structure, when the traveling wave progresses the fluid enters the pocket created by the waveform in the structure. As the wave progresses, the structure pumps the fluid along the direction of the waves and this propels the structures in the opposite direction. Consider a sheet above the ground; if a traveling wave is developed in the sheet, it begins to bend in the shape of a wave and pockets enclosing fluid are generated throughout the sheet. As the traveling wave propagates, the air pocket formed between the sheet and the ground also moves and thus acts as a pump. As the sheet exerts force to move the fluid, the fluid applies an equal and opposite force on the sheet. A preliminary experiment displaying the propulsion capabilities of the traveling waves are shown in Figure 6.1. In this video, traveling waves are generated on aluminum and brass beams. If the beam is unconstrained, the traveling waves result in propulsion of the 1D structure. However, if the beam is bounded, the waves have the capacity to transport materials. Surface properties such

as friction, weight of the structure etc have a major role in propulsion. A full study is required to fully understand the dynamics of such a system.

Figure 6.1: Propulsion based on traveling waves in structures. (Click on the picture for the video to start).

6.2.2 Fluid Structure Interaction (FSI)

The transformation of traveling waves into propulsive force is a complex phenomenon and is dependent on multiple variables. Fluid-structure interaction is one such variable that influences the strength of the traveling waves and thereby the propulsive thrust. For any fluid, the wave amplitude depends on multiple factors such as the voltage signal supplied to the PZT, the pressure of the medium, the carry-on load distribution, and the drag forces due the viscous/frictional elements present at the boundaries. These parameters are further dependent on the shape of the system and the buoyant force distribution on the structure. The study of these parameters will be crucial to understand how the waves and structures can be tailored for different applications such as either vehicle design or pumping mechanisms. An example of FSI is shown in Figure 6.2. In this video, traveling waves are generated in a cylindrical structure immersed in water; as a result vortices are generated in the fluid.

6.2.3 Structural design optimization

Leveraging carefully prescribed structural modes of monolithic structures allows vibration-based motivity in different mediums. Activation of the needed modes is given by the coupling of piezo-ceramics to the structural component. At resonance, smart materials (such as piezo-ceramics) have

Figure 6.2: Cylindrical traveling wave generate vortices in the fluid surrounding it. (Click on the picture for the video to start).

the highest control authority levels and work as excellent sources of excitation. Manipulating structural rigidity increases or decreases the resonant frequencies in order to best suite the application and operational condition. Depending on the application, manipulation of structural modes result in desired dynamics. For example, a single piezo-ceramics bonded at the optimized location on a helmet viser can result in traveling waves. Figure 6.3 shows the experimentally generated traveling waves at a resonant frequency using a single MFC.

6.2.4 Drag reduction

Skin friction drag is a major source of energy loss in transportation, from cars to boats to airplanes. As a result, a large amount of research has focused on reducing the amount of skin friction drag experienced, with recent interest involving the use of span wise (perpendicular to flow) traveling waves with out-of-plane wall deformation. Initial experiments in literature [225] have achieved a 6% drag reduction by actuating a surface and disturbing the boundary layer. Other preliminary studies have resulted in drag reductions of up to 13% [226–228]. However, the focus of these studies has been driven mainly from a fluids standpoint and the traveling waves themselves are not well-characterized, have frequency limitations, or require discrete highly intrusive actuators. Thus, by leveraging our research on traveling wave generation, modeled and experimentally validated traveling waves can be generated at varying frequencies to surpass the 13% drag reduction values already achieved. Since this research takes advantage of low-profile piezoelectric actuators, drag reduction using traveling waves can be achieved in a noninvasive and retro-fittable way and can be

Figure 6.3: Traveling waves generated in a helmet viser using a single MFC (Click on the picture for the video to start).

implemented in a varying degree of applications including airplanes, boats, and pipes.

References

[1] **Inman, D. J.** and **Singh, R. C.**, Engineering vibration, Vol. 3, Prentice Hall Upper Saddle River, 2001. xvii, 4, 16, 17, 18, 109

[2] **Simulia, D. S.**, *Abaqus 6.12 documentation*, Providence, Rhode Island, US, 2012. xvii, 90

[3] **Achenbach, J.**, Wave propagation in elastic solids, Elsevier, 2012. 1

[4] **Brillouin, L.**, Wave propagation in periodic structures: electric filters and crystal lattices, Courier Corporation, 2003. 1

[5] **Doyle, J. F.**, Wave propagation in structures, Springer, 1989. 1

[6] **Graff, K. F.**, Wave motion in elastic solids, Courier Corporation, 2012. 1

[7] **Junger, M. C.** and **Feit, D.**, Sound, structures, and their interaction, Vol. 225, MIT press Cambridge, 1986. 1, 4

[8] **Meirovitch, L.**, Elements of vibration analysis, McGraw-Hill, 1975. 1, 109

[9] **Rao, S. S.** and **Yap, F. F.**, Mechanical vibrations, Vol. 4, Addison-Wesley Reading, 1995. 1

[10] **Ahmadian, M.** and **Deguilio, A. P.**, *Recent advances in the use of piezoceramics for vibration suppression*, The Shock and Vibration Digest, Vol. 33, No. 1, pp. 15–22, 2001. 1, 4

[11] **Sodano, H. A., Inman, D. J.** and **Park, G.**, *A review of power harvesting from vibration using piezoelectric materials*, Shock and Vibration Digest, Vol. 36, No. 3, pp. 197–206, 2004. 1

[12] **Taylor, G.**, *The action of waving cylindrical tails in propelling microscopic organisms*, Proceedings of the Royal Society of London. Series A, Mathematical and Physical Sciences, pp. 225–239, 1952. 1, 2

[13] **Machin, K.**, *Wave propagation along flagella*, J. exp. Biol, Vol. 35, No. 4, pp. 796–806, 1958. 1, 2

[14] **Timoshenko, S., Woinowsky-Krieger, S.** and **Woinowsky-Krieger, S.**, Theory of plates and shells, Vol. 2, McGraw-hill New York, 1959. 1

[15] **Taylor, G.**, *Analysis of the swimming of microscopic organisms*, *Proceedings of the Royal Society of London A: Mathematical, Physical and Engineering Sciences*, Vol. 209, pp. 447–461, The Royal Society, 1951. 2

[16] **Brokaw, C. J.**, *Non-sinusoidal bending waves of sperm flagella*, Journal of Experimental Biology, Vol. 43, No. 1, pp. 155–169, 1965. 2

[17] **Rikmenspoel, R.**, *The tail movement of bull spermatozoa: Observations and model calculations*, Biophysical journal, Vol. 5, No. 4, pp. 365–392, 1965. 2

[18] **Brokaw, C. J.**, *Bend propagation by a sliding filament model for flagella*, Journal of Experimental Biology, Vol. 55, No. 2, pp. 289–304, 1971. 2

[19] **Brokaw, C. J.**, *Flagellar Movement: A Sliding Filament Model An explanation is suggested for the spontaneous propagation of bending waves by flagella*, Science, Vol. 178, No. 4060, pp. 455–462, 1972. 2

[20] **Rikmenspoel, R.**, *Algebraic expressions for the waveforms of sea urchin sperm flagella*, Journal of theoretical biology, Vol. 116, No. 1, pp. 127–147, 1985. 2

[21] **Sleigh, M.**, *Mechanisms of flagellar propulsion*, Protoplasma, Vol. 164, No. 1-3, pp. 45–53, 1991. 2

[22] **Ehlers, K. M., Samuel, A., Berg, H. C.** and **Montgomery, R.**, *Do cyanobacteria swim using traveling surface waves?*, Proceedings of the National Academy of Sciences, Vol. 93, No. 16, pp. 8340–8343, 1996. 2

[23] **Dreyfus, R., Baudry, J., Roper, M. L., Fermigier, M., Stone, H. A.** and **Bibette, J.**, *Microscopic artificial swimmers*, Nature, Vol. 437, No. 7060, pp. 862–865, 2005. 2

[24] **Gauger, E.** and **Stark, H.**, *Numerical study of a microscopic artificial swimmer*, Physical Review E, Vol. 74, No. 2, pp. 021907, 2006. 2

[25] **Lauga, E.** and **Powers, T. R.**, *The hydrodynamics of swimming microorganisms*, Reports on Progress in Physics, Vol. 72, No. 9, pp. 096601, 2009. 2

[26] **Williams, B. J., Anand, S. V., Rajagopalan, J.** and **Saif, M. T. A.**, *A self-propelled biohybrid swimmer at low Reynolds number*, Nature communications, Vol. 5, 2014. 2, 3

[27] **Moses, E., Fineberg, J.** and **Steinberg, V.**, *Multistability and confined traveling-wave patterns in a convecting binary mixture*, Physical Review A, Vol. 35, No. 6, pp. 2757, 1987. 2, 144

[28] **Linz, S., Lucke, M., Muller, H.** and **Niederlander, J.**, *Convection in binary fluid mixtures: Traveling waves and lateral currents*, Physical Review A, Vol. 38, No. 11, pp. 5727, 1988. 2

[29] **Barten, W., Lucke, M.** and **Kamps, M.**, *Localized traveling-wave convection in binary-fluid mixtures*, Physical review letters, Vol. 66, No. 20, pp. 2621, 1991. 2, 144

[30] **Barten, W., Lucke, M., Kamps, M.** and **Schmitz, R.**, *Convection in binary fluid mixtures. I. Extended traveling-wave and stationary states*, Physical Review E, Vol. 51, No. 6, pp. 5636, 1995. 2

[31] **Barten, W., Lucke, M., Kamps, M.** and **Schmitz, R.**, *Convection in binary fluid mixtures. II. Localized traveling waves*, Physical Review E, Vol. 51, No. 6, pp. 5662, 1995. 2

[32] **von Bekesy, G.**, *Travelling waves as frequency analysers in the cochlea*, Nature, Vol. 225, pp. 1207–1209, 1970, this is one of the important paper on cochlea. it is important author. A nobel laureate. 2, 3

[33] **Hubbard, A.**, *A traveling-wave amplifier model of the cochlea*, Science, Vol. 259, No. 5091, pp. 68–71, 1993, this is one of the important paper on cochlea. it is important author. A nobel laureate. 2, 3

[34] **Ghaffari, R., Aranyosi, A. J., Richardson, G. P.** and **Freeman, D. M.**, *Tectorial membrane travelling waves underlie abnormal hearing in Tectb mutant mice*, Nat Commun, Vol. 1, pp. 96, 2010. 2, 3

[35] **Dong, W.** and **Olson, E.**, *Supporting evidence for reverse cochlear traveling waves*, The Journal of the Acoustical Society of America, Vol. 123, No. 1, pp. 222–240, 2008, this is one of the important paper on cochlea. it is important author. A nobel laureate. 2, 3

[36] **Ghaffari, R., Aranyosi, A. J.** and **Freeman, D. M.**, *Longitudinally propagating traveling waves of the mammalian tectorial membrane*, Proceedings of the National Academy of Sciences, Vol. 104, No. 42, pp. 16510–16515, 2007, this is one of the important paper on cochlea. it is important author. A nobel laureate. 2, 3

[37] **Inaoka, T., Shintaku, H., Nakagawa, T., Kawano, S., Ogita, H., Sakamoto, T., Hamanishi, S., Wada, H.** and **Ito, J.**, *Piezoelectric materials mimic the function of the cochlear sensory epithelium*, Proceedings of the National Academy of Sciences, Vol. 108, No. 45, pp. 18390–18395, 2011, this is one of the important paper on cochlea. it is important author. A nobel laureate . HI. 2, 3

[38] **Temchin, A. N., Recio-Spinoso, A., Cai, H.** and **Ruggero, M. A.**, *Traveling waves on the organ of Corti of the chinchilla cochlea: spatial trajectories of inner hair cell depolarization inferred from responses of auditory-nerve fibers*, The Journal of Neuroscience, Vol. 32, No. 31, pp. 10522–10529, 2012, this is one of the important paper on cochlea. it is important author. A nobel laureate. 2, 3

[39] **Nam, J.-H.**, *Microstructures in the Organ of Corti Help Outer Hair Cells Form Traveling Waves along the Cochlear Coil*, Biophysical Journal, Vol. 106, No. 11, pp. 2426–2433, 2014, this is one of the important paper on cochlea. it is important author. A nobel laureate. 2, 3

[40] **Kim, S., Song, W. J., Jang, J., Jang, J. H.** and **Choi, H.**, *Mechanical frequency selectivity of an artificial basilar membrane using a beam array with narrow supports*, Journal of Micromechanics and Microengineering, Vol. 23, No. 9, pp. 095018, 2013, this is one of the important paper on cochlea. it is important author. A nobel laureate. 2

[41] **Loh, B.-G.** and **Ro, P. I.**, *An object transport system using flexural ultrasonic progressive waves generated by two-mode excitation*, Ultrasonics, Ferroelectrics and Frequency Control, IEEE Transactions on, Vol. 47, No. 4, pp. 994–999, 2000. 2, 7, 15, 29, 57, 97

[42] **Nomura, S., Matula, T. J., Satonobu, J.** and **Crum, L. A.**, *Noncontact transportation in water using ultrasonic traveling waves*, The Journal of the Acoustical Society of America, Vol. 121, No. 3, pp. 1332–1336, 2007. 2, 5

[43] **Weiss, J. B.**, *Transport and mixing in traveling waves*, Physics of Fluids A: Fluid Dynamics (1989-1993), Vol. 3, No. 5, pp. 1379–1384, 1991. 2, 5

[44] **Hashimoto, Y., Koike, Y.** and **Ueha, S.**, *Transporting objects without contact using flexural traveling waves*, The Journal of the Acoustical Society of America, Vol. 103, No. 6, pp. 3230–3233, 1998. 2, 5

[45] **fang Liu, J., You, H., Jiao, X. Y.** and **Jiang, H.**, *Non-contact transportation of heavy load objects using ultrasonic suspension and aerostatic suspension*, Proceedings of the In-

stitution of Mechanical Engineers, Part C: Journal of Mechanical Engineering Science, p. 0954406213492483, 2013. 2, 5

[46] **Faisst, H.** and **Eckhardt, B.**, *Traveling waves in pipe flow*, Physical Review Letters, Vol. 91, No. 22, pp. 224502, 2003. 2, 5

[47] **Alben, S., Witt, C., Baker, T. V., Anderson, E.** and **Lauder, G. V.**, *Dynamics of freely swimming flexible foils*, Physics of Fluids (1994-present), Vol. 24, No. 5, pp. 051901, 2012. 2, 3

[48] **Kosa, G., Shoham, M.** and **Zaaroor, M.**, *Propulsion of a swimming micro medical robot*, *Robotics and Automation, 2005. ICRA 2005. Proceedings of the 2005 IEEE International Conference on*, pp. 1327–1331, IEEE, 2005. 2, 3

[49] **Edd, J., Payen, S., Rubinsky, B., Stoller, M. L.** and **Sitti, M.**, *Biomimetic propulsion for a swimming surgical micro-robot*, *Intelligent Robots and Systems, 2003.(IROS 2003). Proceedings. 2003 IEEE/RSJ International Conference on*, Vol. 3, pp. 2583–2588, IEEE, 2003. 2, 3

[50] **Liu, F., Lee, K.-M.** and **Yang, C.-J.**, *Hydrodynamics of an undulating fin for a wave-like locomotion system design*, Mechatronics, IEEE/ASME Transactions on, Vol. 17, No. 3, pp. 554–562, 2012. 2, 3

[51] **Ramananarivo, S., Godoy-Diana, R.** and **Thiria, B.**, *Propagating waves in bounded elastic media: Transition from standing waves to anguilliform kinematics*, EPL (Europhysics Letters), Vol. 105, No. 5, pp. 54003, 2014. 2, 3

[52] **Shirgaonkar, A. A., Curet, O. M., Patankar, N. A.** and **MacIver, M. A.**, *The hydrodynamics of ribbon-fin propulsion during impulsive motion*, Journal of Experimental Biology, Vol. 211, No. 21, pp. 3490–3503, 2008. 2, 3

[53] **Bose, N.** and **Lien, J.**, *Propulsion of a fin whale (Balaenoptera physalus): why the fin whale is a fast swimmer*, Proceedings of the Royal Society of London B: Biological Sciences, Vol. 237, No. 1287, pp. 175–200, 1989. 2, 3

[54] **Barrett, D., Grosenbaugh, M.** and **Triantafyllou, M.**, *The optimal control of a flexible hull robotic undersea vehicle propelled by an oscillating foil*, *Autonomous Underwater Vehicle Technology, 1996. AUV'96., Proceedings of the 1996 Symposium on*, pp. 1–9, IEEE, 1996. 2, 3

[55] **Sfakiotakis, M., Lane, D. M.** and **Davies, J. B. C.**, *Review of fish swimming modes for aquatic locomotion*, Oceanic Engineering, IEEE Journal of, Vol. 24, No. 2, pp. 237–252, 1999. 2

[56] **Chen, L., Wang, Y., Ma, S.** and **Li, B.**, *Analysis of traveling wave locomotion of snake robot*, *Robotics, Intelligent Systems and Signal Processing, 2003. Proceedings. 2003 IEEE International Conference on*, Vol. 1, pp. 365–369, IEEE, 2003. 2

[57] **Roh, Y., Lee, S.** and **Han, W.**, *Design and fabrication of a new traveling wave-type ultrasonic linear motor*, Sensors and Actuators A: Physical, Vol. 94, No. 3, pp. 205–210, 2001. 2

[58] **Plat, H.** and **Bucher, I.**, *Parametric excitation of traveling waves in a circular non-dispersive medium*, Journal of Sound and Vibration, Vol. 333, No. 5, pp. 1408–1420, 2014. 2

[59] **Minikes, A., Bucher, I.** and **Haber, S.**, *Levitation force induced by pressure radiation in gas squeeze films*, The Journal of the Acoustical Society of America, Vol. 116, No. 1, pp. 217–226, 2004. 2, 97

[60] **Setter, E.** and **Bucher, I.**, *Robotic swimmer/pump based on an optimal wave generating mechanism*, Mechanism and Machine Theory, Vol. 70, pp. 266–277, 2013. 2

[61] **Setter, E., Bucher, I.** and **Haber, S.**, *Low-Reynolds-number swimmer utilizing surface traveling waves: Analytical and experimental study*, Physical Review E, Vol. 85, No. 6, pp. 066304, 2012. 2

[62] **Minikes, A.** and **Bucher, I.**, *Noncontacting lateral transportation using gas squeeze film generated by flexural traveling waves Numerical analysis*, The Journal of the Acoustical Society of America, Vol. 113, No. 5, pp. 2464–2473, 2003. 2, 4

[63] **Gabai, R.** and **Bucher, I.**, *Excitation and sensing of multiple vibrating traveling waves in one-dimensional structures*, Journal of sound and vibration, Vol. 319, No. 1, pp. 406–425, 2009. 2, 4, 7

[64] **Gabai, R.** and **Bucher, I.**, *Generating Traveling Vibration Waves in Finite Structures*, *ASME 2008 9th Biennial Conference on Engineering Systems Design and Analysis*, pp. 761–770, American Society of Mechanical Engineers, 2008. 2, 4, 7

[65] **Bucher, I.**, *Estimating the ratio between travelling and standing vibration waves under non-stationary conditions*, Journal of sound and vibration, Vol. 270, No. 1, pp. 341–359, 2004. 2, 7, 144, 145

[66] **Chen, L., Ma, S., Wang, Y., Li, B.** and **Duan, D.**, *Design and modelling of a snake robot in traveling wave locomotion*, Mechanism and Machine Theory, Vol. 42, No. 12, pp. 1632–1642, 2007. 2

[67] **Bolborici, V., Dawson, F. P.** and **Pugh, M. C.**, *A finite volume method and experimental study of a stator of a piezoelectric traveling wave rotary ultrasonic motor*, Ultrasonics, Vol. 54, No. 3, pp. 809–20, 2014. 2

[68] **Hariri, H., Bernard, Y.** and **Razek, A.**, *A traveling wave piezoelectric beam robot*, Smart Materials and Structures, Vol. 23, No. 2, pp. 025013, 2014. 2

[69] **Jones, L., Spahnie, J., Lefeave, K., Haltom, C., Underwood, A., Aber, J., Malladi, V. S., Joyce, B.** and **Tarazaga, P. A.**, *Vehicle Propulsion by Solid State Motion*, *ASME 2014 Conference on Smart Materials, Adaptive Structures and Intelligent Systems*, American Society of Mechanical Engineers, 2014. 2, 5, 108

[70] **Malladi, V. S., Avirovik, D., Priya, S.** and **Tarazaga, P. A.**, *Traveling wave phenomenon through piezoelectric actuation of a free-free beam"*, *ASME 2014 Conference on Smart Materials, Adaptive Structures and Intelligent Systems*, American Society of Mechanical Engineers, 2014. 2, 53, 97, 108, 146

[71] **Brennen, C.** and **Winet, H.**, *Fluid mechanics of propulsion by cilia and flagella*, Annual Review of Fluid Mechanics, Vol. 9, No. 1, pp. 339–398, 1977. 2

[72] **Kancharala, A. K., Dewillie, K.** and **Philen, M. K.**, *Influence of bending mode shape and trailing edge deflection on propulsive performance of flexible heaving fins using digital image correlation*, *SPIE Smart Structures and Materials+ Nondestructive Evaluation and Health Monitoring*, pp. 90550Q–90550Q–10, International Society for Optics and Photonics, 2014. 2

[73] **Kancharala, A.** and **Philen, M.**, *Study of flexible fin and compliant joint stiffness on propulsive performance: theory and experiments*, Bioinspiration and Biomimetics, Vol. 9, No. 3, pp. 036011, 2014. 2

[74] **Wu, T.-t.**, *Swimming of a waving plate*, Journal of Fluid Mechanics, Vol. 10, No. 03, pp. 321–344, 1961. 2

[75] **Kancharala, A.** and **Philen, M.**, *Enhanced hydrodynamic performance of flexible fins using macro fiber composite actuators*, Smart Materials and Structures, Vol. 23, No. 11, pp. 115012, 2014. 2

[76] **Lighthill, M.**, *Note on the swimming of slender fish*, Journal of fluid Mechanics, Vol. 9, No. 02, pp. 305–317, 1960, the paper talks about tasl. 3

[77] **Lighthill, M.**, *Hydromechanics of aquatic animal propulsion*, Annual review of fluid mechanics, Vol. 1, No. 1, pp. 413–446, 1969. 3

[78] **Taylor, G.**, *Analysis of the swimming of long and narrow animals*, *Proceedings of the Royal Society of London A: Mathematical, Physical and Engineering Sciences*, Vol. 214, pp. 158–183, The Royal Society, 1952. 3

[79] **Yan, Y.**, *Recent advances in computational simulation of macro-, meso-, and micro-scale biomimetics related fluid flow problems*, Journal of Bionic Engineering, Vol. 4, No. 2, pp. 97–107, 2007. 3

[80] **Rosen, M. W.** and **Cornford, N. E.**, *Fluid friction of fish slimes*, Nature, Vol. 234, No. 5323, pp. 49–51, 1971. 3

[81] **Pedley, T.** and **Hill, S.**, *Large-amplitude undulatory fish swimming: fluid mechanics coupled to internal mechanics*, Journal of Experimental Biology, Vol. 202, No. 23, pp. 3431–3438, 1999. 3

[82] **Lu, X.-Y.** and **Yin, X.-Z.**, *Propulsive performance of a fish-like travelling wavy wall*, Acta Mechanica, Vol. 175, No. 1-4, pp. 197–215, 2005. 3

[83] **Avron, J., Gat, O.** and **Kenneth, O.**, *Optimal swimming at low Reynolds numbers*, Physical review letters, Vol. 93, No. 18, pp. 186001, 2004. 3

[84] **Adkins, D.** and **Yan, Y.**, *CFD simulation of fish-like body moving in viscous liquid*, Journal of Bionic Engineering, Vol. 3, No. 3, pp. 147–153, 2006. 3

[85] **Zhang, Y., He, J.** and **Low, K.**, *Parametric study of an underwater finned propulsor inspired by bluespotted ray*, Journal of Bionic Engineering, Vol. 9, No. 2, pp. 166–176, 2012. 3

[86] **Yang, S.-b., Qiu, J.** and **Han, X.-y.**, *Kinematics modeling and experiments of pectoral oscillation propulsion robotic fish*, Journal of Bionic engineering, Vol. 6, No. 2, pp. 174–179, 2009. 3

[87] **Transeth, A. A., Pettersen, K. Y.** and **Liljeback, P.**, *A survey on snake robot modeling and locomotion*, Robotica, Vol. 27, No. 07, pp. 999–1015, 2009. 3

[88] **Raz, O.** and **Leshansky, A.**, *Efficiency of cargo towing by a microswimmer*, Physical Review E, Vol. 77, No. 5, pp. 055305, 2008. 3, 5

[89] **Low, K.**, *Modelling and parametric study of modular undulating fin rays for fish robots*, Mechanism and Machine Theory, Vol. 44, No. 3, pp. 615–632, 2009. 3

[90] **Crespi, A., Badertscher, A., Guignard, A.** and **Ijspeert, A. J.**, *AmphiBot I: an amphibious snake-like robot*, Robotics and Autonomous Systems, Vol. 50, No. 4, pp. 163–175, 2005. 3

[91] **Chen, L., Wang, Y., Ma, S.** and **Li, B.**, *Analysis of traveling wave locomotion of snake robot*, *Robotics, Intelligent Systems and Signal Processing, 2003. Proceedings. 2003 IEEE International Conference on*, Vol. 1, pp. 365–369, IEEE, 2003. 3

[92] **Chen, L., Ma, S., Wang, Y., Li, B.** and **Duan, D.**, *Design and modelling of a snake robot in traveling wave locomotion*, Mechanism and Machine Theory, Vol. 42, No. 12, pp. 1632–1642, 2007. 3

[93] **Chan, B., Balmforth, N.** and **Hosoi, A.**, *Building a better snail: Lubrication and adhesive locomotion*, Physics of Fluids (1994-present), Vol. 17, No. 11, pp. 113101, 2005. 3

[94] **Wang, Z., Hang, G., Wang, Y., Li, J.** and **Du, W.**, *Embedded SMA wire actuated biomimetic fin: a module for biomimetic underwater propulsion*, Smart Materials and Structures, Vol. 17, No. 2, pp. 025039, 2008. 3

[95] **Udayashankar, A. P., Kossl, M.** and **Nowotny, M.**, *Tonotopically arranged traveling waves in the miniature hearing organ of bushcrickets*, PloS one, Vol. 7, No. 2, pp. e31008–e31008, 2012. 3

[96] **Ruggero, M. A.**, *Cochlear Delays and Traveling Waves: Comments on'Experimental Look at Cochlear Mechanics':[A. Dancer, Audiology 1992; 31: 301-312] Ruggero*, International Journal of Audiology, Vol. 33, No. 3, pp. 131–142, 1994. 3

[97] **Johnstone, B., Patuzzi, R.** and **Yates, G.**, *Basilar membrane measurements and the travelling wave*, Hearing research, Vol. 22, No. 1, pp. 147–153, 1986. 3

[98] **Taft, D., Grayden, D. B.** and **Burkitt, A. N.**, *Across-frequency delays based on the cochlear traveling wave: Enhanced speech presentation for cochlear implants*, Biomedical Engineering, IEEE Transactions on, Vol. 57, No. 3, pp. 596–606, 2010. 3

[99] **Shintaku, H., Nakagawa, T., Kitagawa, D., Tanujaya, H., Kawano, S.** and **Ito, J.**, *Development of piezoelectric acoustic sensor with frequency selectivity for artificial cochlea*, Sensors and Actuators A: Physical, Vol. 158, No. 2, pp. 183–192, 2010. 3

[100] **Loizou, P. C.**, *Mimicking the human ear*, Signal Processing Magazine, IEEE, Vol. 15, No. 5, pp. 101–130, 1998. 3

[101] **Gan, R. Z., Reeves, B. P.** and **Wang, X.**, *Modeling of sound transmission from ear canal to cochlea*, Annals of biomedical engineering, Vol. 35, No. 12, pp. 2180–2195, 2007. 3

[102] **Fahy, F. J.**, Foundations of engineering acoustics, Academic press, 2000. 4

[103] **Craig, R. R.** and **Kurdila, A. J.**, Fundamentals of structural dynamics, John Wiley and Sons, 2006. 4

[104] **Rayleigh, L.**, *XVII. On the maintenance of vibrations by forces of double frequency, and on the propagation of waves through a medium endowed with a periodic structure*, The London, Edinburgh, and Dublin Philosophical Magazine and Journal of Science, Vol. 24, No. 147, pp. 145–159, 1887. 4

[105] **Mead, D.**, *Wave propagation in continuous periodic structures: research contributions from Southampton, 1964–1995*, Journal of Sound and Vibration, Vol. 190, No. 3, pp. 495–524, 1996. 4

[106] **Von Flotow, A.** and **Schafer, B.**, *Wave-absorbing controllers for a flexible beam*, Journal of Guidance, Control, and Dynamics, Vol. 9, No. 6, pp. 673–680, 1986. 4

[107] **Von Flotow, A.**, *Traveling wave control for large spacecraft structures*, Journal of Guidance, Control, and Dynamics, Vol. 9, No. 4, pp. 462–468, 1986. 4

[108] **McKinnell, R.**, *Active vibration isolation by cancelling bending waves*, *Proceedings of the Royal Society of London A: Mathematical, Physical and Engineering Sciences*, Vol. 421, pp. 357–393, The Royal Society, 1989. 4

[109] **Spadoni, A., Ruzzene, M.** and **Cunefare, K.**, *Vibration and wave propagation control of plates with periodic arrays of shunted piezoelectric patches*, Journal of Intelligent Material Systems and Structures, Vol. 20, No. 8, pp. 979–990, 2009. 4

[110] **Casadei, F., Ruzzene, M., Dozio, L.** and **Cunefare, K.**, *Broadband vibration control through periodic arrays of resonant shunts: experimental investigation on plates*, Smart materials and structures, Vol. 19, No. 1, pp. 015002, 2010. 4

[111] **Beck, B. S., Cunefare, K. A., Ruzzene, M.** and **Collet, M.**, *Experimental analysis of a cantilever beam with a shunted piezoelectric periodic array*, Journal of Intelligent Material Systems and Structures, p. 1045389X11411119, 2011. 4

[112] **Park, C. H.** and **Baz, A.**, *Vibration control of beams with negative capacitive shunting of interdigital electrode piezoceramics*, Journal of Vibration and Control, Vol. 11, No. 3, pp. 331–346, 2005. 4

[113] **Tarazaga, P. A., Inman, D. J.** and **Wilkie, W. K.**, *Control of a space rigidizable inflatable boom using macro-fiber composite actuators*, Journal of Vibration and Control, Vol. 13, No. 7, pp. 935–950, 2007. 4

[114] **Mizutani, K., Yatomi, C.** and **Inoue, K.**, *Active vibration control for flexible structures using a wave-absorbing control method*, JSME international journal. Ser. C, Dynamics, control, robotics, design and manufacturing, Vol. 39, No. 2, pp. 188–194, 1996. 4

[115] **Casadei, F., Ruzzene, M., Beck, B.** and **Cunefare, K.**, *Vibration control of plates featuring periodic arrays of hybrid shunted piezoelectric patches*, *SPIE Smart Structures and Materials+ Nondestructive Evaluation and Health Monitoring*, pp. 72881J–72881J, International Society for Optics and Photonics, 2009. 4

[116] **O'Connor, W. J.**, *Wave-echo control of lumped flexible systems*, Journal of Sound and Vibration, Vol. 298, No. 4, pp. 1001–1018, 2006. 4

[117] **O'Connor, W. J.**, *Wave-based analysis and control of lump-modeled flexible robots*, Robotics, IEEE Transactions on, Vol. 23, No. 2, pp. 342–352, 2007. 4

[118] **Gabai, R.** and **Bucher, I.**, *Spatial and temporal excitation to generate traveling waves in structures*, Journal of Applied Mechanics, Vol. 77, No. 2, pp. 021010, 2010. 4, 7, 97

[119] **Roy, R.** and **Kailath, T.**, *ESPRIT-estimation of signal parameters via rotational invariance techniques*, Acoustics, Speech and Signal Processing, IEEE Transactions on, Vol. 37, No. 7, pp. 984–995, 1989. 4

[120] **Radcliffe, C. J.** and **Mote, J. C. D.**, *Identification and Control of Rotating Disk Vibration*, Journal of Dynamic Systems, Measurement, and Control, Vol. 105, No. 1, pp. 39–45, 1983, 10.1115/1.3139726. 4

[121] **Lin, F.-J., Wai, R.-J.** and **Hong, C.-M.**, *Identification and control of rotary traveling-wave type ultrasonic motor using neural networks*, Control Systems Technology, IEEE Transactions on, Vol. 9, No. 4, pp. 672–680, 2001. 4

[122] **Tanaka, N.** and **Kikushima, Y.**, *Active Wave Control of a Flexible Beam. Fundamental Characteristics of an Active-Sink System and Its Verification*, JSME international journal. Ser. 3, Vibration, control engineering, engineering for industry, Vol. 35, No. 2, pp. 236–244, 1992. 4

[123] **Tanaka, N.** and **Kikushima, Y.**, *Optimal vibration feedback control of an Euler-Bernoulli beam: Toward realization of the active sink method*, Journal of vibration and acoustics, Vol. 121, No. 2, pp. 174–182, 1999. 4

[124] **Wang, Q., Zhi, Y.** and **Wang, D.**, *A note on wave control in lumped parameter system*, Computers and structures, Vol. 57, No. 1, pp. 177–181, 1995. 4

[125] **Tanaka, N.** and **Kikushima, Y.**, *Active Wave Control of a Flexible Beam. Proposition of the Active Sink Method*, JSME international journal. Ser. 3, Vibration, control engineering, engineering for industry, Vol. 34, No. 2, pp. 159–167, 1991. 4

[126] **Tan, C.** and **Ying, S.**, *Active wave control of the axially moving string: theory and experiment*, Journal of sound and vibration, Vol. 236, No. 5, pp. 861–880, 2000. 4

[127] **Pines, D.** and **Von Flotow, A.**, *Active control of bending wave propagation at acoustic frequencies*, *American Control Conference, 1989*, pp. 221–230, IEEE, 1989. 4

[128] **Minikes, A., Gabay, R., Bucher, I.** and **Feldman, M.**, *On the sensing and tuning of progressive structural vibration waves*, Ultrasonics, Ferroelectrics and Frequency Control, IEEE Transactions on, Vol. 52, No. 9, pp. 1565–1576, 2005. 4, 7

[129] **Mei, C.**, *The analysis and control of longitudinal vibrations from wave viewpoint*, Journal of vibration and acoustics, Vol. 124, No. 4, pp. 645–649, 2002. 4

[130] **Iwamoto, H.** and **Tanaka, N.**, *Adaptive feed-forward control of flexural waves propagating in a beam using smart sensors*, Smart materials and structures, Vol. 14, No. 6, pp. 1369, 2005. 4

[131] **Gardonio, P.** and **Elliott, S.**, *Active control of waves on a one-dimensional structure with a scattering termination*, Journal of sound and vibration, Vol. 192, No. 3, pp. 701–730, 1996. 4

[132] **Chung, C. H.** and **Tan, C. A.**, *Active Vibration Control of the Axially Moving String by Wave Cancellation*, Journal of Vibration and Acoustics, Vol. 117, No. 1, pp. 49–55, 1995, 10.1115/1.2873866. 4, 15

[133] **Chen, L.-Q.**, *Analysis and control of transverse vibrations of axially moving strings*, Applied Mechanics Reviews, Vol. 58, No. 2, pp. 91–116, 2005. 4, 15

[134] **Böhringer, K. F.** and **Choset, H.**, Distributed manipulation, Springer Science & Business Media, 2012. 4

[135] **Luntz, J. E.** and **Messner, W.**, *A distributed control system for flexible materials handling*, Control Systems, IEEE, Vol. 17, No. 1, pp. 22–28, 1997. 4

[136] **Böhringer, K.-F., Bhatt, V.** and **Goldberg, K. Y.**, *Sensorless manipulation using transverse vibrations of a plate*, *Robotics and Automation, 1995. Proceedings., 1995 IEEE International Conference on*, Vol. 2, pp. 1989–1996, IEEE, 1995. 4

[137] **Luntz, J. E., Messner, W.** and **Choset, H.**, *Distributed manipulation using discrete actuator arrays*, The International Journal of Robotics Research, Vol. 20, No. 7, pp. 553–583, 2001. 4

[138] **Argentina, M., Skotheim, J.** and **Mahadevan, L.**, *Settling and swimming of flexible fluid-lubricated foils*, Physical review letters, Vol. 99, No. 22, pp. 224503, 2007. 5

[139] **Jafferis, N. T.**, The flying carpet and other tales, Ph.D. thesis, Princeton University, 2012. 5

[140] **Wickert, J.** and **Mote, C.**, *Current research on the vibration and stability of axially-moving materials*, The Shock and vibration digest, 1988. 5

[141] **Wang, J.** and **Li, Q.**, *Active vibration control methods of axially moving materials-a review*, Journal of Vibration and Control, Vol. 10, No. 4, pp. 475–491, 2004. 5

[142] **Pisarski, D.** and **Bajer, C.**, *Smart Suspension System for Linear Guideways*, Journal of Intelligent and Robotic Systems, Vol. 62, No. 3-4, pp. 451–466, 2011. 5

[143] **Ishii, T., Mizuno, Y., Koyama, D., Nakamura, K., Harada, K.** and **Uchida, Y.**, *Plate-shaped non-contact ultrasonic transporter using flexural vibration*, Ultrasonics, Vol. 54, No. 2, pp. 455–460, 2014. 5

[144] **Bai, D., Ishii, T., Nakamura, K., Ueha, S., Yonezawa, T.** and **Takahashi, T.**, *An ultrasonic motor driven by the phase-velocity difference between two traveling waves*, Ultrasonics, Ferroelectrics, and Frequency Control, IEEE Transactions on, Vol. 51, No. 6, pp. 680–685, 2004. 5

[145] **Duan, W., Quek, S. T.** and **Wang, Q.**, *A novel ring type ultrasonic motor with multiple wavenumbers: design, fabrication and characterization*, Smart Materials and Structures, Vol. 18, No. 12, pp. 125025, 2009. 5

[146] **Jafferis, N. T.** and **Sturm, J. C.**, *Fundamental and experimental conditions for the realization of traveling-wave-induced aerodynamic propulsive forces by piezoelectrically deformed plastic substrates*, Microelectromechanical Systems, Journal of, Vol. 22, No. 2, pp. 495–505, 2013. 5

[147] **Zhao, S.** and **Wallaschek, J.**, *A standing wave acoustic levitation system for large planar objects*, Archive of Applied Mechanics, Vol. 81, No. 2, pp. 123–139, 2011. 5

[148] **Vandaele, V., Lambert, P.** and **Delchambre, A.**, *Non-contact handling in microassembly: Acoustical levitation*, Precision engineering, Vol. 29, No. 4, pp. 491–505, 2005. 5

[149] **Ueha, S., Hashimoto, Y.** and **Koike, Y.**, *Non-contact transportation using near-field acoustic levitation*, Ultrasonics, Vol. 38, No. 1, pp. 26–32, 2000. 5

[150] **Ueha, S., Hashimoto, Y.** and **Koike, Y.**, *Ultrasonic actuators using near field acoustic levitation*, *Ultrasonics Symposium, 1998. Proceedings., 1998 IEEE*, Vol. 1, pp. 661–666, IEEE, 1998. 5

[151] **Xing, Z., He, B., Li, R., Dong, S., Gao, G.** and **Feng, K.**, *Bi-direction quasi-travelling wave piezoelectric rotary motor with single vibrator*, Materials Research Innovations, Vol. 18, No. S4, pp. S4–559–S4–563, 2014. 5

[152] **Uchino, K.**, *Piezoelectric ultrasonic motors: overview*, Smart Materials and structures, Vol. 7, No. 3, pp. 273, 1998. 5

[153] **Morita, T.**, *Miniature piezoelectric motors*, Sensors and Actuators A: Physical, Vol. 103, No. 3, pp. 291–300, 2003. 5

[154] **Meng, A. H., Nguyen, N.-T.** and **White, R. M.**, *Focused flow micropump using ultrasonic flexural plate waves*, Biomedical Microdevices, Vol. 2, No. 3, pp. 169–174, 2000. 5

[155] **Kurosawa, M. K., Chiba, M.** and **Higuchi, T.**, *Evaluation of a surface acoustic wave motor with a multi-contact-point slider*, Smart materials and structures, Vol. 7, No. 3, pp. 305, 1998. 5

[156] **Kurosawa, M. K.**, *State-of-the-art surface acoustic wave linear motor and its future applications*, Ultrasonics, Vol. 38, No. 1, pp. 15–19, 2000. 5

[157] **Iula, A.** and **Pappalardo, M.**, *A high-power traveling wave ultrasonic motor*, Ultrasonics, Ferroelectrics, and Frequency Control, IEEE Transactions on, Vol. 53, No. 7, pp. 1344–1351, 2006. 5

[158] **Hirata, H.** and **Ueha, S.**, *Design of a traveling wave type ultrasonic motor*, Ultrasonics, Ferroelectrics, and Frequency Control, IEEE Transactions on, Vol. 42, No. 2, pp. 225–231, 1995. 5

[159] **Hirata, H.** and **Ueha, S.**, *Characteristics estimation of a traveling wave type ultrasonic motor*, Ultrasonics, Ferroelectrics, and Frequency Control, IEEE Transactions on, Vol. 40, No. 4, pp. 402–406, 1993. 5

[160] **Flynn, A. M., Tavrow, L. S., Bart, S. F., Brooks, R., Ehrlich, D. J., Udayakumar, K.** and **Cross, L. E.**, *Piezoelectric micromotors for microrobots*, Microelectromechanical Systems, Journal of, Vol. 1, No. 1, pp. 44–51, 1992. 5

[161] **Ting, Y., Chen, L.-C., Li, C.-C.** and **Huang, J.-L.**, *Traveling-wave piezoelectric linear motor. I. The stator design*, Ultrasonics, Ferroelectrics, and Frequency Control, IEEE Transactions on, Vol. 54, No. 4, pp. 847–853, 2007. 5

[162] **Seemann, W.**, *A linear ultrasonic traveling wave motor of the ring type*, Smart materials and structures, Vol. 5, No. 3, pp. 361, 1996. 5

[163] **Hatsuzawa, T., Toyoda, K.** and **Tanimura, Y.**, *Speed control characteristics and digital servosystem of a circular traveling wave motor*, Review of Scientific Instruments, Vol. 57, No. 11, pp. 2886–2890, 1986. 5

[164] **Chen, Y., Liu, Q.** and **Zhou, T.**, *A traveling wave ultrasonic motor of high torque*, Ultrasonics, Vol. 44, pp. e581–e584, 2006. 5

[165] **Ro, J.-S., Yi, K.-P.** and **Jung, H.-K.**, *Characteristic analysis of an traveling wave ultrasonic motor using the cylindrical dynamic contact model*, *Electrical Machines and Systems (ICEMS), 2012 15th International Conference on*, pp. 1–6, IEEE, 2012. 5

[166] **Rajkumar, R.** and **Nogai, T.**, *A new method of improving the torque of a travelling wave ultrasonic motor*, *Advanced Intelligent Mechatronics, 1999. Proceedings. 1999 IEEE/ASME International Conference on*, pp. 109–113, IEEE, 1999. 5

[167] **Kurosawa, M., Takahashi, M.** and **Higuchi, T.**, *An ultrasonic XY stage using 10 MHz surface acoustic waves*, *Ultrasonics Symposium, 1994. Proceedings., 1994 IEEE*, Vol. 1, pp. 535–538, IEEE, 1993. 5

[168] **Kawai, T., Katsuma, M., Murakami, H., Hiramatsu, A.** and **Kaneda, N.**, *Piezoelectric vibration wave motor with multiple traveling wave generating members*, 1984. 5

[169] **Jingzhuo, S., Yu, L., Jingtao, H., Meiyu, X., Juwei, Z.** and **Lei, Z.**, *Novel intelligent PID control of traveling wave ultrasonic motor*, ISA transactions, Vol. 53, No. 5, pp. 1670–1679, 2014. 5

[170] **Chen, W., Liu, Y., Yang, X.** and **Liu, J.**, *Ring-type traveling wave ultrasonic motor using a radial bending mode*, IEEE transactions on ultrasonics, ferroelectrics, and frequency control, Vol. 61, No. 1, pp. 197–202, 2014. 5

[171] **Chau, K., Chung, S.** and **Chan, C.**, *Neuro-fuzzy speed tracking control of traveling-wave ultrasonic motor drives using direct pulsewidth modulation*, Industry Applications, IEEE Transactions on, Vol. 39, No. 4, pp. 1061–1069, 2003. 5

[172] **Gabay, R.** and **Bucher, I.**, *On Vibrating Traveling Waves Actuation, Sensing, and Tuning in Finite Structures*, *ASME 2006 International Mechanical Engineering Congress and Exposition*, pp. 809–817, American Society of Mechanical Engineers, 2006. 7, 97

[173] **Bani-Hani, M.** and **Karami, M.**, *Analytical structural optimization and experimental verifications for traveling wave generation in self-assembling swimming smart boxes*, Smart Materials and Structures, Vol. 24, No. 9, pp. 094005, 2015. 8

[174] **Leo, D. J.**, *Book-Engineering Analysis of Smart Material Systems, Johns wiley & sons*, Inc., Hoboken, New Jersey, 2007. 46, 86

[175] **Avirovik, D., Karami, M. A., Inman, D.** and **Priya, S.**, *L-shaped piezoelectric motor-part II: Analytical modeling*, Ultrasonics, Ferroelectrics, and Frequency Control, IEEE Transactions on, Vol. 59, No. 1, pp. 108–120, 2012. 48

[176] **Allemang, R. J.** and **Brown, D. L.**, *A correlation coefficient for modal vector analysis*, *Proceedings of the 1st international modal analysis conference*, Vol. 1, pp. 110–116, SEM, Orlando, 1982. 55, 96

[177] **Albakri, M. I.** and **Tarazaga, P. A.**, *Dynamics analysis of a piezoelectric augmented beam system with adhesive bonding layer effects*, Journal of Intelligent Material Systems and Structures, 2016. 84

[178] **Schwarz, B. J.** and **Richardson, M. H.**, *Introduction to operating deflection shapes*, CSI Reliability Week, Vol. 10, pp. 121–126, 1999. 90, 114

[179] **Rocklin, G. T., Crowley, J.** and **Vold, H.**, *A comparison of H1, H2, and Hv frequency response functions*, *Proceedings of the 3rd international Modal Analysis Conference*, Vol. 1, pp. 272–278, 1985. 91

[180] **Ewins, D. J.**, Modal testing: theory and practice, Vol. 15, Research studies press Letchworth, 1984. 91, 96, 114

[181] **Peeters, B., Van der Auweraer, H., Guillaume, P.** and **Leuridan, J.**, *The PolyMAX frequency-domain method: a new standard for modal parameter estimation?*, Shock and Vibration, Vol. 11, No. 3-4, pp. 395–409, 2004. 92

[182] **Schwarz, B.** and **Richardson, M.**, *Proportional Damping from Experimental Data*, *Topics in Modal Analysis, Volume 7*, pp. 179–186, Springer, 2014. 93

[183] **Avirovik, D., Malladi, V. S., Priya, S.** and **Tarazaga, P. A.**, *Theoretical and experimental correlation of mechanical wave formation on beams*, Journal of Intelligent Material Systems and Structures, 2016. 97, 108

[184] **Malladi, V. S., Avirovik, D., Priya, S.** and **Tarazaga, P. A.**, *Characterization and representation of mechanical waves generated in piezo-electric augmented beams*, Smart Materials and Structures, Vol. 24, No. 10, pp. 105026, 2015. 97, 98, 104, 108, 122

[185] **Malladi, V. S., Albakri, M., Tarazaga, P. A.** and **Gugercin, S.**, *Reduced Plate Model Used for 2D Traveling Wave Propagation*, *ASME 2015 Conference on Smart Materials, Adaptive Structures and Intelligent Systems*, pp. V001T03A021–V001T03A021, American Society of Mechanical Engineers, 2015. 97

[186] **Musgrave, F. P., Malladi, V. S.** and **Tarazaga, P. A.**, *Generation of Traveling Waves in a 2D Plate for Future Drag Reduction Manipulation*, *IMAC XXXIV A Conference and Exposition on Structural Dynamics*, 2016. 97

[187] **Phoenix, A., Malladi, V. S.** and **Tarazaga, P. A.**, *Traveling Wave Phenomenon Through Piezoelectric Actuation of a Free-Free Cylindrical Tube*, *ASME 2015 Conference on Smart Materials, Adaptive Structures and Intelligent Systems*, pp. V002T04A018–V002T04A018, American Society of Mechanical Engineers, 2015. 97

[188] **Antoulas, A. C.**, Approximation of large-scale dynamical systems, Vol. 6, Siam, 2005. 105, 112, 116, 122

[189] **Baur, U., Benner, P.** and **Feng, L.**, *Model order reduction for linear and nonlinear systems: a system-theoretic perspective*, Archives of Computational Methods in Engineering, Vol. 21, No. 4, pp. 331–358, 2014. 105

[190] **Benner, P., Gugercin, S.** and **Willcox, K.**, *A survey of projection-based model reduction methods for parametric dynamical systems*, SIAM Review, Vol. 57, No. 4, pp. 483–531, 2015. 105

[191] **Obinata, G.** and **Anderson, B. D.**, Model reduction for control system design, Springer Science & Business Media, 2012. 105

[192] **Benner, P., Mehrmann, V.** and **Sorensen, D. C.**, Dimension reduction of large-scale systems, Vol. 45, Springer, 2005. 105

[193] **Hesthaven, J. S., Rozza, G.** and **Stamm, B.**, Certified Reduced Basis Methods for Parametrized Partial Differential Equations, Springer, 2015. 105

[194] **Antoulas, A. C., Sorensen, D. C.** and **Gugercin, S.**, *A survey of model reduction methods for large-scale systems*, Contemporary mathematics, Vol. 280, pp. 193–220, 2001. 105

[195] **Antoulas, A. C., Beattie, C. A.** and **Gugercin, S.**, *Interpolatory model reduction of large-scale dynamical systems*, *Efficient Modeling and Control of Large-Scale Systems*, pp. 3–58, Springer, 2010. 105, 125, 126, 128

[196] **Beattie, C.** and **Gugercin, S.**, *Model reduction by rational interpolation*, arXiv preprint arXiv:1409.2140, 2014. 105

[197] **Craig, R.**, *A brief tutorial on substructure analysis and testing*, *SPIE proceedings series*, pp. 899–908, Society of Photo-Optical Instrumentation Engineers, 2000. 109

[198] **Fregolent, A.** and **Sestieri, A.**, *Identification of rigid body inertia properties from experimental data*, Mechanical systems and signal processing, Vol. 10, No. 6, pp. 697–709, 1996. 109

[199] **Bretl, J.** and **Conti, P.**, *Rigid body mass properties from test data*, *Proceedings of the 5th International Modal Analysis Conference*, pp. 6–9, 1987. 109

[200] **Balmès, E.**, *Use of generalized interface degrees of freedom in component mode synthesis*, OFFICE NATIONAL D ETUDES ET DE RECHERCHES AEROSPATIALES ONERA-PUBLICATIONS-TP, 1996. 109

[201] **Bai, Z.** and **Demmel, J. W.**, *On swapping diagonal blocks in real Schur form*, Linear Algebra and Its Applications, Vol. 186, pp. 75–95, 1993. 110, 111

[202] **Granat, R., Kågström, B.** and **Kressner, D.**, *Parallel eigenvalue reordering in real Schur forms*, Concurrency and Computation: Practice and Experience, Vol. 21, No. 9, pp. 1225–1250, 2009. 110

[203] **Golub, G. H.** and **Van Loan, C. F.**, Matrix computations, Vol. 3, JHU Press, 2012. 110

[204] **Pastor, M., Binda, M.** and **Harčarik, T.**, *Modal assurance criterion*, Procedia Engineering, Vol. 48, pp. 543–548, 2012. 114

[205] **Moore, B.**, *Principal component analysis in linear systems: Controllability, observability, and model reduction*, Automatic Control, IEEE Transactions on, Vol. 26, No. 1, pp. 17–32, 1981. 115, 119

[206] **Mullis, C.** and **Roberts, R.**, *Synthesis of minimum roundoff noise fixed point digital filters*, IEEE Transactions on Circuits and Systems, Vol. 23, No. 9, pp. 551–562, 1976. 119

[207] **Hammarling, S.**, *Numerical solution of the stable, non-negative definite lyapunov equation lyapunov equation*, IMA Journal of Numerical Analysis, Vol. 2, No. 3, pp. 303–323, 1982. 120

[208] **Sorensen, D. C.** and **Zhou, Y.**, *Direct methods for matrix Sylvester and Lyapunov equations*, Journal of Applied Mathematics, Vol. 2003, No. 6, pp. 277–303, 2003. 120

[209] **Gugercin, S.** and **Antoulas, A. C.**, *A survey of model reduction by balanced truncation and some new results*, International Journal of Control, Vol. 77, No. 8, pp. 748–766, 2004. 122

[210] **Benner, P., Kürschner, P.** and **Saak, J.**, *Frequency-Limited Balanced Truncation with Low-Rank Approximations*, SIAM Journal on Scientific Computing, Vol. 38, No. 1, pp. A471–A499, 2016. 122

[211] **Benner, P., Li, J.-R.** and **Penzl, T.**, *Numerical solution of large-scale Lyapunov equations, Riccati equations, and linear-quadratic optimal control problems*, Numerical Linear Algebra with Applications, Vol. 15, No. 9, pp. 755–777, 2008. 123

[212] **Sabino, J.**, Solution of large-scale Lyapunov equations via the block modified Smith method, Ph.D. thesis, Citeseer, 2006. 123

[213] **Gugercin, S., Sorensen, D. C.** and **Antoulas, A. C.**, *A modified low-rank Smith method for large-scale Lyapunov equations*, Numerical Algorithms, Vol. 32, No. 1, pp. 27–55, 2003. 123

[214] **Penzl, T.**, *A cyclic low-rank Smith method for large sparse Lyapunov equations*, SIAM Journal on Scientific Computing, Vol. 21, No. 4, pp. 1401–1418, 1999. 123

[215] **Benner, P., Kürschner, P.** and **Saak, J.**, *Self-generating and efficient shift parameters in ADI methods for large Lyapunov and Sylvester equations*, Electronic Transactions on Numerical Analysis, Vol. 43, pp. 142–162, 2014. 123

[216] **Druskin, V., Knizhnerman, L.** and **Simoncini, V.**, *Analysis of the rational Krylov subspace and ADI methods for solving the Lyapunov equation*, SIAM Journal on Numerical Analysis, Vol. 49, No. 5, pp. 1875–1898, 2011. 123

[217] **Stykel, T.** and **Simoncini, V.**, *Krylov subspace methods for projected Lyapunov equations*, Applied Numerical Mathematics, Vol. 62, No. 1, pp. 35–50, 2012. 123

[218] **Gugercin, S., Antoulas, A. C.** and **Beattie, C.**, *H_2 model reduction for large-scale linear dynamical systems*, SIAM journal on matrix analysis and applications, Vol. 30, No. 2, pp. 609–638, 2008. 124, 126, 127, 128, 129

[219] **Gallivan, K., Vandendorpe, A.** and **Van Dooren, P.**, *Model Reduction of MIMO Systems via Tangential Interpolation*, SIAM Journal on Matrix Analysis and Applications, Vol. 26, No. 2, pp. 328–349, 2005. 125

[220] **Meier III, L.** and **Luenberger, D.**, *Approximation of linear constant systems*, IEEE Transactions on Automatic Control, Vol. 12, No. 5, pp. 585–588, 1967. 126

[221] **Beattie, C. A.** and **Gugercin, S.**, *Model Reduction by Rational Interpolation*, *Model Reduction and Approximation: Theory and Algorithms*, edited by Benner, P., Cohen, A., Ohlberger, M. and Willcox, K., SIAM, Philadelphia, PA, 2016. 126

[222] **Beattie, C.** and **Gugercin, S.**, *Realization-independent $\mathcal{H}_2$-approximation*, 51st IEEE Conference on Decision and Control, Maui, HI, 2012. 126

[223] **Van Dooren, P., Gallivan, K.** and **Absil, P.**, *$\mathcal{H}_2$-optimal model reduction of MIMO systems*, Applied Mathematics Letters, Vol. 21, No. 12, pp. 1267–1273, 2008. 126

[224] **Clark, R. L.** and **Fuller, C. R.**, *Active control of structurally radiated sound from an enclosed finite cylinder*, Journal of intelligent material systems and structures, Vol. 5, No. 3, pp. 379–391, 1994. 145

[225] **Itoh, M., Tamano, S., Yokota, K.** and **Taniguchi, S.**, *Drag reduction in a turbulent boundary layer on a flexible sheet undergoing a spanwise traveling wave motion*, Journal of Turbulence, Vol. 7, pp. N27, 2006. 164

[226] **Klumpp, S., Meinke, M.** and **Schröder, W.**, *Drag reduction by spanwise transversal surface waves*, Journal of Turbulence, Vol. 11, pp. N22, 2010. 164

[227] **Tamano, S.** and **Itoh, M.**, *Drag reduction in turbulent boundary layers by spanwise traveling waves with wall deformation*, Journal of Turbulence, Vol. 13, pp. N9, 2012. 164

[228] **Bai, H., Zhou, Y., Zhang, W., Xu, S., Wang, Y.** and **Antonia, R.**, *Active control of a turbulent boundary layer based on local surface perturbation*, Journal of Fluid Mechanics, Vol. 750, pp. 316–354, 2014. 164